

MARTTA HÄKLI

Stem Cell-Based Cardiac Ischemia Model

Tampere University Dissertations 640

MARTTA HÄKLI

Stem Cell-Based Cardiac Ischemia Model

ACADEMIC DISSERTATION

To be presented, with the permission of
the Faculty of Medicine and Health Technology
of Tampere University,
for public discussion in the auditorium F114
of the Arvo-building, Arvo Ylpön katu 34, Tampere,
on 19th of August 2022, at 12 o'clock.

ACADEMIC DISSERTATION

Tampere University, Faculty of Medicine and Health Technology
Finland

<i>Responsible supervisor</i>	Docent Mari Pekkanen-Mattila Tampere University Finland	
<i>Supervisors</i>	Professor Katriina Aalto-Setälä Tampere University Finland	Professor Minna Kellomäki Tampere University Finland
<i>Pre-examiners</i>	Professor Juha Hartikainen University of Eastern Finland Finland	Docent Riikka Martikainen University of Eastern Finland Finland
<i>Opponent</i>	Professor Robert Passier University of Twente The Netherlands	
<i>Custos</i>	Professor Katriina Aalto-Setälä Tampere University Finland	

The originality of this thesis has been checked using the Turnitin OriginalityCheck service.

Copyright ©2022 Martta Häkli

Cover design: Roihu Inc.

ISBN 978-952-03-2500-8 (print)

ISBN 978-952-03-2501-5 (pdf)

ISSN 2489-9860 (print)

ISSN 2490-0028 (pdf)

<http://urn.fi/URN:ISBN:978-952-03-2501-5>

PunaMusta Oy – Yliopistopaino
Joensuu 2022

ACKNOWLEDGEMENTS

The research for this dissertation was carried out in Heart Group at Tampere University, Faculty of Medicine and Health Technology during 2018–2022 as a part of Center of Excellence in Body on-Chip Research. I want to thank the former and current deans of this faculty, Prof. Tapio Visakorpi and Prof. Seppo Parkkila for the provision of the excellent research facilities as well as the interdisciplinary working environment during my studies. I am grateful for all the financial supporters of this dissertation work, including the Doctoral Programme in Biomedical Sciences and Engineering at Tampere University, Finnish Cultural Foundation, Maud Kuistila Memorial Foundation, Inkeri and Mauri Vänskä Foundation, and Paavo Nurmi Foundation.

I want to thank Prof. Katriina Aalto-Setälä, the principal investigator of Heart Group, who gave me the opportunity to work in her research group since 2017. I am forever grateful for having been a part of your group and being allowed and encouraged to learn conducting research in an inspiring and skilled environment. Furthermore, I want to express my deepest gratitude towards my main supervisor Doc. Mari Pekkanen-Mattila for guiding and encouraging me through my doctoral studies and research, and for giving me confidence to go on through the obstacles I have encountered. I want to also thank Prof. Minna Kellomäki for her input in my research as my supervisor.

I am grateful for my thesis committee members Prof. Pasi Kallio, Prof. Jari Hyttinen and Adj. Prof. Virpi Talman for their comments and contribution throughout my doctoral studies. I want to further thank my pre-examiners Prof. Juha Hartikainen and Doc. Riikka Martikainen for their input and constructive criticism on my thesis. Moreover, I want to thank all my coauthors for their contribution to this thesis, as without their expertise this would not have been possible. Particularly, I want to thank Dr. Antti-Juhana Mäki for doing an enormous work in the development of the field potential analysis during my thesis project, MSc. Tech. Joose Kreutzer for helping me to get to know the ischemia modelling platform, and Dr. Hannu Välimäki for helping me with the oxygen measurements. In addition, I am grateful for Prof.

Susanna Narkilahti, MSc. Satu Jäntti and Dr. Tiina Joki for introducing me to the world of neurons and cardiac innervation for a truly interesting project.

I further want to thank the core facilities of Tampere University, including Electrophysiology core and Juha Heikkilä for his assistance and teaching of the MEA measurements, as well as Imaging core and Outi Paloheimo for her assistance and teaching of fluorescent imaging. I am also grateful for the enormously skilled and committed laboratory technicians Henna Lappi and Markus Haponen for the maintenance of Heart lab, and their guidance, help and insights with cell culture and differentiation, as well as the company and time spend in the lab. Further, I want to thank the whole Heart Group for guiding me into the world of research and allowing me to grow towards an independent researcher. I have been truly fortunate and privileged to work with you all. You have created a wonderful working environment where each of us is allowed to be themselves. I have really enjoyed being a part of the group. I want to further extend my gratitude towards all my colleagues for sharing your knowledge of research and life with me.

I want to thank all my friends, my tricking and taido families, with whom I have been able to get my mind off of work and balancing my life. Especially, I want to thank Helmiina for being able to share the ups and downs of life for a long time already. Your support has been invaluable.

I am forever grateful for my amazing family for their support throughout my whole life. I want to thank my mom Pirkko-Liisa Nykänen for all her unconditional love and support. I want to thank my dad Prof. Jouni Häkli and my stepmom Prof. Kirsi Kallio-Häkli for setting an example for my career as a researcher and supporting me throughout the journey. I want to thank my sisters Silja, Miina and Olga for their love and support.

Finally, I want to thank my life partner Hannu Nieminen. I have always been able to count on you and your support when I needed it. You have taught me to show compassion to myself, although I am still learning. I am so excited about what the future holds for us.

Tampere, August 2022

A handwritten signature in black ink, appearing to read 'Mervi Häkli', written in a cursive style.

ABSTRACT

Ischemic heart disease is the most common cardiovascular disease and causes more deaths and morbidity than any other disease. A lot of effort has been put into research of drugs and treatments for alleviating the ischemia-reperfusion injury and for minimizing the infarct size after reperfusion. However, most of the research has been conducted in different animal models and reproducing the results in human has proven difficult. Difference in physiology and disease mechanism stemming from the species difference has been suggested as one reason for the failure. Thus, human based models are needed.

The main aim of this dissertation was to establish a human based model of cardiac ischemia-reperfusion. Human adult cardiomyocytes are difficult to acquire due to invasive harvesting, but human induced pluripotent stem cells (hiPSC) can be endlessly differentiated into cardiomyocytes (CM), providing an unlimited source of human cardiomyocytes. Nevertheless, hiPSC-derived CMs (hiPSC-CMs) are developmentally immature resembling more foetal than adult CMs hindering their utilization in several applications. Especially the metabolic immaturity has been suggested to make hiPSC-CMs resistant to hypoxia induced injury limiting their use in modelling cardiac ischemia-reperfusion. Despite the immature phenotype, hiPSC-CMs have recently been utilized in modelling myocardial ischemia-reperfusion. However, these studies have focused on cell viability and molecular markers of hypoxia and cell injury, but the functional responses have been significantly less characterized.

The first study of this dissertation focused on inducing maturation of the hiPSC-CMs by culturing them on polyethylene terephthalate textiles, which was observed to improve structural maturation of the CMs. In addition to topographical cues, coculture with other cell types is known to improve hiPSC-CM maturation. Furthermore, cardiac function is tightly regulated by cardiac autonomic nervous system (cANS), which is also known to contribute to ischemia-reperfusion injury and related arrhythmias. Thus, the second study of this thesis focused on establishing a cardiac innervation model, which in

the future could be used in studying the effect of cANS to the ischemia-reperfusion injury and its treatments. In the third and fourth study of this dissertation, cardiac ischemia and reperfusion were modelled by inducing hypoxia and reoxygenation to hiPSC-CMs. As electrophysiology is an important aspect of CM function and contraction, microelectrode array technology was used to capture the electrophysiological responses of the hiPSC-CMs to different oxygen conditions and the observed changes were compared to the electrophysiological changes known to occur in adult CMs during ischemia and reperfusion.

The results presented in this dissertation show that hiPSC-CMs have potential as a cell model of cardiac ischemia-reperfusion. The platform utilized for inducing hypoxia and reoxygenation to the hiPSC-CMs allows the use of extensive set of methods for thorough characterization of the hiPSC-CM response to the ischemic insult. Furthermore, the incorporated continuous measurement of oxygen partial pressure further improves the understanding of the cellular responses to hypoxia and reoxygenation and allows the validation of specific oxygen conditions experienced by the cells. The platform for the ischemia modelling could be utilized with the presented cardiac innervation model, which would allow the modelling of the cANS in ischemia-reperfusion and be the next step for *in vitro* ischemia modelling.

TIIVISTELMÄ

Sydän- ja verisuonitaudit aiheuttavat maailmanlaajuisesti enemmän kuolemia kuin mikään muu tauti, ja iskeeminen sydänsairaus on näistä taudeista yleisin. Iskemia-reperfuusioaurion ja sen hoitojen tutkimukseen on panostettu paljon, mutta eläinkokeista saatuja tuloksia on ollut vaikea toistaa ihmisissä. Yhdeksi syyksi epäonnistumisiin on ehdotettu lajien välisiä fysiologisia eroja, jotka johtavat eroihin myös taudin mekanismeissa. Tämän vuoksi on tarve myös ihmisperäisille solumalleille iskeemiseen sydänsairauteen.

Tämän väitöskirjan päätavoite oli kehittää ihmispohjainen malli iskeemisen sydänsairauden tutkimukseen. Aikuisen sydänlihassoluja ei kuitenkaan ole helposti saatavilla tutkimuskäyttöön, koska niiden kerääminen ihmisestä on hankalaa ja vaatii invasiivisen toimenpiteen. Ihmisen indusoiduista erittäin monikykyisistä kantasoluista (hiPSC) erilaistetut sydänlihassolut ovat ihanteellinen vaihtoehto aikuisen sydänlihassoluille, koska niitä voidaan erilaistaa loputtomasti. hiPSC-sydänlihassolut ovat kuitenkin enemmän sikiön kuin aikuisen sydänlihassolujen kaltaisia, mikä rajoittaa niiden hyödyntämistä eri sovelluksissa. Erityisesti iskeemisen sydänsairauden mallintamisessa hiPSC-sydänlihassolujen glykolyysiin perustuva metabolia on ongelma, koska sen tiedetään parantavan sydänlihassolujen sietokykyä hapettomille olosuhteille. Siitä huolimatta viime aikoina on julkaistu muutamia hiPSC-sydänlihassoluja hyödyntäviä malleja iskeemiselle sydänsairaudelle, mutta niissä on keskitytty solukuolemaan sekä iskemian molekulaarisiin vasteisiin vähähappisissa olosuhteissa, elektrofysiologisten ja toiminnallisten vasteiden jäädessä paitsioon.

Väitöskirjan ensimmäinen osatyö keskittyi parantamaan hiPSC-sydänlihassolujen kypsyttä kasvattamalla niitä poyletyleenitereftalaattitekstiilien päällä, sillä topografisten kasvualustojen on tutkimuksissa havaittu parantavan hiPSC-sydänlihassolujen rakenteellisia ominaisuuksia. Topografisten kasvatusalustojen lisäksi yhteisviljelyn muiden sydämelle ominaisten solutyyppeiden kanssa on havaittu parantavan hiPSC-sydänlihassolujen ominaisuuksia. Sydämen toimintaan vaikuttaa oleellisesti sydämen

autonominen hermosto, joka vaikuttaa sydämen toimintaan myös iskeemisessä sydänsairaudessa sekä muun muassa iskemia-reperfuusio-vaurioon liittyvissä rytmihäiriöissä. Tämän väitöskirjan toisessa osatyössä kehitettiin sydämen hermotusmalli hiPSC-sydänlihassoluista ja hiPSC-hermosoluista, jota voitaisiin tulevaisuudessa hyödyntää muun muassa iskeemisen sydänsairauden ja sen hoitojen mallintamisessa siten, että voidaan arvioida myös hermosolujen vaikutusta iskemia-reperfuusio-vaurioon. Väitöskirjan kolmas ja neljäs osatyö keskittyivät hiPSC-sydänlihassolujen hyödyntämiseen iskemiamallinnuksessa. Iskemiaa mallinnettiin hypoksialla, jonka jälkeen soluviljelmien uudelleenhapetus jäljitteli reperfuusiota. Sydänlihassolujen elektrofysiologia on tärkeä osa niiden toiminnallisuutta, ja sitä tutkittiin osatöissä mikroelektrodisiru-tekniikan avulla. hiPSC-sydänlihassoluissa havaittuja vasteita verrattiin aikuisen sydänlihassolujen tunnettuihin vasteisiin iskemian ja reperfuusion aikana.

Tämän väitöskirjan tulokset osoittivat, että hiPSC-sydänlihassoluja voidaan hyödyntää sydämen iskemiamallinnuksessa. Hypoksian ja uudelleenhapetuksen luomiseen käytetty laitteisto mahdollistaa useiden eri menetelmien käyttämisen solujen vasteiden perusteelliseen tutkimukseen. Laitteistoon yhdistetty hapen osapaineen reaaliaikainen ja jatkuva mittaus suoraan soluviljelymediumista mahdollistaa soluviljelmän happipitoisuuden tarkkailun sekä solujen vasteiden vertaamiseen mediumin happipitoisuuden muutoksiin. Tulevaisuudessa väitöskirjan toisessa osatyössä kehitettyä sydämen hermotusmallia voidaan hyödyntää yhdessä hypoksian ja uudelleenhapetuksen luomiseen käytettyä laitteistoa, minkä avulla on mahdollista tutkia sydämen autonomisen hermoston vasteita ja vaurioita iskeemisessä sydänsairaudessa.

CONTENTS

1	Introduction	19
2	Literature review.....	22
2.1	Heart and cardiomyocytes.....	22
2.1.1	Structure and function of healthy heart.....	22
2.1.2	Cardiac function in ischemic heart disease.....	31
2.2	Human induced pluripotent stem cell-derived cardiomyocytes.....	37
2.2.1	Stem cells and induced pluripotent stem cells.....	37
2.2.2	Differentiation	38
2.2.3	Maturation	40
2.3	Modelling ischemic heart disease	46
2.3.1	In vivo models	46
2.3.2	Ex vivo models.....	51
2.3.3	In vitro models.....	51
3	Aims of the study.....	59
4	Materials and methods.....	60
4.1	Ethical considerations	60
4.2	Cell culture and differentiation	60
4.2.1	Human induced pluripotent stem cells.....	60
4.2.2	Differentiation	61
4.2.3	Magnetic activated cell sorting.....	62
4.3	Polyethylene terephthalate textiles.....	63
4.3.1	Textile preparation.....	63
4.3.2	Cell culture on textiles.....	64
4.4	Coculture of neurons and cardiomyocytes on 3D3C chip	64

4.4.1	3D3C chip preparation.....	64
4.4.2	Coculture of neurons and cardiomyocytes.....	65
4.4.3	Neuronal stimulation and cardiomyocyte video recording.....	65
4.5	Modelling ischemia and reperfusion.....	66
4.5.1	Seeding cardiomyocytes on 1-wells on glass and microelectrode array.....	66
4.5.2	OxyGenie and 1-well assembly for control of oxygen partial pressure.....	67
4.5.3	Modelling chronic ischemia and reperfusion.....	67
4.5.4	Modelling acute ischemia and reperfusion.....	68
4.5.5	Measurement of oxygen partial pressure.....	69
4.6	Microelectrode array.....	70
4.6.1	Field potential recording.....	70
4.6.2	Field potential analysis.....	70
4.7	Protein and gene expression.....	72
4.7.1	Immunocytochemistry.....	72
4.7.2	Western blot.....	74
4.7.3	Reverse transcription quantitative polymerase chain reaction.....	75
4.8	Quantitative analysis of the fluorescent images.....	77
4.8.1	Cell and sarcomere alignment.....	77
4.8.2	Sarcomere coverage and size of nuclei.....	78
4.9	Statistical analysis.....	78
5	Results.....	79
5.1	Maturation of hiPSC-CMs cultured on PET textiles.....	79
5.1.1	Morphology and sarcomere orientation.....	79
5.1.2	Expression of cardiac specific genes.....	79
5.2	Coculture of hiPSC-CMs and hiPSC-neurons on 3D3C chip.....	81
5.2.1	Coculture and viability.....	81

5.2.2	3D3C chip application for RT-qPCR and functionality studies	83
5.3	Modelling ischemia and reperfusion with hiPSC-CMs	83
5.3.1	Oxygen dynamics in the 1-well assemblies	84
5.3.2	hiPSC-CM morphology and protein expression	85
5.3.3	Expression of hypoxia related genes	88
5.3.4	Electrophysiological response of hiPSC-CMs to hypoxia and reoxygenation	89
6	Discussion	96
6.1	Improved structural maturation of hiPSC-CMs	96
6.2	Cardiac innervation model on 3D3C chip	99
6.3	Modelling cardiac ischemia and reperfusion with hiPSC-CMs	101
6.3.1	Deterioration of hiPSC-CM sarcomere structure and expression of sarcomeric genes	102
6.3.2	Increased glycolysis-related gene expression	104
6.3.3	hiPSC-CM electrophysiological properties changed during hypoxia	105
6.4	Limitations of the study	109
6.5	Future perspectives	111
7	Conclusion	114

ABBREVIATIONS

<i>A_{dep}</i>	Field potential depolarization amplitude
AP	Action potential
ATP	Adenosine triphosphate
AV node	Atrioventricular node
BL	Baseline
BNP	B-type natriuretic peptide
BSA	Bovine serum albumin
cANS	Cardiac autonomic nervous system
CCS	Cardiac conduction system
cFPD	Corrected field potential duration
CICR	Calcium induced calcium release
CM	Cardiomyocyte
cMyBP-C	Cardiac myosin binding protein C
CoPP	Cobalt protoporphyrin
cTnT	Cardiac troponin T
EB	Embryoid body
EC coupling	Excitation-contraction coupling
ECG	Electrocardiogram
ESC	Embryonic stem cell
FA	Fatty acid
FPD	Field potential duration
FPP	Field potential propagation

HCM	Human cardiac myocytes
hESC	Human embryonic stem cell
HFF	Human foreskin fibroblast
HIF	Hypoxia inducible factor
HIF1- α	Hypoxia inducible factor 1 alpha
hiPSC	Human induced pluripotent stem cell
hiPSC-CM	Human induced pluripotent stem cell-derived cardiomyocyte
ICC	Immunocytochemistry
$I_{Ca,L}$	Inward L-type Ca^{2+} current
IHD	Ischemic heart disease
I_{K1}	Inward rectifying K^+ current
I_{Kr}	Rapid delayed rectifier K^+ current
I_{Ks}	Slow delayed rectifier K^+ current
I_{Kur}	Ultrarapid voltage-dependent K^+ current
I_{Na}	Inward Na^+ current
iPSC	induced pluripotent stem cell
IR	Ischemia-reperfusion
IRI	Ischemia-reperfusion injury
I_{to}	Transient outward K^+ currents
$I_{to,fast}$	Fast transient outward K^+ current
$I_{to,slow}$	Slow transient outward K^+ current
MACS	Magnetic activated cell sorting
MEA	Microelectrode array
MEF	Mouse embryonic fibroblast

MI	Myocardial infarction
mPTP	Mitochondrial permeability transition pore
MyBP-C	Myosin binding protein C
MyHC	Myosin heavy chain
NCX	Na ⁺ -Ca ²⁺ exchanger
NF-H	Neurofilament NF-H 200
NHE	Na ⁺ -H ⁺ exchanger
NKA	Na ⁺ -K ⁺ ATPase
PET	Polyethylene terephthalate
pO ₂	Oxygen partial pressure
PSC	Pluripotent stem cell
ROS	Reactive oxygen species
RT	Room temperature
RT-qPCR	Reverse transcription quantitative polymerase chain reaction
RyR2	Ryanodine receptor 2
SA node	Sinoatrial node
SERCA	Sarcoplasmic Ca ²⁺ ATPase
SR	Sarcoplasmic reticulum
TBS	Tris-buffered saline
<i>t_{dep}</i>	Field potential depolarization time
<i>t_{FPP}</i>	Field potential propagation time
T-tubule	Transverse tubule
βIII-Tub	β-tubulin III

ORIGINAL PUBLICATIONS

This dissertation is based on three original and peer-reviewed publications listed below and referred in the text as studies I-III.

- I** Pekkanen-Mattila, M., **Häkli, M.**, Pölönen, R.-P., Mansikkala, T., Junnila, A., Talvitie, E., Koivisto, J.T., Kellomäki, M. & Aalto-Setälä, K. (2019). Polyethylene terephthalate textiles enhance the structural maturation of human induced pluripotent stem cell-derived cardiomyocytes, *Materials (Basel)*, Vol. 12, No. 1805, <https://doi.org/10.3390/ma12111805>
- II** **Häkli, M.***, Jäntti, S.*, Joki, T., Sukki, L., Tornberg, K., Aalto-Setälä, K. Kallio, P., Pekkanen-Mattila, M. & Narkilahti, S. (2022) Human neurons form axon-mediated functional connections with human cardiomyocytes in compartmentalized microfluidic chip, *International Journal of Molecular Sciences*, Vol. 23, No. 3148, <https://doi.org/10.3390/ijms23063148>
- III** **Häkli, M.**, Kreutzer, J., Mäki, A.-J., Välimäki, H., Lappi, H., Huhtala, H., Kallio, P., Aalto-Setälä, K. & Pekkanen-Mattila, M. (2021). Human induced pluripotent stem cell-based platform for modeling cardiac ischemia, *Scientific Reports*, Vol. 11, No. 4153, <https://doi.org/10.1038/s41598-021-83740-w>

This dissertation is also based on the following unpublished manuscript, which is later in the text referred to as study IV.

- IV** **Häkli, M.**, Kreutzer, J., Mäki, A.-J., Välimäki, H., Cherian, R.M., Kallio, P., Aalto-Setälä, K. & Pekkanen-Mattila, M. Electrophysiological changes of human induced pluripotent stem cell-derived cardiomyocytes during acute hypoxia and reoxygenation.

* These authors contributed equally to this work.

AUTHOR'S CONTRIBUTION

- I** This study was designed by M. Pekkanen-Mattila. M. Häkli was responsible for majority of the cell culture experiments and data analysis and assembly in the experiment phase. M. Häkli wrote the manuscript with the first author M. Pekkanen-Mattila.
- II** This study was done as cooperation by K. Aalto-Setälä's Heart Group and S. Narkilahti's Neuro Group. The study was codesigned by M. Häkli, T. Joki, M. Pekkanen-Mattila and S. Narkilahti. M. Häkli was responsible for hiPSC-CM differentiation and dissociation, whereas the coculture of hiPSC-CMs and hiPSC-neurons was performed by T. Joki and S. Jäntti. Sample collection and downstream analyses were done together with Neuro Group's master's degree student S. Jäntti. M. Häkli was responsible for data analysis and assembly. M. Häkli and S. Jäntti cowrote the manuscript as a shared first author.
- III–IV** These studies were designed by M. Häkli, who also conducted the cell culture experiments, major part of the data analysis and assembly as well as wrote the manuscripts as a first author.

1 INTRODUCTION

Ischemic heart disease (IHD) is the most common cardiovascular disease and a major cause of death worldwide (M. A. Khan et al., 2020). The cardiomyocytes (CMs) responsible for the contractile function of the heart are injured or die as a result of IHD, due to the lack of oxygen and nutrients as well as due to the accumulation of metabolic waste in the cells and their environment (Ambrose & Singh, 2015). Furthermore, reperfusion of the heart by re-establishing blood flow into the ischemic area causes further injury to the CMs (Kalogeris et al., 2016). As CMs have only little tendency to regeneration, the healing of the injured tissue occurs via scarring, formation of non-specific and non-functional tissue, which can induce arrhythmias in the IHD patient (Lerman et al., 2016). Currently, animals and primary animal CMs are the most used models of IHD and in testing of new treatment options. However, majority of the drugs showing promising results in animal trials have not been successful in human trials due to various reasons (T. Chen & Vunjak-Novakovic, 2019). Thus, reliable human-based models are needed for modelling cardiac ischemia-reperfusion injury (IRI) and for developing new treatments to the injury.

Human induced pluripotent stem cells (hiPSCs) can be endlessly differentiated into CMs for example for research purposes and clinical applications, which makes them an attractive source of human CMs (Karakikes et al., 2015). However, hiPSC-derived CMs (hiPSC-CMs) resemble more foetal than adult CMs regarding structure, function, metabolism as well as gene and protein expression, which can hinder their utilization in different applications (Ahmed et al., 2020). For example, it is known that foetal and hiPSC-CMs are more resistant to low environmental oxygen, i.e., hypoxia, as they rely more on glycolytic metabolism whereas adult CMs rely mainly on fatty acid (FA) oxidation (Hidalgo et al., 2018). However, researchers have developed several methods to improve different aspects of the hiPSC-CM maturity, such as culturing in a conditioned medium supporting the shift of the CM metabolism towards fatty acid oxidation (Feyen

et al., 2020), different structured cell culture substrates to guide the structure and morphology of the CMs (J. Han et al., 2016; Rao et al., 2013), and electrical or mechanical conditioning to improve the electrophysiological and contractile properties of the CMs (Ruan et al., 2016). Furthermore, coculture with other cell types characteristic to cardiac tissue has been shown to improve hiPSC-CM maturation (Vuorenpää et al., 2017). Despite the advancements in the differentiation and maturation of hiPSC-CMs, there still are no protocols for producing fully mature and adult-like CMs (Ahmed et al., 2020; Liao et al., 2021).

Despite these limitations, hiPSC-CMs have lately been utilized in cardiac ischemia modelling (Canfield et al., 2016; T. Chen & Vunjak-Novakovic, 2019; Fernández-Morales et al., 2019; Fiedler et al., 2019; Hidalgo et al., 2018; Lu et al., 2018; Sebastião et al., 2020; Shah et al., 2019; Veldhuizen et al., 2022; H. Wei et al., 2019; W. Wei et al., 2017). These models have successfully reproduced several known responses of ischemia and reperfusion, including cell death (T. Chen & Vunjak-Novakovic, 2019; Hidalgo et al., 2018; Lu et al., 2018; W. Wei et al., 2017), structural disruption of the sarcomeres (T. Chen & Vunjak-Novakovic, 2019; Sebastião et al., 2020), changes in the beating frequency and contractility (Shah et al., 2019; Veldhuizen et al., 2022; W. Wei et al., 2017), as well as calcium overload (W. Wei et al., 2017) and arrhythmias (Veldhuizen et al., 2022; W. Wei et al., 2017). Although some evaluation of the hiPSC-CM functional response to ischemia-reperfusion (IR) has been done (Shah et al., 2019; Veldhuizen et al., 2022; H. Wei et al., 2019; W. Wei et al., 2017), the focus of the studies has been more on the molecular responses of the CMs during hypoxia and reoxygenation. Significantly less research has been conducted on the detailed electrophysiological response of hiPSC-CMs in the ischemia models. However, CMs are electrically active cells and their major function as the contractile cells of the heart is tightly coupled to their electrophysiology (Eisner et al., 2017).

The main aim of this thesis was to establish a hiPSC-CM based model for cardiac ischemia-reperfusion. Furthermore, as was already established, the hiPSC-CM maturation impacts their utilization in ischemia modelling and disease modelling in general. Thus, one aim was to improve the hiPSC-CM maturation by culturing them on polyethylene terephthalate (PET) textiles. Moreover, a cardiac innervation model was established for future studies in

cardiac ischemia modelling, as cardiac function is known to be tightly regulated by cardiac autonomic nervous system (cANS) (Végh et al., 2016) and cardiac ischemia-reperfusion is known to affect the functioning of the cANS (Hadaya & Ardell, 2020; Kolettis et al., 2015). The focus in the ischemia modelling was on the electrophysiological changes observed using microelectrode array (MEA) technology combined with real-time monitoring of the oxygen partial pressure (pO_2) directly from the cell culture, which allowed comparison of hiPSC-CM electrophysiology and functionality to the oxygen level of the cell culture. Despite their immature phenotype the hiPSC-CMs successfully reproduced many key electrophysiological changes observed in the adult CMs during ischemia-reperfusion, demonstrating their usefulness in modelling IHD mechanisms and treatments. The extensive electrophysiological data collected from the hiPSC-CMs in the chronic and acute setup for inducing hypoxia and reoxygenation strongly contributes to the hiPSC-CM based ischemia-reperfusion modelling.

2 LITERATURE REVIEW

2.1 Heart and cardiomyocytes

2.1.1 Structure and function of healthy heart

The heart is an electromechanical pump (Nerbonne & Kass, 2005) in cardiovascular system. In this circulatory system cells, oxygen, nutrients, carbon dioxide, waste products, hormones and antibodies are transported between the tissues of the body via blood. The heart consists of four chambers and four valves, fibrous skeleton, heart wall and pericardium (Iaizzo, 2009). Furthermore, contraction of the heart is coordinated by cardiac conduction system (CCS) (Kennedy et al., 2016) and regulated by the metabolic state of the heart (Kolwicz et al., 2013) as well as by the cardiac autonomic nervous system (Habecker et al., 2016; Hasan, 2013; Végh et al., 2016). Cardiomyocytes are the contractile cells residing in myocardium and responsible for the heart contraction. CMs occupy approximately 70-85% of the myocardial volume but constitute only 20-30% of the total cell number. The other cell types interacting with CMs and residing in myocardium include endothelial cells, fibroblasts and leukocytes (Guo & Pu, 2020).

Heart structure

The four chambers of heart include left atrium and ventricle, and right atrium and ventricle (Figure 1A). The left and right sides are separated by interventricular and interatrial septa and they work as separate pumps, the left side pumping blood to systemic circulation, and right side pumping blood to pulmonary circulation (Iaizzo, 2009). The atrioventricular valves between atria and ventricles (tricuspid valve on the right and mitral valve on the left) as well as semilunar valves between ventricles and outgoing arteries (pulmonary artery on the right and aorta on the left) prevent the blood from flowing backwards (O'Donnell & Yutzey, 2020). Blood passively enters the relaxed right atrium from the systemic circulation. Upon atrial contraction the blood is further pumped into the relaxed right ventricle, from where the blood

is pumped to pulmonary circulation for oxygenation upon ventricular contraction. From the pulmonary circulation, the oxygenated blood enters the left atrium, which contracts and pumps the blood further to the left ventricle. Upon the ventricle contraction, the oxygenated blood is pumped into systemic circulation to be transferred to all tissues of the body (Figure 1A) (Iaizzo, 2009).

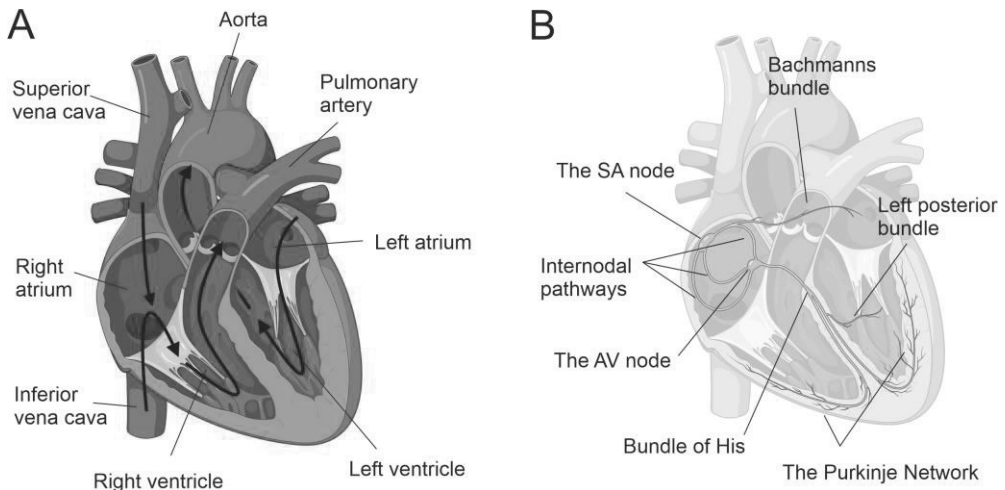


Figure 1. Structure of heart and cardiac conduction system (CCS) (created with BioRender.com). A) Heart consists of four chambers, left and right atria and ventricles. From the systemic circulation, blood enters the right chamber of heart, and is pumped into the right ventricle and further into the pulmonary circulation for oxygenation. Oxygenated blood enters the left atrium to be pumped into the left ventricle and back to systemic circulation. B) CCS consists of SA and AV nodes, bundle of His, bundle branches and Purkinje network. The SA node generates the electrical impulse leading to cardiac contraction, from where it rapidly propagates through the CCS and enables coordinated and synchronous contraction of the heart.

The heart wall consists of three layers, epicardium, myocardium and endocardium (Weinhaus & Roberts, 2009). Endocardium lines the inner surface of atria and ventricles and consists of endothelial tissue. The myocardium is the thick middle muscle layer, where the CMs responsible for the heart contraction reside in a highly organized structure (Weinhaus & Roberts, 2009). Epicardium is the outer layer of heart wall, consisting of mesothelial cells and connective and adipose tissues, where also the blood vessels (coronary arteries) and nerves that supply the heart are located

(Quijada et al., 2020). The heart resides within pericardium, a fibrous sack consisting of two layers with lubricating pericardial fluid in between, allowing the heart to move easily during contraction and relaxation (Weinhaus & Roberts, 2009).

Cardiac conduction system

Cardiac conduction system enables synchronous and coordinated contraction of the heart (Figure 1B). CCS consists of sinoatrial (SA) node, atrioventricular (AV) node, the bundle of His, bundle branches and the network of Purkinje cells (Anderson et al., 2009; Kennedy et al., 2016; Padala et al., 2021). The electrical impulse initiating the heart contraction is generated in the SA node, from where it propagates freely to the left and right atria, resulting in atrial contraction. However, the impulse does not propagate directly from the atria to the ventricles, as they are separated by the nonconducting fibrous skeleton. Thus, the electrical impulse is conducted from the SA node to the AV node via internodal pathway (Anderson et al., 2009; Padala et al., 2021). The AV node delays the impulse ensuring that the atria have enough time to pump the blood to the ventricles before their contraction. The impulse is further conducted from the AV node to the bundle of His, from where it continues to the left and right bundle branches of left and right ventricles and further to the Purkinje network. The CCS allows the impulse to proceed significantly faster compared to the CMs and enables the impulse conduction across the fibrous skeleton, resulting in a coordinated contraction of the ventricles (Kennedy et al., 2016).

In the myocardium, the electrical impulse is further conducted by the working CMs via gap junctions (Kennedy et al., 2016; Smit & Coronel, 2014; Weinhaus & Roberts, 2009) and other ion channels such as voltage gated Na^+ channels (Manring et al., 2018) present in the intercalated disks connecting adjacent CMs. These junctions allow adjacent cells to work synchronously by enabling fast conduction of the action potential from one CM to the next. Gap junctions are pore type channels between the CMs and composed of altogether 12 transmembrane connexin proteins. Six connexins form a connexon on the membrane of one cell, which then connects with a connexon of the adjacent cell to form a gap junction. The most abundant type of connexin in CMs is connexin 43. Gap junctions allow the flowing of ions and signalling molecules in both directions and significantly improve the conduction velocity and electrical activation of the CMs (Smit & Coronel, 2014).

Cardiac electrophysiology and excitation-contraction coupling

Heart contraction starts from the impulse from the SA node, from where the excitation propagates via the CCS throughout the whole myocardium (Figure 1B, 2A) (Kennedy et al., 2016). When the excitation reaches the cardiomyocytes, it results in the generation of an action potential (AP) (Figure 2B) and contraction via mechanism called excitation-contraction (EC) coupling (Figure 3) (Crocini & Gotthardt, 2021; Eisner et al., 2017; Kockskämper, 2016; Mahmoodzadeh & Dworatzek, 2019). There are generally five distinct phases in the AP (phases 0–4), however, they appear differently in different types of CMs (Figure 2A) depending on the expression of the specific ion channels contributing to each phase (Nerbonne & Kass, 2005). The excitation of a CM leads to rapid depolarization (phase 0), where the CM resting membrane potential (from -75 mV to -85 mV) quickly increases to 20–40 mV. This is followed by fast repolarization (phase 1) to 20–0 mV. After the fast repolarization, the ventricular CMs exhibit a long plateau phase (phase 2) of 200–300 msec, whereas it is less pronounced in atrial and nodal CMs. Late repolarization (phase 3) returns the membrane potential back to resting state (phase 4) (Kockskämper, 2016).

The negative resting membrane potential in CMs is mostly due to the inward rectifying K^+ current (I_{K1}), and the rapid depolarization is due to inward Na^+ current (I_{Na}). At the end of phase 0 I_{Na} inactivates and phase 1 fast repolarization is caused by the activation of the transient outward K^+ currents (I_{to}), which for ventricular CMs consist of both fast ($I_{to,fast}$) and slow ($I_{to,slow}$) component, but for atrial CMs only of the fast $I_{to,fast}$ component. The plateau phase is carried out by inward L-type and T-type Ca^{2+} current ($I_{Ca,L}$ and $I_{Ca,T}$) triggering also the calcium release from sarcoplasmic reticulum (calcium induced calcium release, CICR) to the cytoplasm. Repolarization in phase 3 in ventricular CMs is caused by rapid and slow delayed rectifier K^+ currents (I_{Kr} and I_{Ks}) as well as the I_{K1} responsible for the negative resting membrane potential, however these are less dominant in atrial CMs. On the other hand, the atrial CMs express ultrarapid voltage-dependent K^+ current (I_{Kur}), which contributes to both early and late repolarization in atrial CMs but is absent in ventricular CMs. (Kockskämper, 2016; Nerbonne & Kass, 2005)

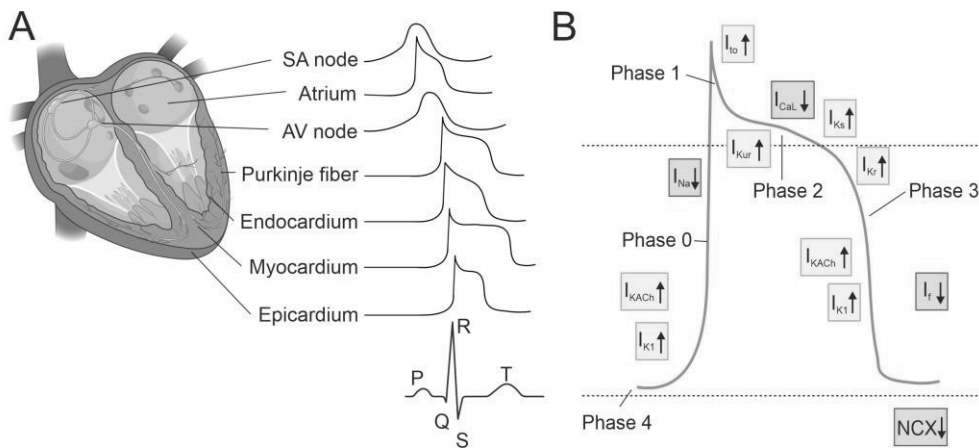


Figure 2. Cardiomyocyte action potential (AP) (created with BioRender.com). A) The AP morphology and timing varies between the different locations of heart and the different types of cardiomyocytes. The phases of the cardiac action potential also correspond with the surface electrocardiogram (ECG). B) Phases of the cardiomyocyte AP include upstroke (phase 0), early repolarization (phase 1), plateau phase (phase 2), final repolarization (phase 3) and resting phase (phase 4). Several ion currents are contributing to different phases of the cardiac action potential.

Pacemaker cells exhibit significantly different action potentials compared to the contracting myocardium. They have characteristically only three phases in the action potential, including phases 4, 3 and 0, and their resting membrane potential is more depolarized compared to working CMs. The phase 4 of pacemaker cells is called pacemaker potential to which the pacemaker current, or funny current (I_f) is characteristic. I_f results from the activation of hyperpolarization activated cyclic nucleotide gated channels that allow slow depolarization by Na^+ entry to the cell and are activated when the membrane potential becomes lower than -50 mV, which in turn allows the automatic initiation of the electrical impulse in the pacemaker cells. Furthermore, phase 0 depolarization starts in pacemaker cells when the membrane potential reaches -40 mV, however, whereas the phase 0 in working CMs is a result of I_{Na} , in pacemaker cells it results from $I_{Ca,L}$ and $I_{Ca,T}$. At the end of phase 0, the calcium channels inactivate, and potassium channels open resulting in I_{Ks} and I_{Kr} and phase 3 repolarization. When the repolarization of the membrane reaches the threshold for reactivation of the I_f , the pacemaker action potential initiates again. (Grant, 2009)

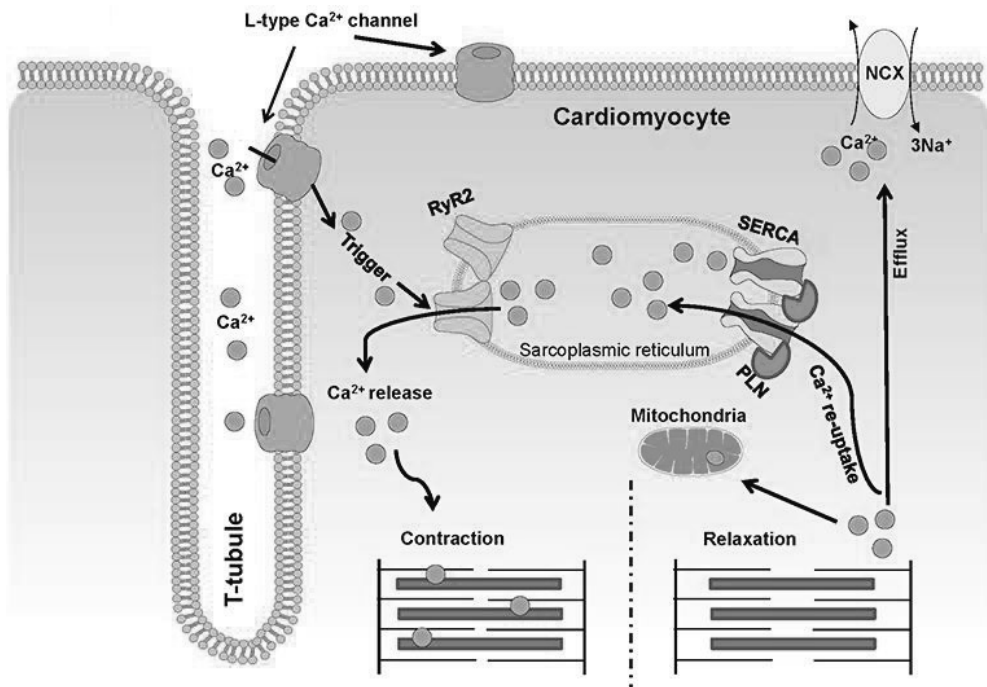


Figure 3. Excitation-contraction (EC) coupling in cardiomyocytes. Action potential results in opening of L-type Ca²⁺ channels, and Ca²⁺ enters the cell inducing further release of Ca²⁺ from sarcoplasmic reticulum (SR) via ryanodine receptors (RyR2). Intracellular Ca²⁺ binds to myofibril troponin leading to revelation of myosin binding sites of the actin filaments. Myosin binds to actin and crawls along the filament leading to sarcomere contraction. Relaxation occurs when Ca²⁺ is removed from the cytoplasm either to SR via SERCA or outside the cell via NCX (adapted from (Mahmoodzadeh & Dworatzek, 2019) under CC BY license: <https://creativecommons.org/licenses/by/4.0/>).

The contraction occurs via EC coupling (Figure 3) when the AP depolarizes the cell membrane leading to the opening of the L-type Ca²⁺ channels in the cell membrane and transverse tubules (T-tubules) (Eisner et al., 2017). T-tubules are invaginations of the cell membrane rich with ion channels and extend to the CM interior and form a network essential for the EC coupling process around the myofibrils (Figure 4A) (Crocini & Gotthardt, 2021; Hong & Shaw, 2017). As Ca²⁺ enters the CM cytoplasm, the increase in the intracellular Ca²⁺ concentration leads to CICR via ryanodine receptors from the sarcoplasmic reticulum (SR), which is a membranous tubule network around myofibrils (Eisner et al., 2017; Kockskämper, 2016). CM contraction occurs as the Ca²⁺ released to the cytoplasm binds to troponin in the myofibrils, the contractile structures of the CMs (Crocini & Gotthardt, 2021).

Sarcomere structure and function

Myofibrils consist of sarcomeres, the smallest contractile units of the CMs (Figure 4B) (Crocini & Gotthardt, 2021; Sarantitis et al., 2012). Sarcomeres in turn consist of thick myosin filaments attached to M-band in the middle of the sarcomere. Myosin filaments are interlocked with the thin actin filaments attached to the Z-disk at each end of the sarcomere (Sarantitis et al., 2012). In addition to thick and thin filaments, sarcomeres are composed of titin and several accessory proteins. The myosin filaments consist mainly of myosin heavy chain (MyHC), myosin essential and regulatory light chains and myosin binding proteins, of which type C (MyBP-C) is the most common. Thin filaments consist of actin, alpha tropomyosin, and troponin, which in turn is a heterotrimer consisting of C, I and T subunits (Crocini & Gotthardt, 2021; Sarantitis et al., 2012). Troponin C is the Ca^{2+} binding subunit, whereas troponin I is the inhibitory subunit that binds to actin in the absence of Ca^{2+} . Troponin T on the other hand anchors the troponin complex to the actin filaments and to tropomyosin (Gomes et al., 2002). Titin brings stability to the sarcomere structure and is connected to the Z-disk and myosin filaments through MyBP-C. It also acts as a spring during CM contraction and relaxation (Crocini & Gotthardt, 2021; Sarantitis et al., 2012).

The contraction occurs, when Ca^{2+} ions in the cytoplasm bind to troponin C, inducing its conformational rearrangement. This allows the interaction of troponin C with troponin I, resulting in dissociation of the troponin I from actin filaments. Upon the conformational changes due to Ca^{2+} binding of troponin C, the troponin and tropomyosin complexes move and thus, the myosin binding sites of the acting filaments are revealed (De Tombe, 2003; Gomes et al., 2002). This further leads to cross-bridge formation between myosin heads and myosin binding sites on the actin filaments and thus the myosin heads bind to the actin filaments. The myosin head binds ATP and detaches from the actin filament. When the ATP is hydrolysed, the conformation of the myosin head changes, and it can bind again further in the actin filament (Sarantitis et al., 2012). The shortening of the sarcomere and CM occur when the myosin heads crawl towards the Z-disks of the sarcomeres by subsequent releasing and binding of the myosin heads to the actin filaments (Crocini & Gotthardt, 2021).

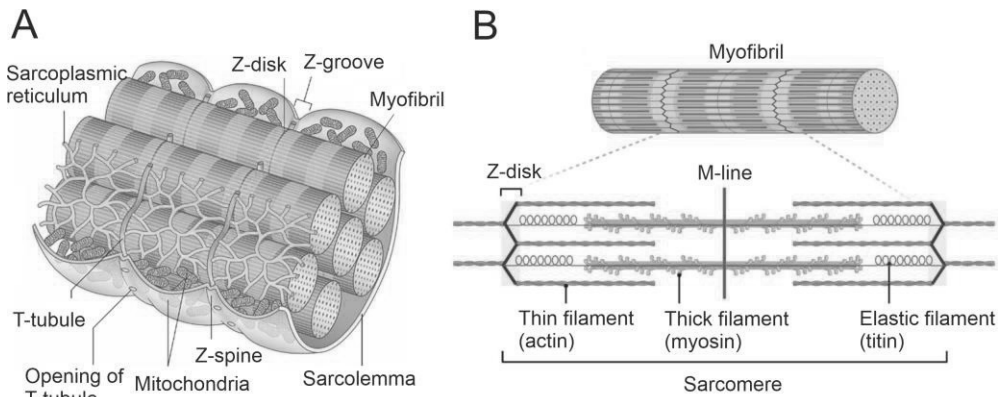


Figure 4. Structure of cardiomyocyte and sarcomere. A) Cardiomyocytes have highly organized cellular structure. The contractile myofibrils are surrounded by sarcoplasmic reticulum that contains Ca^{2+} ions essential for cardiac contraction. T-tubules, invaginations of sarcolemma are rich with ion channels and enhance the depolarization of the sarcolemma and EC coupling of the CMs (adapted from (Lipsett et al., 2019) under CC BY license: <https://creativecommons.org/licenses/by/4.0/>). B) Myofibrils consist of sarcomeres, which are the smallest contractile units of the CM. The contraction occurs when thick myosin filaments bind to the thin actin filaments and crawl along them towards the Z-disk. Titin stabilizes the sarcomere structure and acts as a spring during CM contraction and relaxation (adapted from (Santiago et al., 2021) under CC BY license: <https://creativecommons.org/licenses/by/4.0/>).

Cardiomyocyte relaxation occurs when the cytoplasmic Ca^{2+} is removed (Kockskämper, 2016). SR Ca^{2+} ATPase (SERCA) pumps the Ca^{2+} from cytoplasm back to SR, whereas the sarcolemmal $\text{Na}^{+}\text{-Ca}^{2+}$ exchanger (NCX) extrudes one Ca^{2+} for three Na^{+} ions into the extracellular space. NCX can work in forward (Na^{+} influx and Ca^{2+} efflux) or reverse (Ca^{2+} influx and Na^{+} efflux) mode, depending on the transsarcolemmal gradients of the ions as well as membrane potential. In the beginning of the AP when the cell membrane depolarizes and Na^{+} rapidly enters the cell via voltage gated Na^{+} channels, NCX works on the reverse mode bringing Ca^{2+} into the cell while extruding Na^{+} , resulting in a repolarizing outward current during AP phases 0 and 1. On the other hand, during AP phases 2–4, NCX works in the forward mode removing Ca^{2+} from the CM and resulting in a depolarizing inward current, and thus is one of the main Ca^{2+} efflux mechanisms in CMs. $\text{Na}^{+}\text{-K}^{+}$ ATPase (NKA) acts in the opposite direction, and actively transports three Na^{+} ions out of the cell in exchange for two K^{+} ions, thus generating an outward current and maintaining Na^{+} and K^{+} homeostasis. NKA utilizes adenosine triphosphate (ATP) hydrolysis to move the ions against their gradients and

contributes to the phase 3 repolarization as well as reducing the plateau phase and making the resting membrane potential more negative (Eisner et al., 2017; Kockskämper, 2016; Shattock et al., 2015).

Cardiac autonomic nervous system

Although heart can contract independently of any stimulation from the nervous system, the cardiac contraction is further regulated by cANS. cANS does not directly initiate the cardiac contraction, but can regulate all aspects of cardiac function, including chronotropy (heart rate), inotropy (contractile force), dromotropy (conduction velocity) and lusitropy (relaxation speed) (Hadaya & Ardell, 2020). cANS has an important role in physiological responses and regulation of the cardiovascular system, (Bairey Merz et al., 2015; van Bilsen et al., 2017; Végh et al., 2016), which starts already during the innervation of the developing heart when the neurons and cardiomyocytes undergo maturation. The cardiac maturation is affected by the innervating axons of the neurons, whereas the growth, patterning and transmission properties of the neurons are influenced by the cardiac tissue (Habecker et al., 2016).

cANS constitutes both sympathetic nerves with excitatory effect and parasympathetic nerves with inhibitory effect (Kingma et al., 2018; Végh et al., 2016). Sympathetic nerve fibres terminate at SA and AV nodes, but also innervate the myocardium and extend to coronary arteries. Parasympathetic nerve fibres on the other hand do not innervate myocardium but terminate mainly at SA and AV nodes reaching also to the coronary arteries (Végh et al., 2016). Sympathetic branch of the cANS secretes norepinephrine, which regulates the impulse rate of the SA node leading to increase in the cardiac contraction rate and force, as well as dilation of the coronary arteries. Instead, the parasympathetic branch of the cANS releases acetylcholine leading to decrease in heart rate and contraction force as well as constriction of the coronary arteries (Hadaya & Ardell, 2020).

Cardiac metabolism

Cardiac tissue has high energy demand due to the complex electrophysiological, biochemical and mechanical events resulting in the cardiac contraction (Martínez et al., 2017). As a source of energy, CMs can utilize fatty acids, glucose, ketone bodies as well as other substrates. Although glucose is the most energy efficient substrate, FAs are the main source of

energy during aerobic conditions at rest, when FAs account for 60–90% of the generated energy while only 10–40% of the energy is generated from glucose (Martínez et al., 2017; Rosano et al., 2008). However, CMs cannot synthesize these molecules efficiently themselves, and thus are depending on the FA influx from the blood (Martínez et al., 2017). At rest, the excess glucose in the CMs is stored into glycogen for utilization during increased metabolic demand (Rosano et al., 2008). Cardiac energy metabolism consists of three main components: the uptake and utilization of the primary substrates (FA by β -oxidation and glucose by glycolysis) with the incorporation of their metabolites into tricarboxylic acid cycle, oxidative phosphorylation of adenosine diphosphate into ATP in the mitochondrial respiratory chain, and utilizing ATP as energy for contraction or for storing of the energy from ATP to creatine for high-demand conditions (Martínez et al., 2017; Rosano et al., 2008).

2.1.2 Cardiac function in ischemic heart disease

Ischemic heart disease is the most common cardiovascular disease and a major cause of morbidity and mortality globally (M. A. Khan et al., 2020). In IHD, the blood flow into the cardiac tissue is reduced or blocked, causing oxygen and nutrient deprivation and accumulation of metabolic waste in the CMs and their extracellular space. This on the other hand leads to injury and death of the cardiomyocytes, compromising the heart function. Coronary artery disease is the most common reason for IHD. There plaque builds up the coronary arteries supplying blood flow to the heart, leading to narrowing of the lumen of the artery and decreased blood flow to the myocardium. If the plaque ruptures, it can cause a sudden block in the artery preventing blood flow altogether and result in CM death unless the restoration of blood flow by early reperfusion (Ambrose & Singh, 2015). Although rare, also coronary spasm as in e.g. takotsubo cardiomyopathy (stress cardiomyopathy) (Pelliccia et al., 2017) can cause IHD, when the muscles lining the coronary arteries suddenly tighten, narrowing the artery and decreasing the blood flow to the myocardium (Matta et al., 2020). Depending on the cause, acute IHD event can occur acutely as in the case of plaque rupture, or IHD can be a chronic state of decreased blood flow to the heart leading to heart failure (Libby & Theroux, 2005). Although timely reperfusion is required to salvage the ischemic area, it initially further damages the tissue (Hausenloy & Yellon, 2013).

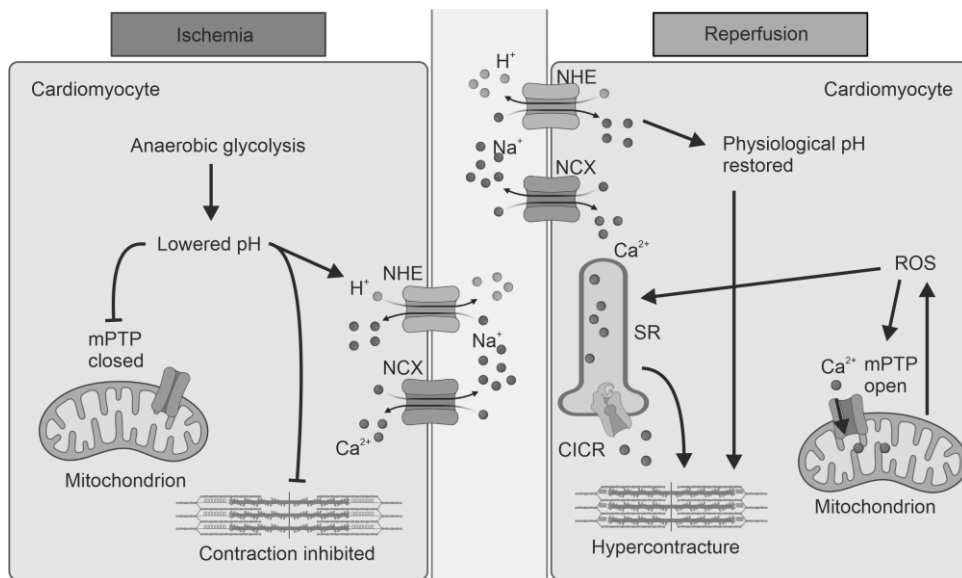


Figure 5. Main events of ischemia and reperfusion in cardiomyocytes (created with BioRender.com). Decrease in oxygen and ATP content of the CM lead to a metabolic shift from fatty acid oxidation to anaerobic glycolysis, which further leads to lactate production and lowered pH. Lowered pH activates Na⁺-H⁺ exchanger (NHE) leading to reverse activation of Na⁺-Ca²⁺ exchanger (NCX) and calcium overload. Lowered pH prevents opening of mitochondrial permeability transition pores (mPTP) and inhibits myofibril contraction. Reperfusion restores the physiological pH, but further enhances the intracellular calcium overload. Production of reactive oxygen species (ROS) mediates dysfunctioning of sarcoplasmic reticulum (SR). Increased intracellular calcium leads to calcium induced calcium release (CICR), which together with the ROS induce opening of mPTPs. Restoration of physiological pH enables Ca²⁺ binding to myofibrils and elevated Ca²⁺ levels cause myofibril hypercontracture.

Switch to glycolytic metabolism and pH decrease

Oxygen and nutrient deprivation during ischemia result in a series of changes in the metabolic, biochemical and electrophysiological processes of the CMs (Figure 5) (Hausenloy & Yellon, 2013). The lack of oxygen prevents oxidative phosphorylation, leading to switch from aerobic FA metabolism to inefficient and insufficient anaerobic glycolysis (Martínez et al., 2017; Rosano et al., 2008). This results in ATP depletion and increase in lactate reducing the intracellular pH (Hausenloy & Yellon, 2013; Martínez et al., 2017). Na⁺-H⁺ exchanger (NHE) activates upon H⁺ accumulation, extruding one H⁺ ion for import of one Na⁺ ion, leading to intracellular Na⁺ accumulation. The lack of ATP prevents NKA functioning, thus activating NCX in reverse mode

extruding Na^+ and leading to intracellular calcium overload (Garcia-Dorado et al., 2012; Kalogeris et al., 2016; Sanada et al., 2011). The lowered pH causes troponin C to become insensitive to Ca^{2+} , preventing the revelation of myosin binding site and consequently, CM contraction (Sanada et al., 2011).

Electrophysiological changes during ischemia

Calcium overload together with lowered pH during ischemia have several consequences, including cell-to-cell uncoupling, opening of non-junctional connexin hemichannels as well as overactivation of calpains (Garcia-Dorado et al., 2012). The cell-to-cell electrical uncoupling is caused by closing of the gap junctions due to connexin phosphorylation, which can induce arrhythmias (De Vuyst et al., 2011; Garcia-Dorado et al., 2012). Furthermore, Ca^{2+} overload can induce opening of non-junctional connexin hemichannels, which can contribute to cellular injury and arrhythmias, but can also have cardioprotective effects; the opening releases intracellular metabolites to the extracellular space, which may be involved in paracrine cardioprotective signalling. Calcium overload can also cause overactivation of calpains, which are Ca^{2+} -dependent thiol proteases participating in basic cellular processing, such as differentiation, proliferation and migration (Garcia-Dorado et al., 2012). This can cause damage to structural and functional proteins of the CMs and mitochondria leading to damaged contractile structures as well as impaired energy production (Garcia-Dorado et al., 2012; Kalogeris et al., 2016).

Ischemia affects the AP shape of the cardiomyocytes due to changes in the function of the ion channels and pumps (Figure 6A). Ischemia also affects the shape of surface electrocardiogram (ECG), depending on whether the ischemia is present in the entire heart wall thickness (transmural ischemia) or is confined to the subendocardial layer of the heart wall (subendocardial ischemia) (Figure 6B). The lack of ATP during ischemia leads to inactivation of ion channels and pumps depending on ATP hydrolysis. During ischemia, intracellular K^+ decreases and extracellular K^+ increases, causing CM resting membrane potential to be more depolarized (less negative). Furthermore, the depolarization inactivates Na^+ channels responsible for rapid depolarization of the cell membrane during AP phase 0, leading to slower depolarization (upstroke) (Klabunde, 2017).

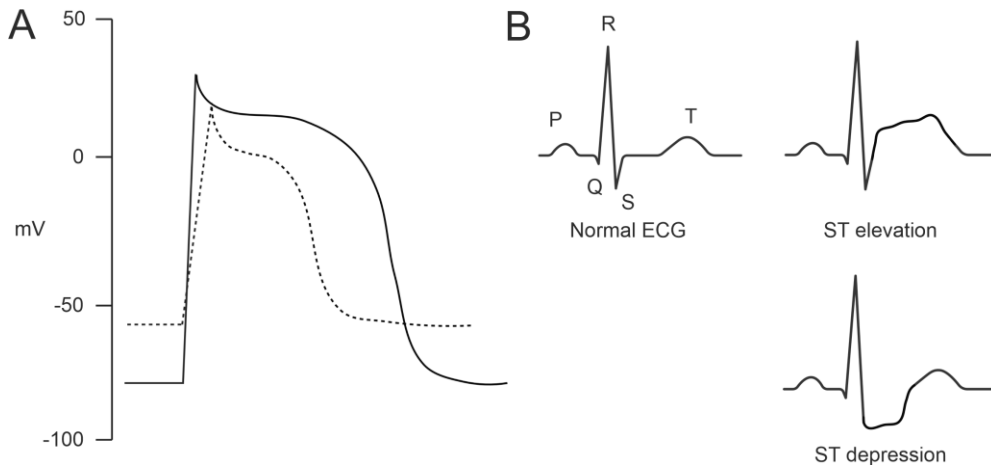


Figure 6. Changes in the action potential and surface ECG shape during ischemia (created with BioRender.com). A) Ischemia reduces the resting membrane potential and the upstroke velocity of the CM. Furthermore, AP duration decreases. B) Ischemia affects the shape of the surface ECG differently, depending on whether the ischemia is transmural or subendocardial. Transmural ischemia causes ST elevation, whereas subendocardial ischemia results in ST depression.

Together with the gap junctional cell-to-cell uncoupling (De Vuyst et al., 2011; Garcia-Dorado et al., 2012) the inactivation of the Na^+ channels reduces the conduction velocity of the action potential, as it primarily depends on the opening of the fast Na^+ channels inactivated by the ischemia-induced depolarization of the CMs (Klabunde, 2017). If the resting membrane potential reaches -55 mV, all fast Na^+ channels inactivate, however, action potential can still occur via slow inward Ca^{2+} current via the L-type Ca^{2+} channels, although the depolarization rate will be significantly slower. In addition to the less negative resting membrane potential and slower upstroke in phase 0, the repolarization of the CM occurs earlier, shortening the AP duration possibly due to opening of K^+ channels (Klabunde, 2017).

Reperfusion injury

When the blood flow is restored to the cardiac tissue during reperfusion, substrates, oxygen and physiological extracellular pH are restored allowing ATP production via fatty acid oxidation (Hausenloy & Yellon, 2013). Removal of the H^+ ions from the extracellular space creates a large proton gradient across the cell membrane further accelerating the NHE and NCX activity and increasing intracellular calcium levels. The elevated intracellular

calcium also activates calcium-induced calcium release from SR, further aggravating the calcium overload (Wang et al., 2020). Elevated cytoplasmic Ca^{2+} and restored energy production lead to arrhythmias, myofibril hypercontracture, uncontrolled and sustained contraction of the CMs (Figure 5) (Garcia-Dorado et al., 2012; Sanada et al., 2011). Mitochondrial permeability transition pores (mPTPs) open during reperfusion triggered by pH normalization, increased intracellular calcium levels, and oxidative stress from reactive oxygen species (ROS) that are produced by the reactivated electron transport chain (Turer & Hill, 2010). Opening of the mPTPs allows the excessive calcium in the cytoplasm to enter the mitochondria, which reduces the cytoplasmic Ca^{2+} levels. However, their opening further induces oxidative stress due to ROS produced in the mitochondria (Hausenloy & Yellon, 2013). ROS in turn can induce damage in both nuclear and mitochondrial DNA. Furthermore, the electrophysiological changes in the CM electrophysiology are reversed during reperfusion, although it does not necessarily occur rapidly or synchronously (Manning & Hearse, 1984).

Reperfusion can cause both reversible and irreversible types of injury in CMs. Reperfusion can induce arrhythmias, which can be treated with antiarrhythmic medication and are usually temporary if there is no permanent scarring (Hausenloy & Yellon, 2013). Ventricular fibrillations can occur due to inhomogeneity in action potentials in the border of previously ischemic and healthy tissue (Manning & Hearse, 1984). Moreover, delayed afterdepolarizations can stem from release of Ca^{2+} from the SR outside the normal EC coupling cycle (S. Chen & Li, 2012). In addition, microvascular obstruction meaning inability to reperfuse the ischemic region can occur due to capillary damage, external capillary compression by swelling of the cells and microthrombosis. With severe microvascular obstruction, intramyocardial haemorrhage in the area of infarction can occur. Lethal myocardial reperfusion injury refers to the death of CMs that were still viable at the end of the ischemic period. This type of injury is due to oxidative stress, calcium overload, mPTP opening as well as hypercontracture of the CMs, and can account up to 50% of the final size of the infarction size (Hausenloy & Yellon, 2013).

Another reversible injury is myocardial stunning, which means the prolonged dysfunction of the injured cardiac tissue and myocardial contractile apparatus due to the adverse effects of the oxidative stress as well as

intracellular calcium overload (Hausenloy & Yellon, 2013). As opposed to myocardial hibernation that occurs during ischemia, myocardial stunning occurs after reperfusion of a short ischemic event that does not cause infarction or death of the CMs but depresses the cardiac contractility. Myocardial stunning can take several days to recover and stems from the abnormal energy utilization, ROS production, calcium abnormalities, microvascular abnormalities, and white cell accumulation in the injured area. Myocardial hibernation on the other hand occurs in ischemic myocardium, where the blood flow is decreased. However, the CMs remain viable with depressed contractile function, reducing the oxygen demand of the tissue and thus protecting the CMs (Richard Conti, 1991; Ytrehus, 2006).

Hypoxia inducible factors

Hypoxia inducible factors (HIFs) are heterodimeric transcription factors consisting of alpha and beta subunits, and they are major mediators of adaptive responses to cellular oxidative stress (Graham & Presnell, 2017). Several alpha and beta subunits are known to bind to form HIFs, however, HIF1 is the most studied. The beta subunit of HIF resides in nucleus and is not affected by the presence of oxygen, whereas the alpha subunit rapidly degrades in the presence of oxygen by ubiquitin-proteasome pathway. The overall degradation of the alpha subunit decreases under hypoxia, which allows exquisite temporal control over the expression of HIFs as well as the hypoxia response (Semenza, 2012; Tennant & Howell, 2014; Zheng et al., 2021). Under hypoxic conditions, the HIF alpha subunit accumulates in the cytoplasm and translocates into the nucleus, where it binds to the beta subunit to form functional HIF. HIF in turn binds to hypoxia responsive element promoter region identified in numerous gene loci in the DNA. Subsequent recruiting of CREB binding protein and p300 results in the transcription of over hundred downstream target genes (Zheng et al., 2021).

During cardiac ischemic event, HIFs mediate several adaptive responses to the hypoxic conditions. HIFs increase the expression of vascular endothelial growth factor, increasing angiogenesis in the ischemic area. Furthermore, HIFs can regulate the mitochondria-specific gene expression to improve mitochondrial function during oxidative stress and improve the cellular glucose uptake by increasing the expression of glucose transporters on the cell membrane (Zheng et al., 2021). Furthermore, HIFs affect the expression of other glycolysis related genes, thus improving ATP production from glucose

(Tennant & Howell, 2014). HIFs can decrease ROS production as well as increase the production of antioxidants via several pathways and thus alleviate the oxidative stress experienced by the cells and the HIF pathway activation regulates the expression of genes involved in decreasing apoptosis during both ischemia and reperfusion. Moreover, HIFs can reduce tissue inflammation by attenuating pro-inflammatory cytokine production (Zheng et al., 2021).

Cardiac autonomic nervous system in ischemia-reperfusion

cANS is an important regulation of the cardiac function, and as the cANS and cardiac function are intertwined, dysregulations of this system due to different causes contribute to cardiovascular pathology and can lead to fatal outcomes (Bairey Merz et al., 2015; Kolettis et al., 2015; van Bilsen et al., 2017; Végh et al., 2016). For example, dysfunction of cANS can lead to arrhythmogenic consequences during IHD (Hadaya & Ardell, 2020; Kingma et al., 2018; Kolettis et al., 2015; Tapa et al., 2020), as myocardial ischemia causes the local sympathetic nerve terminals to release norepinephrine. This elicits increased contractility of the CMs serving to maintain the cardiac output, however, the local surge of norepinephrine alters the CM electrophysiology, which in turn creates a milieu susceptible for arrhythmic events (Kolettis et al., 2015). Furthermore, alterations in sympathetic nerve density, electrical excitability and neurotransmitter content occur during ischemic heart disease (Hadaya & Ardell, 2020; Kolettis et al., 2015; Tapa et al., 2020).

2.2 Human induced pluripotent stem cell-derived cardiomyocytes

2.2.1 Stem cells and induced pluripotent stem cells

Stem cells are characterized by the ability for self-renewal and differentiation into specialized cell types and categorized based on their ability to differentiate into multiple cell types. Totipotent stem cells can differentiate into any cell type including cells of the extraembryonic tissues, pluripotent stem cells can differentiate into the cells of all three embryonic lineages but not extraembryonic tissues, multipotent stem cells can differentiate into multiple specialized cells of a specific tissue, and unipotent stem cells can only differentiate into one cell type (Daley, 2015; Dulak et al., 2015). Stem cells can also be categorized based on the source; adult stem cells include multi- or

unipotent stem cells found throughout the body after embryonic development, embryonic stem cells (ESCs) are pluripotent stem cells isolated from the inner cell mass of blastocysts (Daley, 2015), whereas induced pluripotent stem cells (iPSCs) are somatic cells reprogrammed into an embryonic-like state by forced expression of transcription factors responsible for cellular pluripotency, such as *OCT4*, *SOX2*, *KLF4* and *c-MYC* (Takahashi et al., 2007; Takahashi & Yamanaka, 2006).

Induced pluripotent stem cells can be produced from human somatic cells (Takahashi et al., 2007), and they have a wide range of applications, including tissue engineering, treatment of immunodeficient diseases, disease modelling as well as drug development and testing (A. S. T. Smith et al., 2017; Yin et al., 2016). PSCs can be culture *in vitro*, however, their culture requires specific conditions mimicking the stem cell niche *in vivo* to maintain the pluripotency of the cells. This can be achieved with several methods, the most important being the cell culture medium and culture substrate. PSCs are typically cultured in growth medium containing growth factors and cytokines supporting the self-renewal and pluripotent state of the cells. Furthermore, the cells can be cultured on supporting feeder cells such as mouse embryonic fibroblasts, that support the growth of the PSCs and prevent their differentiation. Alternatively, feeder-free culture on extracellular protein matrices such as Matrigel, fibronectin or laminin can be used (van der Sanden et al., 2010). For therapeutic and translational applications, PSC culture in xeno-free conditions is crucial, meaning that all culture components are human-derived or synthetic (Kaur et al., 2013).

2.2.2 Differentiation

As hiPSCs are pluripotent, they can be differentiated into all cell types of all tissue types in the body, including cardiomyocytes. Several methods have been described for differentiation of hiPSC-CMs, including embryoid body (Kehat et al., 2001), coculture (Mummery et al., 2003) and monolayer differentiation (Laflamme et al., 2007). Despite the different approaches, each method mimics the embryonic cardiac development *in vivo*. During embryonic development, distal visceral endoderm expresses Nodal, while its antagonists are expressed in visceral endoderm inducing a gradient change of Nodal and WNT signals in the front and rear directions. This promotes the

development of the primitive streak as well as the development of trilaminar embryonic disk comprised of ectoderm, mesoderm, and endoderm. Extracellular signalling molecules including Wnt3a, BMP4, Nodal and Activin A control cardiac mesoderm and cardiac progenitor cell induction and induce the expression Brachyury T and Eomes, markers of early mesoderm formation. During the primitive streak, Mesp1 is temporarily expressed in the cells, and a subset of these cells then start to express Nkx2.5, Tbx5 and Isl1 representing cardiac lineage markers in the early stages of heart field development. Subsequent activation of CM related genes including α -actinin, myosin light and heavy chains, troponin and myocyte enhancer factor 2 occurs, leading to proliferation and maturation of CMs (Bruneau, 2013).

Embryoid body differentiation is based on the property of PSCs to form aggregates, embryoid bodies (EBs) when cultured in suspension. When cultured in a medium that does not support pluripotency, the PSCs start to spontaneously differentiate into cells of all three germ layers, including mesodermal CMs (Talkhabi et al., 2016). Another method for CM differentiation relies on coculture of PSCs with the visceral endoderm-like cell line END2. This method is based on the knowledge that endoderm and cardiac crescent have close interaction during cardiac embryonic development when the endoderm provides inductive and inhibitory signals essential for cardiac development, which leads to CM differentiation (Mummery et al., 2003). Monolayer-based hiPSC-CM differentiation is based on the epithelial cell-like morphology of the PSCs in adherent cultures and timely introduction of right dose and combination of growth factors such as BMP4 and Activin A (Laflamme et al., 2007), or small molecules affecting the GSK3 and WNT signalling of the PSCs (Lian et al., 2012, 2013). The cardiac differentiation is shown to produce a mixture of nodal, ventricular, and atrial CMs (Q. Zhang et al., 2011) and not all PSCs differentiate into CMs but also into other cell types, such as smooth muscle cells, endothelial cells (Balafkan et al., 2020; Jiang et al., 2022) and fibroblasts (Jiang et al., 2022).

The advantages and disadvantages of the different differentiation methods have been previously reviewed (Mummery et al., 2012; A. S. T. Smith et al., 2017; Talkhabi et al., 2016). EB differentiation of hiPSC-CMs is spontaneous and robust, however, it has low efficiency without any growth factors or small molecules mediating the differentiation. Furthermore, the variability in the EB size affects the efficiency and reproducibility of the CM differentiation via EB

method. The efficiency can be enhanced significantly by timely addition of cardiogenic growth factors such as BMP4, bFGF and Activin A in the beginning of the differentiation for more direct differentiation into cardiac lineage cells. Similarly, END2 differentiation efficiency was initially very low, but was shown to be improved by introduction of growth factors and small molecules. Monolayer-based differentiation allows better means to control the introduction of growth factors or small molecules due to the lack of complex diffusional barriers present in EBs (Mummery et al., 2012; A. S. T. Smith et al., 2017) theoretically enabling more reproducible method for CM differentiation. Moreover, the highest differentiation efficiencies have been reported for monolayer-based methods (A. S. T. Smith et al., 2017; Talkhabi et al., 2016).

The ease and efficiency are not the only aspects to be considered regarding the differentiation method, but also the properties of the produced CMs. For example, there are methods to guide the hiPSC-CM differentiation into atrial or ventricular type (J. H. Lee et al., 2017; Q. Zhang et al., 2011), and it has been shown that the hiPSC-CM electrophysiological properties are affected by the differentiation method (Prajapati et al., 2021). In the study by Prajapati and co-workers, END2 differentiation was shown to produce most mature hiPSC-CMs regarding the electrophysiological properties although the inefficiency of the method can affect the applicability to studies requiring large batches of CMs. EB method was observed to be the most efficient regarding the differentiation of hiPSC-CMs with also fairly mature electrophysiological properties, whereas the monolayer method used in that study was observed to yield least CMs with also the least developed electrophysiology (Prajapati et al., 2021). However, despite the differentiation method, the produced hiPSC-CMs resemble rather foetal than adult CM phenotype and require further maturation step to improve the properties for several applications (Ahmed et al., 2020; Feyen et al., 2020; A. S. T. Smith et al., 2017).

2.2.3 Maturation

Human induced pluripotent stem cell-derived cardiomyocytes express rather foetal than adult CM phenotype, which is a disadvantage hindering their utilization on several aspects, including cardiac disease modelling and

pharmacological and toxicological screening. The maturation of the hiPSC-CMs has been extensively researched and reviewed, and the hiPSC-CMs have been shown to differ from adult CMs with regard to gene and protein expression, expression of specific ion channels and pumps, contractile and electrophysiological properties, metabolism as well as structural and morphological properties (Ahmed et al., 2020; Karbassi et al., 2020; Liao et al., 2021). Several methods have been developed to induce more mature phenotype in hiPSC-CMs, however, fully adult-like hiPSC-CMs have not yet been produced. The maturation methods include prolonged *in vitro* culture (Lewandowski et al., 2018; Lundy et al., 2013), topographical cues guiding hiPSC-CM orientation (J. Han et al., 2016; Huethorst et al., 2016; Rao et al., 2013), substrate stiffness (Martewicz et al., 2017), medium additives (Feyen et al., 2020; Yang, Rodriguez, et al., 2014), mechanical or electrical stimulation (Ruan et al., 2016) as well as coculture with other cell types typical to cardiac tissue (Vuorenää et al., 2017).

hiPSC-CM immature phenotype

hiPSC-CMs differ from adult CMs on several aspects (Figure 7), including morphology and function. Adult CMs are rod-like and well-aligned cells expressing highly organized sarcomeres and well-developed T-tubule system and SR. hiPSC-CMs on the other hand are smaller and round, have shorter and disorganized sarcomeres and poorly developed SR, and lack clear longitudinal axis and T-tubules (Ahmed et al., 2020). The underdeveloped SR and lack of T-tubules together with low expression of key proteins regulating CICR lead to slow EC coupling in hiPSC-CMs compared to adult CMs (Veerman et al., 2015). hiPSC-CMs beat spontaneously, whereas adult CMs beat only when stimulated. Furthermore, hiPSC-CMs exhibit much lower contractile force as well as slower conduction and upstroke velocities. Furthermore, their action potential morphology is mixed and can be categorized as atrial, nodal or ventricular (Karakikes et al., 2015).

hiPSC-CMs generate the most important cardiac currents but lack the I_{K1} responsible for stabilizing the resting membrane potential and for shaping the initial depolarization and final repolarization of the AP, which can fundamentally affect the modelling of specific cardiac diseases (Karakikes et al., 2015; Karbassi et al., 2020). Furthermore, although hiPSC-CMs express a functional pacemaker I_f current, the current density on its own is not enough for the spontaneous AP generation and contraction, but the spontaneous

activity in hiPSC-CMs resembles that of nodal cells of the SA node, and relies on the activity of ryanodine and inositol-1,4,5-trisphosphate receptors leading to spontaneous Ca^{2+} release from SR. This results in increased intracellular Ca^{2+} concentration triggering a depolarizing current via NCX and serving as a trigger for AP (Koivumäki et al., 2018).

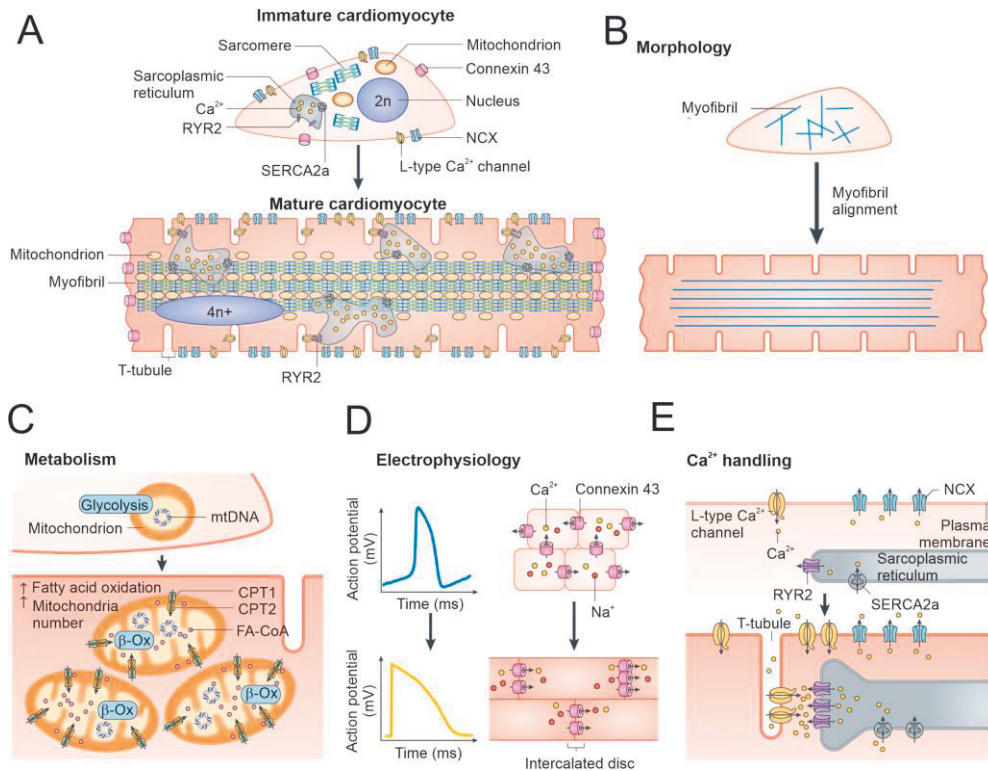


Figure 7. Human induced pluripotent stem cell-derived cardiomyocytes differ from adult CMs regarding several structural and functional properties. Adapted from (Karbassi et al., 2020) (reprinted with permission from Springer Nature: Nature Reviews Cardiology; Cardiomyocyte maturation: advances in the knowledge and implications for regenerative medicine. Karbassi et al., © 2020; permission conveyed through Copyright Clearance Center). A) hiPSC-CMs are small and round cells lacking T-tubules and well-developed organized sarcoplasmic reticulum. Furthermore, ion channels are expressed differentially in hiPSC-CMs and adult CMs. B) hiPSC-CM myofibrils and sarcomeres are underdeveloped and disorganized. C) hiPSC-CMs rely on glycolysis, whereas adult CMs prefer fatty acid oxidation. D) hiPSC-CM action potential morphology is different from that of an adult CM. E) Calcium kinetics of hiPSC-CMs are slower compared to adult CMs.

Adult CMs are highly metabolically active cells due to the high demand of energy and ATP for proper heart function. Thus, adult CMs rely mostly on β -oxidation of FAs for energy production, which is a robust and effective pathway for ATP production. The metabolism of hiPSC-CMs resemble more foetal CM, which rely mostly on glycolysis of glucose for ATP production (Ahmed et al., 2020; Hu et al., 2018; Ulmer & Eschenhagen, 2020). Moreover, adult CMs express more mitochondria, which also have higher cristae density and tubular network. Subsarcolemmal mitochondria are located close the sarcolemma, where they provide energy for electrolyte and metabolite transfer. Interfibrillar mitochondria on the other hand span the SR aligning with the sarcomeres where they provide ATP for SR Ca^{2+} uptake and the contractile system. However, in foetal and hiPSC-CMs, most mitochondria are perinuclear with lesser degree of cristae and tubular networking (Ulmer & Eschenhagen, 2020).

hiPSC-CMs differ from adult CM also regarding gene expression, the gene expression profile resembling more first trimester foetal heart than adult heart (Robertson et al., 2013; van den Berg et al., 2015). Although hiPSC-CMs express mostly same genes as adult CMs, there are differences in the relative expression of the genes (Karakikes et al., 2015). For example, CMs express *MYH6* and *MYH7*, which encode two isoforms of myosin heavy chain, alpha and beta, respectively. *MYH7* is predominant in adult CMs, whereas *MYH6* is predominant in hiPSC-CMs (Ahmed et al., 2020; Denning et al., 2016). In addition, *TNNI1*, *TNNI2* and *TNNI3* encode three troponin I isoforms, slow skeletal, fast skeletal and cardiac isoform, respectively. *TNNI3* is highly expressed in adult CMs, whereas *TNNI1* is the primary isoform in hiPSC-CMs (Ahmed et al., 2020; Bedada et al., 2014). A third sarcomeric protein expressed differentially in adult and hiPSC-CMs is titin, which also has three major isoforms encoded by *N2B*, *N2BA* and *FCT* genes. *N2B* is primarily expressed in adult CMs, while in hiPSC-CMs, the predominant isoform is *N2BA* (Ahmed et al., 2020; Denning et al., 2016). Furthermore, compared to hiPSC-CMs, adult CMs have significantly higher expression of several calcium handling related genes and ion channels (Ahmed et al., 2020; Denning et al., 2016; Rao et al., 2013).

Methods to improve hiPSC-CM maturation

Several methods have been introduced to improve the maturation of hiPSC-CMs (Figure 8), however, none has yet been able to produce completely adult-

like CMs. As the CM maturation from foetal to adult phenotype takes years *in vivo*, long term *in vitro* culture from half a year to one year has been utilized in inducing hiPSC-CM maturation (Lewandowski et al., 2018; Lundy et al., 2013). Although hiPSC-CMs have shown improved morphological and structural properties, including larger size, increased myofibril density and sarcomere alignment, as well as improved physiology regarding calcium handling, such long culture periods are not feasible for research or for clinical applications (Lewandowski et al., 2018; Lundy et al., 2013). Topographical cues have been suggested for hiPSC-CM maturation, as cardiac tissue has high level of directional organization, whereas hiPSC-CMs exhibit disorganized sarcomere structure and round morphology. The use of topographical cues, such as microgrooves or textile fibres, aim to guide the growth of the hiPSC-CMs in specific direction, inducing alignment of the cells and their sarcomeres. However, there have been controversial results on how topographical cues affect the functionality of the hiPSC-CMs, as some studies showed improvement in calcium handling (Rao et al., 2013) or contractile (Huethorst et al., 2016) properties of the hiPSC-CMs, whereas others did not (J. Han et al., 2016).

In native myocardium, CMs are under constant electrical stimulus and mechanical loading, which also affects their functionality and maturation. Electrical and mechanical stimulation have been shown to improve hiPSC-CM maturation regarding contractility, alignment and size, as well as *SERCA2* expression (Ruan et al., 2016). Furthermore, culture substrate stiffness affects hiPSC-CM maturation and culturing hiPSC-CMs on hydrogels with elastic modulus close to that of native cardiac tissue around 16 kPa has been shown to induce alignment of sarcomeres and improve calcium handling properties of the cells (Martewicz et al., 2017). Moreover, coculture with other cell types of cardiac tissue has been shown to induce hiPSC-CM improvements in their morphology, sarcomere alignment, expression of genes encoding structural properties as well as electrophysiological properties, when the hiPSC-CMs were cocultured in a preformed network of fibroblasts and endothelial cells (Vuorenää et al., 2017).

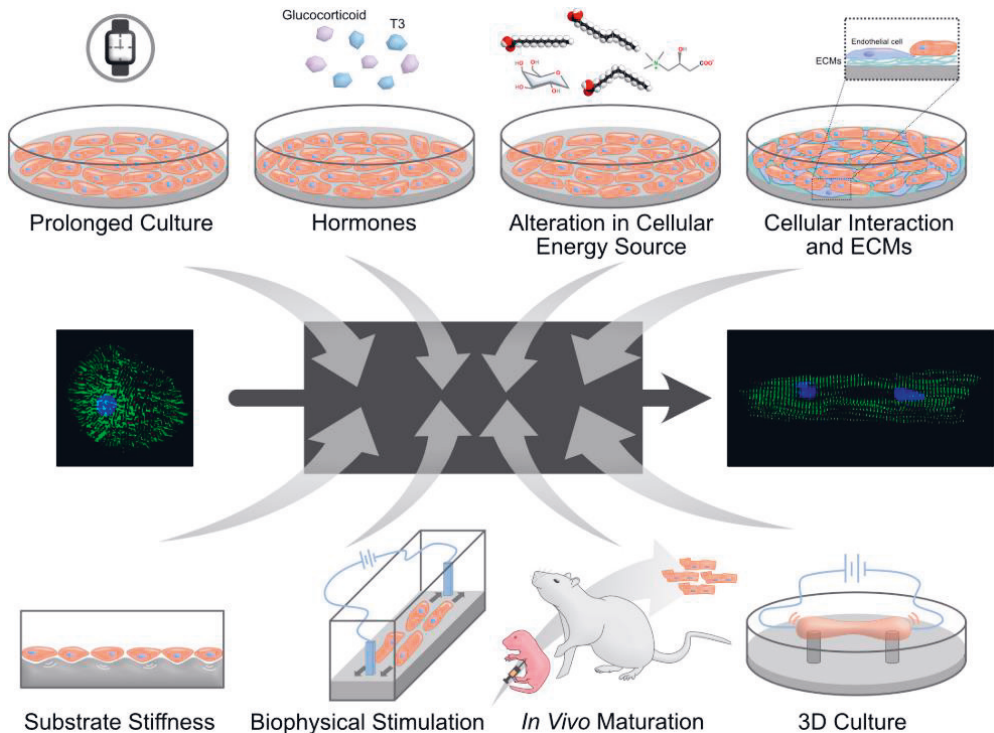


Figure 8. Several methods to induce hiPSC-CM maturation have been developed (adapted from (Ahmed et al., 2020) under CC BY license: <https://creativecommons.org/licenses/by/4.0/>). These include prolonged culture, media additives including hormones or additives guiding to preferred energy metabolism, coculture with other cell types, substrate stiffness and topographical cues, electrical or mechanical stimulation, *in vivo* maturation, and culture in 3D.

hiPSC-CM maturation can also be improved with modified chemical composition of the culture medium. Different medium additives include triiodothyronine, a thyroid hormone known to improve hiPSC-CM size, elongation, sarcomere length, calcium handling and contractility (Yang, Rodriguez, et al., 2014). The culture medium can also be modified to favour FA oxidation instead of glycolysis as the primary pathway for energy metabolism in hiPSC-CM, thus inducing metabolic maturation (Feyen et al., 2020; Knight et al., 2021). This has been shown to further improve hiPSC-CM physiological properties, electrophysiology and calcium handling (Feyen et al., 2020), as well as sarcomere morphology and contractility (Knight et al., 2021). Lastly, *in vivo* transplantation to for example rat heart has been shown to induce accelerated maturation, the hiPSC-CMs adapting almost adult-like

function, structure, and gene expression. This indicates that the hiPSC-CMs have the capacity to mature to adult-like CMs in their natural environment. The mechanism of the *in vivo* maturation may involve electrical and mechanical stress, interaction and signalling with non-CMs of the cardiac tissue, as well as paracrine or endocrine signalling and other systemic factors including neurohormones and metabolic fuels (Kadota et al., 2017).

2.3 Modelling ischemic heart disease

The pathophysiology, mechanisms, and consequences of ischemic heart disease or ischemia-reperfusion injury are not yet fully understood (Lindsey et al., 2018). Thus, good IHD models are needed for modelling the disease and the injury mechanism both at cellular and tissue level, as well as for developing new interventions (Ytrehus, 2006). Currently animal models (Ludman et al., 2010), cell models (C. C. Chen et al., 2016; Hidalgo et al., 2018; Ronkainen et al., 2011; J. Wei et al., 2015), isolated perfused hearts (S. B. Smith et al., 2017) and computational models (McDougal & Dewey, 2017) are used for modelling IHD. The advantages and disadvantages of these models have been extensively reviewed (Camacho et al., 2016; T. Chen & Vunjak-Novakovic, 2018; Emini Veseli et al., 2017; Harding, 2017; Milani-Nejad & Janssen, 2014; Patten & Hall-Porter, 2009; Ytrehus, 2006) and recently, guidelines for conducting studies with the different animal and cell models have been published (Lindsey et al., 2018).

2.3.1 In vivo models

Animal models for cardiac ischemia-reperfusion are valuable in cardiovascular research and in preclinical studies, and include small animals such as mouse (Qiao et al., 2017), rat (Francis et al., 2017) and rabbit (Pennella et al., 2017), as well as large animals such as pig (Quevedo et al., 2009), dog (Damiano et al., 2015) and sheep (Ménard et al., 2005). Although animal models are frequently used in ischemia modelling, they have several disadvantages. In most cases, ischemia is modelled in healthy young animals and the ischemia is created by mechanically restricting the blood flow in the coronary arteries (Lindsey et al., 2018), whereas age is a known risk factor for IHD and atherosclerosis is known to develop over time (Hajar, 2017). There

are some genetically modified strains of mice and rabbit that spontaneously develop atherosclerosis (Emini Veseli et al., 2017), however, from the used animal models, they are physiologically the furthest from human (Lindsey et al., 2018).

Due to differences in physiology between humans and animals, the studies should be repeated with several different animal models to discover whether the results are translatable across species, and even then the results must be translated to humans with caution (Milani-Nejad & Janssen, 2014). However, the usefulness of the results is still under debate, as for example pharmaceutical companies have had difficulties in reproducing results published even in highly regarded peer reviewed journals (Harding, 2017). Furthermore, the ethical problems related to animal models must be considered, and although animal experiments cannot be completely abandoned, they should be used only when necessary. Each animal model has their advantages and disadvantages (Table 1); however, several are based on the size of the animal.

Larger animals have higher maintenance costs but more similar heart physiology and function to humans compared to smaller animals (Lindsey et al., 2018). They allow the use of similar techniques as for humans, whereas modifications or development of completely new techniques is required for small animals due to the size difference (Patten & Hall-Porter, 2009). However, faster gestation time, lower costs and the possibility for gene manipulation in smaller animals gives them a significant advantage as cardiac ischemia models (Camacho et al., 2016). Small animal models are typically used for studying mechanisms driving atherosclerosis that leads to myocardial infarction (MI) and IRI, whereas large animal models are required for translating these findings into enhanced prevention or intervention in humans (Emini Veseli et al., 2017), where the treatment effectiveness is typically evaluated by infarct size (Lindsey et al., 2018) Furthermore, initial testing is more easy to perform with small animal models, whereas large animal models are imperative for further confirming these results before human trials (Camacho et al., 2016).

Table 1. Advantages and disadvantages of animal models of ischemic heart disease.

Animal	Advantages	Disadvantages
<i>Large animals</i>		
Pig	+ Heart resembles young human heart	- More frequent ischemia-induced arrhythmias compared to humans - Collateral vessel growth
Dog	+ Heart resembles older human heart	- Excessive collateral vessel growth - Special approval required for experiments
Sheep	+ Good resemblance to human heart	- Some imaging techniques are difficult to apply
Non-human primate	+ Most similar to human heart	- Ethical issues and high regulation - Special approval required for experiments
<i>Small animals</i>		
Rabbit	+ More similar to human heart than mouse and rat + Significantly lower maintenance costs than with large animals	- Higher maintenance costs than with rat and mouse
Rat	+ Ten times bigger heart than mouse	- Not as many transgenic and knockout strains
Mouse	+ Comparison to <i>in vitro</i> cell models and <i>ex vivo</i> perfused heart models + No collateral vessel growth + Well-defined genetic map + Transgenic and knockout strains	- Most remote cardiac contractile function and size compared to human - Small heart size makes handling difficult - Transgenic and knockout mice have higher costs and developmental defects can lead to death before birth

Small animal models

Mouse models of cardiac ischemia are attractive as they enable the comparison of *in vitro* and *in vivo* results, as mouse primary CMs and perfused hearts are frequently used for ischemia-reperfusion modelling (Ytrehus, 2006). Furthermore, mice, rats and rabbits have no coronary collaterals, which are characteristic for especially dog models, but less so in humans (Camacho et al., 2016; Lindsey et al., 2018). Coronary collaterals are connections between different coronary arteries providing an alternative source of blood supply when the primary artery supplying a region of the myocardium is blocked (Koerselman et al., 2003; Seiler et al., 2013). In humans, some individuals have well developed collaterals, whereas some do not. It has been estimated, that approximately one fifth to one third of coronary artery disease patients have sufficient collateral blood flow to prevent myocardial ischemia during a

brief occlusion (Seiler et al., 2013). Furthermore, mice have a well-defined genetic map and can be genetically modified to produce knockout or transgenic individuals (Conci et al., 2006; Lindsey et al., 2018; Milani-Nejad & Janssen, 2014; Ytrehus, 2006), allowing evaluation of the function of a specific gene in the disease mechanism. However, the cardiac contractile function and heart size are most remote from humans (Camacho et al., 2016; Lindsey et al., 2018; Milani-Nejad & Janssen, 2014) and the short life-span can affect the disease development and phenotype (Milani-Nejad & Janssen, 2014). In addition, the gene-modified animals require special facilities, which leads to higher costs, and the developmental defects in them can lead to death before birth (Conci et al., 2006).

Rat and mouse models share many advantages and disadvantages; however, rat hearts are ten times bigger allowing easier handling of the heart (Patten & Hall-Porter, 2009). On the other hand, some study setups are limited by the lack of transgenic and knockout strains (Milani-Nejad & Janssen, 2014). Together the mouse and rat models are the most used animal model for cardiac physiology, disease, pharmacology and genetics (Milani-Nejad & Janssen, 2014). For example, the development of ischemia can be studied in double knockout apoE^{-/-}/LDLR^{-/-} mouse strain spontaneously developing atherosclerosis (Tyrankiewicz et al., 2016). Rat models on the other hand have been used for example in testing interventions such as human placenta hydrogel (Francis et al., 2017) and CMX-2043 drug (Baguisi et al., 2016) for reducing scarring and decreasing IRI and arrhythmias, thus leading to improved recovery from ischemia-reperfusion injury. Another small animal model used for ischemia modelling is rabbit, which shares more similarities with human heart than rat and mouse, including heart rate, force-frequency response, expression of certain proteins and calcium handling. The maintenance costs are higher than with mouse and rat but still significantly lower than with large animals (Milani-Nejad & Janssen, 2014). Similarly to mouse and rat, rabbit models have been used for studying interventions such as stem cell therapy (Pennella et al., 2017) and drugs (Tanimoto et al., 2017) to improve IRI.

Large animal models

Pig is the most attractive large animal model, as they have similar organ size, coronary anatomy, immunology and physiology to young human heart (Camacho et al., 2016; Lindsey et al., 2018) as well as similar excitation-

contraction coupling, heart rate and force-frequency relationship (Milani-Nejad & Janssen, 2014). However, the more frequent ischemia-induced arrhythmias (Camacho et al., 2016) and increased collateral circulation compared to humans are considered disadvantages (Lindsey et al., 2018; Verdouw et al., 1998). Dog heart on the other hand resembles older human heart (Camacho et al., 2016), and has similar advantages and disadvantages to those with pigs with addition of more excessive collateral vessel growth (Camacho et al., 2016; Verdouw et al., 1998). Sheep models have similar advantages and disadvantages to pig models, however, some imaging techniques can be difficult to apply to sheep due to their gastrointestinal anatomy and thoracic contours limiting their utilization in specific applications (Dixon & Spinale, 2009).

Although non-human primates have significant physiological, metabolic, biochemical and genetic similarities to humans (Camacho et al., 2016; Cox et al., 2017; Harding, 2017; Phillips et al., 2014; X.-L. Zhang et al., 2014), they are not widely used for modelling cardiac ischemia due to ethical issues, and their use is highly regulated (Emini Veseli et al., 2017). However, they usually are an essential part of translational research developing interventions to human diseases. Thus, they are often used in research with other animal models as the last step before human trials (Harding, 2017). Large animal models are typically used for verifying results from small animal studies before translation to humans (Emini Veseli et al., 2017). For example, pigs have been used to study the effect of cell therapy to chronic ischemic cardiomyopathy (Quevedo et al., 2009) and drug effects in hibernating myocardium model after coronary artery bypass graft surgery (Hocum Stone et al., 2016). Dogs have been used to model transient myocardial ischemia for drug testing (Damiano et al., 2015) and sheep have been used to study integration and differentiation of mouse ESCs in a MI model (Ménard et al., 2005).

2.3.2 Ex vivo models

Perfused isolated heart is simple, relatively low cost and reproducible method to model cardiac ischemia. The heart is removed from the animal and perfused with physiological saline solution, and continues to beat for several hours after removal (Lindsey et al., 2018; Skrzypiec-Spring et al., 2007; Ytrehus, 2006). The model allows studying IR without the effect of systemic blood circulation or circulating neurohormonal factors (Verdouw et al., 1998). Furthermore, it enables accurate measurement of infarct size and has capacity for higher throughput (Lindsey et al., 2018; Skrzypiec-Spring et al., 2007). Disadvantages include tissue oedema, limited stability, excessive coronary flow (Skrzypiec-Spring et al., 2007) and glucose being the sole energy source of the cells (Lindsey et al., 2018). Although large animal isolated hearts have been perfused, the most used and best characterized is rat heart model (Clements-Jewery et al., 2002; Farkas et al., 1999; Petkovic et al., 2018; Skrzypiec-Spring et al., 2007). In addition, mouse (Mattiuzzi et al., 2015), rabbit (Salameh et al., 2018) and guineapig (Muto et al., 2014) have been used. Isolated perfused hearts are often used when studying intervention of chemical species on ischemic heart (Farkas et al., 1999; Muto et al., 2014; Petkovic et al., 2018; Salameh et al., 2018), but also to study mechanism of cardiac ischemia and IRI (Clements-Jewery et al., 2002; Mattiuzzi et al., 2015).

2.3.3 In vitro models

In vitro models of ischemia include primary CMs harvested from humans or animals (T. Chen & Vunjak-Novakovic, 2018), and CMs differentiated from ESCs (Luo et al., 2014) or iPSCs (Hidalgo et al., 2018). Also, commercial cardiac-like cells that have either been immortalized or acquired from tumour samples are available. They all have advantages and disadvantages regarding acquiring and culturing as well as similarity to adult human CMs (Table 2) (T. Chen & Vunjak-Novakovic, 2018). Overall, advantages of the *in vitro* models include high throughput and control over the culture conditions, and the possibility to study hypoxia and reoxygenation without the intervention of other cell types or circulating factors. However, these models are considered to be reductionist and CM viability is the most commonly evaluated parameter, although does not necessarily predict the infarct size *in vivo*

(Lindsey et al., 2018). Moreover, there is large variation in the experimental setups, which can make the comparison of the studies difficult.

Several parameters can be evaluated from *in vitro* cardiac ischemia models, such as contractile properties, proton accumulation and increased free cellular phosphate. In addition, arrhythmias due to partial depolarization, conduction delay or AP shortening are important regarding the CM functionality. The cause of CM death can be determined from *in vitro* models, including mitochondrial permeability transition, cytosolic calcium overload, caspases, hypercontraction and sarcolemma rupture (Ytrehus, 2006). However, the lack of common established setting for the experiments makes it difficult to compare results (Table 3). Cell sources include primary animal CMs from different animals, PSC-derived CMs and immortalized CM lines. Furthermore, hypoxia can be induced via low oxygen gas, oxygen scavengers or biochemical method (Kobuszewska et al., 2020), and the duration of the hypoxia and reoxygenation vary from a couple of minutes (Fernández-Morales et al., 2019) to several days (Veldhuizen et al., 2022). The speed with which the hypoxia is achieved in the cell culture can vary from seconds (Liu et al., 2020) to hours (Välimäki et al., 2017), and the medium composition varies regarding the presence of serum and glucose (Hidalgo et al., 2018; Shah et al., 2019), as well as acidity (Fernández-Morales et al., 2019; Hidalgo et al., 2018) and hyperkalemia (Diaz & Wilson, 2006).

Table 2. Cell types used in modelling of myocardial ischemia and reperfusion. The goal in *in vitro* IR modelling is primary adult human CMs, however, they are not readily available due to difficult harvesting and poor survival in long term cultures.

Cell type	Advantages	Disadvantages
<i>Human CMs</i>		
hESC-CMs	+ Unlimited supply of human CMs + Easy culture and acquiring	- Immature - Ethical considerations
hiPSC-CMs	+ Unlimited supply of human CMs + Easy culture and acquiring + Genetic disease cell lines + Personalized medicine	- Immature
Commercial CM lines (HCM, AC16)	+ Easy culture and acquiring	- Proliferating
<i>Animal CMs</i>		
Primary adult mouse and rat CMs	+ Comparison to <i>in vivo</i> and <i>ex vivo</i> models	- Interspecies differences - Requires harvesting - Difficult to culture - Ethical considerations
Primary neonatal mouse and rat CMs	+ Comparison to <i>in vivo</i> and <i>ex vivo</i> models + Better survival in <i>in vitro</i> compared to primary adult CMs	- Interspecies differences - Immature - Requires harvesting - Ethical considerations
Mouse and rat iPSC-CMs	+ Easy culture and acquiring	- Interspecies differences - Immature
Immortalized CM lines (H9c2 and HL-1)	+ Easy culture and acquiring	- Interspecies differences - Proliferating

Table 3. Examples of experimental setups in *in vitro* cardiac ischemia-reperfusion modelling. There is variation regarding the used cell types, medium, method for inducing hypoxia and reoxygenation, length of hypoxia and reoxygenation, measurement of pO₂ and the evaluated parameters. Cell death is the most evaluated parameter, although it does not necessarily correlate with the infarct size. Electrophysiological parameters are less evaluated.

Study	Cell type	Medium	Hypoxia	Reoxygenation	pO ₂ measured	Evaluated parameters
Hidalgo et al., 2018	Metabolically matured hiPSC-CM	Hypoxia: pH 6.4, nutrient deprived Reoxygenation: pH 7.4	2 hours in 0% O ₂ incubator	4 hours in 20% O ₂ incubator	No	Cell death ROS production
Luo et al., 2014	hESC-CM with and without 24-hour CoPP preconditioning	Hypoxia: nutrient deprived	16 hours in 0.5% O ₂ in anaerobic chamber	24 hours in 21% O ₂ incubator	No	Cell death ROS production
Veldhuizen et al., 2022	hiPSC-CMs cocultured with fibroblasts in collagen hydrogel in microfluidic chip	Normal	24 hours in 1% O ₂ incubator	1- or 24-hour reperfusion in 21% O ₂ incubator	2D control after 3 hours Not chip samples Oxygen sensitive dye	Cell death Fibrosis Contraction Cell toxicity Gene expression
C.C. Chen et al., 2016	Commercial HCM line	Normal or supplemented with 30 μM caffeic acid phenyl ester	1% O ₂ in hypoxia chamber	No	No	Cell death Cx43 expression
Casals et al., 2009	Commercial AC16 line	Serum-free	5% O ₂ incubator for 6–48 hours	No	No	Cell death HIF-1-α activity Gene expression
Kuznetsov et al., 2015	Commercial H9c2 and HL-1 lines	Serum-free	2–24 hours in 0.4% O ₂ hypoxia chamber	24 hours in 21% O ₂ incubator	No	Cell death Mitochondrial respiration Protein expression
Yu et al., 2015	Commercial H9c2 line	Hypoxia: glucose-free Reoxygenation: normal	2–12 hours in 2% oxryase and 0% O ₂ hypoxia chamber	No	Continuous	Cell death ROS Protein and gene expression
Liu et al., 2020	Commercial HL-1 line in microfluidic chip	Hypoxia: deoxygenated normal medium (1–4% O ₂) Reoxygenation: normal	2.5–5 hours of 1–4% O ₂ medium flow	21% O ₂ medium flow	Continuous from medium	Electrophysiology (field potentials and AP-like signals) HIF-1-α expression
Ronkainen et al., 2011	Embryonic mouse CM	Normal	24 hours in 1% O ₂ incubator	No	No	Cell death Protein and gene expression

Human CMs

Human adult CMs are the goal in *in vitro* ischemia modelling. However, primary human CMs are not readily available, as the only way for acquiring these cells is harvesting them from adult human hearts. In addition, they are difficult to dissociate into single cells and have poor survival over long culture periods (Sharma et al., 2015; Yang, Pabon, et al., 2014). hiPSCs as well as human ESCs (hESCs) can be differentiated into CMs providing an unlimited source of human CMs. However, as established before, CMs produced this way are developmentally immature (A. S. T. Smith et al., 2017), and especially the immature energy metabolism relying on glycolysis makes hiPSC-CMs more resistant to hypoxia and reoxygenation injury (Hidalgo et al., 2018), making it difficult to transfer the results to clinical situation (Ytrehus, 2006).

Hidalgo and co-workers used metabolically matured hiPSC-CMs to model ischemia and reperfusion *in vitro*. The maturation was done by depriving the hiPSC-CMs of glucose while adding galactose to enhance long-chain FA oxidation in the mitochondria. Ischemia was mimicked by inducing hypoxia in low pH (6.2) medium that was deprived of nutrients and oxygen and by placing the cells to 0% oxygen incubator for two hours. After this reperfusion was mimicked by providing the cells oxygenated medium containing glucose with pH adjusted to 7.4 and placed the cells to 20% oxygen incubator for four hours. Comparison of the non-maturated and matured hiPSC-CMs showed that the release of lactate dehydrogenase, an indication of cell death, was increased from approximately 5% up to 30% indicating that the matured hiPSC-CMs were more susceptible to IR injury (Hidalgo et al., 2018).

Luo and co-workers studied the survival of hESC-derived CMs in hypoxic conditions with and without preconditioning with cobalt protoporphyrin (CoPP), which could be utilized in improving the survival of hESC-CMs transplanted to ischemic area of the heart in MI patients. CoPP is a transcriptional activator of heme oxygenase-1 known to have a protective effect in CMs exposed to hypoxia. In this study, Luo and co-workers pretreated hESC-CMs in CoPP for 24 hours under normoxic conditions, after which they exposed the cells to 0.5% oxygen for 16 hours and 21% oxygen for 24 hours. They showed that heme oxygenase-1 expression was increased

in CoPP preconditioned hESC-CMs and their survival was improved in IR compared to control group (Luo et al., 2014).

Veldhuizen and co-workers developed a microfluidic heart-on-a-chip model utilizing 3D anisotropic cardiac tissue construct consisting of hiPSC-CMs and fibroblasts cultured in a collagen-based hydrogel for modelling IRI. 1% oxygen hypoxia was induced for 24 hours, after which samples were collected or continued to 1- or 24-hour reoxygenation. They observed that the cardiac tissue construct reproduced several responses of myocardial ischemia, including tissue fibrosis, tissue contraction dysregulation, upregulation of hypoxia-response genes, downregulation of contractile-specific genes as well as transcriptomic pathway regulation of hypoxic tissue. Furthermore, during reoxygenation, cell toxicity, contractile irregularities and reestablishment of lactate levels and gene expression were observed, as is characteristic to reperfusion injury (Veldhuizen et al., 2022).

Commercially available human CM cell lines used in modelling MI include Human Cardiac Myocytes (HCMs) by PromoCell (C. C. Chen et al., 2016) and AC16 Human Cardiomyocyte Cell Line (Casals et al., 2009). HCMs are primary cells harvested from normal human adult heart ventricle tissue of patients who underwent heart transplantation. These cells are cardiac progenitor cells that unlike adult CMs are still able to proliferate and can be passaged up to 8 times. The cells can be cultured for long term in *in vitro* conditions unlike adult human primary CMs. AC16 line is another proliferating human CM-like line that is created from primary human adult CMs by fusing the primary CMs with SV40 transformed fibroblasts (Davidson et al., 2005).

Chen and co-workers used HCMs to study the effect of caffeic acid phenethyl ester on expression of connexin 43 under hypoxic conditions as connexin 43 is known to have a role in regulating heart function in hypoxia. They cultured the cells in 1% oxygen conditions for 30 minutes and observed an increase in connexin 43 expression and CM survival when they were exposed to caffeic acid phenethyl ester (C. C. Chen et al., 2016). Casals and co-workers studied the effect of hypoxia on release of B-type natriuretic peptide (BNP) hormone in AC16 cells, as BNP has significant cardio-protective properties. In this study, normoxia was defined as 21% oxygen and hypoxia as 5% oxygen. The BNP release was shown to increase gradually during hypoxia and was 2–3-fold higher in hypoxic CMs compared to control.

Furthermore, increase in BNP mRNA expression was observed, indicating changes in the transcriptional level. It was known that BNP levels increase in MI, but this study showed that the mechanism of BNP release is oxygen-mediated (Casals et al., 2009).

Animal cardiomyocytes

Using animal primary cell models has several advantages over adult human CMs. For example, they are more easily harvestable and the results from the cell experiments can be compared to results from *in vivo* settings without a change in the species. However, species difference makes it difficult to compare the results from animal and animal cell models to the actual clinical situation in human patients. Mostly rat and mouse primary CMs are used, but also rabbit cells have been studied. For research purposes, the cells are often harvested from neonatal (J. Wei et al., 2015) or embryonic (Ronkainen et al., 2011) stage animals. However, especially adult primary CMs have poor survival in *in vitro* culture conditions, although neonatal and embryonic CMs remain viable for longer (Ehler et al., 2013). There are also commercial immortalized CM-like cell lines, such as rat H9c2 line (Kuo et al., 2015; Tong et al., 2013; Yu et al., 2015) and mouse HL-1 line (Kuznetsov et al., 2015), as well as commercial animal ESC-lines, such as mouse P19 EC (Parameswaran et al., 2013).

H9c2 and HL-1 cells are both frequently used in *in vitro* ischemia studies. Kuznetsov and co-workers determined differences in metabolism and mitochondrial function as well as the sensitivity of the cells to IR. They observed significant differences mitochondrial organization, beta tubulin II (a regulator of cardiac energy metabolism) expression and localization, ATP levels, and activity of citrate synthase (a mitochondrial marker enzyme). In addition to the general differences in energy metabolism, significantly lower viability and decreased mitochondrial respiration after hypoxia and reoxygenation were observed in H9c2 cells compared to HL-1 cells. These evidence indicated that H9c2 cells are more similar to adult CMs and more susceptible to IRI than HL-1 cells, thus making them a better model for MI (Kuznetsov et al., 2015). Yu and co-workers studied the role of S100A1 calcium sensor protein in the inflammatory response of CMs during hypoxia and found that it activates the inflammatory response in H9c2 cells via TLR/ROS/NF- κ B signal pathway. In this study, ischemia was mimicked by

inducing hypoxia for 6 hours using oxygen binding enzyme oxyrase in 0% oxygen incubator (Yu et al., 2015).

Liu and co-workers developed a microfluidic chip incorporating intra- and extracellular bioelectronics for evaluating cardiac electrophysiology during hypoxia (Liu et al., 2020). In their chip, hypoxia was achieved within seconds, and the chip allowed continuous monitoring of extracellular field potentials of the CMs, whereas intracellular AP-like signals could be recorded with the intracellular bioelectronics via transient electroporation. They showed HL-1 cells to reproduce several electrophysiological changes characteristic to IR, including tachycardia, arrhythmias, and decreased conduction velocity. Their microfluidic chip was also capable of multiplexing, allowing high-throughput data collection of electrophysiological properties of the CMs on the chip (Liu et al., 2020). Primary mouse embryonic CMs were utilized by Ronkainen and co-workers in a study evaluating the effects of hypoxia to calcium handling of CMs (Ronkainen et al., 2011). They observed decrease in SERCA2a protein expression in CMs cultured in 1 % oxygen gas mixture for 24 hours. They also noticed differences in the calcium transients of the cells, which can be one reason of the functional depression of CMs upon ischemia (Ronkainen et al., 2011).

3 AIMS OF THE STUDY

The main aim of this thesis was to establish an *in vitro* model of ischemic heart disease using hiPSC-CMs. hiPSC-CMs are known to express more foetal than adult CM phenotype, which has been shown to affect their utilization in modelling ischemia-reperfusion injury. Thus, this thesis focused on finding similarities between hiPSC-CM and adult CM responses to hypoxia and reoxygenation. Another aspect considered in this thesis is the maturation of the hiPSC-CMs, and development of cardiac innervation model for disease modelling and drug screening applications. The specific aims for each study were as follows:

1. Induce hiPSC-CM maturation by culturing them on polyethylene terephthalate textiles (study I).
2. Establish a cardiac innervation model by coculturing hiPSC-CMs and hiPSC-neurons in compartmentalized microfluidic chip, which allows only axon-mediated interaction between the CMs and the neurons (study II).
3. Establish a model of ischemic heart disease utilizing hiPSC-CMs by optimizing the disease conditions and characterize the hiPSC-CM response to hypoxia and reoxygenation (studies III and IV).
4. Compare the hiPSC-CM response to chronic and acute hypoxia and reoxygenation (studies III and IV), and more comprehensively characterize the hiPSC-CM electrophysiological response to acute hypoxia-reoxygenation (study IV).

4 MATERIALS AND METHODS

4.1 Ethical considerations

In this study, hiPSC lines produced in Heart Group (BioMediTech, Tampere University) were used. Heart Group has the permission of the ethics committee of Pirkanmaa Hospital District for generating hiPSC lines from skin biopsies collected from donors (Aalto-Setälä R08070) and for cardiac differentiation of the hiPSCs (Aalto-Setälä R12123) and Neuro Group for neuronal differentiation of the hiPSCs (Narkilahti R05116). All donors gave a signed informed consent.

4.2 Cell culture and differentiation

4.2.1 Human induced pluripotent stem cells

Four control hiPSC-lines produced from donor cells of four healthy individuals were used in the studies of this thesis, including UTA.04602.WT (studies I–IV), UTA.10212.EURCCS (study II), UTA.11311.EURCCS (study IV) and UTA.10211.EURCCS (study IV). The hiPSCs lines UTA.04602.WT, UTA.10211.EURCCS and UTA.11311.EURCCS were expanded and maintained on mouse embryonic fibroblast (MEF) feeder cells (Merck-Millipore, Burlington, MA, USA) in KSR medium containing KnockOut DMEM with 10% KnockOut Serum Replacement, 1% MEM NEAA, 1% GlutaMAX, 0.2% β -mercaptoethanol (all from Gibco, Thermo Fisher Scientific, Waltham, MA, USA) and 0.5% Penicillin/streptomycin (Lonza, Basel, Switzerland). The hiPSC line UTA.10212.EURCCS was maintained and expanded on human foreskin fibroblast (HFF) feeder cells (ATCC, Manassas, VA, USA) in DMEM (Gibco) containing 20% KnockOut Serum Replacement and 0.1% Penicillin/streptomycin.

4.2.2 Differentiation

Cardiac differentiation

Small molecule differentiation (Lian et al., 2013) was used in study I for cardiac differentiation. The hiPSCs were transferred from MEFs to feeder-free culture on Geltrex-coated (Gibco) 6-well plates and maintained in mTeSR1 medium (STEMCELL Technologies, Vancouver, Canada) containing 0.5% Penicillin/streptomycin. Before starting the differentiation, the hiPSCs were transferred to Geltrex-coated 12-well plates and cultured in mTeSR1 medium until 100% confluent (day 0). The differentiation was initiated by changing the medium to insulin-free RPMI/B27 (Gibco) supplemented with 8 μM CHIR99021 (BPS Bioscience, San Diego, CA, USA) and 0.5% Penicillin/streptomycin. After 24 hours, fresh insulin-free RPMI/B27 medium was exchanged to the cells. On differentiation day 3, half of the old medium was collected from each well and mixed to the same volume of fresh insulin-free RPMI/B27 medium. The medium was supplemented with 5 μM IWP-4 (Tocris, Bristol, UK). Rest of the old medium was aspirated and IWP-4 containing medium was added to the cells. Days 5 and 7 of differentiation, all medium was exchanged to fresh insulin-free RPMI/B27 medium, and from day 10 forward, half of the medium was changed to insulin containing RPMI/B27 medium (Gibco) three times a week.

Embryoid body differentiation (Prajapati et al., 2021) modified from protocols by Karakikes and co-workers (Karakikes et al., 2014) and Lian and co-workers (Lian et al., 2013) was used in studies II–IV for cardiac differentiation. On day 0 of differentiation, the hiPSCs were transferred from MEFs to ultra-low attachment 6-well plates in mTeSR1 medium supplemented with 5 μM Blebbistatin (Sigma-Aldrich, Saint Louis, MO, USA) and 0.5% Penicillin/streptomycin to form embryoid bodies. On day 1, all medium was exchanged to insulin-free RPMI/B27 supplemented with 5 $\mu\text{l/ml}$ Ascorbic Acid (Sigma-Aldrich), 10 ng/ml BMP4 (R&D Systems, Minneapolis, MN, USA) and 25 ng/ml Activin A (PeproTech, Rocky Hill, NJ, USA). On day 3, all medium was exchanged to insulin-free RPMI/B27 supplemented with 5 $\mu\text{g/ml}$ Ascorbic Acid, and on day 4, all medium was exchanged to insulin-free RPMI/B27 supplemented with 2.5 μM IWP-4. On day 7, all medium was exchanged to insulin-free RPMI/B27 and from day 9 forward, half of the medium was exchanged three times a week. From day 11 on, medium was changed to insulin containing RPMI/B27 medium.

Neuronal differentiation

Before neuronal differentiation (Hyvärinen et al., 2019), hiPSCs were transferred from HFFs to feeder-free culture on 15 µg/ml human recombinant laminin-521 (BioLamina, Sundbyberg, Sweden) in E8 medium (Gibco) supplemented with 0.1% Penicillin/streptomycin. On day 0 of differentiation, hiPSCs were seeded on laminin-521 in E8 medium containing 10 µM ROCK Inhibitor (Sigma-Aldrich). Neural maintenance medium containing 1:1 DMEM/F12 with GlutaMAX and Neurobasal, 0.5% N2, 1% B27 with Retinoic Acid, 0.5 mM GlutaMAX, 0.5% NEAA, 50 µM β-mercaptoethanol (all from Gibco), 2.5 µg/ml Insulin (Sigma-Aldrich) and 0.1% Penicillin/streptomycin was used as the basal medium. During the neural induction stage on days 1–12, the medium was exchanged daily to neural induction medium, which was the neural maintenance medium supplemented with 100 nM LDN193189 and 10 µM SB431542 (both from Sigma-Aldrich). On day 12, the cells were detached with StemPro Accutase (Gibco) and seeded on 100 µg/ml poly-L-ornithine (PLO) (Sigma-Aldrich) on laminin-521 in the neural induction medium supplemented with 10 µM ROCK Inhibitor. On days 13–25 neural proliferation medium (maintenance medium supplemented with 20 ng/ml fibroblast growth factor) was exchanged daily to induce neural proliferation. The neural progenitor cells were passaged with StemPro Accutase and seeded in neural proliferation medium supplemented with 10 µM ROCK Inhibitor on days 17, 21 and 25. On day 26, the medium was changed to neural maturation medium (neural maintenance medium supplemented with 20 ng/ml brain-derived neurotrophic factor (R&D Systems), 10 ng/ml glial-derived neurotrophic factor (R&D Systems), 500 µM dibutyryl-cyclicAMP (Sigma-Aldrich) and 200 µM Ascorbic Acid) and the medium was exchanged three times a week.

4.2.3 Magnetic activated cell sorting

Magnetic activated cell sorting (MACS) was performed for hiPSC-CMs on day 21–27 of differentiation to improve cardiomyocyte purity before the experiments in all studies. First, the cells were dissociated with MultiTissue Dissociation Kit 3 (Miltenyi Biotec, Bergisch Gladbach, Germany) according to kit instructions. The cells were washed with 1×PBS (Lonza) and incubated at 37 °C for 10 min in Buffer X containing 10% Enzyme T provided by the

kit. Equal volume of 20% EB medium (KnockOut DMEM containing 20% FBS (Gibco), 1% GlutaMAX, 1% MEM NEAA, and 0.5% Penicillin/streptomycin) was added to the cells, and the cells were suspended into single cells and transferred to a Falcon tube.

MACS was performed with PSC-Derived Cardiomyocyte Isolation Kit, human (Miltenyi Biotec) according to kit instructions. The cells were centrifuged at $200\times g$ for 5 min at 4°C and the medium was aspirated. The cells were incubated in 1:5 Non-Cardiomyocyte Depletion Cocktail and MACS buffer ($1\times\text{PBS}$ containing 0.5% BSA (Sigma-Aldrich), 2 mM EDTA (Sigma-Aldrich), pH balanced to 7.2) at 4°C for 5 min ($100\ \mu\text{l}$ of solution/5 million total cells). The cell suspension was washed with $1\times\text{PBS}$ and centrifuged at $200\times g$ for 5 min at 4°C . 1 ml MACS buffer was added, and the cells were centrifuged as before. The supernatant was aspirated, and the cells were incubated in 1:5 Anti-Biotin Microbeads and MACS buffer at 4°C for 10 min. The LS Column attached to MACS Separator magnet was rinsed with MACS buffer and the cell suspension was applied onto the column. The column was rinsed three times with MACS buffer and the flowthrough containing the CMs was collected. The cell suspension was centrifuged once more, and the cells were resuspended to prewarmed 20% EB medium and were ready for seeding.

4.3 Polyethylene terephthalate textiles

4.3.1 Textile preparation

Polyethylene terephthalate textiles were used in study I aiming to improve hiPSC-CM maturation. The PET textiles were woven by narrow-weaving, and had aligned fibres as warps in their structure, whereas perpendicular to the warps the wefts formed the textile structure. The textile pattern was inhouse developed plain-weave derivative and produced at Tampere University of Technology from commercial yarn (Finn-Nauha Oy, Haapamäki, Finland). The textiles were 9 mm wide and heat treated before experiments to stabilize the textile structure. The textiles were cut into 7–8 mm pieces and sterilized for cell culture by soaking them into 70% ethanol. After the textiles had dried, they were coated with a thin layer of 0.1% gelatine (Type A Porcine Gelatine (Sigma-Aldrich) dissolved into $1\times\text{PBS}$ to form 0.1% solution) for one hour at

room temperature (RT) to improve cell attachment without compromising the textile topography. Excess coating was aspirated just prior the cell seeding.

4.3.2 Cell culture on textiles

After MACS, small molecule differentiated hiPSC-CMs were seeded on the gelatine coated PET textiles. 175 000 cells were seeded on the textile pieces as well as on 13 mm glass coverslips coated with 0.1% gelatine and used as control samples. The hiPSC-CMs were cultured for 11 days in 20% EB medium, changing half of the medium three times a week. After the culture on the textiles or coverslips, the samples were collected for immunocytochemical staining and RT-qPCR. For qPCR, samples from coverslips were collected also one day after seeding the cells.

4.4 Coculture of neurons and cardiomyocytes on 3D3C chip

4.4.1 3D3C chip preparation

In study II, hiPSC-neurons and hiPSC-CMs were cocultured on 3D3C chip that isolates the neuronal somas to one cell culture compartment and allowing only the neuronal axons to grow from the one compartment to the next via connecting microtunnels. This enables modelling axon-mediated interaction between the neurons and CMs (Ristola et al., 2019, 2021). The 3D3C chip is a PDMS-based compartmentalized microfluidic chip consisting of three separate cell culture compartments connected in series via microtunnels. Each cell culture compartment has its own medium chamber, allowing the culture of each cell type in their respective medium. The chip consists of two PDMS parts; the lower cell culture part contains the cell culture compartments and the microtunnels, whereas the top medium chamber part contains the separate medium chambers for each cell culture compartment. The cell culture part is attached on glass coverslip and the medium chamber part is attached on top of the cell culture part.

The 3D3C chips were prepared for coculture by coating HCl-washed 22×22 mm coverslips with 0.25 mg/ml PLO for 1.5 hours at 37 °C and washing them with sterile H₂O three times. After airdrying, the chips were

stored at 4 °C. The 3D3C chips were treated with polyvinylpyrrolidone and sterilized by soaking into 70% ethanol. After airdrying, the chips were attached on the PLO-treated coverslips. 30 µg/ml laminin-521 was used to coat the side cell culture compartments for neuronal culture, whereas 0.1% gelatine was used to coat the middle compartments for cardiomyocytes. The coating was done for overnight at 4 °C.

4.4.2 Coculture of neurons and cardiomyocytes

On day 32 of neuronal differentiation, 40 000 hiPSC-neurons were seeded to one side compartment of the 3D3C chips. The neurons were detached using StemPro Accutase and seeded to the 3D3C chips in the neural maturation medium supplemented with 10 µM ROCK Inhibitor. The hiPSC-neurons were cultured on the 3D3C chips for one week before seeding the hiPSC-CMs to allow axonal growth from the neuronal compartment to the middle compartment and during that time, the neural maturation medium was used in all compartments. 3 000–4 000 MACS-sorted hiPSC-CMs were seeded in 20% EB medium to the middle compartment one week after seeding the neurons. During the coculture, neural maturation medium was exchanged to both side compartments, whereas 20% EB medium was exchanged to middle cardiac compartment three times a week. The cells were cocultured on the 3D3C chips for 2 or 4 weeks, with a few cocultures followed up to 8 weeks.

As control samples, hiPSC-neurons and hiPSC-CMs were cultured separately on plastic and MatTek 48-well plates. The 48-well plates were coated similarly as the 3D3C chips, except 0.1 mg/ml PLO with 1 hour incubation and 15 mg/ml laminin-521 was used for coating the wells for neuronal culture. Cardiomyocytes were cultured on 0.1% gelatine coating. hiPSC-neurons were cultured in neural maturation medium and hiPSC-CMs on 20% EB medium, and the medium was exchanged three times a week. The 2D monocultures were continued for as long as the cocultures.

4.4.3 Neuronal stimulation and cardiomyocyte video recording

To evaluate the functionality of the interaction between the hiPSC-neurons and hiPSC-CMs, the neurons were stimulated with high-K⁺ extracellular solution after 2 or 4 weeks of coculture. The high extracellular K⁺ is known to

induce neural depolarization, and the extracellular solution consisted of 93 mM NaCl, 10 mM 4-(2-hydroxyethyl)-1-piperazineethanesulfonic acid (HEPES), 10 mM D-glucose, 50 mM KCl, 1.25 mM NaH₂PO₄, 2 mM CaCl₂ and 1 mM MgCl₂ (pH adjusted to 7.4 with NaOH). hiPSC-CM contraction was recorded for baseline before the neuronal stimulation (1. rec), during medium change to the neuronal compartment to evaluate the effect of liquid change to the hiPSC-CM functionality (2. rec), during high-K⁺ stimulation of the neurons to evaluate the immediate response of the hiPSC-CMs (3. rec) and after approximately 2 minutes of the neuronal stimulation as a follow-up (4. rec). Furthermore, hiPSC-CM response to direct exposure to the high-K⁺ solution in monoculture was recorded as control. The videos were analysed for peak-to-peak time, time-to-peak, relaxation time and contraction duration (10% above baseline) using MUSCLEMOTION (Sala et al., 2018). After the neuronal stimulation, the samples were collected for immunocytochemical staining and RT-qPCR.

4.5 Modelling ischemia and reperfusion

4.5.1 Seeding cardiomyocytes on 1-wells on glass and microelectrode array

In studies III and IV, MACS-sorted hiPSC-CMs were seeded on PDMS 1-wells attached on glass or microelectrode arrays (60MEA200/30iR-Ti, 8×8) (Multichannel Systems MCS GmbH, Reutlingen, Germany). In study III, the glass and MEA substrates were coated with 0.1% gelatine for 1.5 hours at RT, whereas in study IV the substrates were coated with 2% Geltrex (Geltrex stock solution mixed to KnockOut DMEM to form 2% solution). Approximately 95 000 cells/cm² were seeded in 20% EB medium on the 1-wells on glass and MEA to form hiPSC-CM sheets. The cells were cultured for 7–9 days before starting the hypoxia and reoxygenation experiments, and half of the of 20% EB medium was exchanged to fresh three times a week. On the day before the experiments, the whole medium was exchanged to serum- and glucose free medium (glucose-free DMEM (Gibco) supplemented with 1% MEM NEAA, 1% GlutaMAX and 0.5% Penicillin/streptomycin) for all samples. Glucose-free medium was used as it is known that glucose improves CM survival under hypoxia (Jovanović et al., 2006; Laubriet et al., 2001).

4.5.2 OxyGenie and 1-well assembly for control of oxygen partial pressure

OxyGenie (The Baker Company, Sanford, ME, USA) was used to induce hypoxia and reoxygenation for 1-well assemblies on glass (Figure 9A) (Kreutzer et al., 2016, 2017; Metsälä et al., 2018). OxyGenie allows the induction of hypoxia or reoxygenation for six parallel samples simultaneously. 1-well assembly consists of the 1-well on glass or MEA, Cover and Cover lock, as well as Lid and Lid lock (Figure 9B). This airtight chamber allows the precise control of oxygen partial pressure in the cell culture, as well as collection of the samples one by one, thus minimizing the time the samples are exposed to ambient air during sample collection. In study III, solid glass-made lid (Figure 9C) was used for modelling chronic IR, whereas in study IV, hollow Acute lid covered with gas permeable polyethylene membrane (Figure 9D) was used for modelling acute IR as it allows rapid change in the oxygen partial pressure due to the proximity of the membrane and the cells (500 μm).

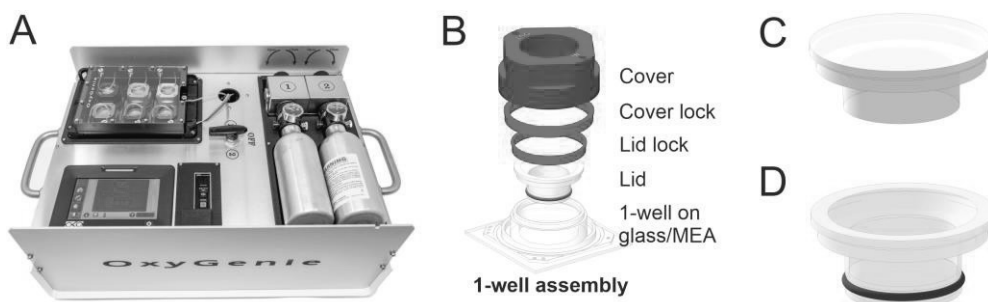


Figure 9. OxyGenie and 1-well assembly with different Lid options. A) OxyGenie was used to induce hypoxia and reoxygenation to 1-well assemblies on glass and enables simultaneous exposure of six parallel samples. B) 1-well assembly consists of 1-well on glass or MEA, Cover, Cover lock, Lid and Lid lock. The assembly is airtight allowing precise control over the oxygen partial pressure in the cell culture. C) Solid glass-made lid was used in the modelling of chronic ischemia-reperfusion. D) Hollow Acute lid covered with gas permeable polyethylene membrane was used in the modelling of acute ischemia-reperfusion.

4.5.3 Modelling chronic ischemia and reperfusion

For modelling of chronic ischemia and reperfusion in study III, solid glass-made lids were used with the 1-well assemblies. 1-well assemblies on glass were connected to OxyGenie and 0% O₂ 5% CO₂ 95% N₂ (hypoxic) gas was used to induce hypoxia for 8 or 24 hours. After the hypoxia, samples were

either collected as hypoxia end point samples (8h H and 24h H) or continued to reoxygenation using 19% O₂ 5% CO₂ 76% N₂ (normoxic) gas for 24 hours (8h HR and 24h HR). The control samples were kept in a standard humidified CO₂ incubator inside Petri dishes but without the Lids and Covers for the duration of the hypoxia and hypoxia-reoxygenation experiments. Control samples for 8h and 24h hypoxia samples were collected after the hypoxia period (8h C_H and 24h C_H) and control samples for the 8h and 24h hypoxia-reoxygenation were collected after the hypoxia-reoxygenation period (8h C_{HR} and 24h C_{HR}). After the experiments, the samples were collected one by one for immunocytochemical staining, western blotting or RT-qPCR.

After changing the serum- and glucose-free medium, the 1-well assemblies on MEA were connected to the recording system and normoxic gas for overnight baseline recording of the hiPSC-CM field potentials. On the next day, hypoxia was induced for 24 hours using the hypoxic gas, after which reoxygenation was induced for another 24 hours using the normoxic gas.

4.5.4 Modelling acute ischemia and reperfusion

For modelling of acute ischemia and reperfusion in study IV, Acute lids were used with the 1-well assemblies. 1-well assemblies on glass were connected to OxyGenie and hypoxic gas was used to induce hypoxia for three hours. After the hypoxia, samples were either collected as hypoxia end point samples (H), or reoxygenation was induced to the samples using normoxic gas for 24 hours (HR). The control samples were kept in a standard humidified CO₂ incubator inside Petri dishes but without the Lids and Covers for the duration of the experiments. Hypoxia control (C_H) samples were collected after the 3-hour hypoxia, whereas hypoxia-reoxygenation control (C_{HR}) samples were collected after 3-hour hypoxia and 24-hour reoxygenation. After the experiments, the samples were collected one by one for immunocytochemical staining, western blotting or RT-qPCR.

Similar to chronic hypoxia-reoxygenation, the 1-well assemblies on MEA were connected to the recording system and normoxic gas for overnight baseline recording immediately after changing the serum- and glucose-free medium. On the next day, hypoxia was induced for three hours using the hypoxic gas, after which reoxygenation was induced for 24 hours using the

normoxic gas. Figure 10 presents the timeline for the experiments for both chronic and acute hypoxia-reoxygenation.

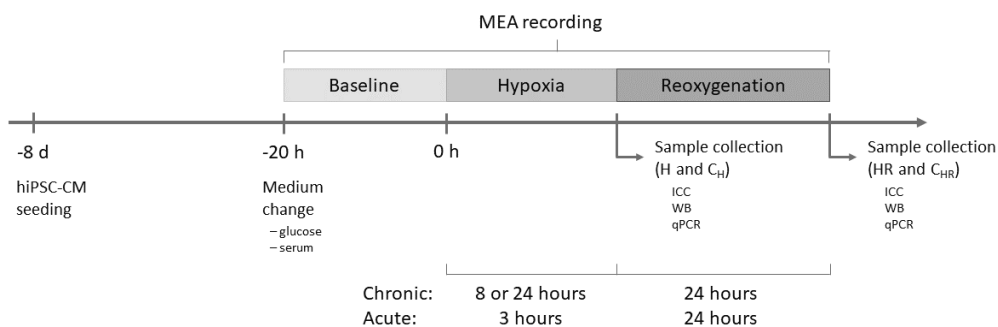


Figure 10. Timeline for chronic and acute hypoxia-reoxygenation experiments. The samples were connected to OxyGenie and hypoxia was induced for 8 or 24 hours in chronic experiments, or 3 hours in acute experiments. After hypoxia, the samples were either collected (H) or continued to reoxygenation (HR) for 24 hours. Control samples were kept in normoxic conditions in a standard incubator for the duration of the hypoxia (C_H) or hypoxia-reoxygenation (C_{HR}).

4.5.5 Measurement of oxygen partial pressure

Oxygen partial pressure was measured to evaluate the oxygen dynamics in the samples as well as to compare the electrophysiological response of the hiPSC-CMs to the changing pO₂ during hypoxia and reoxygenation. pO₂ was measured with a luminescence-based sensor with a biocompatible sensing material (Rajan et al., 2018; Välimäki et al., 2017, 2020) attached to the MEA disk close to the middle electrode area where the cells were cultured, allowing the pO₂ measurement directly from the cell culture. In study III, pO₂ was measured once every minute, which was sufficient to monitor the slower oxygen dynamics of the glass Lid. In study IV, pO₂ was measured every 15 seconds to monitor the rapid changes in the oxygen partial pressure allowed by the Acute lid. After the cell experiments, the measurements were calibrated using the same MEA after detaching the cells.

4.6 Microelectrode array

4.6.1 Field potential recording

The microelectrode arrays used in studies III and IV were 60MEA200/30iR-Ti, 8×8 (Multichannel Systems MCS GmbH). Multichannel Experimenter (Multichannel Systems MCS GmbH) was used to record hiPSC-CM field potentials during baseline, hypoxia and reoxygenation. The 1-well assemblies on MEAs were placed on MEA2100 System (sampling frequency 25 kHz) or on MEA2100 Lite System (pO₂ samples, sampling frequency 20 kHz) and connected to normoxic gas for overnight baseline recording. On the following day, hypoxia was induced using the hypoxic gas for 24 hours in study III and for three hours in study IV. After hypoxia, reoxygenation was induced for 24 hours in both studies.

In study III, baseline was recorded for one minute every hour, whereas during hypoxia and reoxygenation, the recording was done for one minute every 30 minutes. In study IV, baseline was recorded for one minute every hour, except for the last hour before initiating the hypoxia, when one minute every five minutes was recorded. For the first 30 minutes of the hypoxia, one minute every other minute was recorded, after which, one minute every five minutes was recorded until one hour of hypoxia. For the last two hours of hypoxia, one minute every ten minutes was recorded. The first three hours of reoxygenation were recorded as the three hours of hypoxia, after which one minute every 30 minutes was recorded. For the pO₂ samples in study IV, the recording protocol was slightly different. The baseline was recorded similarly as with the other MEA samples, but the hypoxia and first three hours of reoxygenation were recorded for one minute every five minutes. After this, the rest of the reoxygenation period was recorded one minute every 30 minutes.

4.6.2 Field potential analysis

The analysis of the recorded MEA data was done using inhouse developed scripts. Beating frequency, field potential duration, depolarization time and depolarization amplitude were analysed using MATLAB (MathWorks, Inc.,

Natick, MA, USA), whereas field potential propagation was analysed using R (R Foundation for Statistical Computing, Vienna, Austria).

For the MATLAB analysis, the recorded files were converted from MSRD to HDF5 using Multichannel DataManager (Multichannel Systems MCS GmbH) and five electrodes with strong baseline signal were chosen from each MEA sample for the analysis. Beating frequency was normalized to mean beating frequency of the three baseline values recorded just before initiating hypoxia, to be able to better compare the results despite the variation of the baseline beating frequency between different samples. The depolarization time (t_{dep}) was determined as the time from 10% deviation from the baseline to the maximum value of the depolarization peak and the depolarization amplitude (A_{dep}) was defined as the maximum value of the depolarization peak. Field potential duration (FPD) was defined as the time from the 10% deviation from the baseline to the depolarization peak to the return from repolarization wave to 10% of the baseline (Figure 11). FPD was beat rate corrected (corrected FPD, cFPD) using Izumi-Nakaseko formula (Izumi-Nakaseko et al., 2017) in study IV.

For the field potential propagation (FPP) analysis with R, timestamps for the field potentials on each electrode were detected and converted to text-files using Multichannel Analyzer (Multichannel Systems MCS GmbH). The text-files were further analysed for FPP using inhouse developed scripts in R (R Foundation for Statistical Computing, Vienna, Austria). Based on the field potential timestamps, propagation of the field potential between adjacent electrodes throughout the hiPSC-CM sheet on the MEA electrode grid was calculated. The data from study III was reanalysed compared to the original publication, as the analysis was further developed for study IV, so that the results from studies III and IV could be better compared to each other, thus the FPP time values differ from the original publication. However, the end result remains.

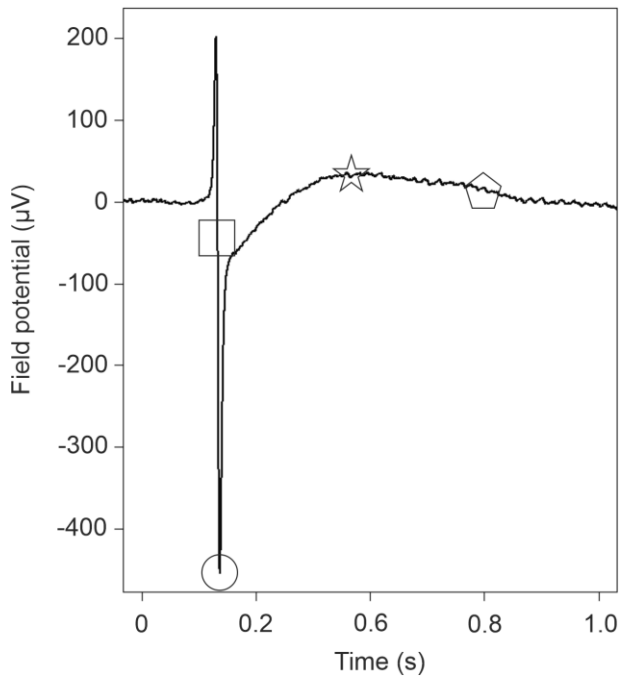


Figure 11. Field potential parameters extracted from the field potential signals with MATLAB. Square indicates the 10% deviation from the baseline compared to the maximum depolarization amplitude marked by circle. Depolarization time was the time from the square to the circle. Field potential duration was calculated from the square to the pentagon, which marks 10% deviation from the baseline compared to the maximum repolarization amplitude indicated by the star.

4.7 Protein and gene expression

4.7.1 Immunocytochemistry

Immunocytochemistry (ICC) was performed in all studies to evaluate hiPSC-CM structure, morphology, and protein expression, as well as for evaluating hiPSC-CM and hiPSC-neuron physical connections. In study I, ICC was performed after culturing hiPSC-CMs on the PET textiles for 11 days. In study II, ICC was performed after the neuronal stimulation with high- K^+ solution at 2 or 4 weeks of coculture. In studies III and IV, ICC was performed immediately after hypoxia for H and C_H samples, or after hypoxia-reoxygenation for HR and C_{HR} samples. In study I, basic double fluorescence protocol (Ojala et al., 2012) was used for ICC, whereas the protocol was

slightly modified for studies II–IV. In study II, fixing of the 3D3C samples was done for 45 minutes by replacing half of the culture medium with the fixing solution and all washing steps after primary antibody incubation were increased to 30 minutes. Furthermore, the secondary antibody incubation was increased to 1.5 hours. These modifications ensured proper washing, fixing and staining of the microtunnels. Furthermore, after secondary antibody incubation, the samples were washed with DAPI diluted in PBS (1:5000). In studies III and IV, the initial washing steps were reduced to approximately 10 seconds, to ensure that hypoxia inducible factor 1 alpha (HIF1- α) did not degrade before fixing.

The samples were fixed with 4% and blocked with 10% normal donkey serum (Biowest, Nuaille, France), and labelled against goat anti-Cardiac Troponin T (cTnT) (1:1000 (studies I and IV) and 1:750 (study II), ab64623, Abcam, Cambridge, UK), mouse anti-MyBPC3 (cMyBP-C) (1:500, sc-166081, Santa Cruz Biotechnology, Dallas, TX, USA) (studies I, III and IV), rabbit anti-HIF1 α (1:1000, 700505, Invitrogen, Waltham, MA, USA) (studies III and IV), mouse anti-neurofilament NF-H 200 (1:500, N5389, Sigma-Aldrich) (study II), mouse anti- β -tubulin III (1:500, T8660, Sigma-Aldrich) (study II) and rabbit anti-synapsin I (1:500, 574777, Merck-Millipore) (study II). In each study, primary antibody incubation was done at 4 °C for overnight. As secondary antibodies, donkey anti-goat Alexa Fluor 568 (studies I and IV), donkey anti-mouse Alexa Fluor 488 (study I), donkey anti-rabbit Alexa Fluor 488 (studies III and IV), donkey anti-mouse 647 (study IV) were used (all secondary antibodies were diluted 1:800 and ordered from Invitrogen). In study II, the secondary antibodies donkey anti-rabbit Alexa Fluor 488 and donkey anti-goat 568 (Invitrogen) were diluted 1:400 for 48-well plate controls and 1:200 for 3D3C chip cocultures. Donkey anti-mouse Alexa Fluor 647 (Invitrogen) was diluted 1:200 for 48-well plate controls and 1:125 for 3D3C chip cocultures. Secondary antibody incubation was done for one hour at RT, except in study II for 1.5 hours. Cell nuclei were visualized using Vectashield Mounting Medium with DAPI (Vector Laboratories, Burlingame, CA, USA).

The fluorescence was visualized using different methods in different studies. In study I, Nikon A1R+ Laser Scanning Confocal Microscope (Nikon, Tokyo, Japan) using Apo 60 \times 1.40NA oil objective (Nikon), as well as Axio Imager.M2 (Zeiss, Oberkochen, Germany) with ApoTome.2 (Zeiss) and

AxioCamHRm3 camera (Zeiss) using EC Plan-Neofluar 40× 1.30NA oil objective (Zeiss) were used for fluorescence visualization. In studies II and IV, IX51 Inverted Fluorescence Microscope (Olympus, Tokio, Japan) using either LUCPlan FL N 40×/0.60, WD 3.0–4.2 mm (Air) objective (Olympus), Olympus LUCPlan FL N 20×/0.45, WD 6.6–7.8 mm (Air) objective (Olympus) or CPlanFL N 10×/0.30, WD 9.5 mm (Air) objective (Olympus) with Orca Flash4.0LT+ sCMOS camera (Hamamatsu Photonics, Hamamatsu, Japan) was used for fluorescence visualization. In addition, in study II, LSM 780 Laser Scanning Confocal Microscope (Zeiss) using Plan Apo 40×/1.40, WD 0.24 mm (Oil) objective (Zeiss) with 32-channel QUASAR GaAsP PMT array detector was used. The confocal images in study II were deconvoluted with Hyugens and processed with Imaris (Oxford Instruments, Abingdon, UK). In studies III and IV, LSM 800 Laser Scanning Confocal Microscope (Zeiss) with EC Plan-Neofluar 40×/0.75, WD 0.71 mm (Air) objective (Zeiss) and 2 channel spectral detection with high-sensitivity PMT detector was used for visualizing the fluorescence.

4.7.2 Western blot

In studies III and IV, hiPSC-CM expression of sarcomeric proteins (study III) and HIF1- α (studies III and IV) was evaluated using western blot. Immediately after the hypoxia or hypoxia-reoxygenation and minimizing the exposure to ambient air, the protein samples were collected in 150 μ l of 2×Laemmli Sample Buffer (Bio-Rad, Hercules, CA, USA) containing 5% β -mercaptoethanol (Sigma-Aldrich) and heated at 95 °C for 5 minutes. 4–20% Mini PROTEAN TGX Precast Protein Gel with 10 50 μ l wells (Bio-Rad) was used for SDS-PAGE, and 20 μ l of protein samples were pipetted into the gel wells. Trans-Blot Turbo RTA Mini PVDF Transfer Kit (Bio-Rad) was used with Trans-Blot Turbo Transfer System (Bio-Rad) to blot the samples from the gels to the PVDF membranes. The membranes were blocked for three hours at RT in 3% bovine serum albumin (BSA) in 0.1% Tween20 (Sigma-Aldrich) in tris-buffered saline (TBS) (0.1% TBS-Tween).

After the blocking, the membranes were incubated in primary antibody solution for overnight at 4 °C. Mouse anti- β -actin (1:1000, sc-47778, Santa Cruz Biotechnology) and rabbit anti-HIF1 α (1:1000) were used as primary antibodies in both studies III and IV, whereas mouse anti-Cardiac Troponin T

(1:1000, ab33589, Abcam) and mouse anti-MyBPC3 (1:500) were used only in study III. Secondary antibody incubation was done at RT for one hour using horseradish peroxidase-conjugated recombinant anti-mouse IgG (1:3000, sc-516102, Santa Cruz Biotechnology) and swine anti-rabbit IgG (1:2000, P0217, Dako, Agilent, Santa Clara, CA, USA) as secondary antibodies. Both primary and secondary antibodies were diluted in 3% BSA in 0.1% TBS-Tween and after each antibody incubation, the membranes were washed in 0.5%, 0.1% and 0.05% TBS-Tween. The detection of the protein-antibody complexes was done with Amersham ECL Prime Western Blot Detection Reagent (Cytiva, Marlborough, MA, USA) and ChemiDoc MP Imaging System (Bio-Rad). The antibodies were stripped at 56 °C for 30 minutes in a buffer containing 0.705% β -mercaptoethanol, 2% SDS (Sigma-Aldrich) and 0.03125 M Tris (VWR, Radnor, PA, USA in Milli-Q water. The membranes were washed in TBS before starting new blocking.

4.7.3 Reverse transcription quantitative polymerase chain reaction

Reverse transcription quantitative polymerase chain reaction (RT-qPCR) was performed to evaluate the gene expression of the hiPSC-CMs regarding maturation (study I), the expression of genes showing cardiac and neuronal identity as well as genes encoding proteins required for functional CM-neuron interaction (study II), as well as the response to hypoxia and reoxygenation (studies III and IV). The evaluated genes and their TaqMan 20 \times Assay IDs are presented in Table 3. In studies III and IV, samples were collected after hypoxia or hypoxia-reoxygenation one by one minimizing the exposure of the samples to ambient air.

Table 4. The 20× TaqMan Assays used in RT-qPCR in each study. In study I, the focus was on genes indicating cardiac maturation and in study II, on genes indicating cardiac or neuronal identity as well as genes responsible for functional interaction between the cell types. In studies III and IV, the focus was on genes, whose expression is known to change during ischemia and reperfusion.

Gene	Function	Assay ID	Study
<i>MYL2</i>	Sarcomeric gene	Hs00166405_m1	I
<i>MYL7</i>	Sarcomeric gene	Hs01085598_g1	I
<i>MYL9</i>	Sarcomeric gene	Hs00697086_m1	I
<i>MYH6</i>	Sarcomeric gene	Hs01101425_m1	I
<i>MYH7</i>	Sarcomeric gene	Hs01110632_m1	I, IV
<i>TNNC1</i>	Sarcomeric gene	Hs00896999_g1	I
<i>ACTN2</i>	Sarcomeric gene	Hs00153809_m1	I
<i>TTN</i>	Sarcomeric gene	Hs00399225_m1	I
<i>TPM1</i>	Sarcomeric gene	Hs00165966_m1	I
<i>MYBPC3</i>	Sarcomeric gene	Hs00165232_m1	I–III
<i>TNNT2</i>	Sarcomeric gene	Hs00165960_m1	I–III
<i>SCN5A</i>	Sodium channel	Hs00165693_m1	I
<i>KCNH2</i>	Potassium channel	Hs04234270_g1	I
<i>KCNH6</i>	Potassium channel	Hs00229215_m1	I
<i>KCNA10</i>	Potassium channel	Hs01563550_s1	I
<i>KCND3</i>	Potassium channel	Hs00542597_m1	I
<i>KCNQ1</i>	Potassium channel	Hs00923522_m1	I
<i>HCN4</i>	Potassium channel	Hs00975492_m1	I
<i>CACNA1C</i>	Calcium channel	Hs00167681_m1	I
<i>PLN</i>	Calcium handling	Hs01848144_s1	I
<i>CHRM2</i>	Acetylcholine (ACh) receptor	Hs00265208_s1	II
<i>ADRB2</i>	Adrenergic receptor	Hs00240532_s1	II
<i>ADRB3</i>	Adrenergic receptor	Hs00609046_m1	II
<i>CHAT</i>	ACh synthesis	Hs00758143_m1	II
<i>DBH</i>	Dopamine to noradrenaline	Hs01089840_m1	II
<i>TH</i>	Tyrosine to dopamine	Hs00165941_m1	II
<i>TUBB3</i>	Neuronal microtubular protein	Hs00801390_s1	II
<i>ATP2A2</i>	Calcium handling	Hs00544877_m1	I, III
<i>SLC8A1</i>	Calcium handling	Hs01062258_m1	I, III
<i>RYR2</i>	Calcium handling	Hs00892883_m1	III
<i>HIF1A</i>	Hypoxia marker	Hs00153153_m1	III
<i>MAP4K4</i>	Hypoxia marker	Hs00377415_m1	III
<i>CASP3</i>	Apoptotic (pro)	Hs00234387_m1	III
<i>BAX</i>	Apoptotic (pro)	Hs00180269_m1	IV
<i>BCL2</i>	Apoptotic (anti)	Hs00608023_m1	IV
<i>ACADM</i>	Fatty acid metabolism	Hs00936584_m1	III
<i>ACAA1</i>	Fatty acid metabolism	Hs01576070_m1	III
<i>PFKM</i>	Glycolysis	Hs01576070_m1	III
<i>SLC2A1</i>	Glycolysis	Hs00892681_m1	III, IV
<i>PKM isoform 1</i>	Glycolysis	Custom	IV
<i>PKM isoform 2</i>	Glycolysis	Custom	IV
<i>HSP1A1</i>	Cellular stress response	Hs00359163_s1	IV
<i>VEGFA</i>	Angiogenesis	Hs00900055_m1	IV
<i>GUSB</i>	Housekeeping	Hs00939627_m1	II
<i>GAPDH</i>	Housekeeping	Hs02758991_g1	I–IV
<i>EEF1A1;EE+</i>	Housekeeping	Hs00265885_g1	I–IV
<i>TBP</i>	Housekeeping	Hs00427620_m1	I, III, IV

In study I, samples were collected on days 1 and 11. CellsDirect One-Step qRT-PCR Kit (Invitrogen) was used for lysing and RT-qPCR according to kit instructions. qPCR was performed using 48.48 Dynamic Array IFC for Gene Expression (Fluidigm Corporation, South San Francisco, Ca, USA). In study II, the samples were lysed in Buffer RA1 containing 1% β -mercaptoethanol (Sigma-Aldrich) and NucleoSpin RNA kit (Macherey-Nagel, Düren, Germany) was used for RNA extraction according to kit instructions. In study III, samples were collected in QIAzol Lysis Reagent (Qiagen, Hilden, Germany) and RNA was extracted using miRNeasy Mini Kit (Qiagen) according to kit instructions. In study IV, RNA extraction was performed with Monarch Total RNA Miniprep Kit (New England BioLabs, Ipswich, MA, USA) following the kit instructions.

In studies II–IV, reverse transcription was performed using High-Capacity cDNA Reverse Transcription Kit (Applied Biosystems, Waltham, MA, USA) according to kit instructions. In studies II and IV, pre-amplification of the inspected genes was performed using TaqMan Pre-Amp Master Mix (Applied Biosystems) according to kit instructions and TaqMan Fast Advanced Master Mix (Applied Biosystems) was used according to kit instructions for qPCR. In study III, qPCR was performed using TaqMan Gene Expression Master Mix (Applied Biosystems) according to kit instructions without the pre-amplification step. The $2^{-\Delta\Delta C_t}$ method (Livak & Schmittgen, 2001) was used to calculate the relative expressions of the genes in all studies. *GAPDH*, *EEF1A1;EE+* and *TBP* were used in studies I, III and IV, whereas *GAPDH*, *EEF1A1;EE+* and *GUSB* were used in study II as endogenous controls.

4.8 Quantitative analysis of the fluorescent images

4.8.1 Cell and sarcomere alignment

In study I, the morphological and structural properties of the hiPSC-CMs were evaluated from the fluorescent images taken from hiPSC-CMs cultured on PET textiles or coverslips using CytoSpectre (Kartasalo et al., 2015). Cardiac troponin T (cTnT) channel was used for masking to determine individual cells with ImageJ and cardiac myosin binding protein C (cMyBP-C) channel was used for determining the sarcomere properties of the individual cells.

Analysed properties included sarcomere orientation and length, as well as the aspect ratio (ratio of length to width) of the cells. Sarcomere orientation is described by circular variance with values ranging from zero to one, zero describing perfect sarcomere alignment into one direction, and one describing equal orientation into all directions. Wavelength of the detailed spectral component was used for determining the modal sarcomere length. In addition, the software calculates the minor and major axes of the individual cells from the masks defined from the cTNT channel, which can be used for calculation the aspect ratio of the hiPSC-CMs.

4.8.2 Sarcomere coverage and size of nuclei

In study III, sarcomere coverage and size of the nuclei were analysed from the fluorescent images. Sarcomere coverage was determined as the ratio of the area presenting clear sarcomere structures to the total area of the cells. ImageJ (Schindelin et al., 2012) was used to calculate the areas from the fluorescent images. Nuclei size from the DAPI channel of the fluorescent images was determined using CellProfiler (McQuin et al., 2018). IdentifyPrimaryObjects was used to identify the nuclei in the images, with the object size limit set to 50–250. Objects outside the size limit as well as objects touching the image borders were excluded. Global was set as the threshold strategy and two class Otsu was used as the method for thresholding. The method for distinguishing clumped objects was set as shape and the nuclei area was determined using MeasureObjectShape from the objects that were identified from the images as primary objects.

4.9 Statistical analysis

Statistical analysis of the data was performed using rstatix package (Kassambra, 2021) for R. Kruskal-Wallis test with Dunn's post hoc test with Holm correction was used for all individual data acquired from RT-qPCR, analysis of the fluorescent images of the immunocytochemical staining, western blot and for field potential propagation. The paired electrophysiological and functional data was tested statistically using paired Wilcoxon Signed Rank Test with Bonferroni correction.

5 RESULTS

5.1 Maturation of hiPSC-CMs cultured on PET textiles

In study I, hiPSC-CMs were cultured on 0.1% gelatine-coated polyethylene terephthalate textiles for 11 days to induce cell alignment along the textile fibres, as hiPSC-CMs typically exhibit small and round morphology with disoriented sarcomere alignment. After the 11-day culture on PET textiles, hiPSC-CMs cultured on the textiles and control cells cultured on glass coverslips were fixed for ICC or lysed for RT-qPCR, to evaluate the structural properties and cardiac-specific gene expression, respectively. For qPCR, also 1-day coverslip samples were collected and used for normalization of the data.

5.1.1 Morphology and sarcomere orientation

Significant improvement was observed in the morphology and sarcomere alignment of the hiPSC-CMs after the culture of PET textiles ($n = 98$) compared to control ($n = 174$) (Figure 12). CytoSpectre software was used to analyse the fluorescent images of the ICC staining for hiPSC-CM morphological properties including aspect ratio, sarcomere orientation and sarcomere length. hiPSC-CMs cultured on PET textiles showed significantly improved sarcomere orientation described by circular variance, which was 0.61 ± 0.16 for hiPSC-CMs cultured on PET textiles and 0.88 ± 0.07 for hiPSC-CMs cultured on coverslips ($p < 0.0001$). Moreover, the aspect ratio of the hiPSC-CMs cultured on PET textiles was 4.91 ± 2.26 and significantly higher compared to hiPSC-CMs cultured on coverslips, for which it was 1.57 ± 0.46 ($p < 0.0001$). However, there was no improvement in the sarcomere length between the groups (1.74 ± 0.19 for PET and 1.75 ± 0.12 for coverslip).

5.1.2 Expression of cardiac specific genes

The expression of the cardiac specific genes was not observed to improve significantly between PET ($n = 6$) and coverslip ($n = 6$) samples after 11 days

of culture, however, the gene expression improved overall in both groups compared to the coverslip samples cultured for one day ($n = 4$). Furthermore, an increasing trend was observed in the expression of several sarcomeric genes, including *TNNT2* encoding cardiac troponin T (1.07 ± 0.43 for day 1 coverslip, 4.21 ± 3.39 for day 11 coverslip and 9.22 ± 6.58 for PET), *ACTN2* encoding cardiac alpha actinin (1.48 ± 1.46 for day 1 coverslip, 14.95 ± 18.53 for day 11 coverslip and 20.05 ± 21.40 for PET) and *MYBPC3* encoding cardiac myosin binding protein C (1.10 ± 0.58 for day 1 coverslip, 7.24 ± 5.73 for day 11 coverslip and 14.82 ± 12.89 for PET).

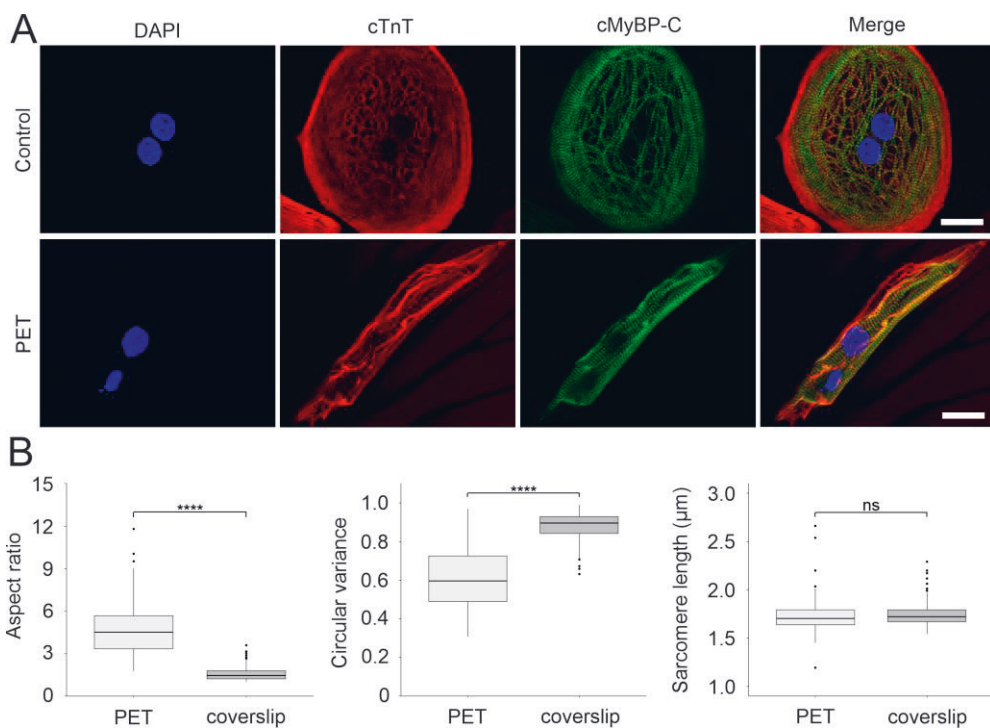


Figure 12. Structural properties of the hiPSC-CMs were observed to improve significantly when cultured on PET textiles compared to coverslips. A) Examples of ICC staining of hiPSC-CMs cultured on PET textiles and coverslips. hiPSC-CMs exhibited more elongated morphology and increased sarcomere orientation when cultured on PET textiles (scale bar 25 μm). B) Aspect ratio (the ratio of major to minor axis) improved in hiPSC-CMs cultured on PET textiles compared to control. Furthermore, circular variance was lower in hiPSC-CMs cultured on PET textiles, indicating improved sarcomere orientation. However, culturing hiPSC-CMs on PET textiles did not improve their sarcomere length. **** $p < 0.0001$

5.2 Coculture of hiPSC-CMs and hiPSC-neurons on 3D3C chip

In study II, hiPSC-CMs and hiPSC-neurons were cocultured on a compartmentalized microfluidic 3D3C chip designed for neuronal soma isolation (Ristola et al., 2019, 2021). hiPSC-neurons were cultured in one side compartment and hiPSC-CMs in the middle compartment. The neuronal axons traversed from the neuronal to the cardiac compartment via connecting microtunnels, allowing only axon-mediated interaction between the cell types. The cocultures were characterized at 2 and 4 weeks timepoints via ICC and fluorescence imaging, RT-qPCR, and video recording of the hiPSC-CMs during neuronal stimulation with high-K⁺ solution.

5.2.1 Coculture and viability

The 3D3C chip restricts neuronal somas into one compartment allowing only the axons growing from the one compartment to the next via microtunnels connecting the compartments (Figure 13A). This allows modelling the axon-mediated neuron-cardiomyocyte interaction as it occurs *in vivo*, where the neuronal axons of cANS innervate the heart. hiPSC-neurons were cultured on the side compartment for one week before seeding hiPSC-CMs into the middle compartment, which allowed the axons to grow to the cardiac compartment beforehand. The separate medium chambers for each cell culture compartment allow the culture of each cell type in their corresponding medium without the need to compromise the specific medium needs of neither cell type.

The viability of the hiPSC-CMs and hiPSC-neurons during coculture on the 3D3C chips was observed from the phase-contrast images of the cocultures and video recordings of the hiPSC-CMs. Both cell types were viable and the hiPSC-CMs exhibited normal beating characteristics also in contact with the neuronal axons for the whole duration of the coculture (2 and 4 weeks, with a few being followed up to 8 weeks). Fluorescent images of the ICC staining showed that both cell types expressed their typical proteins. hiPSC-CMs expressed cardiac troponin T (cTnT) and hiPSC-neurons expressed synapsin I (SynI), neurofilament NF-H 200 (NF-H) and β -tubulin III (β III-Tub). Furthermore, the axons and hiPSC-CMs were in close contact with each other making the functional interaction possible on the physical level (Figure 13B).

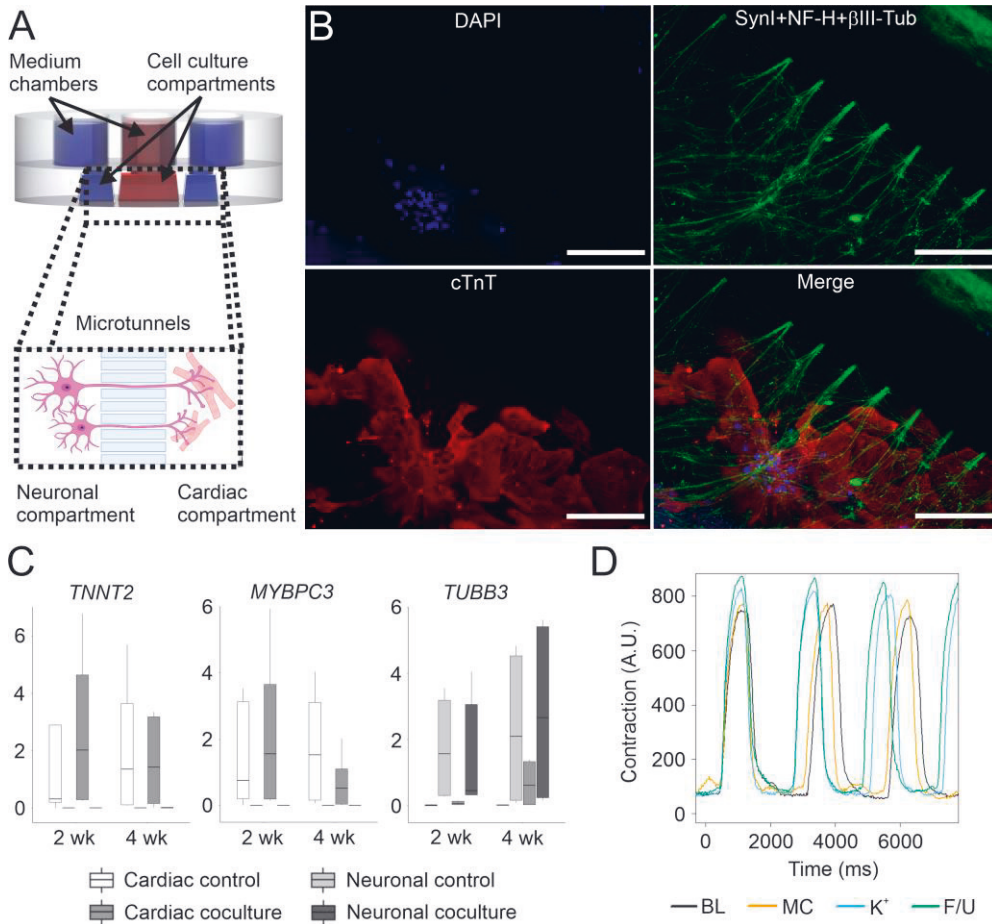


Figure 13. Coculture of hiPSC-CMs and hiPSC-neurons in a compartmentalized microfluidic 3D3C chip. A) Schematic illustration of the 3D3C chip. hiPSC-CMs and hiPSC-neurons were cultured in their own compartments connected via microtunnels that allow growth of the neuronal axons from one compartment to another. Separate medium chambers allow culture of the cells in their respective media. B) ICC staining of the cocultures in the 3D3C chip (scale bar 200 μ m). hiPSC-CMs (red, cTnT) were viable in the cocultures among the axons (green, Syn1, NF-H and β III-Tub). The axons grew from the neuronal compartment to the cardiac compartment via microtunnels. Cell nuclei were counterstained with DAPI (blue). C) RT-qPCR results showed that the samples from cardiac and neuronal compartments can be extracted without the samples mixing. Cardiac-specific *TNNT2* and *MYBPC3* were expressed only in cardiac samples, whereas neuron-specific *TUBB3* was expressed only in neuronal samples, although low expression of *TUBB3* was observed in 4-week cardiac coculture samples. This could be due to increased axonal density in 4-week cocultures as well as increased axonal expression of *TUBB3*. D) Neuronal stimulation was observed to affect hiPSC-CM functionality. Compared to baseline (BL), a slight increase in beating frequency and decrease in contraction duration, contraction and relaxation times were observed during (K⁺) and after (F/U) neuronal stimulation with high-K⁺ solution. Medium change (MC) was used as control for the effects of liquid change alone.

5.2.2 3D3C chip application for RT-qPCR and functionality studies

The 3D3C chip allowed the collection of cell lysis for RNA extraction from each cell culture compartment separately without mixing of the neuronal and cardiac samples, which was shown from the RT-qPCR results. The neuronal samples were observed to express only the neuron-specific *TUBB3*, whereas the cardiac samples expressed only cardiac-specific *TNNT2* (Figure 13C). The slight increase in *TUBB3* expression in the cardiac samples at 4 weeks of coculture could be explained by increased axonal density and increased expression of *TUBB3* in the axons. Furthermore, qPCR results showed that each cell type expressed the genes required for the formation of the functional interaction between the cell types. hiPSC-neurons were observed to express *CHAT* related to cholinergic signalling, as well as *TH* and *DBH* related to adrenergic signalling. On the other hand, hiPSC-CMs were shown to express *CHRM2* related to cholinergic signalling and *ADRB2* and *ADRB3* related to adrenergic signalling.

The functionality of the interaction between hiPSC-CMs and hiPSC-neurons was evaluated from video microscopy videos of hiPSC-CMs during stimulation of hiPSC-neurons with high-K⁺ solution using MUSCLE-MOTION. As the medium change to the hiPSC-neurons was observed to affect the hiPSC-CM contractile properties, the medium change was considered as the baseline response to which the immediate effect of neuronal high-K⁺ stimulation as well as the follow-up were compared to. Neuronal stimulation was observed to have an excitatory effect on the hiPSC-CM functionality, including slight increase in the peak-to-peak time describing hiPSC-CM beating frequency, and slight decreases in the contraction duration, time-to-peak (contraction) and relaxation time (Figure 13D).

5.3 Modelling ischemia and reperfusion with hiPSC-CMs

In studies III and IV, hiPSC-CMs were utilized in modelling chronic and acute cardiac ischemia-reperfusion, respectively. Ischemia and reperfusion were induced using OxyGenie platform for controlling the oxygen level in the hiPSC-CM cultures. The MACS-sorted hiPSC-CMs were seeded as cell sheets on 0.1% gelatine- or 2% Geltrex-coated 1-wells on glass or microelectrode arrays without any maturation step. After one week of culture, serum- and glucose-free medium was exchanged to all samples, and on the following day,

Covers and Lids were assembled on the 1-wells and hypoxia and reoxygenation were induced using 0% O₂ 5% CO₂ 95% N₂ gas (hypoxic gas) or 19% O₂ 5% CO₂ 76% N₂ gas (normoxic gas), respectively. With chronic hypoxia, the 1-well assembly was used with a solid glass-made lid, whereas with acute hypoxia, the hollow Acute lid covered with gas permeable polyethylene membrane was used.

For chronic ischemia modelling in study III, hypoxia was induced for 8 or 24 hours, whereas for acute ischemia modelling in study IV, hypoxia was induced for three hours. Reoxygenation was induced for 24 hours in both studies. After hypoxia or hypoxia-reoxygenation, the samples were collected one by one minimizing the exposure to ambient air for ICC, western blot, and RT-qPCR. hiPSC-CM electrophysiological response to hypoxia and reoxygenation was recorded with MEA. Baseline was recorded after medium change in normoxic gas for approximately 20 hours (overnight), after which hypoxia was induced for 24 or 3 hours for chronic and acute models respectively, and reoxygenation was induced for 24 hours. Oxygen partial pressure was measured from MEA samples in chronic and acute hypoxia-reoxygenation to evaluate the oxygen dynamics of the hiPSC-CM cultures.

5.3.1 Oxygen dynamics in the 1-well assemblies

Oxygen partial pressure was measured from the hiPSC-CM cultures using a highly biocompatible sensing material and a luminescence-based sensor (Välimäki et al., 2017). In study III, pO₂ was measured from one sample to verify that the oxygen dynamics were as expected, whereas in study IV, the Acute lid was more thoroughly characterized both without ($n = 6$) and with ($n = 5$) hiPSC-CMs as it was not previously published. With the glass lid in study III, the fall time (from 90% to 10%) in step response measurement from 19% kPa to 0% kPa pO₂ was 2.18 hours (131 min) with the hiPSC-CMs. On the other hand, with the Acute lid used in study IV, the fall time in the same step response measurement was 6.28 ± 2.28 min without the hiPSC-CMs and 18.97 ± 15.86 min with the hiPSC-CMs (Figure 14A). Thus, the hypoxia and reoxygenation were induced to the cells significantly faster with the Acute lid compared to the glass lid (Figure 14A, B), although there was some variation in the oxygen dynamics when Acute lid was used (Figure 14C). Rise time (from 10% to 90%) in the step response measurement from 0% kPa to 19%

kPa pO_2 was 2.53 hours (152 min) with the glass lid in study III, and 12.61 ± 1.94 min with the Acute lid with the hiPSC-CMs in study IV.

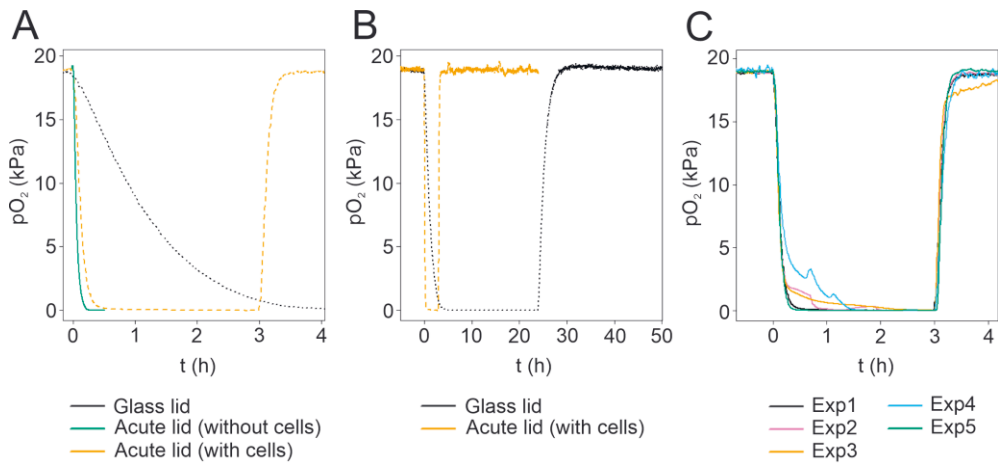


Figure 14. Oxygen dynamics in the 1-well assemblies using the solid glass-made lid and the hollow Acute lid. A) Representative measurements of the oxygen partial pressure (pO_2) from experiments where 1-well assembly was used with glass lid in the experiment with hiPSC-CMs and Acute lid was used in the experiment without and with hiPSC-CMs. Oxygen dynamics are significantly faster with the Acute lid compared to the glass lid. B) Oxygen dynamics from representative measurements using glass and Acute lid from experiments with hiPSC-CMs. In study III, hypoxia was induced for 24 hours using the glass lid for chronic ischemia modelling, whereas in study IV, hypoxia was induced for three hours using the Acute lid for acute ischemia modelling. Reoxygenation was for 24 hours in both studies. C) Oxygen dynamics had some variation in the experiments with the hiPSC-CMs and the Acute lid. However, the dynamics are still significantly faster compared to the glass lid, and especially immediate drop in the pO_2 after the initiation of the hypoxia.

5.3.2 hiPSC-CM morphology and protein expression

In studies III and IV, hiPSC-CM morphology and sarcomere structure were evaluated from fluorescent images taken from ICC staining of the samples after hypoxia and hypoxia-reoxygenation. Significant differences were observed in hypoxia and hypoxia-reoxygenation samples compared to the control samples. Both the overall morphology of the hiPSC-CMs and the sarcomere structure were deteriorated in the fluorescent images (Figure 15A). In addition, decrease in the size of the cell nuclei were observed. The observed changes were predominant in study III 24 h hypoxia samples and were not

observed to improve during reoxygenation. In study IV the changes were lesser, but still notable especially in hypoxia-reoxygenation samples.

Sarcomere coverage and nuclei size

In study III, the morphological changes were quantitated by calculating sarcomere coverage based on the ratio of cellular area exhibiting distinct sarcomere structure to the total area of the cells. The mean sarcomere coverage was $69.4 \pm 24\%$ in control samples ($n_{images} = 124$), whereas after 8- and 24-hour hypoxia, the coverage was $30.1 \pm 36.0\%$ ($n_{images} = 47$, $p < 0.0001$ vs control) and $16.1 \pm 24.8\%$ ($n_{images} = 50$, $p < 0.0001$ vs control), respectively. The mean nuclei size of the hiPSC-CMs was $35.7 \pm 16.4 \mu\text{m}^2$ for control ($n_{nuclei} = 3632$), and was observed to decrease in hypoxia samples, being $27.2 \pm 15.2 \mu\text{m}^2$ for 8-hour H samples ($n_{nuclei} = 685$, $p < 0.0001$ vs control) and $22.3 \pm 13.5 \mu\text{m}^2$ 24-hour H samples ($n_{nuclei} = 833$, $p < 0.0001$ vs control). Furthermore, the mean nuclei size for the hypoxia-reoxygenation samples was $19.8 \pm 11.1 \mu\text{m}^2$ for 8-hour HR samples ($n_{nuclei} = 392$, $p < 0.0001$ vs control) and $25.4 \pm 14.6 \mu\text{m}^2$ for 24-hour HR samples ($n_{nuclei} = 782$, $p < 0.0001$ vs control). In study IV, similar observations were made from the fluorescence images, however, the differences were not quantified.

Expression of sarcomeric proteins

The changes in the morphology observed from the ICC fluorescent images were further supported in study III by the western blot analysis of the sarcomeric proteins cTNT and cMyBP-C, as their expression was observed to decrease statistically significantly after hypoxia and reoxygenation (Figure 15B). The mean cTNT expression in the control samples ($n = 26$) was 0.96 ± 0.55 , whereas it was 0.47 ± 0.14 for 8-hour hypoxia ($n = 6$, $p < 0.01$ vs control) and 0.32 ± 0.27 for 24-hour hypoxia ($n = 6$, $p < 0.01$ vs control). In the 8- and 24-hour hypoxia-reoxygenation samples, the mean expressions were 0.37 ± 0.26 ($n = 4$, $p < 0.05$ vs control) and 0 ($n = 4$, $p < 0.001$ vs control), respectively. The mean cMyBP-C expression in the control samples was 1.11 ± 0.76 , whereas it was 0.53 ± 0.18 and 0.28 ± 0.32 for 8- ($p < 0.01$ vs control) and 24-hour ($p < 0.0001$ vs control) hypoxia samples. For the 8- and 24-hour hypoxia-reoxygenation samples, the mean expressions were 0.52 ± 0.22 ($p < 0.05$ vs control) and 0.11 ± 0.02 ($p < 0.001$ vs control), respectively.

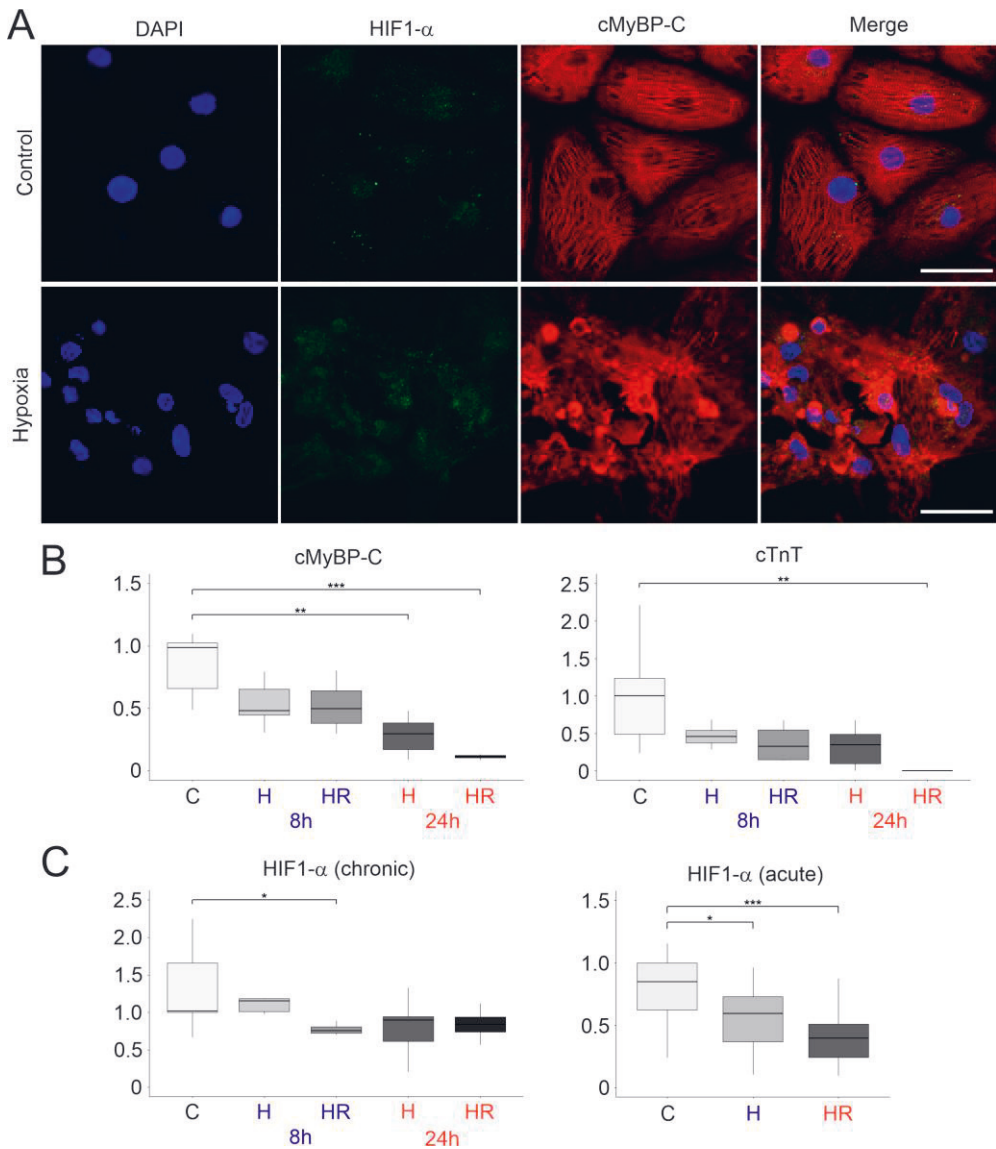


Figure 15. The hiPSC-CM morphology and protein expression changed as a response to hypoxia and reoxygenation. A) Representative examples of the fluorescent images taken from the hiPSC-CMs after ICC from control and hypoxia samples (scale bar 50 μ m). The observed changes included decrease in nuclei (blue, DAPI) size and deterioration of the sarcomere structure (red, cMyBP-C) after hypoxia and hypoxia-reoxygenation compared to control. The changes were most predominant in study III 24-hour hypoxia and reoxygenation samples, but notable also after 8-hour hypoxia as well as acute hypoxia in study IV. On the other hand, differences in the HIF1- α (green) expression were not observed from the fluorescent images. B) cMyBP-C and cTnT expressions were observed to decrease from western blot analysis in study III. C) HIF1- α expression was not observed to increase as a response to hypoxia, but rather decrease. * $p < 0.05$, ** $p < 0.01$, *** $p < 0.001$

Expression of HIF1- α

In both studies III and IV, HIF1- α expression was also evaluated via western blot. However, no increase in its expression was observed after chronic or acute hypoxia and reoxygenation. On the contrary, the expression was observed to decrease (Figure 15C). In study III, the mean HIF1- α expression in the control samples was 1.39 ± 0.68 , and after 8- and 24-hour hypoxia it was 1.05 ± 0.20 (ns vs control) and 0.80 ± 0.39 ($p < 0.01$ vs control), respectively. After 8- and 24-hour hypoxia-reoxygenation, the mean expression of HIF1- α was 0.77 ± 0.08 ($p < 0.01$ vs control) and 0.84 ± 0.23 ($p < 0.05$ vs control), respectively. In study IV, the mean HIF1- α expression in hypoxia control samples ($n = 16$) was 0.89 ± 0.21 and hypoxia-reoxygenation control samples ($n = 14$) 0.78 ± 0.58 . In hypoxia ($n = 16$) and hypoxia-reoxygenation ($n = 14$) samples, the mean expressions were 0.55 ± 0.25 ($p < 0.001$ vs hypoxia control) and 0.78 ± 0.58 ($p < 0.0001$ vs hypoxia control).

5.3.3 Expression of hypoxia related genes

In both studies III and IV, RT-qPCR was used to evaluate the relative expression of several genes known to be differentially expressed in ischemia and reperfusion (Table 4). Gene expression of the hiPSC-CMs after hypoxia and hypoxia-reoxygenation were evaluated in study III regarding fatty acid (*ACAA1*, *ACADM*) and glycolytic metabolism (*SLC2A1*, *PFKM*), general hypoxia markers (*HIF1A*, *MAP4K4*), sarcomere genes (*TNNT2*, *MYBPC3*), calcium handling genes (*RYR2*, *ATP2A2*, *SLC8A1*) and apoptosis related gene (*CASP3*). In study IV, the focus was on glycolysis related genes (*SLC2A1*, *PKM* isoforms 1 and 2), general cellular stress markers (*HSPA1A*, *MYH7*) and apoptosis related genes (*BAX*, *BCL2*).

In study III, the relative expression of the evaluated genes did not change statistically significantly during hypoxia, except for increased mean expression of *SLC2A1* encoding glucose transporter 1 in both 8- ($n = 6$) and 24-hour ($n = 5$) hypoxia samples (28.32 ± 24.13 and 48.22 ± 42.47 , respectively) compared to their respective controls (8h C_H: 1.70 ± 1.65 , $n = 5$, $p < 0.05$ vs 8 h hypoxia and 24h C_H: 1.88 ± 1.33 , $n = 6$, $p < 0.01$ vs 24 h hypoxia). Furthermore, the expressions of several genes were observed to decrease after 24-hour hypoxia-reoxygenation ($n = 4$) compared to its respective control (24h C_{HR}, $n = 4$), including *ACADM*, *PFKM*, *TNNT2*,

MYBPC3, *MAP4K4*, *RYR2*, *SLC8A1* and *ATP2A2*. However, the expression of *SLC2A1* was still upregulated compared to the control, its mean expressions being 3.76 ± 0.88 for 24h HR and 1.77 ± 0.68 for 24h C_{HR} ($p < 0.05$) On the other hand, in study IV, the expression of any of the evaluated genes did not change statistically significantly.

5.3.4 Electrophysiological response of hiPSC-CMs to hypoxia and reoxygenation

hiPSC-CM electrophysiology was evaluated using MEA technology in studies III and IV modelling chronic and acute ischemia-reperfusion, respectively. MEA was recorded overnight for baseline, during hypoxia and reoxygenation in both studies and significant changes in the hiPSC-CM electrophysiology were observed, including beating frequency, depolarization time and amplitude and field potential propagation time. On the other hand, beat rate corrected field potential duration (Izumi-Nakaseko formula (Izumi-Nakaseko et al., 2017)) was not observed to change during hypoxia or reoxygenation compared to baseline in study IV, however, the raw values were shortened FPD in both studies.

Beating frequency

hiPSC-CM beating frequency was observed to decrease during hypoxia and increase during reoxygenation in both studies III and IV (Figure 16). In study III, hypoxia was divided into two periods based on the oxygen dynamics and the hiPSC-CM behaviour during hypoxia. Normalized beating frequency was determined from 7–15 hours of hypoxia and from 15–24 hours of hypoxia, as after 7 hours, the pO₂ had already stabilized and the hiPSC-CM beating frequency was lowest during the period of 7–15 hours. On the other hand, the hiPSC-CM beating was observed to improve during 15–24 hours of hypoxia already before the start of the reoxygenation. Reoxygenation was divided into two groups as well, including 0–6 hours of reoxygenation to evaluate the response of the hiPSC-CMs at the start of the reoxygenation, and 6–24 hours when the hiPSC-CM beating had had time to stabilize. The mean normalized beating frequency ($n_{electrodes} = 41$, 4–6 electrodes from 3 parallel samples from 3 differentiation batches) during baseline was 1.08 ± 0.17 , whereas it decreased to 0.36 ± 0.34 during 7–15 hours of hypoxia ($p < 0.0001$ vs baseline). During 15–24 hours of hypoxia, the mean beating frequency

increased 0.66 ± 0.40 ($p < 0.0001$ vs baseline, $p < 0.0001$ vs 7–15 h hypoxia). During the first six hours of reoxygenation, the mean beating frequency further increased to 1.27 ± 0.40 ($p < 0.0001$ vs 15–24 h hypoxia) and returned close to the baseline level during 6–24 hours of reoxygenation to 0.98 ± 0.33 ($p < 0.0001$ vs 0–6 h reoxygenation).

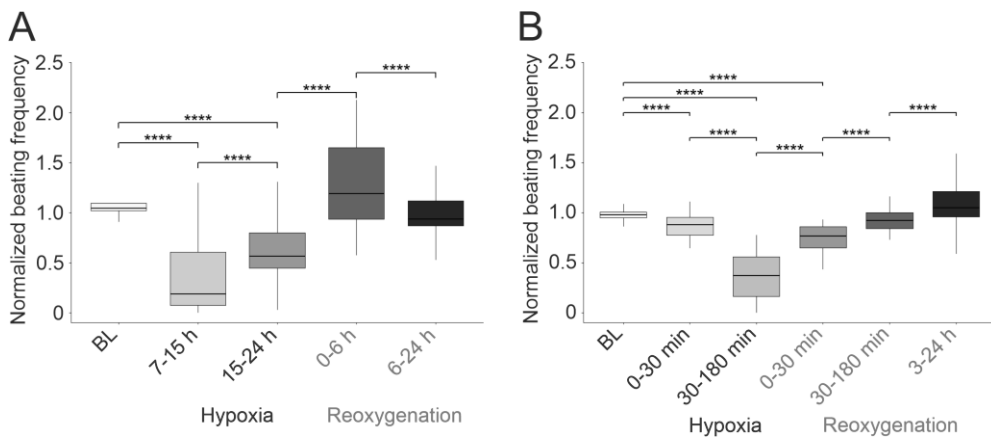


Figure 16. hiPSC-CM beating frequency changed during hypoxia and reoxygenation. A) During chronic ischemia and reperfusion in study III, lowest beating frequency was observed between 7–15 hours of hypoxia, after which an increase was observed during the rest of the hypoxia. Reoxygenation increased the beating frequency, and initially (0–6 hours of reoxygenation) the hiPSC-CM beating frequency surpassed the baseline level, however, it stabilized close to the baseline level during 6–24 hours of reoxygenation. B) Similarly, during acute ischemia and reperfusion in study IV, the beating frequency was observed to decrease during hypoxia and increase during reoxygenation, however, the beating frequency did not increase at the end of the hypoxia period. **** $p < 0.0001$

Similar observations on the beating frequency were done in study IV with acute ischemia model ($n_{electrodes} = 110$, 5 electrodes from 22 MEA samples from 3 cell lines: 3–4 parallel samples per experiment). There, hypoxia was divided into 0–30 minutes and 30–180 minutes, again based on the pO_2 dynamics and behaviour of the hiPSC-CMs during hypoxia. Similarly, reoxygenation was divided into 0–30 minutes, 30–180 minutes and 3–24 hours. During baseline, the mean normalized beating frequency was 0.94 ± 0.16 and decreased to 0.85 ± 0.17 during the first 30 minutes of hypoxia ($p < 0.0001$ vs baseline), and further to 0.35 ± 0.23 during 30–180 minutes of hypoxia ($p < 0.0001$ vs baseline and 0–30 min hypoxia). During the first 30

minutes of reoxygenation, the mean normalized beating frequency increased to 0.70 ± 0.30 ($p < 0.0001$ vs 30–180 min hypoxia), and further to 0.89 ± 0.32 during 30–180 minutes of reoxygenation ($p < 0.0001$ vs 0–30 min reoxygenation). During the 3–24 hours of reoxygenation, the mean normalized beating frequency was 1.04 ± 0.27 ($p < 0.0001$ vs 30–180 min reoxygenation).

Depolarization time and amplitude

Depolarization time was observed to increase during hypoxia and recover during reoxygenation (Figure 17A) in both studies, however, in study III, it was calculated using different criteria and only from three MEA samples, from one electrode per sample. Thus, the results are only indicative. On the other hand, in study IV, 110 electrodes from 22 individual MEA samples were analysed. The mean t_{dep} during baseline was 3.11 ± 2.62 msec and did not change significantly during the first 30 minutes of hypoxia (3.12 ± 2.76 msec). During 30–180 min hypoxia, the mean t_{dep} was 5.87 ± 4.37 msec ($p < 0.0001$ vs baseline) and remained increased for the first 30 min of reoxygenation (5.63 ± 5.51 msec). However, during 30–180 min reoxygenation, the mean t_{dep} decreased to 3.73 ± 3.00 ms ($p < 0.0001$ vs 30–180 min hypoxia) and remained slightly higher compared to baseline during the rest of the reoxygenation (3.83 ± 2.51 msec, $p < 0.0001$ vs baseline).

In study IV, depolarization amplitude was observed to decrease during hypoxia and recover during reoxygenation (Figure 17B). The mean baseline A_{dep} was -0.26 ± 0.23 mV and -0.25 ± 0.21 mV during the first 30 min of hypoxia. During 30–180 min hypoxia, the mean A_{dep} decreased to -0.13 ± 0.09 mV ($p < 0.0001$ vs baseline) and remained low for the first 30 min of reoxygenation (-0.12 ± 0.07 mV). Slight increase in the mean A_{dep} was observed during 30–180 min reoxygenation (-0.17 ± 0.11 mV, $p < 0.0001$ vs 0–30 min reoxygenation), and further improvement during 3–24 hours of reoxygenation (-0.21 ± 0.14 mV, $p < 0.05$ vs 30–180 min reoxygenation).

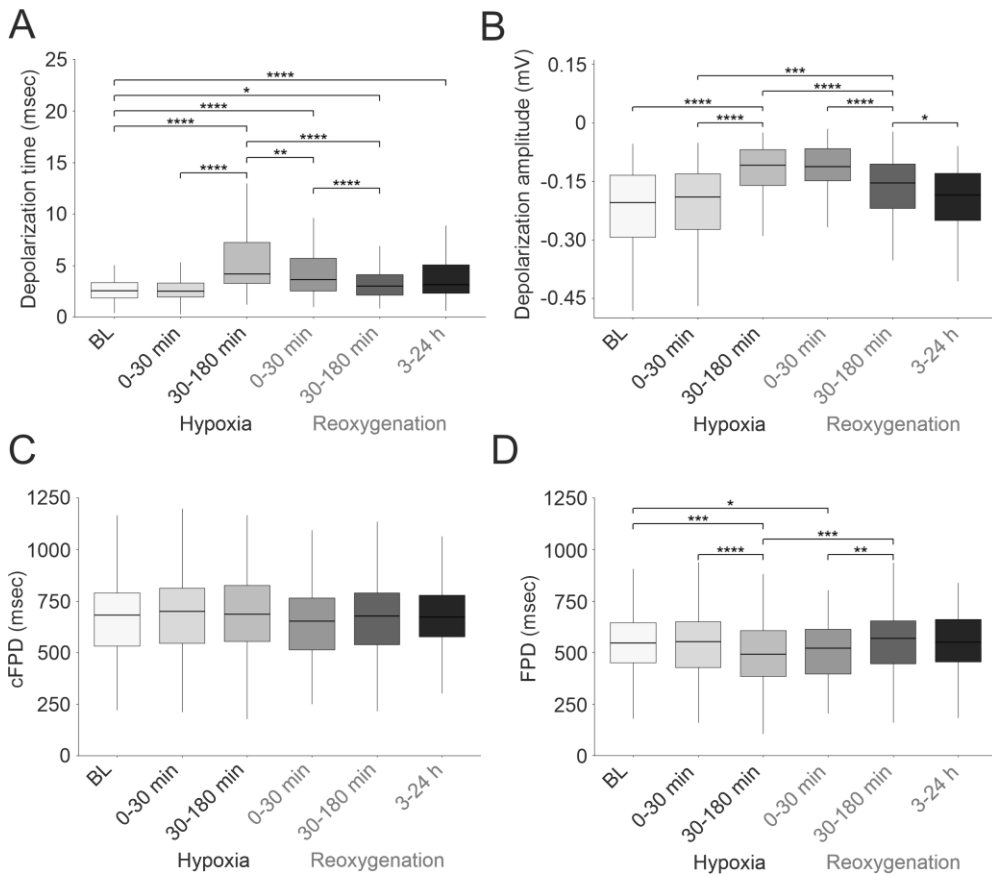


Figure 17. Depolarization time and amplitude, as well as beat rate corrected and raw field potential duration of the hiPSC-CMs during baseline (BL), acute hypoxia and reoxygenation in study IV. A) Depolarization time increased during hypoxia and recovered partially during reoxygenation. B) Depolarization amplitude decreased during hypoxia and recovered during reoxygenation. C) There was no difference in beat rate corrected field potential duration (cFPD, Izumi-Nakaseko formula (Izumi-Nakaseko et al., 2017)) during hypoxia or reoxygenation compared to baseline. D) Raw field potential duration was observed to decrease during hypoxia and recover during reoxygenation. * $p < 0.05$, ** $p < 0.01$, *** $p < 0.001$, **** $p < 0.0001$

Field potential duration

In study III, similar to t_{dep} , FPD was analysed from only three MEA samples, from one electrode per sample. Furthermore, the FPD was not beat rate corrected. There was indication of decrease in the FPD during hypoxia, and recovery of the FPD during reoxygenation, however, the results were again only indicative. In study IV, beat rate corrected field potential duration did not

change statistically significantly during hypoxia or reoxygenation compared to baseline (Figure 17C). The mean cFPD was 0.66 ± 0.20 sec during baseline, 0.69 ± 0.22 sec during first 30 min of hypoxia, 0.72 ± 0.28 sec during 30–180 min hypoxia, 0.66 ± 0.19 sec during the first 30 min of reoxygenation, 0.67 ± 0.19 sec during 30–180 min reoxygenation and 0.67 ± 0.17 sec for 3–24 hours of reoxygenation. However, similar results as in study III were observed in study IV with the raw FPD values (Figure 17D). During baseline, the mean raw FPD was observed to be 0.54 ± 0.15 sec and 0.55 ± 0.16 sec during the first 30 min of hypoxia. From there it decreased to 0.50 ± 0.16 sec during 30–180 min of hypoxia ($p < 0.001$ vs baseline) and gradually increased during reoxygenation, being 0.52 ± 0.15 sec for 0–30 min reoxygenation ($p < 0.05$ vs baseline), 0.54 ± 0.15 sec for 30–180 min reoxygenation ($p < 0.001$ vs 30–180 min hypoxia) and 0.56 ± 0.14 for 3–24 hours of reoxygenation.

Field potential propagation

Field potential propagation was observed to slow down during hypoxia and recover during reoxygenation in both studies III and IV (Figure 18). In study III, the mean field potential propagation time (t_{FPP}) was calculated for 2 individual MEA samples at two baseline timepoints and at 8 and 24 hours of hypoxia as well as at 6 and 24 hours of reoxygenation. The data was reanalysed using the method further developed for study IV to be better able to compare the results between the two studies, thus the t_{FPP} values differ compared to the original publication. The mean t_{FPP} during baseline was observed to be 3.32 ± 0.48 msec ($n_{beats} = 77$), and it increased to 5.95 ± 1.61 msec for 8 hours of hypoxia ($n_{beats} = 14$, $p < 0.0001$ vs baseline). At 24 hours of hypoxia, the mean t_{FPP} was 5.23 ± 0.90 msec ($n_{beats} = 25$, $p < 0.0001$ vs baseline) and had not significantly improved at 6 hours of reoxygenation, for which the mean t_{FPP} was 5.18 ± 0.81 msec ($n_{beats} = 39$, $p < 0.0001$ vs baseline). At 24 hours of reoxygenation the mean t_{FPP} had improved to 3.86 ± 0.94 msec ($n_{beats} = 29$, $p < 0.0001$ vs 6 h reoxygenation).

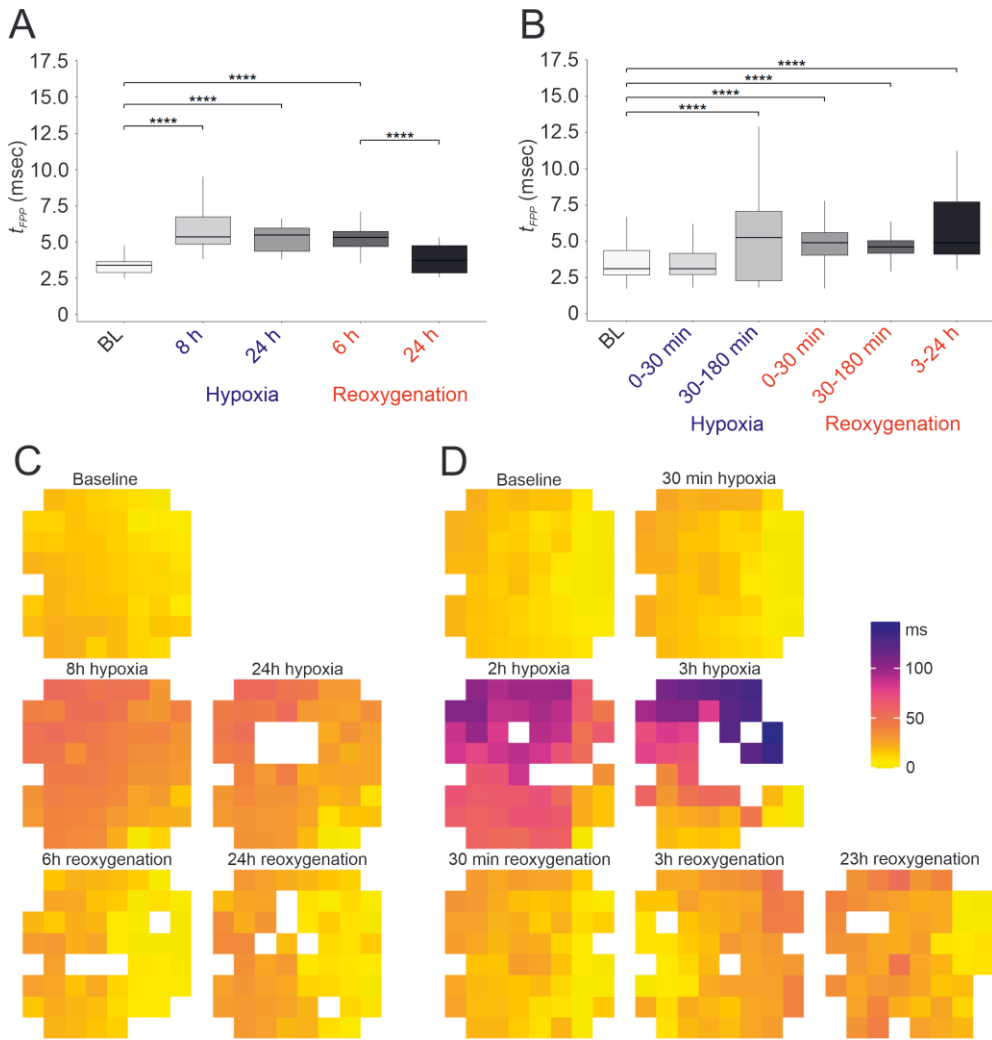


Figure 18. Field potential propagation of the hiPSC-CMs slowed during hypoxia and partially recovered during reoxygation. A) Field potential propagation time (t_{FPP}) slowed during chronic hypoxia and recovered at 24 hours of reoxygation in study III. B) Field potential propagation time slowed during acute hypoxia in study IV, however, the recovery after acute hypoxia was not as pronounced as after the chronic hypoxia, although the duration of the hypoxia was much shorter. C) Example of field potential propagation through the MEA electrode grid in chronic hypoxia and reoxygation from study III. D) Example of field potential propagation through the electrode grid in acute hypoxia and reoxygation in study IV. **** $p < 0.0001$

In study IV, t_{FPP} was calculated from four individual MEA samples for baseline for one hour before hypoxia, for the duration of the hypoxia and 3 hours of reoxygenation as well as at the end of the reoxygenation period. The mean t_{FPP} during baseline was 3.41 ± 1.05 msec ($n_{beats} = 1609$) and did not change significantly during the first 30 min of hypoxia (3.35 ± 1.03 msec, $n_{beats} = 603$), whereas the increase during 30–180 min of hypoxia was significant (5.17 ± 2.74 msec, $n_{beats} = 553$, $p < 0.0001$ vs baseline). The mean t_{FPP} remained elevated during the first 30 min of reoxygenation (5.13 ± 1.94 msec, $n_{beats} = 487$, $p < 0.0001$ vs baseline) and did not fully recover during 30–180 min reoxygenation (4.73 ± 1.43 msec, $n_{beats} = 830$, $p < 0.0001$ vs baseline) or at the end of the reoxygenation (5.87 ± 2.23 msec, $n_{beats} = 283$, $p < 0.0001$ vs baseline).

6 DISCUSSION

Human based models for cardiac ischemia-reperfusion are required for studying the disease mechanisms and new treatment options, as animal and primary animal cell models do not fully recapitulate the human disease mechanisms due to partially different physiology (T. Chen & Vunjak-Novakovic, 2019). hiPSC-CMs provide an unlimited source for human cardiomyocytes although they do not fully resemble adult CMs, which hinders their utilization in different applications (Karakikes et al., 2015). Thus, in study I of this thesis, the hiPSC-CMs were cultured on PET textiles to improve the maturation of the cells, which was observed to affect especially the structural properties of the hiPSC-CMs. In study II, a cardiac innervation model was established for future studies in cardiac ischemia modelling. In studies III and IV of this thesis, hiPSC-CMs were used for modelling cardiac ischemia-reperfusion in chronic and acute setting with the focus on the hiPSC-CM electrophysiological responses. The hiPSC-CMs were shown to reproduce several electrophysiological changes known to occur in adult CMs during ischemia and reperfusion.

6.1 Improved structural maturation of hiPSC-CMs

The immaturity of the hiPSC-CMs is considered one major drawback for their utilization in different applications (Yoshida & Yamanaka, 2017). The immature electrophysiological, structural and metabolic properties of the hiPSC-CMs affect their utilization for example in disease modelling of inherited and acquired cardiovascular diseases and hinders their application as a therapeutic treatment of injured cardiac tissues as recently reviewed (Ahmed et al., 2020; Liao et al., 2021). Several methods have been developed to induce the maturation state of the hiPSC-CMs, however, none has been able to induce fully adult-like CMs. Often the maturation methods affect a specific aspect of the immature phenotype, such as morphology and sarcomere orientation (Parrag et al., 2012; Rao et al., 2013), or metabolic maturation (Feyen et al., 2020; Hidalgo et al., 2018), with possibly less effect on the other properties of

the hiPSC-CMs. However, this can be utilized in producing hiPSC-CMs that are more mature on the most relative way for each application. For example, metabolic maturation is known to be important in ischemia modelling (T. Chen & Vunjak-Novakovic, 2018), whereas structural maturation can be more advantageous in modelling diseases related to CM sarcomere mutations, such as hypertrophic cardiomyopathy (Chou & Chin, 2021).

In study I, hiPSC-CM maturation improved upon culturing them on PET textiles. Significant improvements were observed in the structural properties of the hiPSC-CMs cultured on PET textiles compared to control hiPSC-CMs cultured on coverslips, including increased elongation and sarcomere orientation. However, effects on gene expression were much less pronounced and no improvement in the sarcomere length was observed. Similar results have been observed in several studies, where hiPSC-CM maturation and growth has been guided with topographical cues. Rao and co-workers as well as Han and co-workers reported improved sarcomere orientation and cellular alignment in hiPSC-CMs, when they were cultured on microgrooved substrates (Rao et al., 2013) and aligned electrospun fibres (J. Han et al., 2016). On the other hand, the effects of topographical cues on sarcomere length have been controversial, as it has been observed to improve in some studies (M. Khan et al., 2015; Wanjare et al., 2017) but not in others (J. Han et al., 2016).

Adult CMs exhibit high structural orientation with highly organized myofibrils and aspect ratio of 5–9 (Denning et al., 2016). hiPSC-CMs cultured on PET textiles had mean aspect ratio of approximately 4.9, which is already close to that of the adult CMs and significantly better compared to the hiPSC-CMs cultured on coverslips. On the other hand, the sarcomere length of adult CM is on average 2.2 μm (Sarantitis et al., 2012), which is higher compared to the modal sarcomere length of approximately 1.75 μm observed in the hiPSC-CMs despite the culture substrate in study I. The cellular and sarcomere orientation are important aspects of CMs, as they allow maximum length contraction into one direction, which is crucial for efficient and coordinated contraction of cardiac muscle tissue. Thus, although still not in therapeutic use in clinics, cellular and sarcomere orientation are especially important in applications aiming for transplantation of hiPSC-CMs into injured myocardium after for example ischemic heart disease, as disorganized tissue

structure along with immature electrophysiology and poor integration to host tissue can lead to inefficient contraction and arrhythmias (Silver et al., 2021).

Furthermore, cellular and sarcomere orientation can be beneficial and bring more insights into the disease phenotype and mechanisms in modelling diseases related to CM sarcomere structure and mutations, such as hypertrophic cardiomyopathy (Chou & Chin, 2021; Knight et al., 2021), although immature hiPSC-CMs have been shown to express the disease phenotype including cellular enlargement, abnormal calcium handling and increased arrhythmogenicity (Ojala et al., 2016; Prajapati et al., 2018). On the other hand, modelling other diseases not related to the sarcomeric structure or cell-to-cell connections may not require improved structural properties. For example, hiPSC-CMs have been successfully utilized in modelling catecholaminergic polymorphic ventricular tachycardia, where calcium handling of the CMs is impaired due to mutations in genes encoding calcium handling proteins, such as *RYR2*, *CALMI*, *CASQ2* and *TRDN*, but mainly due to mutations in *RYR2*. The hiPSC-CMs with mutations in *RYR2* have been shown to reproduce calcium related arrhythmias similar to the clinical phenotype (Pölonen et al., 2018).

In modelling of ischemic heart disease and ischemia-reperfusion injury, perhaps the most important aspect of hiPSC-CM maturation is the metabolic maturation, as foetal CMs as well as hiPSC-CMs are known to be resistant to ischemic injury due to their metabolism relying more on glycolysis than fatty acid oxidation (Hidalgo et al., 2018). To induce severe ischemic insult to the hiPSC-CMs, hypoxia has often been induced for a prolonged period (T. Chen & Vunjak-Novakovic, 2019; Lu et al., 2018; Veldhuizen et al., 2022), whereas adult CM viability decreases quickly when oxygen is deprived (van der Weg et al., 2019). However, regarding different aspects of the disease mechanism, structural maturation of the CMs used for modelling the disease can be advantageous. For example, ischemia-reperfusion has been shown to decrease conduction velocity in cardiac tissue, which is known to be an anisotropic, orientation dependent property (Kotadia et al., 2021). Thus, adult-like structural properties, especially the cellular and sarcomere alignment can be beneficial in the modelling of ischemic heart disease as well.

6.2 Cardiac innervation model on 3D3C chip

Cardiac autonomic nervous system innervates the cardiac tissue and affects greatly the functioning of the heart with respect to heart rate, contractility, and conduction velocity. As the two systems are functionally involved, dysfunction of one also affects the other (Hadaya & Ardell, 2020). Thus, human based cardiac innervation models can be valuable tools for disease modelling as well as drug and toxicology testing. However, culturing neurons with CMs without any restrictions does not correspond to the *in vivo* situation, where only the neuronal axons innervate the cardiac tissue (Végh et al., 2016). Thus, in study II, 3D3C chip restricting neuronal somas into one compartment and allowing only the axons growing from the neuronal to the cardiac compartment was used for coculturing hiPSC-CMs and hiPSC-neurons and for modelling cardiac innervation.

The 3D3C chip enabled long-term cocultures of hiPSC-CMs and hiPSC-neurons up to eight weeks, and based on video microscopy, phase-contrast images, and fluorescent images of the ICC staining, both cell types remained viable for the duration of the cultures. Furthermore, each cell type expressed their specific markers, which was observed via RT-qPCR and gene expression evaluation, as well as by immunolabelling neuron and cardiac specific proteins. RT-qPCR results showed that the samples from each compartment can be lysed, and the RNA can be extracted without the samples mixing. The 3D3C chip allowed evaluation of the cell functionality and properties via versatile methods, including phase-contrast imaging, ICC and fluorescent imaging, cell type specific gene expression and video microscopy. Although not used in study II, as the cells could be lysed for RT-qPCR, they could most likely be lysed for protein expression studies via western blotting. Thus, the 3D3C chip permits thorough characterization of the coculture and its functionality.

Previously, cardiac innervation has been modelled by coculturing neurons and cardiomyocytes in free cocultures without restricting the cellular contacts (Oh et al., 2016; Takayama et al., 2020; Winbo et al., 2020), as well as in similar PDMS chips as used in study II, where the interaction is only allowed via axons (Oiwa et al., 2016; Sakai et al., 2017; Takayama & Kida, 2016; Takeuchi et al., 2011). In several of these studies, it has been shown that cardiomyocytes and neurons can form functional axon-mediated connections in restricted cocultures *in vitro*, however, only in studies where either or both

cell types were harvested from an animal source (Oiwa et al., 2016; Sakai et al., 2017; Takeuchi et al., 2011). Furthermore, hiPSC-derived neurons and CMs have been shown to form functional connections *in vitro* in free cocultures, where the neurons and CMs were seeded into the same culture dish (Takayama et al., 2020; Winbo et al., 2020), but that does not resemble the *in vivo* situation, where the neurons and CMs interact only via neuronal axons (Végh et al., 2016). On the other hand, the results from study II indicate, that the hiPSC-derived neuron and CMs can also form axon-mediated functional connections under restricted coculture *in vitro*.

The hiPSC-neurons used in study II were derived using a protocol guiding their differentiation towards central nervous system cortical neurons (Hyvärinen et al., 2019), whereas the neurons in cANS consist of sympathetic and parasympathetic peripheral neurons (Végh et al., 2016). There are protocols for differentiation of sympathetic- and parasympathetic-like peripheral neurons (Oh et al., 2016; Takayama et al., 2020), which could be better suitable for cANS and cardiac innervation modelling. These could be incorporated into the model described in study II for better mimicking the neuron-CM interactions in cANS. Furthermore, incorporation of MEA and the possibility for electrical stimulation of the neurons and CMs could further improve the experimental setup for evaluating the interaction between the two cell types without inducing any disturbances to the cells, as the introduction of the chemical stimulation itself could induce a response from the neurons or the CMs, as they also respond to mechanical stimulation caused by the liquid change as showed in the study II.

The cardiac innervation on a chip could be utilized in several applications, including disease modelling, developmental biology, drug screening and toxicology testing. For example, ischemic heart disease is known to affect the functioning of the axons and induce arrhythmias in the cardiac tissue (Kolettis et al., 2015). If this could be reproduced *in vitro*, also alleviating drugs could be screened and tested as treatment. Furthermore, coculture of several cell types of native cardiac tissue is known to improve hiPSC-CM maturation (Vuorenperä et al., 2017), and neurons and CMs are known to undergo comaturation during embryonic development of the heart and cANS (Habecker et al., 2016), which indicates that the coculture of the hiPSC-CMs and hiPSC-neurons could also improve the maturation state of each cell type,

and thus allow more mature disease models for cardiac and cANS related diseases and their treatments.

6.3 Modelling cardiac ischemia and reperfusion with hiPSC-CMs

Lately, several cardiac ischemia-reperfusion models utilizing hiPSC-CMs have emerged (Canfield et al., 2016; T. Chen & Vunjak-Novakovic, 2019; Fernández-Morales et al., 2019; Fiedler et al., 2019; Hidalgo et al., 2018; Kirby et al., 2018; Lu et al., 2018; Robertson-Gray et al., 2019; Sebastião et al., 2019, 2020; Shah et al., 2019; Välimäki et al., 2017; Veldhuizen et al., 2022; Ward & Gilad, 2019; H. Wei et al., 2019; W. Wei et al., 2017; Zhao et al., 2018). However, most studies have focused on molecular markers, cell viability and structural markers of injury and stress to evaluate their models, with few evaluating the functionality, mostly concerning the contractile properties via video microscopy. Electrophysiology is an important aspect of the cardiomyocyte function (Eisner et al., 2017), but it has been less studied in hiPSC-CM based models of ischemia-reperfusion.

In studies III and IV, chronic and acute ischemia and reperfusion were modelled respectively by inducing hypoxia and reoxygenation for hiPSC-CM. The advanced platform utilized for the ischemia modelling allowed exposure of individual samples to hypoxic conditions, as well as utilization of several methods for evaluating the hiPSC-CM response to hypoxia including immunocytochemistry, RT-qPCR, western blot and MEA. The individual gas-tight chambers allowed collection of the samples one by one, minimizing the exposure to ambient air, which can be crucial for some hypoxia markers, such as HIF1- α that has half-life of 5 minutes under normoxia (Yin et al., 2016). Furthermore, the incorporation of the oxygen partial pressure measurement allowed real time monitoring of the oxygen level directly from the cell culture as well as comparison of the hiPSC-CM electrophysiological changes to the oxygen dynamics in the culture. In study III, hypoxia and reoxygenation were induced slowly over the course of hours, whereas in study IV, hypoxia and reoxygenation were achieved within 20 minutes. This allowed modelling of chronic and acute ischemia, respectively.

Chronic myocardial ischemia develops slowly when the narrowing the coronary artery occurs due to build-up of plaque in the artery over time. As the blood supply to the myocardium decreases slowly over the course of years,

the cells of the myocardium may have time to initiate adaptive responses to the decreased oxygen and nutrient levels (Libby & Theroux, 2005), such as are observed in ischemic preconditioning when several transient ischemic episodes protect against ischemic injury (Ytrehus, 2006). Alternatively, acute myocardial ischemia occurs suddenly when a blood clot due to a rupture in the plaque immediately blocks the artery (Libby & Theroux, 2005). During chronic ischemia and reduced coronary perfusion, cardiac hibernation meaning reversible reduction in the CM contractile function occurs to reduce oxygen demand of the CMs (Ytrehus, 2006). Furthermore, myocardial stunning can occur up to several days after reperfusion, when CMs present contractile dysfunctions after re-establishing the coronary blood flow (Richard Conti, 1991).

When blood flow is blocked to the myocardium, the aerobic metabolism ceases within 10 seconds, and within 20 seconds, anaerobic glycolysis becomes the primary pathway to produce high energy ATP. However, within 90 seconds, glycolysis starts to slow due to lowered pH and sarcoplasmic NADH₂/NAD ratio and most of the available ATP is used, at which point also myocardial contraction ceases. Within 15 minutes, intracellular pH has lowered below 6 and intracellular sodium slightly decreases due to NKA activity. After 20–40 minutes, irreversible injury starts when glycogen has been depleted, the mitochondria swell and intracellular Ca²⁺ and Na⁺ rise further (van der Weg et al., 2019). In addition, reperfusion is also typically an acute event, as the blood flow is restored to the myocardium by surgery (Bagai et al., 2014). The different disease mechanisms thus require different experimental modelling setups.

6.3.1 Deterioration of hiPSC-CM sarcomere structure and expression of sarcomeric genes

The morphological and structural changes observed in the hiPSC-CMs after hypoxia and reoxygenation included decrease of distinct sarcomere structures as well as decreased size of the nuclei. This was observed in both study III with the chronic IR model and study IV with the acute IR model, although the changes were most pronounced in study III samples that underwent chronic 24-hour hypoxia-reoxygenation. However, similar observations were made in study IV acute hypoxia and hypoxia-reoxygenation samples, with more

notable changes in the hypoxia-reoxygenation samples. Similar observations regarding sarcomere deterioration have been made in other studies modelling IRI with hiPSC-CMs *in vitro* (T. Chen & Vunjak-Novakovic, 2019; Sebastião et al., 2020).

Together the deterioration of the cellular structure and the observed decrease in the nuclei area are indications of cellular damage and apoptotic cell death (Fink & Cookson, 2005; Kwon et al., 2015). However, the morphological changes could also be indications of necrotic cell death, which is a known mechanism of cell death in IR (Wu et al., 2018), as no significant changes in the apoptotic genes were observed in neither study III nor IV. In study III, the morphological changes were further supported by western blot analysis of the sarcomeric proteins cTnT and cMyBP-C, which were expressed less especially in hypoxia-reoxygenation samples compared to control samples. Although it was not measured, the decreased expression in cTnT could be the result of its release from the hiPSC-CMs to the medium, as cTnT release is a marker of MI used in clinics (Mair et al., 2018).

Studies III and IV differed from each other regarding the speed and duration of the hypoxia. In study III chronic model, 8- and 24-hour hypoxia periods were used, and the induction of hypoxia was slow, occurring over several hours, whereas in study IV acute model, hypoxia lasted only for three hours and could be induced within 20 minutes. The length of the hypoxia was observed to affect the morphological changes. The samples in study IV underwent acute 3-hour hypoxia period and presented better cellular morphology compared to the chronic 8-hour hypoxia samples in study III, which in turn presented better morphology compared to chronic 24-hour hypoxia samples. Also, reoxygenation was observed to induce morphological changes, which was clearer in study IV, where the acute 3-hour hypoxia induced relatively mild morphological changes, whereas the morphology and sarcomere deterioration were more visible after reoxygenation. This indicates, that the reoxygenation further induced cellular damage in the hiPSC-CMs, however, this was not as distinctive in study III chronic model, likely because the longer hypoxia periods already alone caused more severe hypoxia induced morphological changes. Although there were differences in the 8-hour hypoxia and hypoxia-reoxygenation samples, they were not as distinct as in study IV.

HIF1- α expression was not observed to increase in any hypoxia or hypoxia-reoxygenation samples in study III or IV. On the contrary, its expression rather decreased. Furthermore, the fluorescence images of the ICC staining did not show HIF1- α translocation into the cell nucleus. It is possible that the HIF1- α expression peaked at some other timepoint not evaluated in these studies. On the other hand, there was variation in the expression of HIF1- α already in the control samples, so it is possible that a subtle increase of the protein could be masked by the inter-sample variation at the early hypoxia timepoints. Moreover, in the later hypoxia timepoints, HIF1- α could have been degraded via oxygen independent pathways (Iommarini et al., 2017). In study III, also the gene expression of *HIF1A* was evaluated, but there were no significant differences in its expression in hypoxia, hypoxia-reoxygenation and control samples. However, the regulation of HIF1- α is known to occur more on the protein level than on the gene expression level (J. W. Lee et al., 2019).

6.3.2 Increased glycolysis-related gene expression

The relative gene expression of the hiPSC-CMs after hypoxia and hypoxia-reoxygenation was evaluated in studies III and IV regarding metabolism, hypoxia markers, cellular stress markers, sarcomeric genes, calcium handling genes and apoptotic genes. In study III, the relative expression of the evaluated genes was not observed to change statistically significantly after hypoxia, except for *SLC2A1*, which had higher mean expression in both 8- and 24-hour hypoxia samples compared to control samples. Furthermore, 24-hour hypoxia samples had higher mean expression of *SLC2A1* compared to 8-hour hypoxia, and its mean expression was still elevated after 24-hour hypoxia-reoxygenation, whereas no difference was observed between control and 8-hour hypoxia-reoxygenation. On the other hand, no significant differences in the relative expressions of the glycolysis related genes *SLC2A1* or *PKM* isoform 1 and 2 were observed in study IV after hypoxia or hypoxia-reoxygenation.

SLC2A1 encodes glucose transporter 1 protein, which is a transmembrane protein responsible for glucose uptake to the cell. As anaerobic glycolysis is relatively inefficient regarding ATP production, more glucose is required to produce enough energy for the cell to function leading to increase of glucose transporters on the cell membrane (Rosano et al., 2008). Thus, the elevation

in its expression in study III after hypoxia is expected, and similar increase has been observed in other studies modelling ischemia *in vitro* (Choi et al., 2021; J. Wei et al., 2015). *SLC2A1* expression was observed to increase temporally during hypoxia, as no increase in its expression was observed in study IV after the acute 3-hour hypoxia, whereas in study III, the *SLC2A1* expression was elevated after 8-hour hypoxia and further increased in during 24-hour hypoxia. The increase in the *SLC2A1* expression did not stem from the glucose-free medium, as also the control hiPSC-CMs were cultured in the same medium.

In study IV, the expression of two isoforms of *PKM* gene encoding muscle type pyruvate kinase M1/2 related to glycolysis was also evaluated, as ischemia is known to induce switch in the *PKM* isoform expression, so that the isoform 1 is the dominant in normal conditions, but during ischemia, the expression the isoform 2 increases (Williams et al., 2018). However, there were no significant changes in their expression after hypoxia or hypoxia-reoxygenation. In study III, also the expression of *ACAA1* or *ACADM* related to FA metabolism was inspected, but no significant decrease was observed during hypoxia. Shift from FA to glycolytic metabolism is a known consequence of ischemia, and also been shown to occur *in vitro* with primary neonatal rat CMs (J. Wei et al., 2015). Thus, it is likely that the hiPSC-CMs used in these studies are not utilizing FA as a primary energy source, which is typical to immature hiPSC-CMs (Hidalgo et al., 2018). However, the increase in *SLC2A1* expression during hypoxia in study III indicates that the hiPSC-CMs are enhancing their glycolytic metabolism by increasing the expression of the respective glucose transporter and thus trying to increase the glucose uptake to the cell.

6.3.3 hiPSC-CM electrophysiological properties changed during hypoxia

Significant differences in the hiPSC-CM electrophysiology were observed during hypoxia compared to baseline regarding beating frequency, depolarization time and amplitude, as well as field potential propagation. On the other hand, beating rate corrected field potential duration was not observed to change significantly, whereas the raw values of the field potential duration showed decrease during hypoxia. The parameters mostly recovered to baseline level during reoxygenation, although for example depolarization time and

field potential propagation remained elevated even at the end of the reoxygenation period, indicating of the ability of the hiPSC-CMs to reproduce both ischemic hibernation type of injury during hypoxia as well as reperfusion related stunning type of injury after reoxygenation (Richard Conti, 1991; Ytrehus, 2006). The observed changes correlated well with the changes known to occur in adult CMs during ischemia (Klabunde, 2017) and reperfusion (Manning & Hearse, 1984).

Hypoxia decreased hiPSC-CM beating frequency

Beating frequency was observed to decrease as a response to hypoxia and recover during reoxygenation in both studies III and IV. In the chronic ischemia model in study III, the decrease in the beating frequency occurred gradually and started five hours after the initiation of the hypoxia, whereas with the acute ischemia model in study IV, the response was much quicker, and the decrease started within 15–30 minutes of hypoxia. This was expected, as the decrease in the pO₂ occurred much more rapidly in the acute compared to the chronic model. Furthermore, the hiPSC-CMs in the chronic model were observed to adapt to the hypoxic conditions during the late phases of hypoxia, as the beating frequency was observed to increase already before the start of the reoxygenation. On the other hand, no similar adaptation of the hiPSC-CMs to the hypoxic conditions was observed in the acute ischemia model, but the beating frequency recovered only after the reoxygenation started. This could be due to the shorter hypoxia period, during which the hiPSC-CMs did not have time to adapt, as in the chronic model, the recovery only started between 10–15 hours of hypoxia.

Hypoxia has been shown to decrease cardiomyocyte beating frequency and reoxygenation has been shown to recover it in several studies (Durot et al., 1997; Laubriet et al., 2001; Liu et al., 2020; Shah et al., 2019; Välimäki et al., 2017, 2020; Wenzel et al., 2002). This is expected, as cardiomyocyte excitation-contraction coupling is an energy-consuming phenomenon, and the lack of oxygen during hypoxia and ischemia prevents the CMs from producing sufficient amount of energy for the contraction (Martínez et al., 2017). Furthermore, the restoration of oxygen allows the recovery of the energy production, which in turn enables the contraction to continue (Hausenloy & Yellon, 2013). However, interestingly the hiPSC-CM beating was observed to recover in study III already at late phases of hypoxia when oxygen was still not present in the culture.

This adaptation of the hiPSC-CMs to the hypoxia in study III chronic model is likely due to balancing of energy supply and demand (Stecyk et al., 2008), however, the mechanisms behind the balancing can only be speculated. Most likely the hiPSC-CM immature phenotype is at least partially responsible for the adaptation, as they are known to be more resistant to hypoxia due to their better ability to increase glycolytic flux and utilize anaerobic glycolysis for energy production (J. Patterson & Zhang, 2010; Neary et al., 2014). This hypothesis is supported by the increase in the *SLC2A1* expression, indicating that the cells are enhancing their glucose uptake and glycolysis. Although the medium used in the experiments was glucose-free and it was exchanged to the cells on the day before inducing hypoxia, it is possible that the hiPSC-CMs have had some residual glucose left, which has been utilized for energy production at late phases of hypoxia. However, it is possible that other mechanisms might be behind the adaptation as well. Furthermore, the adaptation shows that the pH in the cultures did not decrease during hypoxia, as lowered pH is known cause troponin C insensitivity to Ca^{2+} , which inhibits CM contraction (Sanada et al., 2011). This is probably due to the large volume of the medium compared to the number of cells in the culture.

Depolarization time and amplitude

During hypoxia, hiPSC-CM field potential depolarization time was observed to increase at the same time as the FP depolarization amplitude was observed to decrease. Both were observed to recover during reoxygenation, although the depolarization time did not fully recover to baseline level. These changes were observed in both chronic ischemia model in study III and acute ischemia model in study IV, although the results from study III are only indicative due to low number of analysed samples. Similar decrease in the FP depolarization time was observed by Liu and co-workers in their HL-1 cell model of ischemia (Liu et al., 2020), however, otherwise the detailed electrophysiological properties of CMs have not been extensively evaluated, especially from hiPSC-CM models of ischemia-reperfusion.

FP depolarization is thought to correlate to the upstroke (phase 0) of action potential (Tertoolen et al., 2018), although the FP in studies III and IV is a combined extracellular signal of the group of hiPSC-CMs above the recording electrode, whereas AP is a property of a single CM. The upstroke is known to have lower peak-to-peak amplitude in ischemia due to partial depolarization of the CMs. Furthermore, the upstroke phase is known to be slower during

ischemia (Klabunde, 2017). Thus, the changes observed in the hiPSC-CM t_{dep} and A_{dep} in studies III and IV correlate well with the changes known to occur in cardiomyocyte action potential during ischemia. Furthermore, these changes recovered close to baseline during reoxygenation, which is known to occur in reperfusion when the blood flow is restored to the ischemic area (Manning & Hearse, 1984). These results indicate that the models reproduce relevant electrophysiological changes when exposed to hypoxia and reoxygenation, thus suggesting their usefulness in modelling ischemia-reperfusion.

Field potential duration

Beat rate corrected field potential duration was not observed to change when hiPSC-CMs were exposed to acute hypoxia and reoxygenation in study IV. However, although it is known that beating rate affects the field potential duration, correction formulas designed for physiological range of beating rate, such as Bazett's or Fridericia's formulas, may not work as that well for extremely low or high beating frequencies (Funk-Brentano & Jaillon, 1993). In study IV, the hiPSC-CM mean baseline beating frequency was generally relatively low, only 27.18 ± 11.94 beats per minute, and even lower during hypoxia (9.21 ± 6.84 beats per minute during 30–180 min hypoxia). Thus, also the raw FPD was evaluated, which showed a decrease in FPD during hypoxia and recovery of the FPD during reoxygenation.

Liu and co-workers observed a decrease in the duration of AP-like signals they recorded from the HL-1 cell model during hypoxia using electroporation and intracellular electronics. In their system, they also had incorporated extracellular electronics recording field potentials, however, they did not analyse the FPD for comparison with the AP-like signal duration (Liu et al., 2020). Overall, the decrease in the raw FPD values during hypoxia observed in study IV would be in line with the decreased AP duration known to occur during ischemia (Klabunde, 2017), however, the reliability of the results can be argued due to the lack of correction with regard to the beating rate. Pacing of the hiPSC-CMs would have been optimal to eliminate the effect of variability in the beating rate and for evaluating the effect of hypoxia and reoxygenation on FPD in both studies. However, pacing was not available in the used experimental setup. In the future, this could bring further insights into the described ischemia models and would be a valuable addition to the system.

Field potential propagation

Field potential propagation through the hiPSC-CM sheet over the MEA electrode grid was observed to decrease during hypoxia and recover during reoxygenation in both studies III and IV, however, it did not fully recover to the baseline level during reoxygenation in neither study. Similar results were reported by Liu and co-workers in their HL-1 cell model of ischemia (Liu et al., 2020), and the slowing of the cardiac conduction velocity is known to occur during ischemia and reperfusion due to several reasons. Generally, the cardiac conduction velocity is affected by upstroke velocity, cell-to-cell coupling (De Boer et al., 2008; B. Han et al., 2021) as well as size and shape of the cardiomyocytes. Furthermore, during the healing of the infarcted area after ischemia-reperfusion, formation of non-specific scar tissue reduces conduction velocity in the cardiac tissue (B. Han et al., 2021).

In the presented chronic and acute ischemia-reperfusion models, the reduction of the FP propagation time most likely stems from the reduced depolarization time and cell-to-cell uncoupling. Furthermore, morphological changes observed in the hiPSC-CMs could be partially responsible for the slowing the FP propagation, as these changes were not observed to recover during reoxygenation, which could explain why the FP propagation did not fully recover either. On the other hand, as the models consisted of purified hiPSC-CM samples and there were no fibroblasts present in the cultures, fibroblast proliferation related to scar formation and reduced conduction in the heart after ischemia-reperfusion is not likely cause for the slowing of the conduction in the presented models. However, the observed changes indicate that the hiPSC-CMs successfully reproduced yet another electrophysiological change characteristic to ischemic heart disease, supporting their usefulness in modelling the disease.

6.4 Limitations of the study

One major limitation in utilizing hiPSC-CMs in different application is their immature phenotype compared to adult CMs (Ahmed et al., 2020; Liao et al., 2021). This becomes a disadvantage especially regarding the modelling of the cardiac ischemia-reperfusion as was done in studies III and IV, as the hiPSC-CMs are known to rely more on glycolysis than fatty acid oxidation for energy production (Hidalgo et al., 2018), whereas many of the ischemic responses in

cardiomyocytes stem from the switch from FA oxidation to anaerobic glycolysis when oxygen is deprived of the cardiac tissue (Martínez et al., 2017). Moreover, ischemia is known to be accompanied by decrease of pH (Hausenloy & Yellon, 2013) and known to affect the ischemic response of the CMs. Lowered pH inhibits the cardiac contraction during ischemia, as it causes troponin C to become insensitive to Ca^{2+} , which prevents the revelation of myosin binding sites in the actin filaments (Sanada et al., 2011). However, acidic medium was not used in studies III or IV as it has been used in some *in vitro* models of cardiac ischemia where hiPSC-CMs have been used (Fernández-Morales et al., 2019; Hidalgo et al., 2018). In study IV, pH was measured after hypoxia and hypoxia-reoxygenation, but it was not observed to change most likely due to the large volume of the cell culture medium compared to the number of the cells per sample.

The heart comprises of several other cell types, such as fibroblasts and endothelial cells, in addition to cardiomyocytes, which also contribute to the cardiac response to ischemia and reperfusion and the disease pathophysiology (Flores-Vergara et al., 2021). The ischemia-reperfusion models presented in studies III and IV lacked the other cell types, which can affect the utility and application of these models. However, several key electrophysiological changes were observed in the hiPSC-CM models of chronic and acute ischemia-reperfusion, indicating that they could be useful for example for drug screening and studying electrophysiology-related mechanisms of the disease and its treatments.

Maturation of the hiPSC-CMs in study I was induced by culturing them on PET textiles. However, this method was not used for maturation of the hiPSC-CMs in later studies II–IV. This was thought not feasible, as the textiles would not have allowed the use of such extensive set of analysis methods, including MEA and video microscopy. In a study by Han and co-workers, hiPSC-CMs were replated on flat surface after maturation period on fibrous scaffolds (J. Han et al., 2016), which could have been considered in study I. Yet, detaching and reseeding the cells could revert the achieved structural maturation and thus, the method was not used in subsequent studies for hiPSC-CM maturation. Also, the PET textiles do not resemble the cardiac tissue regarding softness and elasticity and although structural maturation was observed after culturing hiPSC-CMs on the textiles, it can be argued that softer and more

elastic material allowing the hiPSC-CMs to really shorten during contraction would be more optimal for culturing and maturing them.

In studies I–III, one limitation was the number of hiPSC lines used in the experiments, as only one hiPSC line was used for cardiac differentiation, while cell line variability is a well-known concern. However, in study IV, three individual control hiPSC lines were used for cardiac differentiation, and the electrophysiological responses of the hiPSC-CMs to hypoxia and reoxygenation were similar. On the other hand, results from studies I and II could be beneficial to repeat with additional cell lines. Furthermore, in study II, the neuronal differentiation was originally developed to induce cortical neurons (Hyvärinen et al., 2019), whereas cANS consists of sympathetic and parasympathetic peripheral neurons (Végh et al., 2016). There are several protocols for differentiation of specific types of neurons (Oh et al., 2016; Takayama et al., 2020), which could be utilized in the cardiac innervation model in the future experiments.

6.5 Future perspectives

Although the immaturity of the hiPSC-CMs hinders their application in disease modelling and drug screening, they are a desirable source of human cardiomyocytes, which are otherwise difficult to harvest and culture (Karakikes et al., 2015). The basic pathophysiology of the ischemic heart disease and cardiac ischemia-reperfusion injury are relatively well characterized (Hausenloy & Yellon, 2013). However, there is still a lot to be revealed on the detailed disease mechanisms, and currently there are no effective treatments to reduce the infarct size (T. Chen & Vunjak-Novakovic, 2018). To better understand the ischemia-reperfusion injury and to develop relevant treatments, also relevant models are required. Animal models are imperative for translating *in vitro* results into humans, however, due to ethical considerations and translational difficulties due to species differences, their usage should be minimized. Here, hiPSC-CM based *in vitro* models give the opportunity to rigorously evaluate pathways important in IRI as well as initial testing of therapeutic options in human cell models with the possibility for better control and manipulation of the experimental conditions compared to animal models (T. Chen & Vunjak-Novakovic, 2018).

There are already several studies where hiPSC-CMs have been utilized in modelling of myocardial IRI (Canfield et al., 2016; T. Chen & Vunjak-Novakovic, 2019; Fernández-Morales et al., 2019; Fiedler et al., 2019; Hidalgo et al., 2018; Sebastião et al., 2020; Shah et al., 2019; Veldhuizen et al., 2022; H. Wei et al., 2019; W. Wei et al., 2017) and many aspects of the IRI have been successfully reproduced with hiPSC-CMs. The immaturity of the hiPSC-CMs has been considered in a few studies for example by inducing metabolic maturation (Hidalgo et al., 2018) and low pH and nutrient deprivation, which are known to accompany hypoxia and contribute to the ischemic injury, have been incorporated in several studies as well (T. Chen & Vunjak-Novakovic, 2019; Hidalgo et al., 2018; Sebastião et al., 2020). However, few of the models have incorporated any functional evaluation of the cells, but the focus in *in vitro* models has generally been in cell viability and molecular markers of ischemia.

Contractility is an important aspect of CMs and tightly coupled with the electrophysiology of the cells (Eisner et al., 2017) but only a few studies where ischemia has been modelled with hPSC-CMs have incorporated functional evaluation, and mostly just beating frequency (Choi et al., 2021; Shah et al., 2019; Välimäki et al., 2017, 2020; Veldhuizen et al., 2022), although calcium kinetics have also been evaluated (Fernández-Morales et al., 2019; W. Wei et al., 2017). In this thesis, the focus was on the detailed electrophysiological responses of the hiPSC-CMs to hypoxia and reoxygenation acquired with MEA. The electrophysiological data, including beating frequency, FP depolarization time and amplitude, FP duration and FP propagation time could be combined with real time pO₂ measurement directly from the cell cultures, which allowed comparison of the occurred changes to the oxygen level of the cultures. Taken together, the accumulating knowledge of hiPSC-CMs responses to hypoxia and reoxygenation will likely enhance their utilization as a human based *in vitro* model of ischemia-reperfusion in the future and contribute to revealing disease mechanisms and drug development for alleviating the IR injury.

The ischemia-reperfusion models presented in studies III and IV can be further combined with the knowledge acquired from studies I and II regarding the maturation and the cardiac innervation modelling. Coculture with other cell types present in cardiac tissue, including fibroblasts and endothelial cells is known to improve hiPSC-CM maturation (Vuorenää et al., 2017), and

could also be important regarding ischemia modelling, as the other cell types are also known to participate in the tissue response to IRI (Flores-Vergara et al., 2021). Furthermore, IRI is known to affect the innervating axons of the neurons of cANS, and known to result in cardiac arrhythmias (Kolettis et al., 2015). By combining a cardiovascular construct consisting of hiPSC-CMs, endothelial cells and fibroblasts to the compartmentalized microfluidic 3D3C chip for coculture with sympathetic or parasympathetic peripheral hiPSC-neurons could provide a relevant human based model for studying the mechanisms and pathophysiology of cardiac ischemia-reperfusion as well as for screening therapeutics and treatments for reducing the injury to the cells.

7 CONCLUSION

This thesis focused on modelling cardiac ischemia and reperfusion utilizing hiPSC-CMs. The knowledge acquired from studies I–IV is aimed for further development of human based *in vitro* disease models, especially for ischemic heart disease and ischemia-reperfusion injury. Based on these studies, following conclusions can be drawn:

1. The platform for inducing chronic and acute hypoxia and reoxygenation to hiPSC-CMs allows the easy use of several methods for characterization of the culture conditions and the cellular responses to the oxidative stress, including measurement of oxygen partial pressure, recording hiPSC-CM field potentials, evaluating cellular morphology as well as protein and gene expression.
2. hiPSC-CMs reproduce several electrophysiological changes characteristic to ischemia and reperfusion when subjected to both chronic and acute hypoxia and reoxygenation. These include decrease in beating frequency, depolarization amplitude, as well as increase in depolarization time and field potential propagation time.
3. Hypoxia and reoxygenation induce morphological changes in hiPSC-CMs, including deterioration of the sarcomeres as well as decreased nuclei size both in chronic and acute model. In the acute model, the changes were more pronounced in hiPSC-CMs after hypoxia-reoxygenation compared to hypoxia alone indicating that reoxygenation further injures the hiPSC-CMs, and that the models are capable of mimicking also reperfusion injury.
4. The structural maturation of hiPSC-CMs improves upon culturing them on PET textiles, which is indicated by improved cellular alignment and sarcomere orientation. However, effects on other aspects of maturation, including the expression of cardiac genes or sarcomere length were not significant. Furthermore, application of these textiles in other experiments proved to be difficult.

5. Coculture of hiPSC-CMs and hiPSC-neurons in compartmentalized microfluidic chip allows modelling cardiac innervation via axon-mediated interaction between cardiomyocytes and neurons. Further development with incorporation of peripheral sympathetic or parasympathetic neurons, microelectrode array technology and combining the coculture with the hypoxia and reoxygenation equipment could create a powerful tool for modelling cardiac ischemia in a cardiac innervation model.

In conclusion, these studies show that hiPSC-CMs can reproduce several key changes characteristic to ischemia and ischemia-reperfusion in a platform allowing the utilization of extensive set of methods for evaluating the hiPSC-CM responses. The advantage of the presented model is its simplicity, and the possibility to incorporate several methods for thorough characterization of the hiPSC-CM response to hypoxia and reoxygenation. Furthermore, incorporation of continuous pO₂ measurement further improves the understanding of the cellular responses to hypoxia and reoxygenation and allows the validation of specific oxygen conditions experienced by the cells. In the future, combining the ischemia modelling platform with the compartmentalized coculture chip for modelling ischemia-reperfusion in cardiac innervation model could be the next step for *in vitro* ischemia modelling.

REFERENCES

- Ahmed, R. E., Anzai, T., Chanthra, N., & Uosaki, H. (2020). A Brief Review of Current Maturation Methods for Human Induced Pluripotent Stem Cells-Derived Cardiomyocytes. *Frontiers in Cell and Developmental Biology*, 8, 178. <https://doi.org/10.3389/fcell.2020.00178>
- Ambrose, J. A., & Singh, M. (2015). Pathophysiology of coronary artery disease leading to acute coronary syndromes. *F1000Prime Reports*, 7, 08. <https://doi.org/10.12703/P7-08>
- Anderson, R. H., Yanni, J., Boyett, M. R., Chandler, N. J., & Dobrzynski, H. (2009). The anatomy of the cardiac conduction system. *Clinical Anatomy*, 22(1), 99–113. <https://doi.org/10.1002/ca.20700>
- Bagai, A., Dangas, G. D., Stone, G. W., & Granger, C. B. (2014). Reperfusion strategies in acute coronary syndromes. *Circulation Research*, 114(12), 1918–1928. <https://doi.org/10.1161/CIRCRESAHA.114.302744>
- Baguisi, A., Casale, R. A., Kates, S. A., Lader, A. S., Stewart, K., & Beeuwkes, R. (2016). CMX-2043 Efficacy in a Rat Model of Cardiac Ischemia-Reperfusion Injury. *Journal of Cardiovascular Pharmacology and Therapeutics*, 21(6), 563–569. <https://doi.org/10.1177/1074248416640118>
- Bairey Merz, C. N., Elboudwarej, O., & Mehta, P. (2015). The autonomic nervous system and cardiovascular health and disease. A complex balancing act. *JACC: Heart Failure*, 3(5), 383–385. <https://doi.org/10.1016/j.jchf.2015.01.008>
- Balafkan, N., Mostafavi, S., Schubert, M., Siller, R., Liang, K. X., Sullivan, G., & Bindoff, L. A. (2020). A method for differentiating human induced pluripotent stem cells toward functional cardiomyocytes in 96-well microplates. *Scientific Reports*, 10(1), 1–14. <https://doi.org/10.1038/s41598-020-73656-2>
- Bedada, F. B., Chan, S. S. K., Metzger, S. K., Zhang, L., Zhang, J., Garry, D. J., Kamp, T. J., Kyba, M., & Metzger, J. M. (2014). Acquisition of a quantitative, stoichiometrically conserved ratiometric marker of maturation status in stem cell-derived cardiac myocytes. *Stem Cell Reports*, 3(4), 594–605. <https://doi.org/10.1016/j.stemcr.2014.07.012>
- Bruneau, B. G. (2013). Signaling and Transcriptional Networks in Heart Development and Regeneration. *Cold Spring Harbor Perspectives in Biology*, 5(3), a008292. <https://doi.org/10.1101/cshperspect.a008292>

- Camacho, P., Fan, H., Liu, Z., & He, J. Q. (2016). Large mammalian animal models of heart disease. *Journal of Cardiovascular Development and Disease*, 3(4). <https://doi.org/10.3390/jcdd3040030>
- Canfield, S. G., Zaja, I., Godshaw, B., Twaroski, D., Bai, X., & Bosnjak, Z. J. (2016). High Glucose Attenuates Anesthetic Cardioprotection in Stem-Cell-Derived Cardiomyocytes: The Role of Reactive Oxygen Species and Mitochondrial Fission. *Anesthesia and Analgesia*, 122(5), 1269–1279. <https://doi.org/10.1213/ANE.0000000000001254>
- Casals, G., Ros, J., Sionis, A., Davidson, M. M., Morales-Ruiz, M., & Jiménez, W. (2009). Hypoxia induces B-type natriuretic peptide release in cell lines derived from human cardiomyocytes. *American Journal of Physiology - Heart and Circulatory Physiology*, 297(2), 550–555. <https://doi.org/10.1152/ajpheart.00250.2009>
- Chen, C. C., Kuo, C. Y., & Chen, R. F. (2016). Role of CAPE on cardiomyocyte protection via connexin 43 regulation under hypoxia. *International Journal of Medical Sciences*, 13(10), 754–758. <https://doi.org/10.7150/ijms.15847>
- Chen, S., & Li, S. (2012). The Na⁺/Ca²⁺ exchanger in cardiac ischemia/reperfusion injury. *Medical Science Monitor*, 18(11), 161–165. <https://doi.org/10.12659/MSM.883533>
- Chen, T., & Vunjak-Novakovic, G. (2018). In Vitro Models of Ischemia-Reperfusion Injury. *Regenerative Engineering and Translational Medicine*, 4(3), 142–153. <https://www.ncbi.nlm.nih.gov/pmc/articles/PMC6208331/>
- Chen, T., & Vunjak-Novakovic, G. (2019). Human Tissue-Engineered Model of Myocardial Ischemia-Reperfusion Injury. *Tissue Engineering - Part A*, 25(9–10), 711–724. <https://doi.org/10.1089/ten.tea.2018.0212>
- Choi, S. C., Seo, H. R., Cui, L. H., Song, M. H., Noh, J. M., Kim, K. S., Choi, J. H., Kim, J. H., Park, C. Y., Joo, H. J., Hong, S. J., Ko, T. H., Choi, J. Il, Kim, H. J., Kim, J. H., Paek, S. H., Park, J. N., Kim, D. H., Jang, Y., ... Lim, D. S. (2021). Modeling hypoxic stress in vitro using human embryonic stem cells derived cardiomyocytes matured by fgf4 and ascorbic acid treatment. *Cells*, 10(10). <https://doi.org/10.3390/cells10102741>
- Chou, C., & Chin, M. T. (2021). Pathogenic Mechanisms of Hypertrophic Cardiomyopathy beyond Sarcomere Dysfunction. *International Journal of Molecular Sciences*, 22(16), 8933. <https://doi.org/10.3390/ijms22168933>
- Clements-Jewery, H., Hearse, D. J., & Curtis, M. J. (2002). The isolated blood-perfused rat heart: An inappropriate model for the study of ischaemia- and infarction-related ventricular fibrillation. *British Journal of Pharmacology*, 137(7), 1089–1099. <https://doi.org/10.1038/sj.bjp.0704977>

- Conci, E., Pachinger, O., & Metzler, B. (2006). Mouse models for myocardial ischaemia/reperfusion. In *Journal fur Kardiologie* (Vol. 13, Issues 7–8, pp. 239–244).
- Cox, L. A., Olivier, M., Spradling-Reeves, K., Karere, G. M., Comuzzie, A. G., & VandeBerg, J. L. (2017). Nonhuman primates and translational research-Cardiovascular disease. *ILAR Journal*, 58(2), 235–250. <https://doi.org/10.1093/ilar/ilx025>
- Crocini, C., & Gotthardt, M. (2021). Cardiac sarcomere mechanics in health and disease. *Biophysical Reviews*, 13(5), 637–652. <https://doi.org/10.1007/s12551-021-00840-7>
- Daley, G. Q. (2015). Stem cells and the evolving notion of cellular identity. *Philosophical Transactions of the Royal Society B: Biological Sciences*, 370(1680), 20140376. <https://doi.org/10.1098/rstb.2014.0376>
- Damiano, B. P., van der Linde, H. J., Van Deuren, B., Somers, Y., Lubomirski, M., Teisman, A., & Gallacher, D. J. (2015). Characterization of an anesthetized dog model of transient cardiac ischemia and rapid pacing: A pilot study for preclinical assessment of the potential for proarrhythmic risk of novel drug candidates. *Journal of Pharmacological and Toxicological Methods*, 72, 72–84. <https://doi.org/10.1016/j.vascn.2014.10.006>
- Davidson, M. M., Nesti, C., Palenzuela, L., Walker, W. F., Hernandez, E., Protas, L., Hirano, M., & Isaac, N. D. (2005). Novel cell lines derived from adult human ventricular cardiomyocytes. *Journal of Molecular and Cellular Cardiology*, 39(1), 133–147. <https://doi.org/10.1016/j.yjmcc.2005.03.003>
- De Boer, T. P., Van Rijen, H. V. M., Van Der Heyden, M. A. G., De Bakker, J. M. T., & Van Veen, T. A. B. (2008). Adrenergic regulation of conduction velocity in cultures of immature cardiomyocytes. *Netherlands Heart Journal*, 16(3), 106–109. <https://doi.org/10.1007/BF03086127>
- De Tombe, P. P. (2003). Cardiac myofilaments: mechanics and regulation. *Journal of Biomechanics*, 36, 721–730. [https://doi.org/10.1016/S0021-9290\(02\)00450-5](https://doi.org/10.1016/S0021-9290(02)00450-5)
- De Vuyst, E., Boengler, K., Antoons, G., Sipido, K. R., Schulz, R., & Leybaert, L. (2011). Pharmacological modulation of connexin-formed channels in cardiac pathophysiology. *British Journal of Pharmacology*, 163(3), 469–483. <https://doi.org/10.1111/j.1476-5381.2011.01244.x>
- Denning, C., Borgdorff, V., Crutchley, J., Firth, K. S. A., George, V., Kalra, S., Kondrashov, A., Hoang, M. D., Mosqueira, D., Patel, A., Prodanov, L., Rajamohan, D., Skarnes, W. C., Smith, J. G. W., & Young, L. E. (2016). Cardiomyocytes from human pluripotent stem cells: From laboratory curiosity to industrial biomedical platform. *Biochimica et Biophysica Acta - Molecular Cell Research*, 1863(7), 1728–1748. <https://doi.org/10.1016/j.bbamcr.2015.10.014>

- Diaz, R. J., & Wilson, G. J. (2006). Studying ischemic preconditioning in isolated cardiomyocyte models. *Cardiovascular Research*, 70(2), 286–296. <https://doi.org/10.1016/j.cardiores.2005.12.003>
- Dixon, J. A., & Spinale, F. G. (2009). Large animal models of heart failure; A critical link in the translation of basic science to clinical practice. *Circulation: Heart Failure*, 2(3), 262–271. <https://doi.org/10.1161/CIRCHEARTFAILURE.108.814459>
- Dulak, J., Szade, K., Szade, A., Nowak, W., & Józkwicz, A. (2015). Adult stem cells: Hopes and hypes of regenerative medicine. *Acta Biochimica Polonica*, 62(3), 329–337. https://doi.org/10.18388/abp.2015_1023
- Durot, I., Athias, P., Oudot, F., & Grynberg, A. (1997). Influence of phospholipid long chain polyunsaturated fatty acid composition on neonatal rat cardiomyocyte function in physiological conditions and during glucose-free hypoxia-reoxygenation. *Molecular and Cellular Biochemistry*, 175(1–2), 253–262. <https://doi.org/10.1023/A:1006817901323>
- Ehler, E., Moore-Morris, T., & Lange, S. (2013). Isolation and culture of neonatal mouse cardiomyocytes. *Journal of Visualized Experiments*, 79, 1–10. <https://doi.org/10.3791/50154>
- Eisner, D. A., Caldwell, J. L., Kistamás, K., & Trafford, A. W. (2017). Calcium and Excitation-Contraction Coupling in the Heart. *Circulation Research*, 121(2), 181–195. <https://doi.org/10.1161/CIRCRESAHA.117.310230>
- Emini Veseli, B., Perrotta, P., De Meyer, G. R. A., Roth, L., Van der Donckt, C., Martinet, W., & De Meyer, G. R. Y. (2017). Animal models of atherosclerosis. *European Journal of Pharmacology*, 816, 3–13. <https://doi.org/10.1016/j.ejphar.2017.05.010>
- Farkas, A., Qureshi, A., & Curtis, M. J. (1999). Inadequate ischaemia-selectivity limits the antiarrhythmic efficacy of mibefradil during regional ischaemia and reperfusion in the rat isolated perfused heart. *British Journal of Pharmacology*, 128(1), 41–50. <https://doi.org/10.1038/sj.bjp.0702778>
- Fernández-Morales, J.-C., Hua, W., Yao, Y., & Morad, M. (2019). Regulation of Ca²⁺ signaling by acute hypoxia and acidosis in cardiomyocytes derived from human induced pluripotent stem cells. *Cell Calcium*, 78(1), 1–14. <https://doi.org/10.1016/j.ceca.2018.12.006>
- Feyen, D. A. M., McKeithan, W. L., Bruyneel, A. A. N., Spiering, S., Hörmann, L., Ulmer, B., Zhang, H., Briganti, F., Schweizer, M., Hegyi, B., Liao, Z., Pölonen, R., Ginsburg, K. S., Lam, C. K., Serrano, R., Wahlquist, C., Kreymerman, A., Vu, M., Amatya, P. L., ... Mercola, M. (2020). Metabolic Maturation Media Improve Physiological Function of Human iPSC-Derived Cardiomyocytes. *Cell Reports*, 32(3), 107925. <https://doi.org/10.1016/j.celrep.2020.107925>

- Fiedler, L. R., Chapman, K., Xie, M., Maifoshie, E., Jenkins, M., Golfroush, P. A., Bellahcene, M., Nosedá, M., Faust, D., Jarvis, A., Newton, G., Paiva, M. A., Harada, M., Stuckey, D. J., Song, W., Habib, J., Narasimham, P., Aqil, R., Sanmugalingam, D., ... Schneider, M. D. (2019). MAP4K4 Inhibition Promotes Survival of Human Stem Cell-Derived Cardiomyocytes and Reduces Infarct Size In Vivo. *Cell Stem Cell*, 24(4), 579-591.e12. <https://doi.org/10.1016/j.stem.2019.01.013>
- Fink, S. L., & Cookson, B. T. (2005). Apoptosis, Pyroptosis, and Necrosis: Mechanistic Description of Dead and Dying Eucaryotic Cells. *Infection and Immunity*, 73(4), 1907–1916. <https://doi.org/10.1128/IAI.73.4.1907-1916.2005>
- Flores-Vergara, R., Olmedo, I., Aránguiz, P., Riquelme, J. A., Vivar, R., & Pedrozo, Z. (2021). Communication Between Cardiomyocytes and Fibroblasts During Cardiac Ischemia/Reperfusion and Remodeling: Roles of TGF- β , CTGF, the Renin Angiotensin Axis, and Non-coding RNA Molecules. *Frontiers in Physiology*, 12, 716721. <https://doi.org/10.3389/fphys.2021.716721>
- Francis, M. P., Breathwaite, E., Bulysheva, A. A., Varghese, F., Rodriguez, R. U., Dutta, S., Semenov, I., Ogle, R., Huber, A., Tichy, A. M., Chen, S., & Zemlin, C. (2017). Human placenta hydrogel reduces scarring in a rat model of cardiac ischemia and enhances cardiomyocyte and stem cell cultures. *Acta Biomaterialia*, 52, 92–104. <https://doi.org/10.1016/j.actbio.2016.12.027>
- Funck-Brentano, C., & Jaillon, P. (1993). Rate-corrected QT interval: Techniques and limitations. *The American Journal of Cardiology*, 72(6). [https://doi.org/10.1016/0002-9149\(93\)90035-B](https://doi.org/10.1016/0002-9149(93)90035-B)
- Garcia-Dorado, D., Ruiz-Meana, M., Insete, J., Rodriguez-Sinovas, A., & Piper, H. M. (2012). Calcium-mediated cell death during myocardial reperfusion. *Cardiovascular Research*, 94(2), 168–180. <https://doi.org/10.1093/cvr/cvs116>
- Gomes, A. V., Potter, J. D., & Szczesna-Cordary, D. (2002). The Role of Troponins in Muscle Contraction. *IUBMB Life (International Union of Biochemistry and Molecular Biology: Life)*, 54(6), 323–333. <https://doi.org/10.1080/15216540216037>
- Graham, A. M., & Presnell, J. S. (2017). Hypoxia Inducible Factor (HIF) transcription factor family expansion, diversification, divergence and selection in eukaryotes. *PLoS ONE*, 12(6), 1–15. <https://doi.org/10.1371/journal.pone.0179545>
- Grant, A. O. (2009). Cardiac ion channels. *Circulation: Arrhythmia and Electrophysiology*, 2(2), 185–194. <https://doi.org/10.1161/CIRCEP.108.789081>
- Guo, Y., & Pu, W. T. (2020). Cardiomyocyte Maturation. *Circulation Research*, 126(8), 1086–1106. <https://doi.org/10.1161/CIRCRESAHA.119.315862>
- Habecker, B. A., Anderson, M. E., Birren, S. J., Fukuda, K., Herring, N., Hoover, D. B., Kanazawa, H., Paterson, D. J., & Ripplinger, C. M. (2016). Molecular and cellular neurocardiology: development, and cellular and molecular adaptations to heart

- disease. *Journal of Physiology*, 594(14), 3853–3875. <https://doi.org/10.1113/JP271840>
- Hadaya, J., & Ardell, J. L. (2020). Autonomic Modulation for Cardiovascular Disease. *Frontiers in Physiology*, 11, 617459. <https://doi.org/10.3389/fphys.2020.617459>
- Hajar, R. (2017). Risk factors for coronary artery disease: Historical perspectives. *Heart Views*, 18(3), 109. https://doi.org/10.4103/heartviews.heartviews_106_17
- Han, B., Trew, M. L., & Zgierski-Johnston, C. M. (2021). Cardiac conduction velocity, remodeling and arrhythmogenesis. *Cells*, 10(11), 1–28. <https://doi.org/10.3390/cells10112923>
- Han, J., Wu, Q., Xia, Y., Wagner, M. B., & Xu, C. (2016). Cell alignment induced by anisotropic electrospun fibrous scaffolds alone has limited effect on cardiomyocyte maturation. *Stem Cell Research*, 16(3), 740–750. <https://doi.org/10.1016/j.scr.2016.04.014>
- Harding, J. D. (2017). Nonhuman primates and translational research: Progress, opportunities, and challenges. *ILAR Journal*, 58(2), 141–150. <https://doi.org/10.1093/ilar/ilx033>
- Hasan, W. (2013). Autonomic cardiac innervation: Development and adult plasticity. *Organogenesis*, 9(3), 176–193. <https://doi.org/10.4161/org.24892>
- Hausenloy, D. J., & Yellon, D. M. (2013). Myocardial ischemia-reperfusion injury: a neglected therapeutic target. *The Journal of Clinical Investigation*, 123(1), 92–100. <https://doi.org/10.1172/JCI62874.92>
- Hidalgo, A., Glass, N., Ovchinnikov, D., Yang, S. K., Zhang, X., Mazzone, S., Chen, C., Wolvetang, E., & Cooper-White, J. (2018). Modelling ischemia-reperfusion injury (IRI) in vitro using metabolically matured induced pluripotent stem cell-derived cardiomyocytes. *APL Bioengineering*, 2(2), 1–14. <https://doi.org/10.1063/1.5000746>
- Hocum Stone, L., Butterick, T. A., Duffy, C., Swingen, C., Ward, H. B., Kelly, R. F., & McFalls, E. O. (2016). Cardiac Strain in a Swine Model of Regional Hibernating Myocardium: Effects of CoQ10 on Contractile Reserve Following Bypass Surgery. *Journal of Cardiovascular Translational Research*, 9(4), 368–373. <https://doi.org/10.1007/s12265-016-9696-y>
- Hong, T., & Shaw, R. M. (2017). Cardiac T-Tubule Microanatomy and Function. *Physiological Reviews*, 97(1), 227–252. <https://doi.org/10.1152/physrev.00037.2015>
- Hu, D., Linders, A., Yamak, A., Correia, C., Kijlstra, J. D., Garakani, A., Xiao, L., Milan, D. J., Van Der Meer, P., Serra, M., Alves, P. M., & Domian, I. J. (2018). Metabolic maturation of human pluripotent stem cell-derived cardiomyocytes by inhibition of HIF1 α and LDHA. *Circulation Research*, 123(9), 1066–1079. <https://doi.org/10.1161/CIRCRESAHA.118.313249>

- Huethorst, E., Hortigon, M., Zamora-Rodriguez, V., Reynolds, P. M., Burton, F., Smith, G., & Gadegaard, N. (2016). Enhanced Human-Induced Pluripotent Stem Cell Derived Cardiomyocyte Maturation Using a Dual Microgradient Substrate. *ACS Biomaterials Science and Engineering*, 2(12), 2231–2239. <https://doi.org/10.1021/acsbiomaterials.6b00426>
- Hyvärinen, T., Hyysalo, A., Kapucu, F. E., Aarnos, L., Vinogradov, A., Eglen, S. J., Ylä-Outinen, L., & Narkilahti, S. (2019). Functional characterization of human pluripotent stem cell-derived cortical networks differentiated on laminin-521 substrate: comparison to rat cortical cultures. *Scientific Reports*, 9(1), 1–15. <https://doi.org/10.1038/s41598-019-53647-8>
- Iaizzo, P. A. (2009). General Features of the Cardiovascular System. In *Handbook of Cardiac Anatomy, Physiology, and Devices* (pp. 3–12). Humana Press. https://doi.org/10.1007/978-1-60327-372-5_1
- Iommarini, L., Porcelli, A. M., Gasparre, G., & Kurelac, I. (2017). Non-Canonical Mechanisms Regulating Hypoxia-Inducible Factor 1 Alpha in Cancer. *Frontiers in Oncology*, 7, 286. <https://doi.org/10.3389/fonc.2017.00286>
- Izumi-Nakaseko, H., Kanda, Y., Nakamura, Y., Hagiwara-Nagasawa, M., Wada, T., Ando, K., Naito, A. T., Sekino, Y., & Sugiyama, A. (2017). Development of correction formula for field potential duration of human induced pluripotent stem cell-derived cardiomyocytes sheets. *Journal of Pharmacological Sciences*, 135(1), 44–50. <https://doi.org/10.1016/j.jphs.2017.08.008>
- J. Patterson, A., & Zhang, L. (2010). Hypoxia and Fetal Heart Development. *Current Molecular Medicine*, 10(7), 653–666. <https://doi.org/10.2174/156652410792630643>
- Jiang, C. L., Goyal, Y., Jain, N., Wang, Q., Truitt, R. E., Coté, A. J., Emert, B., Mellis, I. A., Kiani, K., Yang, W., Jain, R., & Raj, A. (2022). Cell type determination for cardiac differentiation occurs soon after seeding of human-induced pluripotent stem cells. *Genome Biology*, 23(1), 90. <https://doi.org/10.1186/s13059-022-02654-6>
- Jovanović, S., Jovanović, N., & Jovanović, A. (2006). High glucose protects single beating adult cardiomyocytes against hypoxia. *Biochemical and Biophysical Research Communications*, 341(1), 57–66. <https://doi.org/10.1016/j.bbrc.2005.12.147>
- Kadota, S., Pabon, L., Reinecke, H., & Murry, C. E. (2017). In Vivo Maturation of Human Induced Pluripotent Stem Cell-Derived Cardiomyocytes in Neonatal and Adult Rat Hearts. *Stem Cell Reports*, 8(2), 278–289. <https://doi.org/10.1016/j.stemcr.2016.10.009>
- Kalogeris, T., Baines, C. P., Krenz, M., & Korthuis, R. J. (2016). Ischemia/Reperfusion. In *Comprehensive Physiology* (Vol. 7, Issue 1, pp. 113–170). Wiley. <https://doi.org/10.1002/cphy.c160006>

- Karakikes, I., Mohamed, A., Termglinchan, V., & Wu, J. C. (2015). Human Induced Pluripotent Stem Cell-Derived Cardiomyocytes: Insights into Molecular, Cellular, and Functional Phenotypes. *Circulation Research*, *117*(1), 80–88. <https://doi.org/10.1016/bs.mcb.2015.01.016>. Observing
- Karakikes, I., Senyei, G. D., Hansen, J., Kong, C.-W., Azeloglu, E. U., Stillitano, F., Lieu, D. K., Wang, J., Ren, L., Hulot, J.-S., Iyengar, R., Li, R. A., & Hajjar, R. J. (2014). Small Molecule-Mediated Directed Differentiation of Human Embryonic Stem Cells Toward Ventricular Cardiomyocytes. *STEM CELLS Translational Medicine*, *3*(1), 18–31. <https://doi.org/10.5966/sctm.2013-0110>
- Karbassi, E., Fenix, A., Marchiano, S., Muraoka, N., Nakamura, K., Yang, X., & Murry, C. E. (2020). Cardiomyocyte maturation: advances in knowledge and implications for regenerative medicine. *Nature Reviews Cardiology*, *17*(6), 341–359. <https://doi.org/10.1038/s41569-019-0331-x>
- Kartasalo, K., Pölönen, R.-P., Ojala, M., Rasku, J., Lekkala, J., Aalto-Setälä, K., & Kallio, P. (2015). CytoSpectre: a tool for spectral analysis of oriented structures on cellular and subcellular levels. *BMC Bioinformatics*, *16*(344), 1–23. <https://doi.org/10.1186/s12859-015-0782-y>
- Kassambra, A. (2021). *rstatix: Pipe-Friendly Framework for Basic Statistical Tests* (R package version 0.7.0). <https://cran.r-project.org/package=rstatix>
- Kaur, J., Tilkins, M. L., Eckert, R., & Boucher, S. (2013). Methods for Culturing Human Embryonic Stem Cells in a Xeno-Free System. In *Methods in Molecular Biology* (Vol. 997, pp. 115–126). https://doi.org/10.1007/978-1-62703-348-0_9
- Kehat, I., Kenyagin-Karsenti, D., Snir, M., Segev, H., Amit, M., Gepstein, A., Livne, E., Binah, O., Itskovitz-Eldor, J., & Gepstein, L. (2001). Human embryonic stem cells can differentiate into myocytes with structural and functional properties of cardiomyocytes. *Journal of Clinical Investigation*, *108*(3), 407–414. <https://doi.org/10.1172/JCI200112131>
- Kennedy, A., Finlay, D. D., Guldenring, D., Bond, R., Moran, K., & McLaughlin, J. (2016). The Cardiac Conduction System: Generation and Conduction of the Cardiac Impulse. *Critical Care Nursing Clinics of North America*, *28*(3), 269–279. <https://doi.org/10.1016/j.cnc.2016.04.001>
- Khan, M. A., Hashim, M. J., Mustafa, H., Baniyas, M. Y., Al Suwaidi, S. K. B. M., AlKatheeri, R., Alblooshi, F. M. K., Almatrooshi, M. E. A. H., Alzaabi, M. E. H., Al Darmaki, R. S., & Lootah, S. N. A. H. (2020). Global Epidemiology of Ischemic Heart Disease: Results from the Global Burden of Disease Study. *Cureus*, *12*(7). <https://doi.org/10.7759/cureus.9349>
- Khan, M., Xu, Y., Hua, S., Johnson, J., Belevych, A., Janssen, P. M. L., Gyorke, S., Guan, J., & Angelos, M. G. (2015). Evaluation of changes in morphology and function of human induced pluripotent stem cell derived cardiomyocytes (hiPSC-CMs)

- cultured on an aligned-nanofiber cardiac patch. *PLoS ONE*, *10*(5).
<https://doi.org/10.1371/journal.pone.0126338>
- Kingma, J. G., Simard, D., & Rouleau, J. R. (2018). Autonomic Nervous System and Neurocardiac Physiopathology. In *Autonomic Nervous System*. InTech.
<https://doi.org/10.5772/intechopen.77087>
- Kirby, R. J., Divlianska, D. B., Whig, K., Bryan, N., Morfa, C. J., Koo, A., Nguyen, K. H., Maloney, P., Peddibhotla, S., Sessions, E. H., Hershberger, P. M., Smith, L. H., & Malany, S. (2018). Discovery of novel small-molecule inducers of heme oxygenase-1 that protect human ipsc-derived cardiomyocytes from oxidative stress. *Journal of Pharmacology and Experimental Therapeutics*, *364*(1), 87–96.
<https://doi.org/10.1124/jpet.117.243717>
- Klabunde, R. E. (2017). Cardiac electrophysiology: Normal and ischemic ionic currents and the ECG. *Advances in Physiology Education*, *41*(1), 29–37.
<https://doi.org/10.1152/advan.00105.2016>
- Knight, W. E., Cao, Y., Lin, Y. H., Chi, C., Bai, B., Sparagna, G. C., Zhao, Y., Du, Y., Londono, P., Reisz, J. A., Brown, B. C., Taylor, M. R. G., Ambardekar, A. V., Cleveland, J. C., McKinsey, T. A., Jeong, M. Y., Walker, L. A., Woulfe, K. C., D'Alessandro, A., ... Song, K. (2021). Maturation of Pluripotent Stem Cell-Derived Cardiomyocytes Enables Modeling of Human Hypertrophic Cardiomyopathy. *Stem Cell Reports*, *16*(3), 519–533.
<https://doi.org/10.1016/j.stemcr.2021.01.018>
- Kobuszewska, A., Jastrzębska, E., Żukowski, K., & Brzózka, Z. (2020). Simulation of hypoxia of myocardial cells in microfluidic systems. *Scientific Reports*, *10*(1), 1–11. <https://doi.org/10.1038/s41598-020-72660-w>
- Kockskämper, J. (2016). Excitation–Contraction Coupling of Cardiomyocytes. In *Cardiomyocytes – Active Players in Cardiac Disease* (pp. 67–96). Springer International Publishing. https://doi.org/10.1007/978-3-319-31251-4_3
- Koerselman, J., van der Graaf, Y., de Jaegere, P. P. T., & Grobbee, D. E. (2003). Coronary Collaterals. *Circulation*, *107*(19), 2507–2511.
<https://doi.org/10.1161/01.CIR.0000065118.99409.5F>
- Koivumäki, J. T., Naumenko, N., Tuomainen, T., Takalo, J., Oksanen, M., Puttonen, K. A., Lehtonen, Š., Kuusisto, J., Laakso, M., Koistinaho, J., & Tavi, P. (2018). Structural Immaturity of Human iPSC-Derived Cardiomyocytes: In Silico Investigation of Effects on Function and Disease Modeling. *Frontiers in Physiology*, *9*, 80. <https://doi.org/10.3389/fphys.2018.00080>
- Kolettis, T. M., Kontonika, M., Barka, E., Daskalopoulos, E. P., Baltogiannis, G. G., Tourmousoglou, C., Papalois, A., & Kyriakides, Z. S. (2015). Central Sympathetic Activation and Arrhythmogenesis during Acute Myocardial Infarction: Modulating Effects of Endothelin-B Receptors. *Frontiers in Cardiovascular Medicine*, *2*, 6. <https://doi.org/10.3389/fcvm.2015.00006>

- Kolwicz, S. C., Purohit, S., & Tian, R. (2013). Cardiac Metabolism and its Interactions With Contraction, Growth, and Survival of Cardiomyocytes. *Circulation Research*, *113*(5), 603–616. <https://doi.org/10.1161/CIRCRESAHA.113.302095>
- Kotadia, I., Whitaker, J., Roney, C., Niederer, S., O’Neill, M., Bishop, M., & Wright, M. (2021). Anisotropic cardiac conduction. *Arrhythmia and Electrophysiology Review*, *9*(4), 202–210. <https://doi.org/10.15420/AER.2020.04>
- Kreutzer, J., Rantanen, K., Välimäki, H., Leikkala, J., Jaakkola, P., & Kallio, P. (2016). Mini-incubator For Prolonged Cell Culture And Hypoxia Studies Outside An Incubator. *Frontiers in Neuroscience*, *10*. <https://doi.org/10.3389/conf.fnins.2016.93.00043>
- Kreutzer, J., Ylä-Outinen, L., Mäki, A. J., Ristola, M., Narkilahti, S., & Kallio, P. (2017). Cell culture chamber with gas supply for prolonged recording of human neuronal cells on microelectrode array. *Journal of Neuroscience Methods*, *280*, 27–35. <https://doi.org/10.1016/j.jneumeth.2017.01.019>
- Kuo, C. Y., Chiu, Y. C., Lee, A. Y. L., & Hwang, T. L. (2015). Mitochondrial Lon protease controls ROS-dependent apoptosis in cardiomyocyte under hypoxia. *Mitochondrion*, *23*, 7–16. <https://doi.org/10.1016/j.mito.2015.04.004>
- Kuznetsov, A. V., Javadov, S., Sickinger, S., Frotschnig, S., & Grimm, M. (2015). H9c2 and HL-1 cells demonstrate distinct features of energy metabolism, mitochondrial function and sensitivity to hypoxia-reoxygenation. *Biochimica et Biophysica Acta (BBA) - Molecular Cell Research*, *1853*(2), 276–284. <https://doi.org/10.1016/j.bbamcr.2014.11.015>
- Kwon, H.-K., Lee, J.-H., Shin, H.-J., Kim, J.-H., & Choi, S. (2015). Structural and functional analysis of cell adhesion and nuclear envelope nano-topography in cell death. *Scientific Reports*, *5*(1), 15623. <https://doi.org/10.1038/srep15623>
- Laflamme, M. A., Chen, K. Y., Naumova, A. V., Muskheli, V., Fugate, J. A., Dupras, S. K., Reinecke, H., Xu, C., Hassanipour, M., Police, S., O’Sullivan, C., Collins, L., Chen, Y., Minami, E., Gill, E. A., Ueno, S., Yuan, C., Gold, J., & Murry, C. E. (2007). Cardiomyocytes derived from human embryonic stem cells in pro-survival factors enhance function of infarcted rat hearts. *Nature Biotechnology*, *25*(9), 1015–1024. <https://doi.org/10.1038/nbt1327>
- Laubriet, A., Fantini, E., Assem, M., Cordelet, C., Teyssier, J. R., Athias, P., & Rochette, L. (2001). Changes in HSP70 and P53 expression are related to the pattern of electromechanical alterations in rat cardiomyocytes during simulated ischemia. *Molecular and Cellular Biochemistry*, *220*(1–2), 77–86. <https://doi.org/10.1023/A:1010832731491>
- Lee, J. H., Protze, S. I., Laksman, Z., Backx, P. H., & Keller, G. M. (2017). Human Pluripotent Stem Cell-Derived Atrial and Ventricular Cardiomyocytes Develop from Distinct Mesoderm Populations. *Cell Stem Cell*, *21*(2), 179–194. <https://doi.org/10.1016/j.stem.2017.07.003>

- Lee, J. W., Ko, J., Ju, C., & Eltzschig, H. K. (2019). Hypoxia signaling in human diseases and therapeutic targets. *Experimental and Molecular Medicine*, *51*(6), 1–13. <https://doi.org/10.1038/s12276-019-0235-1>
- Lerman, D. A., Alotti, N., Ume, K. L., & Péault, B. (2016). Cardiac repair and regeneration: The value of cell therapies. *European Cardiology Review*, *11*(1), 43–48. <https://doi.org/10.15420/ecr.2016:8:1>
- Lewandowski, J., Rozwadowska, N., Kolanowski, T. J., Malcher, A., Zimna, A., Rugowska, A., Fiedorowicz, K., Łabędź, W., Kubaszewski, Ł., Chojnacka, K., Bednarek-Rajewska, K., Majewski, P., & Kurpisz, M. (2018). The impact of in vitro cell culture duration on the maturation of human cardiomyocytes derived from induced pluripotent stem cells of myogenic origin. *Cell Transplantation*, *27*(7), 1047–1067. <https://doi.org/10.1177/0963689718779346>
- Lian, X., Hsiao, C., Wilson, G., Zhu, K., Hazeltine, L. B., Azarin, S. M., Raval, K. K., Zhang, J., Kamp, T. J., & Palecek, S. P. (2012). Robust cardiomyocyte differentiation from human pluripotent stem cells via temporal modulation of canonical Wnt signaling. *Proceedings of the National Academy of Sciences of the United States of America*, *109*(27). <https://doi.org/10.1073/pnas.1200250109>
- Lian, X., Zhang, J., Azarin, S. M., Zhu, K., Hazeltine, L. B., Bao, X., Hsiao, C., Kamp, T. J., & Palecek, S. P. (2013). Directed cardiomyocyte differentiation from human pluripotent stem cells by modulating Wnt/ β -catenin signaling under fully defined conditions. *Nature Protocols*, *8*(1), 162–175. <https://doi.org/10.1038/nprot.2012.150>
- Liao, Y., Zhu, L., & Wang, Y. (2021). Maturation Of Stem Cell-Derived Cardiomyocytes: Foe In Translation Medicine. *International Journal of Stem Cells*, *14*(4), 366–385. <https://doi.org/10.15283/ijsc21077>
- Libby, P., & Theroux, P. (2005). Pathophysiology of coronary artery disease. *Circulation*, *111*(25), 3481–3488. <https://doi.org/10.1161/CIRCULATIONAHA.105.537878>
- Lindsey, M. L., Bolli, R., Canty, J. M., Du, X.-J., Frangogiannis, N. G., Frantz, S., Gourdie, R. G., Holmes, J. W., Jones, S. P., Kloner, R. A., Lefer, D. J., Liao, R., Murphy, E., Ping, P., Przyklenk, K., Recchia, F. A., Schwartz Longacre, L., Ripplinger, C. M., Van Eyk, J. E., & Heusch, G. (2018). Guidelines for experimental models of myocardial ischemia and infarction. *American Journal of Physiology-Heart and Circulatory Physiology*, *314*(4), H812–H838. <https://doi.org/10.1152/ajpheart.00335.2017>
- Lipsett, D. B., Frisk, M., Aronsen, J. M., Nordén, E. S., Buonarati, O. R., Cataliotti, A., Hell, J. W., Sjaastad, I., Christensen, G., & Louch, W. E. (2019). Cardiomyocyte substructure reverts to an immature phenotype during heart failure. *Journal of Physiology*, *597*(7), 1833–1853. <https://doi.org/10.1113/JP277273>
- Liu, H., Bolonduro, O. A., Hu, N., Ju, J., Rao, A. A., Duffy, B. M., Huang, Z., Black, L. D., & Timko, B. P. (2020). Heart-on-a-Chip Model with Integrated Extra- And

- Intracellular Bioelectronics for Monitoring Cardiac Electrophysiology under Acute Hypoxia. *Nano Letters*, 20(4), 2585–2593. <https://doi.org/10.1021/acs.nanolett.0c00076>
- Livak, K. J., & Schmittgen, T. D. (2001). Analysis of relative gene expression data using real-time quantitative PCR and 2- $\Delta\Delta$ CT method. *Methods*, 25, 402–408. <https://doi.org/10.1006/meth.2001.1262>
- Lu, Y., Bu, M., & Yun, H. (2018). Sevoflurane prevents hypoxia/reoxygenation-induced cardiomyocyte apoptosis by inhibiting PI3KC3-mediated autophagy. *Human Cell*, 32(2), 150–159. <https://doi.org/10.1007/s13577-018-00230-4>
- Ludman, A. J., Yellon, D. M., & Hausenloy, D. J. (2010). Cardiac preconditioning for ischaemia: Lost in translation. *Disease Models & Mechanisms*, 3(1–2), 35–38. <https://doi.org/10.1242/dmm.003855>
- Lundy, S. D., Zhu, W. Z., Regnier, M., & Laflamme, M. A. (2013). Structural and functional maturation of cardiomyocytes derived from human pluripotent stem cells. *Stem Cells Dev*, 22(14), 1991–2002. <https://doi.org/10.1089/scd.2012.0490>
- Luo, J., Weaver, M. S., Cao, B., Dennis, J. E., Van Biber, B., Laflamme, M. A., & Allen, M. D. (2014). Cobalt Protoporphyrin Pretreatment Protects Human Embryonic Stem Cell-Derived Cardiomyocytes From Hypoxia/Reoxygenation Injury In Vitro and Increases Graft Size and Vascularization In Vivo. *STEM CELLS Translational Medicine*, 3(6), 734–744. <https://doi.org/10.5966/sctm.2013-0189>
- Mahmoodzadeh, S., & Dworatzek, E. (2019). The role of 17 β -estradiol and estrogen receptors in regulation of Ca²⁺ channels and mitochondrial function in Cardio myocytes. *Frontiers in Endocrinology*, 10, 310. <https://doi.org/10.3389/fendo.2019.00310>
- Mair, J., Lindahl, B., Hammarsten, O., Müller, C., Giannitsis, E., Huber, K., Möckel, M., Plebani, M., Thygesen, K., & Jaffe, A. S. (2018). How is cardiac troponin released from injured myocardium? *European Heart Journal. Acute Cardiovascular Care*, 7(6), 553–560. <https://doi.org/10.1177/2048872617748553>
- Manning, A., & Hearse, D. (1984). Reperfusion-induced arrhythmias: Mechanisms and prevention. *Journal of Molecular and Cellular Cardiology*, 16(6), 497–518. [https://doi.org/10.1016/S0022-2828\(84\)80638-0](https://doi.org/10.1016/S0022-2828(84)80638-0)
- Manring, H. R., Dorn, L. E., Ex-Willey, A., Accornero, F., & Ackermann, M. A. (2018). At the heart of inter- and intracellular signaling: the intercalated disc. *Biophysical Reviews*, 10(4), 961–971. <https://doi.org/10.1007/s12551-018-0430-7>
- Martewicz, S., Serena, E., Zatti, S., Keller, G., & Elvassore, N. (2017). Substrate and mechanotransduction influence SERCA2a localization in human pluripotent stem cell-derived cardiomyocytes affecting functional performance. *Stem Cell Research*, 25, 107–114. <https://doi.org/10.1016/j.scr.2017.10.011>

- Martínez, M. S., García, A., Luzardo, E., Chávez-Castillo, M., Olivar, L. C., Salazar, J., Velasco, M., Quintero, J. J. R., & Bermúdez, V. (2017). Energetic metabolism in cardiomyocytes: molecular basis of heart ischemia and arrhythmogenesis. *Vessel Plus*, *1*(12), 230–241. <https://doi.org/10.20517/2574-1209.2017.34>
- Matta, A., Bouisset, F., Lhermusier, T., Campelo-Parada, F., Elbaz, M., Carrié, D., & Roncalli, J. (2020). Coronary Artery Spasm: New Insights. *Journal of Interventional Cardiology*, *2020*, 5894586. <https://doi.org/10.1155/2020/5894586>
- Mattiazzi, A., Argenziano, M., Aguilar-Sanchez, Y., Mazzocchi, G., & Escobar, A. L. (2015). Ca²⁺ Sparks and Ca²⁺ waves are the subcellular events underlying Ca²⁺ overload during ischemia and reperfusion in perfused intact hearts. *Journal of Molecular and Cellular Cardiology*, *79*, 69–78. <https://doi.org/10.1016/j.yjmcc.2014.10.011>
- McDougal, A. D., & Dewey, C. F. (2017). Modeling oxygen requirements in ischemic cardiomyocytes. *Journal of Biological Chemistry*, *292*(28), 11760–11776. <https://doi.org/10.1074/jbc.M116.751826>
- McQuin, C., Goodman, A., Chernyshev, V., Kamensky, L., Cimini, B. A., Karhohs, K. W., Doan, M., Ding, L., Rafelski, S. M., Thirstrup, D., Wiegraebe, W., Singh, S., Becker, T., Caicedo, J. C., & Carpenter, A. E. (2018). CellProfiler 3.0: Next-generation image processing for biology. *PLoS Biology*, *16*(7), 1–17. <https://doi.org/10.1371/journal.pbio.2005970>
- Ménard, C., Hagège, A. A., Agbulut, O., Barro, M., Morichetti, M. C., Brasselet, C., Bel, A., Messas, E., Bissery, A., Bruneval, P., Desnos, M., Pucéat, M., & Menasché, P. (2005). Transplantation of cardiac-committed mouse embryonic stem cells to infarcted sheep myocardium: a preclinical study. *The Lancet*, *366*(9490), 1005–1012. [https://doi.org/10.1016/S0140-6736\(05\)67380-1](https://doi.org/10.1016/S0140-6736(05)67380-1)
- Metsälä, O., Kreutzer, J., Högel, H., Miikkulainen, P., Kallio, P., & Jaakkola, P. M. (2018). Transportable system enabling multiple irradiation studies under simultaneous hypoxia in vitro. *Radiation Oncology*, *13*(1), 1–11. <https://doi.org/10.1186/s13014-018-1169-9>
- Milani-Nejad, N., & Janssen, P. M. L. (2014). Small and large animal models in cardiac contraction research: Advantages and disadvantages. *Pharmacology and Therapeutics*, *141*(3), 235–249. <https://doi.org/10.1016/j.pharmthera.2013.10.007>
- Mummery, C. L., Ward-van Oostwaard, D., Doevendans, P., Spijker, R., Van den Brink, S., Hassink, R., Van der Heyden, M., Opthof, T., Pera, M., Brutel de la Riviere, A., Passier, R., & Tertoolen, L. (2003). Differentiation of human embryonic stem cells to cardiomyocytes: Role of coculture with visceral endoderm-like cells. *Circulation*, *107*(21), 2733–2740. <https://doi.org/10.1161/01.cir.0000068356.38592.68>
- Mummery, C. L., Zhang, J., Ng, E. S., Elliott, D. A., Elefanty, A. G., & Kamp, T. J. (2012). Differentiation of Human Embryonic Stem Cells and Induced Pluripotent

- Stem Cells to Cardiomyocytes. *Circulation Research*, 111(3), 344–358.
<https://doi.org/10.1161/CIRCRESAHA.110.227512>
- Muto, T., Usuda, H., Yamamura, A., Yoshida, K., Ohashi, A., Mitsui-Saitoh, K., Sakai, J., Sugimoto, Y., Mizutani, H., Nonogaki, T., & Hotta, Y. (2014). Protective effects of fluvoxamine against ischemia/reperfusion injury in isolated, perfused guinea-pig hearts. *Biological and Pharmaceutical Bulletin*, 37(5), 731–739.
<https://doi.org/10.1248/bpb.b13-00552>
- Neary, M. T., Ng, K. E., Ludtmann, M. H. R., Hall, A. R., Piotrowska, I., Ong, S. B., Hausenloy, D. J., Mohun, T. J., Abramov, A. Y., & Breckenridge, R. A. (2014). Hypoxia signaling controls postnatal changes in cardiac mitochondrial morphology and function. *Journal of Molecular and Cellular Cardiology*, 74, 340–352. <https://doi.org/10.1016/j.yjmcc.2014.06.013>
- Nerbonne, J. M., & Kass, R. S. (2005). Molecular physiology of cardiac repolarization. *Physiological Reviews*, 85(4), 1205–1253.
<https://doi.org/10.1152/physrev.00002.2005>
- O'Donnell, A., & Yutzey, K. E. (2020). Mechanisms of heart valve development and disease. *Development*, 147(13). <https://doi.org/10.1242/dev.183020>
- Oh, Y., Cho, G.-S., Li, Z., Hong, I., Zhu, R., Kim, M.-J., Kim, Y. J., Tampakakis, E., Tung, L., Haganir, R., Dong, X., Kwon, C., & Lee, G. (2016). Functional Coupling with Cardiac Muscle Promotes Maturation of hPSC-Derived Sympathetic Neurons. *Cell Stem Cell*, 19(1), 95–106.
<https://doi.org/10.1016/j.stem.2016.05.002>
- Oiwa, K., Shimba, K., Numata, T., Takeuchi, A., Kotani, K., & Jimbo, Y. (2016). A device for co-culturing autonomic neurons and cardiomyocytes using micro-fabrication techniques. *Integrative Biology (United Kingdom)*, 8(3), 341–348.
<https://doi.org/10.1039/c5ib00273g>
- Ojala, M., Prajapati, C., Pölönen, R.-P., Rajala, K., Pekkanen-Mattila, M., Rasku, J., Larsson, K., & Aalto-Setälä, K. (2016). Mutation-Specific Phenotypes in hiPSC-Derived Cardiomyocytes Carrying Either Myosin-Binding Protein C Or α -Tropomyosin Mutation for Hypertrophic Cardiomyopathy. *Stem Cells International*, 2016, 1–16. <https://doi.org/10.1155/2016/1684792>
- Ojala, M., Rajala, K., Pekkanen-Mattila, M., Miettinen, M., Huhtala, H., & Aalto-Setälä, K. (2012). Culture Conditions Affect Cardiac Differentiation Potential of Human Pluripotent Stem Cells. *PLoS ONE*, 7(10), e48659.
<https://doi.org/10.1371/journal.pone.0048659>
- Padala, S. K., Cabrera, J. A., & Ellenbogen, K. A. (2021). Anatomy of the cardiac conduction system. *PACE - Pacing and Clinical Electrophysiology*, 44(1), 15–25.
<https://doi.org/10.1111/pace.14107>
- Parameswaran, S., Kumar, S., Verma, R. S., & Sharma, R. K. (2013). Cardiomyocyte culture - an update on the in vitro cardiovascular model and future challenges.

Canadian Journal of Physiology and Pharmacology, 91(12), 985–998.
<https://doi.org/10.1139/cjpp-2013-0161>

- Parrag, I. C., Zandstra, P. W., & Woodhouse, K. A. (2012). Fiber alignment and coculture with fibroblasts improves the differentiated phenotype of murine embryonic stem cell-derived cardiomyocytes for cardiac tissue engineering. *Biotechnology and Bioengineering*, 109(3), 813–822. <https://doi.org/10.1002/bit.23353>
- Patten, R. D., & Hall-Porter, M. R. (2009). Small animal models of heart failure development of novel therapies, past and present. *Circulation: Heart Failure*, 2(2), 138–144. <https://doi.org/10.1161/CIRCHEARTFAILURE.108.839761>
- Pelliccia, F., Kaski, J. C., Crea, F., & Camici, P. G. (2017). Pathophysiology of Takotsubo Syndrome. *Circulation*, 135(24), 2426–2441. <https://doi.org/10.1161/CIRCULATIONAHA.116.027121>
- Pennella, S., Bonetti, L. R., Migaldi, M., Manenti, A., Lonardi, R., Giuliani, E., Barbieri, A., Farinetti, A., & Mattioli, A. V. (2017). Does stem cell therapy induce myocardial neoangiogenesis? Histological evaluation in an ischemia/reperfusion animal model. *Journal of Cardiovascular Medicine*, 18(4), 277–282. <https://doi.org/10.2459/JCM.0000000000000357>
- Petkovic, A. M., Jakovljevic, V. L., Bradic, J. V., Jeremic, J. N., Jeremic, N. S., Nikolic Turnic, T. R., Jovicic, N. U., Rosic, V. Z., Srejovic, I. M., & Zivkovic, V. I. (2018). The Effects of Potassium Cyanide on the Functional Recovery of Isolated Rat Hearts after Ischemia and Reperfusion: The Role of Oxidative Stress. *Oxidative Medicine and Cellular Longevity*, 2018, 5979721. <https://doi.org/10.1155/2018/5979721>
- Phillips, K. A., Bales, K. L., Capitanio, J. P., Conley, A., Czoty, P. W., 't Hart, B. A., Hopkins, W. D., Hu, S.-L., Miller, L. A., Nader, M. A., Nathanielsz, P. W., Rogers, J., Shively, C. A., & Voytko, M. Lou. (2014). Why primate models matter. *American Journal of Primatology*, 76(9), 801–827. <https://doi.org/10.1002/ajp.22281>
- Pölonen, R. P., Penttinen, K., Swan, H., & Aalto-Setälä, K. (2018). Antiarrhythmic Effects of Carvedilol and Flecainide in Cardiomyocytes Derived from Catecholaminergic Polymorphic Ventricular Tachycardia Patients. *Stem Cells International*, 2018, 9109503. <https://doi.org/10.1155/2018/9109503>
- Prajapati, C., Ojala, M., & Aalto-Setälä, K. (2018). Divergent effects of adrenaline in human induced pluripotent stem cell-derived cardiomyocytes obtained from hypertrophic cardiomyopathy. *Disease Models & Mechanisms*, 11(2). <https://doi.org/10.1242/DMM.032896>
- Prajapati, C., Ojala, M., Lappi, H., Aalto-Setälä, K., & Pekkanen-Mattila, M. (2021). Electrophysiological evaluation of human induced pluripotent stem cell-derived cardiomyocytes obtained by different methods. *Stem Cell Research*, 51(September 2020). <https://doi.org/10.1016/j.scr.2021.102176>

- Qiao, X., Jia, S., Ye, J., Fang, X., Zhang, C., Cao, Y., Xu, C., Zhao, L., Zhu, Y., Wang, L., & Zheng, M. (2017). PTPIP51 regulates mouse cardiac ischemia/reperfusion through mediating the mitochondria-SR junction. *Scientific Reports*, 7(1), 45379. <https://doi.org/10.1038/srep45379>
- Quevedo, H. C., Hatzistergos, K. E., Oskouei, B. N., Feigenbaum, G. S., Rodriguez, J. E., Valdes, D., Pattany, P. M., Zambrano, J. P., Hu, Q., McNiece, I., Heldman, A. W., & Hare, J. M. (2009). Allogeneic mesenchymal stem cells restore cardiac function in chronic ischemic cardiomyopathy via trilineage differentiating capacity. *Proceedings of the National Academy of Sciences of the United States of America*, 106(33), 14022–14027. <https://doi.org/10.1073/pnas.0903201106>
- Quijada, P., Trembley, M. A., & Small, E. M. (2020). The Role of the Epicardium During Heart Development and Repair. *Circulation Research*, 126(3), 377–394. <https://doi.org/10.1161/CIRCRESAHA.119.315857>
- Rajan, D. K., Kreutzer, J., Välimäki, H., Pekkanen-Mattila, M., Ahola, A., Skogberg, A., Aalto-Setälä, K., Ihalainen, H., Kallio, P., & Leikkala, J. (2018). A portable live-cell imaging system with an invert-upright-convertible architecture and a mini-bioreactor for long-term simultaneous cell imaging, chemical sensing, and electrophysiological recording. *IEEE Access*, 6, 11063–11075. <https://doi.org/10.1109/ACCESS.2018.2804378>
- Rao, C., Prodromakis, T., Kolker, L., Chaudhry, U. A. R., Trantidou, T., Sridhar, A., Weekes, C., Camelliti, P., Harding, S. E., Darzi, A., Yacoub, M. H., Athanasiou, T., & Terracciano, C. M. (2013). The effect of microgrooved culture substrates on calcium cycling of cardiac myocytes derived from human induced pluripotent stem cells. *Biomaterials*, 34(10), 2399–2411. <https://doi.org/10.1016/j.biomaterials.2012.11.055>
- Richard Conti, C. (1991). The stunned and hibernating myocardium: A brief review. *Clinical Cardiology*, 14(9), 708–712. <https://doi.org/10.1002/clc.4960140903>
- Ristola, M., Fedele, C., Hagman, S., Sukki, L., Kapucu, F. E., Mzezewa, R., Hyvärinen, T., Kallio, P., Priimagi, A., & Narkilahti, S. (2021). Directional Growth of Human Neuronal Axons in a Microfluidic Device with Nanotopography on Azobenzene-Based Material. *Advanced Materials Interfaces*, 8(11), 16–19. <https://doi.org/10.1002/admi.202100048>
- Ristola, M., Sukki, L., Azevedo, M. M., Seixas, A. I., Relvas, J. B., Narkilahti, S., & Kallio, P. (2019). A compartmentalized neuron-oligodendrocyte co-culture device for myelin research: Design, fabrication and functionality testing. *Journal of Micromechanics and Microengineering*, 29(6), 065009. <https://doi.org/10.1088/1361-6439/ab16a7>
- Robertson-Gray, O. J., Walsh, S. K., Ryberg, E., Jönsson-Rylander, A. C., Lipina, C., & Wainwright, C. L. (2019). 1- α -Lysophosphatidylinositol (LPI) aggravates myocardial ischemia/reperfusion injury via a GPR55/ROCK-dependent pathway.

- Robertson, C., Tran, D. D., & George, S. C. (2013). Concise review: maturation phases of human pluripotent stem cell-derived cardiomyocytes. *Stem Cells*, 31(5), 829–837. <https://doi.org/10.1002/stem.1331>
- Ronkainen, V. P., Skoumal, R., & Tavi, P. (2011). Hypoxia and HIF-1 suppress SERCA2a expression in embryonic cardiac myocytes through two interdependent hypoxia response elements. *Journal of Molecular and Cellular Cardiology*, 50(6), 1008–1016. <https://doi.org/10.1016/j.yjmcc.2011.02.017>
- Rosano, G., Fini, M., Caminiti, G., & Barbaro, G. (2008). Cardiac Metabolism in Myocardial Ischemia. *Current Pharmaceutical Design*, 14(25), 2551–2562. <https://doi.org/10.2174/138161208786071317>
- Ruan, J. L., Tulloch, N. L., Razumova, M. V., Saiget, M., Muskheli, V., Pabon, L., Reinecke, H., Regnier, M., & Murry, C. E. (2016). Mechanical Stress Conditioning and Electrical Stimulation Promote Contractility and Force Maturation of Induced Pluripotent Stem Cell-Derived Human Cardiac Tissue. *Circulation*, 134(20), 1557–1567. <https://doi.org/10.1161/CIRCULATIONAHA.114.014998>
- Sakai, K., Shimba, K., Ishizuka, K., Yang, Z., Oiwa, K., Takeuchi, A., Kotani, K., & Jimbo, Y. (2017). Functional innervation of human induced pluripotent stem cell-derived cardiomyocytes by co-culture with sympathetic neurons developed using a microtunnel technique. *Biochemical and Biophysical Research Communications*, 494(1–2), 138–143. <https://doi.org/10.1016/j.bbrc.2017.10.065>
- Sala, L., Van Meer, B. J., Tertoolen, L. G. J., Bakkers, J., Bellin, M., Davis, R. P., Denning, C., Dieben, M. A. E., Eschenhagen, T., Giacomelli, E., Grandela, C., Hansen, A., Holman, E. R., Jongbloed, M. R. M., Kamel, S. M., Koopman, C. D., Lachaud, Q., Mannhardt, I., Mol, M. P. H., ... Mummery, C. L. (2018). Musclemotion: A versatile open software tool to quantify cardiomyocyte and cardiac muscle contraction in vitro and in vivo. *Circulation Research*, 122(3), e5–e16. <https://doi.org/10.1161/CIRCRESAHA.117.312067>
- Salameh, A., Schuster, R., Dähnert, I., Seeger, J., & Dhein, S. (2018). Epigallocatechin gallate reduces ischemia/reperfusion injury in isolated perfused rabbit hearts. *International Journal of Molecular Sciences*, 19(2). <https://doi.org/10.3390/ijms19020628>
- Sanada, S., Komuro, I., & Kitakaze, M. (2011). Pathophysiology of myocardial reperfusion injury: Preconditioning, postconditioning, and translational aspects of protective measures. *American Journal of Physiology - Heart and Circulatory Physiology*, 301(5), 5–7. <https://doi.org/10.1152/ajpheart.00553.2011>

- Santiago, C. F., Huttner, I. G., & Fatkin, D. (2021). Mechanisms of TTNtv-related dilated cardiomyopathy: Insights from zebrafish models. *Journal of Cardiovascular Development and Disease*, *8*(2), 1–18. <https://doi.org/10.3390/jcdd8020010>
- Sarantitis, I., Papanastasopoulos, P., Manousi, M., Baikoussis, N. G., & Apostolakis, E. (2012). The cytoskeleton of the cardiac muscle cell. *Hellenic Journal of Cardiology*, *53*(5), 367–379.
- Schindelin, J., Arganda-Carreras, I., Frise, E., Kaynig, V., Longair, M., Pietzsch, T., Preibisch, S., Rueden, C., Saalfeld, S., Schmid, B., Tinevez, J. Y., White, D. J., Hartenstein, V., Eliceiri, K., Tomancak, P., & Cardona, A. (2012). Fiji: An open-source platform for biological-image analysis. *Nature Methods*, *9*(7), 676–682. <https://doi.org/10.1038/nmeth.2019>
- Sebastião, M. J., Gomes-Alves, P., Reis, I., Sanchez, B., Palacios, I., Serra, M., & Alves, P. M. (2020). Bioreactor-based 3D human myocardial ischemia/reperfusion in vitro model: a novel tool to unveil key paracrine factors upon acute myocardial infarction. *Translational Research*, *215*, 57–74. <https://doi.org/10.1016/j.trsl.2019.09.001>
- Sebastião, M. J., Serra, M., Pereira, R., Palacios, I., Gomes-Alves, P., & Alves, P. M. (2019). Human cardiac progenitor cell activation and regeneration mechanisms: Exploring a novel myocardial ischemia/reperfusion in vitro model. *Stem Cell Research and Therapy*, *10*(1), 1–16. <https://doi.org/10.1186/s13287-019-1174-4>
- Seiler, C., Stoller, M., Pitt, B., & Meier, P. (2013). The human coronary collateral circulation: Development and clinical importance. *European Heart Journal*, *34*(34), 2674–2682. <https://doi.org/10.1093/eurheartj/ehh195>
- Semenza, G. L. (2012). Hypoxia-Inducible Factors in Physiology and Medicine. *Cell*, *148*(3), 399–408. <https://doi.org/10.1016/j.cell.2012.01.021>
- Shah, D., Virtanen, L., Prajapati, C., Kiamehr, M., Gullmets, J., West, G., Kreutzer, J., Pekkanen-Mattila, M., Heliö, T., Kallio, P., Taimen, P., & Aalto-Setälä, K. (2019). Modeling of LMNA-Related Dilated Cardiomyopathy Using Human Induced Pluripotent Stem Cells. *Cells*, *8*(6), 594. <https://doi.org/10.3390/cells8060594>
- Sharma, A., Li, G., Rajarajan, K., Hamaguchi, R., Burridge, P. W., & Wu, S. M. (2015). Derivation of highly purified cardiomyocytes from human induced pluripotent stem cells using small molecule-modulated differentiation and subsequent glucose starvation. *Journal of Visualized Experiments: JoVE*, *97*. <https://doi.org/10.3791/52628>
- Shattock, M. J., Ottolia, M., Bers, D. M., Blaustein, M. P., Boguslavskyi, A., Bossuyt, J., Bridge, J. H. B., Chen-Izu, Y., Clancy, C. E., Edwards, A., Goldhaber, J., Kaplan, J., Lingrel, J. B., Pavlovic, D., Philipson, K., Sipido, K. R., & Xie, Z. J. (2015). Na⁺/Ca²⁺ exchange and Na⁺/K⁺-ATPase in the heart. *Journal of Physiology*, *593*(6), 1361–1382. <https://doi.org/10.1113/jphysiol.2014.282319>

- Silver, S. E., Barrs, R. W., & Mei, Y. (2021). Transplantation of Human Pluripotent Stem Cell-Derived Cardiomyocytes for Cardiac Regenerative Therapy. *Frontiers in Cardiovascular Medicine*, 8. <https://doi.org/10.3389/fcvm.2021.707890>
- Skrzypiec-Spring, M., Grotthus, B., Szelag, A., & Schulz, R. (2007). Isolated heart perfusion according to Langendorff-Still viable in the new millennium. *Journal of Pharmacological and Toxicological Methods*, 55(2), 113–126. <https://doi.org/10.1016/j.vascn.2006.05.006>
- Smit, N. W., & Coronel, R. (2014). Stem cells can form gap junctions with cardiac myocytes and exert pro-arrhythmic effects. *Frontiers in Physiology*, 5, 419. <https://doi.org/10.3389/fphys.2014.00419>
- Smith, A. S. T., Macadangang, J., Leung, W., Laflamme, M. A., & Kim, D. H. (2017). Human iPSC-derived cardiomyocytes and tissue engineering strategies for disease modeling and drug screening. *Biotechnology Advances*, 35(1), 77–94. <https://doi.org/10.1016/j.biotechadv.2016.12.002>
- Smith, S. B., Xu, Z., Novitskaya, T., Zhang, B., Chepurko, E., Pu, X. A., Wheeler, D. G., Ziolo, M., & Gumina, R. J. (2017). Impact of cardiac-specific expression of CD39 on myocardial infarct size in mice. *Life Sciences*, 179, 54–59. <https://doi.org/10.1016/j.lfs.2016.10.016>
- Stecyk, J. A. W., Galli, G. L., Shiels, H. A., & Farrell, A. P. (2008). Cardiac survival in anoxia-tolerant vertebrates: An electrophysiological perspective. *Comparative Biochemistry and Physiology - C Toxicology and Pharmacology*, 148(4), 339–354. <https://doi.org/10.1016/j.cbpc.2008.05.016>
- Takahashi, K., Tanabe, K., Ohnuki, M., Narita, M., Ichisaka, T., Tomoda, K., & Yamanaka, S. (2007). Induction of Pluripotent Stem Cells from Adult Human Fibroblasts by Defined Factors. *Cell*, 131(5), 861–872. <https://doi.org/10.1016/j.cell.2007.11.019>
- Takahashi, K., & Yamanaka, S. (2006). Induction of Pluripotent Stem Cells from Mouse Embryonic and Adult Fibroblast Cultures by Defined Factors. *Cell*, 126(4), 663–676. <https://doi.org/10.1016/j.cell.2006.07.024>
- Takayama, Y., & Kida, Y. S. (2016). In vitro reconstruction of neuronal networks derived from human iPSC cells using microfabricated devices. *PLoS ONE*, 11(2), 1–15. <https://doi.org/10.1371/journal.pone.0148559>
- Takayama, Y., Kushige, H., Akagi, Y., Suzuki, Y., Kumagai, Y., & Kida, Y. S. (2020). Selective Induction of Human Autonomic Neurons Enables Precise Control of Cardiomyocyte Beating. *Scientific Reports*, 10(1), 1–13. <https://doi.org/10.1038/s41598-020-66303-3>
- Takeuchi, A., Nakafutami, S., Tani, H., Mori, M., Takayama, Y., Moriguchi, H., Kotani, K., Miwa, K., Lee, J. K., Noshiro, M., & Jimbo, Y. (2011). Device for co-culture of sympathetic neurons and cardiomyocytes using microfabrication. *Lab on a Chip*, 11(13), 2268–2275. <https://doi.org/10.1039/c0lc00327a>

- Talkhabi, M., Aghdami, N., & Baharvand, H. (2016). Human cardiomyocyte generation from pluripotent stem cells: A state-of-art. *Life Sciences*, *145*, 98–113. <https://doi.org/10.1016/j.lfs.2015.12.023>
- Tanimoto, T., Parseghian, M. H., Nakahara, T., Kawai, H., Narula, N., Kim, D., Nishimura, R., Weisbart, R. H., Chan, G., Richieri, R. A., Haider, N., Chaudhry, F., Reynolds, G. T., Billimek, J., Blankenberg, F. G., Sengupta, P. P., Petrov, A. D., Akasaka, T., Strauss, H. W., & Narula, J. (2017). Cardioprotective Effects of HSP72 Administration on Ischemia-Reperfusion Injury. *Journal of the American College of Cardiology*, *70*(12), 1479–1492. <https://doi.org/10.1016/j.jacc.2017.07.762>
- Tapa, S., Wang, L., Francis Stuart, S. D., Wang, Z., Jiang, Y., Habecker, B. A., & Ripplinger, C. M. (2020). Adrenergic supersensitivity and impaired neural control of cardiac electrophysiology following regional cardiac sympathetic nerve loss. *Scientific Reports*, *10*(1), 1–12. <https://doi.org/10.1038/s41598-020-75903-y>
- Tennant, D., & Howell, N. J. (2014). The role of HIFs in ischemia-reperfusion injury. *Hypoxia*, *2*, 107–115. <https://doi.org/10.2147/HP.S49720>
- Tertoolen, L. G. J., Braam, S. R., van Meer, B. J., Passier, R., & Mummery, C. L. (2018). Interpretation of field potentials measured on a multi electrode array in pharmacological toxicity screening on primary and human pluripotent stem cell-derived cardiomyocytes. *Biochemical and Biophysical Research Communications*, *497*(4), 1135–1141. <https://doi.org/10.1016/j.bbrc.2017.01.151>
- Tong, W., Xiong, F., Li, Y., & Zhang, L. (2013). Hypoxia inhibits cardiomyocyte proliferation in fetal rat hearts via upregulating TIMP-4. *American Journal of Physiology - Regulatory Integrative and Comparative Physiology*, *304*(8), 613–620. <https://doi.org/10.1152/ajpregu.00515.2012>
- Turer, A. T., & Hill, J. A. (2010). Pathogenesis of Myocardial Ischemia-Reperfusion Injury and Rationale for Therapy. *The American Journal of Cardiology*, *106*(3), 360–368. <https://doi.org/10.1016/j.amjcard.2010.03.032>
- Tyrankiewicz, U., Skorka, T., Orzylowska, A., Jablonska, M., Jasinski, K., Jaształ, A., Bar, A., Kostogrys, R., & Chlopicki, S. (2016). Comprehensive MRI for the detection of subtle alterations in diastolic cardiac function in apoE/LDLR^{-/-} mice with advanced atherosclerosis. *NMR in Biomedicine*, *29*(6), 833–840. <https://doi.org/10.1002/nbm.3524>
- Ulmer, B. M., & Eschenhagen, T. (2020). Human pluripotent stem cell-derived cardiomyocytes for studying energy metabolism. *Biochimica et Biophysica Acta - Molecular Cell Research*, *1867*(3), 118471. <https://doi.org/10.1016/j.bbamcr.2019.04.001>
- Välimäki, H., Hyvärinen, T., Leivo, J., Iftikhar, H., Pekkanen-Mattila, M., Rajan, D. K., Verho, J., Kreutzer, J., Ryyänen, T., Pirhonen, J., Aalto-Setälä, K., Kallio, P., Narkilahti, S., & Lekkala, J. (2020). Covalent immobilization of luminescent

- oxygen indicators reduces cytotoxicity. *Biomedical Microdevices*, 22(41).
<https://doi.org/10.1007/s10544-020-00495-3>
- Välimäki, H., Verho, J., Kreutzer, J., Kattippambil Rajan, D., Ryyänen, T., Pekkanen-Mattila, M., Ahola, A., Tappura, K., Kallio, P., & Lekkala, J. (2017). Fluorimetric oxygen sensor with an efficient optical read-out for in vitro cell models. *Sensors and Actuators, B: Chemical*, 249, 738–746.
<https://doi.org/10.1016/j.snb.2017.04.182>
- van Bilsen, M., Patel, H. C., Bauersachs, J., Böhm, M., Borggrefe, M., Brutsaert, D., Coats, A. J. S., de Boer, R. A., de Keulenaer, G. W., Filippatos, G. S., Floras, J., Grassi, G., Jankowska, E. A., Kornet, L., Lunde, I. G., Maack, C., Mahfoud, F., Pollesello, P., Ponikowski, P., ... Lyon, A. R. (2017). The autonomic nervous system as a therapeutic target in heart failure: a scientific position statement from the Translational Research Committee of the Heart Failure Association of the European Society of Cardiology. *European Journal of Heart Failure*, 19(11), 1361–1378. <https://doi.org/10.1002/ejhf.921>
- van den Berg, C. W., Okawa, S., Chuva de Sousa Lopes, S. M., van Iperen, L., Passier, R., Braam, S. R., Tertoolen, L. G., del Sol, A., Davis, R. P., & Mummery, C. L. (2015). Transcriptome of human foetal heart compared with cardiomyocytes from pluripotent stem cells. *Development*, 142(18), 3231–3238.
<https://doi.org/10.1242/dev.123810>
- van der Sanden, B., Dhobb, M., Berger, F., & Wion, D. (2010). Optimizing stem cell culture. *Journal of Cellular Biochemistry*, 111(4), 801–807.
<https://doi.org/10.1002/jcb.22847>
- van der Weg, K., Prinzen, F. W., & Gorgels, A. P. (2019). Editor's Choice- Reperfusion cardiac arrhythmias and their relation to reperfusion-induced cell death. *European Heart Journal: Acute Cardiovascular Care*, 8(2), 142–152.
<https://doi.org/10.1177/2048872618812148>
- Veerman, C. C., Kosmidis, G., Mummery, C. L., Casini, S., Verkerk, A. O., & Bellin, M. (2015). Immaturity of Human Stem-Cell-Derived Cardiomyocytes in Culture: Fatal Flaw or Soluble Problem? *Stem Cells and Development*, 24(9), 1035–1052.
<https://doi.org/10.1089/scd.2014.0533>
- Végh, A., Duim, S., Smits, A., Poelmann, R., ten Harkel, A., DeRuiter, M., Goumans, M., & Jongbloed, M. (2016). Part and Parcel of the Cardiac Autonomic Nerve System: Unravelling Its Cellular Building Blocks during Development. *Journal of Cardiovascular Development and Disease*, 3(3), 28.
<https://doi.org/10.3390/jcdd3030028>
- Veldhuizen, J., Chavan, R., Moghadas, B., Park, J. G., Kodibagkar, V. D., Migrino, R. Q., & Nikkhah, M. (2022). Cardiac ischemia on-a-chip to investigate cellular and molecular response of myocardial tissue under hypoxia. *Biomaterials*, 281, 121336. <https://doi.org/10.1016/j.biomaterials.2021.121336>

- Verdouw, P. D., Van Den Doel, M. A., De Zeeuw, S., & Duncker, D. J. (1998). Animal models in the study of myocardial ischaemia and ischaemic syndromes. *Cardiovascular Research*, *39*(1), 121–135. [https://doi.org/10.1016/S0008-6363\(98\)00069-8](https://doi.org/10.1016/S0008-6363(98)00069-8)
- Vuorenpää, H., Kirsi, P., Tuula, H., Mari, P.-M., Jertta-Riina, S., Timo, Y., Katriina, A.-S., Vuorenpää, H., Heinonen, Á. T., Ylikomi, Á. T., Heinonen, T., Ylikomi, T., Penttinen, K., Pekkanen-Mattila, Á. M., Aalto-Setälä, Á. K., Sarkanen, J.-R., & Aalto-Setälä, K. (2017). Maturation of human pluripotent stem cell derived cardiomyocytes is improved in cardiovascular construct. *Cytotechnology*, *69*, 785–800. <https://doi.org/10.1007/s10616-017-0088-1>
- Wang, R., Wang, M., He, S., Sun, G., & Sun, X. (2020). Targeting Calcium Homeostasis in Myocardial Ischemia/Reperfusion Injury: An Overview of Regulatory Mechanisms and Therapeutic Reagents. *Frontiers in Pharmacology*, *11*, 872. <https://doi.org/10.3389/fphar.2020.00872>
- Wanjare, M., Hou, L., Nakayama, K. H., Kim, J. J., Mezak, N. P., Abilez, O. J., Tzatzalos, E., Wu, J. C., & Huang, N. F. (2017). Anisotropic microfibrous scaffolds enhance the organization and function of cardiomyocytes derived from induced pluripotent stem cells. *Biomaterials Science*, *5*(8), 1567–1578. <https://doi.org/10.1039/C7BM00323D>
- Ward, M. C., & Gilad, Y. (2019). A generally conserved response to hypoxia in iPSC-derived cardiomyocytes from humans and chimpanzees. *eLife*, *8*, 1–32. <https://doi.org/10.7554/eLife.42374>
- Wei, H., Wang, C., Guo, R., Takahashi, K., & Naruse, K. (2019). Development of a model of ischemic heart disease using cardiomyocytes differentiated from human induced pluripotent stem cells. *Biochemical and Biophysical Research Communications*, *520*(3), 600–605. <https://doi.org/10.1016/j.bbrc.2019.09.119>
- Wei, J., Xu, H., Shi, L., Tong, J., & Zhang, J. (2015). Trimetazidine protects cardiomyocytes against hypoxia-induced injury through ameliorates calcium homeostasis. *Chemico-Biological Interactions*, *236*, 47–56. <https://doi.org/10.1016/j.cbi.2015.04.022>
- Wei, W., Liu, Y., Zhang, Q., Wang, Y., Zhang, X., & Zhang, H. (2017). Danshen-Enhanced Cardioprotective Effect of Cardioplegia on Ischemia Reperfusion Injury in a Human-Induced Pluripotent Stem Cell-Derived Cardiomyocytes Model. *Artificial Organs*, *41*(5), 452–460. <https://doi.org/10.1111/aor.12801>
- Weinhaus, A. J., & Roberts, K. P. (2009). Anatomy of the Human Heart. In *Handbook of Cardiac Anatomy, Physiology, and Devices* (pp. 59–85). Humana Press. https://doi.org/10.1007/978-1-60327-372-5_5
- Wenzel, F., Dittrich, M., Hescheler, J., & Grote, J. (2002). Hypoxia influences generation and propagation of electrical activity in embryonic cardiomyocyte clusters.

- Williams, A. L., Khadka, V., Tang, M., Avelar, A., Schunke, K. J., Menor, M., & Shohet, R. V. (2018). HIF1 mediates a switch in pyruvate kinase isoforms after myocardial infarction. *Physiological Genomics*, 50(7), 479–494. <https://doi.org/10.1152/physiolgenomics.00130.2017>
- Winbo, A., Ramanan, S., Eugster, E., Jovinge, S., Skinner, J. R., & Montgomery, J. M. (2020). Functional coculture of sympathetic neurons and cardiomyocytes derived from human-induced pluripotent stem cells. *American Journal of Physiology - Heart and Circulatory Physiology*, 319(5), H927–H937. <https://doi.org/10.1152/AJPHEART.00546.2020>
- Wu, M. Y., Yiang, G. T., Liao, W. T., Tsai, A. P. Y., Cheng, Y. L., Cheng, P. W., Li, C. Y., & Li, C. J. (2018). Current Mechanistic Concepts in Ischemia and Reperfusion Injury. *Cellular Physiology and Biochemistry*, 46(4), 1650–1667. <https://doi.org/10.1159/000489241>
- Yang, X., Pabon, L., & Murry, C. E. (2014). Engineering adolescence: Maturation of human pluripotent stem cell-derived cardiomyocytes. *Circulation Research*, 114(3), 511–523. <https://doi.org/10.1161/CIRCRESAHA.114.300558>
- Yang, X., Rodriguez, M., Pabon, L., Fischer, K. A., Reinecke, H., Regnier, M., Sniadecki, N. J., Ruohola-Baker, H., & Murry, C. E. (2014). Tri-iodo-L-thyronine promotes the maturation of human cardiomyocytes-derived from induced pluripotent stem cells. *Journal of Molecular and Cellular Cardiology*, 72(1), 296–304. <https://doi.org/10.1016/j.yjmcc.2014.04.005>
- Yin, P. T., Han, E., & Lee, K. B. (2016). Engineering Stem Cells for Biomedical Applications. *Advanced Healthcare Materials*, 5(1), 10–55. <https://doi.org/10.1002/adhm.201400842>
- Yoshida, Y., & Yamanaka, S. (2017). Induced Pluripotent Stem Cells 10 Years Later. *Circulation Research*, 120(12), 1958–1968. <https://doi.org/10.1161/CIRCRESAHA.117.311080>
- Ytrehus, K. (2006). Cardiovascular diseases Models of myocardial ischemia. *Drug Discovery Today: Disease Models*, 3(3), 263–271. <https://doi.org/10.1016/j.ddmod.2006.10.013>
- Yu, J., Lu, Y., Li, Y., Xiao, L., Xing, Y., Li, Y., & Wu, L. (2015). Role of S100A1 in hypoxia-induced inflammatory response in cardiomyocytes via TLR4/ROS/NF- κ B pathway. *Journal of Pharmacy and Pharmacology*, 67(9), 1240–1250. <https://doi.org/10.1111/jphp.12415>
- Zhang, Q., Jiang, J., Han, P., Yuan, Q., Zhang, J., Zhang, X., Xu, Y., Cao, H., Meng, Q., Chen, L., Tian, T., Wang, X., Li, P., Hescheler, J., Ji, G., & Ma, Y. (2011). Direct differentiation of atrial and ventricular myocytes from human embryonic stem

cells by alternating retinoid signals. *Cell Research*, 21(4), 579–587. <https://doi.org/10.1038/cr.2010.163>

- Zhang, X.-L., Pang, W., Hu, X.-T., Li, J.-L., Yao, Y.-G., & Zheng, Y.-T. (2014). Experimental primates and non-human primate (NHP) models of human diseases in China: current status and progress. *Dong Wu Xue Yan Jiu = Zoological Research*, 35(6), 447–464. <https://doi.org/10.13918/j.issn.2095-8137.2014.6.447>
- Zhao, X., Chen, H., Xiao, D., Yang, H., Itzhaki, I., Qin, X., Chour, T., Aguirre, A., Lehmann, K., Kim, Y., Shukla, P., Holmström, A., Zhang, J. Z., Zhuge, Y., Ndoye, B. C., Zhao, M., Neofytou, E., Zimmermann, W. H., Jain, M., & Wu, J. C. (2018). Comparison of Non-human Primate versus Human Induced Pluripotent Stem Cell-Derived Cardiomyocytes for Treatment of Myocardial Infarction. *Stem Cell Reports*, 10(2), 422–435. <https://doi.org/10.1016/j.stemcr.2018.01.002>
- Zheng, J., Chen, P., Zhong, J., Cheng, Y., Chen, H., He, Y., & Chen, C. (2021). HIF-1 α in myocardial ischemia-reperfusion injury (Review). *Molecular Medicine Reports*, 23(5), 1–9. <https://doi.org/10.3892/mmr.2021.11991>

PUBLICATION

I

Polyethylene terephthalate textiles enhance the structural maturation of human induced pluripotent stem cell-derived cardiomyocytes

Mari Pekkanen-Mattila, Martta Häkli, Risto-Pekka Pölönen, Tuomas Mansikkala, Anni Junnila, Elina Talvitie, Janne T. Koivisto, Minna Kellomäki and Katriina Aalto-Setälä




Materials (2019), 12(11): 1805
<https://doi.org/10.3390/ma12111805>

Publication reprinted with the permission of the copyright holders.



Article

Polyethylene Terephthalate Textiles Enhance the Structural Maturation of Human Induced Pluripotent Stem Cell-Derived Cardiomyocytes

Mari Pekkanen-Mattila ^{1,*}, Martta Häkli ¹, Risto-Pekka Pölönen ¹, Tuomas Mansikkala ¹ ,
Anni Junnila ¹, Elina Talvitie ¹, Janne T Koivisto ² , Minna Kellomäki ¹ 
and Katriina Aalto-Setälä ³

¹ BioMediTech, Faculty of Medicine and Health Technology, Tampere University, 33140 Tampere, Finland; martta.hakli@tuni.fi (M.H.); risto-pekka.polonen@tuni.fi (R.-P.P.); leo.mansikkala@oulu.fi (T.M.); junnila.anni@gmail.com (A.J.); elina.t.talvitie@gmail.com (E.T.); minna.kellomaki@tuni.fi (M.K.)

² Microelectronics Research Unit, University of Oulu, FI-90014 Oulu, Finland; janne.koivisto@oulu.fi

³ Finland and Heart Hospital, Tampere University Hospital, 33100 Tampere, Finland; katriina.aalto-setala@tuni.fi

* Correspondence: mari.pekkanen-mattila@tuni.fi; Tel.: +358-50-4377153

Received: 15 May 2019; Accepted: 30 May 2019; Published: 3 June 2019



Abstract: Human-induced pluripotent stem cell-derived cardiomyocytes (hiPSC-CMs) have the potential to serve as a model for human cardiomyocytes. However, hiPSC-CMs are still considered immature. CMs differentiated from hiPSCs more resemble fetal than adult cardiomyocytes. Putative factors enhancing maturation include in vitro culture duration, culture surface topography, and mechanical, chemical, and electrical stimulation. Stem cell-derived cardiomyocytes are traditionally cultured on glass surfaces coated with extracellular matrix derivatives such as gelatin. hiPSC-CMs are flat and round and their sarcomeres are randomly distributed and unorganized. Morphology can be enhanced by culturing cells on surfaces providing topographical cues to the cells. In this study, a textile based-culturing method used to enhance the maturation status of hiPSC-CMs is presented. Gelatin-coated polyethylene terephthalate (PET)-based textiles were used as the culturing surface for hiPSC-CMs and the effects of the textiles on the maturation status of the hiPSC-CMs were assessed. The hiPSC-CMs were characterized by analyzing their morphology, sarcomere organization, expression of cardiac specific genes, and calcium handling. We show that the topographical cues improve the structure of the hiPSC-CMs in vitro. Human iPSC-CMs grown on PET textiles demonstrated improved structural properties such as rod-shape structure and increased sarcomere orientation.

Keywords: textile; PET; biomaterials; iPS-cells; cardiomyocytes; maturation; gene expression

1. Introduction

Cardiovascular diseases are the leading cause of death worldwide [1]. Cardiotoxicity is one of the main causes of withdrawal of drugs from the market [2]. Traditionally, new cardiac drugs and the cardiotoxicity of cardiac and non-cardiac drugs have been tested with rodent cardiomyocytes as well as with transfected non-cardiac cells [3–5]. However, the results of these experiments are not always applicable to humans. Therefore, more accurate human cardiomyocyte models are needed for preclinical analysis of drugs as well as for basic research and disease modeling of human cardiac diseases [6]. Human-induced pluripotent stem (hiPS) cells can be reprogrammed from any somatic cell by introducing the pluripotency factors [7] and these cells can be differentiated into functional cardiomyocytes with multiple methods, as recently reviewed [8]. However, these cells

have been criticized as being immature and more resembling fetal than adult cardiomyocytes (CMs) [9]. Compared to adult human CMs, hiPSC-CMs are small in size, round or multi-angular, and typically single-nucleated, whereas adult CMs are rod-like and large, with 25%–57% of the cells multi-nucleated [10,11]. The aspect ratio can be used as an indicator of the cell shape. Due to the round shape, hiPSC-CMs have an aspect ratio of (2–3): 1, whereas adult CMs are clearly longitudinally-oriented with an aspect ratio of (5–9):1. Sarcomeres of the hiPSC-CMs are disorganized and short ($<2 \mu\text{m}$), the sarcoplasmic reticulum is poorly developed, and the sarcolemma exhibits no transverse tubules [10,12]. The electrophysiological properties and the gene expression of the hiPSC-CMs differ from adult CMs [12].

The contractile ability of CMs is enabled by multiple sarcomere units that are integrated in the cytoskeleton of the cell [13]. The efficiency of the CM contraction relies on the proper orientation and length of the sarcomeres and on the rod-like shape of the cell [14]. Thus, the structural maturation of the cells has been the focus when studying maturation methods for hiPSC-CMs. Multiple methods and strategies have been suggested to improve the maturation of hiPSC-CMs *in vitro*, including topographical cues, substrate stiffness, medium additives, mechanical and electrical stimulation, genetic manipulation, and co-culture with other cell types [10,15]. However, a deeper understanding of the maturation process of hiPSC-CMs is still required to develop platforms to promote the maturation of the cells and producing hiPSC-CMs more resembling adult CMs.

Various scaffolds have been studied to orient hiPS-CMs, such as electrospun-aligned fiber textiles [16,17] and micro-grooved culture substrates [18]. Most of the cell cultures *in vitro* are coated on flat surfaces, which provide a two-dimensional (2D) environment for the cells. 2D culture forces cell polarization by providing cell-extra cellular matrix (ECM) connections on only one side of the cells [19,20]. Cells in 2D are usually flat because they try to spread out on the surface. By providing a three-dimensional (3D) environment with proper topographical cues and an extracellular matrix, cells can create more cell–ECM connections, which potentially affect cell proliferation and even differentiation and maturation [20]. Stiffness of a flat, 2D culture substrate affects cell properties, proliferation, and differentiation [21]. To increase the cardiac functionality and maturity, hiPS-CMs have been cultured with, for example, endothelial cells, and this has shown to enhance cardiomyocyte proliferation and functionality [22]. Co-culture of hiPS-CMs with cardiac fibroblasts has improved the structural and functional properties of the cells [23,24]. A similar maturation-enhancing effect was observed when cardiomyocytes were cultured on top of the vascular-like network produced from endothelial cells and fibroblasts [25,26]. Stem-cell-derived cardiomyocytes aligned according to the vascular structures of the network and their sarcomere structures were more oriented.

Textiles create a 3D culture environment and provide topographical support for different types of cells. Having a highly interconnective porous structure, textiles enable access of media and nutrients to the cells inside the material. Weaving is a conventional and basic textile technique that can also be used to fabricate tissue engineering scaffolds. Weaving enables the formation of textile structures with controllable properties, such as porosity, orientation, morphology, and mechanical properties. These parameters can be modified, for example, by changing the number of filaments, filament diameter, and weaving patterns. Biostable polyethylene terephthalate (PET) is one of the most used polyesters, and has many applications including in biomedical applications, for example as hernia meshes. It has also been used in many cell culture studies. The raw material of fibers can be changed too, and in the future, biodegradable textiles could be used as a vehicle for implantation of cardiomyocyte sheets for myocardial ischemia or scar repair applications [27–29].

In this study, PET textiles were used as culture substrates for hiPSC-CMs. The aligned textile fibers were hypothesized to provide sufficient topographical cues to improve the maturation state of hiPSC-CMs. The PET textiles had different weaving patterns, including a plain weave and a plain weave derivative, which altered their topography and other properties. They were coated with different biological compounds: GeltrexTM (Thermo Fisher Scientific) and gelatin were used. The CMs

were characterized by cell morphology, sarcomere organization, expression of cardiac specific genes, and calcium handling properties.

2. Materials and Methods

2.1. 1 Polyethylene Terephthalate Textile

Five different PET textiles were used (PET 1–5, Figure 1). They differed in color, texture of the fibers used as warp and weft, single filament (fiber) thickness, textile density, and pattern of the textile according to the details listed in Table 1. The average single filament thickness (measured from immunostaining images using autofluorescence of the fibers and ImageJ software used in the textiles varied between 20.4 and 24.4 μm without significant differences. All the textiles were of narrow fabric type, i.e., they were woven by a narrow-weaving loom having aligned fibers in their structure as warps. Perpendicular to the warps, the interweaving wefts formed the structure for the textile according to the pattern followed. The textile pattern of PET 1–4 was the same, plain weave, but other parameters varied. PET 5 was an in-house-designed plain weave derivative (pattern drawings in Figure 1). The textiles were woven narrow fabrics and the width of the textiles was 9 mm. The textiles were cut to pieces of 7–8 mm before final sterilization and cell seeding. Textiles were washed with ethanol (3–4 times washing with excess amounts of alcohol), followed by thorough drying before heat treatment. All the textiles were heat treated to stabilize the textile structure for the cell culture experiments.

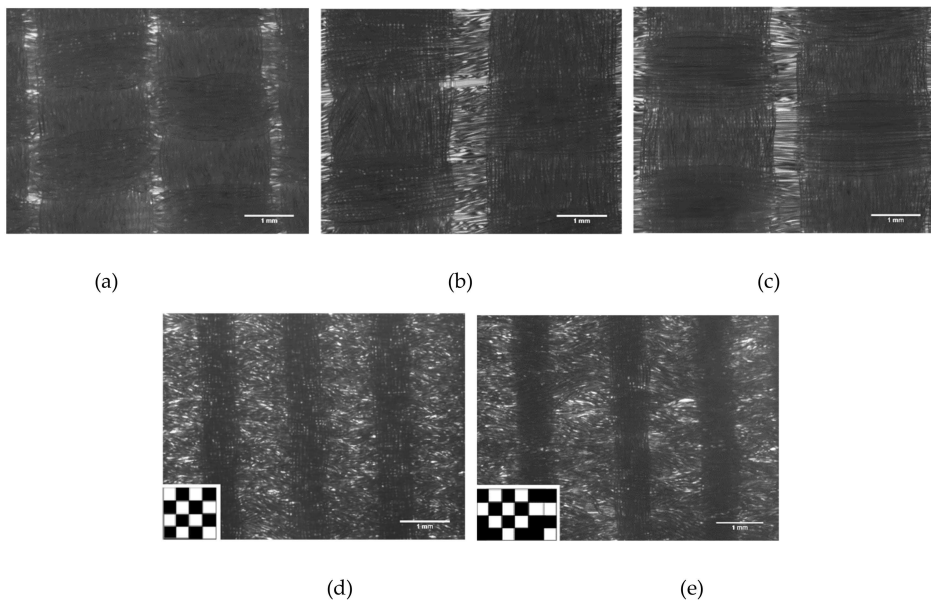


Figure 1. Structures of the polyethylene terephthalate (PET)-based textiles types 1–5 used in the present study, imaged with a Zeiss Axio Vert.A1 microscope (bright field) and AxioCam MRc5 camera using 5 \times objective. PET types 1–3 (A–C, respectively) were commercial textiles produced by Inka Oy, Killinkoski, Finland. PET types 4 and 5 (D,E, respectively) were produced at Tampere University, Tampere, Finland. Warp beams were provided by Finn-Nauha Oy, Haapamäki, Finland (yarn from Sinterama, Biella, Italy). The weaving type of the type 4 and 5 PET textiles were plain weave and plain weave derivative, respectively, as shown in lower left corner of the images.

Table 1. Details, manufacturers, and warp and weft type and diameter of a single filament (mean + SD) of the different PET textiles. Types 1, 2, and 3 were commercial textiles produced by Inka Oy, Killinkoski, Finland. Types 4 and 5 were produced at Tampere University, Tampere, Finland. Warp beams were provided by Finn-Nauha Oy, Haapamäki, Finland (yarn from Sinterama, Biella, Italy).

Textile Type and Details	Figure	Manufacturer	Warp/Weft	Single Filament ϕ (μm)
PET 1 Colorless, heat treated	1A	Inka Oy, Killinkoski, Finland	Textured/textured	24.4 \pm 1.82
PET 2 Colorless, heat treated	1B	Inka Oy, Killinkoski, Finland	Straight/textured	23.2 \pm 1.43
PET 3 Colorless, heat treated	1C	Inka Oy, Killinkoski, Finland	Textured/textured	22.9 \pm 1.91
PET 4 Blue, heat treated	1D	Yarn: Finn-Nauha Oy, Haapamäki, Finland Textile: Tampere University of Technology	Straight/straight	20.4 \pm 1.53
PET 5 Blue, heat treated	1E	Yarn: Finn-Nauha Oy, Haapamäki, Finland Textile: Tampere University of Technology	Straight/straight	22.0 \pm 1.4

2.2. Textile Coating

The PET textiles were coated to create a thin layer on the textile to increase attachment without compromising textile topography. Five different surface coatings were tested in the optimization phase of the present study: GeltrexTM, Gelatin, dopamine-bound gelatin coating, plasma-treatment of the textile without any coating, and plasma-treatment and gelatin-coating. Two replicates of each coating were used in each experiment. The glass coverslips were used as the control surface for hiPS-CMs. During the optimization phase of the experiment, all five PET types were used, and all different coating methods were tested for each PET type. In the experiment phase, only the gelatin coating was used for PET type 5.

To improve the attachment of the coating, as well as the attachment of the cells, PET textile was plasma-treated prior to gelatin coating. The plasma treatment was performed with plasma system Pico, Model 2, standard system controlled via PC and Windows CE operating system (control type C: PCCE control) and with reactive ion etching electrode. The electrode was type E (stainless steel), the generator was type D (13.56 MHz, 0-100W) (Diener electronic GmbH, Ebhausen, Germany) and the vacuum pump was Leybold 19 SC5D (Leybold Vacuum GmbH, Cologne, Germany). The gas used in the plasma treatment was O₂ and PET textiles were treated for 2 min in 0.4 mbar pressure with 50 W.

Prior to coating, the textiles and the coverslips were disinfected by washing with 70% ethanol (Altia, Rajamäki, Finland) and left to dry properly (1–2 h) before coating in the laminar hood.

GeltrexTM and gelatin were used as coating materials. GeltrexTM (Thermo Fisher Scientific, Waltham, Massachusetts, USA) was thawed and diluted 1:100 in KnockOut Dulbecco's Modified Eagle Medium (DMEM) (Thermo Fisher Scientific, Waltham, Massachusetts, USA). We pipetted 500 μL and 150 μL of diluted GeltrexTM on PET textiles and coverslips, respectively, which were incubated at 37 °C for 1 hour. Excess coating was aspirated just prior to the cell plating in all cases.

Gelatin coating was performed in three different ways. In the first method, Type A porcine gelatin (Sigma-Aldrich, Saint Louis, Missouri, USA) was dissolved in phosphate buffered saline (PBS) to form 0.1% solution. We pipetted 500 μL and 150 μL of 0.1% gelatin solution on PET textiles and coverslips, respectively, which were incubated in room temperature for an hour. The second method involved using plasma treatment before gelatin coating. The third method was used to improve the attachment of gelatin to a polymer [27]. Dopamine hydrochloride (Sigma-Aldrich, Saint Louis, Missouri, USA) was used to crosslink gelatin with the PET fibers. The PET fibers were incubated in 2 g/L dopamine solution for 24 h on a shaking bed at room temperature. After washing with distilled water, the samples were incubated in 5% (w/v) Gelatin type A (Sigma-Aldrich, Saint Louis, Missouri, USA) solution for 24 h at 37 °C. After incubation in gelatin, the samples were washed overnight in distilled water at 37 °C to remove non-chemically bound gelatin.

2.3. Cell Culture and Differentiation of hiPSC-CMs

The hiPSC line UTA.04602, produced from dermal fibroblasts of a healthy individual and cultured as previously described [30], was used in the study. The ethical committee of Pirkanmaa Hospital

District (Tampere, Finland) approved collection of biopsies for generating patient-specific hiPSC lines and written informed consent was obtained from all the donors (Aalto-Setälä R08070). The hiPSCs were cultured in mTeSR1 medium (STEMCELL Technologies, Vancouver, Canada) on a GeltrexTM (Thermo Fisher Scientific, Waltham, Massachusetts, USA)-coated surface. The culture medium was changed three times a week for the cells and they were passaged for a one-week culture using Versene (Thermo Fisher Scientific, Cibco, Billings, Montana, USA).

Small molecule differentiation was achieved as previously described [31] with small exceptions. In short, the differentiation was initiated when the hiPSC-culture was 100% confluent (day 0) by changing the mTeSR1 medium to insulin-free RPMI/B27 (Thermo Fisher Scientific, Cibco, Billings, Montana, USA) medium containing 8 μ M CHIR99021 (Tebubio, BPS Bioscience, San Diego, California, USA) and 0.5% penicillin/streptomycin. After 24 hours, the medium was changed to fresh insulin-free RPMI/B27 medium. On day three, half the medium was collected from the wells and mixed with fresh insulin-free RPMI/B27 medium. IWP-4 (Tocris, Bristol, England) was mixed with the medium so that the final concentration was 5 μ M. The rest of the old medium was exchanged to IWP-4-containing medium. On days five and seven, the medium was changed to fresh insulin-free RPMI/B27 medium, and from day 10 forward, half the medium was changed three times a week to fresh RPMI/B27 medium with insulin (Thermo Fisher Scientific, Cibco, Billings, Montana, USA).

2.4. hiPS-CM Dissociation and Magnetic-Activated Cell Sorting

hiPSC-CMs were dissociated using two methods. For the PET coating optimization phase, the hiPSC-CMs were dissociated using Collagenase A and suspended into a suspension medium containing KnockOut DMEM with 10% fetal bovine serum (Biosera, Nuaille, France), 1% non-essential amino acids (NEAA), 1% GlutaMAX-I (100 \times) (all from Thermo Fisher Scientific, Cibco, Billings, Montana, USA), and 0.5% penicillin/streptomycin (Lonza, Basel, Switzerland) [32].

To improve the purity of the hiPSC-CM population in the following experiments with PET 5, the cardiomyocytes were dissociated and separated from other cell types using magnetic-activated cell sorting (MACS) on day 21–27 of the differentiation. The cells were dissociated using a Multi Tissue Dissection Kit 3 (Miltenyi Biotec, Bergisch Gladbach, Germany) following the manufacturer's instructions. MACS sorting was performed using PSC-Derived Cardiomyocyte Isolation Kit, human (Miltenyi Biotec, Bergisch Gladbach, Germany). After cell sorting, the cells were resuspended in the suspension medium described above and the cells were plated on the gelatin-coated PET 5 textiles and gelatin-coated glass coverslips, which were used as controls.

2.5. Calcium Imaging

Calcium imaging was performed on day 12 after plating the cells to the PET 5 textiles. Ten independent PET 5 samples and two control samples were analyzed. Imaging was performed as previously described [33]. Shortly, the cells were loaded with 4 μ M Fluo 4 AM (Thermo Fisher Scientific, Waltham, Massachusetts, USA) for 30 minutes at 37 $^{\circ}$ C. The sample was placed into an imaging chamber (RC-25, Warner Instruments, Hamden, Connecticut, USA) and the chamber was placed onto an Olympus XI71 microscope (Olympus, Tokyo, Japan) and connected to a perfusion system. Cells were perfused with 37 $^{\circ}$ C pre-heated perfusate solution consisting of 137 mM NaCl, 5 mM KCl, 1.2 mM MgCl₂, 0.44 mM KH₂PO₄, 4.2 mM NaHCO₃, 2 mM CaCl₂, 1 mM Na pyruvate, 5 mM D-glucose, and 20 mM HEPES dissolved in distilled water (pH adjusted to 7.4 with NaOH).

The adrenaline response of CMs on PET 5 was evaluated with 1 μ M adrenaline (Sigma Aldrich, Saint Louis, Missouri, USA) from six independent samples. Baseline was recorded and hiPSC-CMs were treated with adrenaline for one minute and their response was recorded. Before a new baseline measurement, the adrenaline was washed off for at least two minutes. The recordings were performed with an Olympus XI71 microscope (Olympus, Tokyo, Japan) using ANDOR iXon+ camera and an Olympus UApo 20 \times 0.75 NA air objective and Live Acquisition software (TILL Photonics, Munich, Germany).

For calcium imaging analysis, single-beating hiPSC-CMs were selected as regions of interest and the analysis of fluorescence ($\Delta F/F_0$) videos were recorded using TILL Photonics Offline Analysis. The clampfit data analysis module of Axon pClamp 10 Electrophysiology Data Acquisition & Analysis software was used for peak detection (Molecular Devices, San Jose, California, USA). The studied peak parameters included peak duration, rise time from 10% to 90%, decay time from 90% to 10%, and peak frequency.

2.6. Immunocytochemistry

Immunocytochemistry was performed on day 10–11 after plating the cells on the PET 5 textile samples. The samples were fixed with 4% paraformaldehyde, blocked with 10% normal donkey serum (Biowest, Nuaille, France) solution, and stained with goat anti-cardiac troponin T (1:1,000, Abcam) and mouse anti-MyBPC3 (1:400, Santa Cruz Biotechnology, Dallas, Texas, USA) at 4 °C overnight. Donkey anti-goat Alexa Fluor 568 and donkey anti-mouse Alexa Fluor 488 (1:800, Thermo Fisher Scientific, Waltham, Massachusetts, USA) were used as secondary antibodies. The cell nuclei were stained using Vectashield mounting medium with DAPI (Vector Laboratories, Burlingame, California, USA). Fluorescence was visualized with a Nikon A1R+ Laser Scanning Confocal Microscope (Nikon, Tokyo, Japan) using a Nikon Apo 60× 1.40NA oil objective and with Zeiss Axio Imager.M2 with ApoTome.2 and AxioCamHRm3 camera using a Zeiss EC Plan-Neofluar 40× 1.30NA oil objective.

2.7. Analysis of Cell Alignment and Sarcomere Orientation

The orientation and sarcomere length of the hiPSC-CMs cultured on the PET textiles were analyzed from microscopy images using a spectral analysis tool, CytoSpectre [34]. CytoSpectre allows quantification of orientation and size distribution of cellular structures by using Fourier transform. In this study, the circular variance and wavelength of the detailed spectral component were used to determine the sarcomere orientation and modal sarcomere length of the hiPSC-CMs, respectively. Circular variance ranges from zero to one, with zero describing perfect anisotropy and one describing perfect isotropy. CytoSpectre determines the axes of the cell, which can be used to determine the aspect ratio. Prior to the analysis, the images were processed with ImageJ for masking.

2.8. Quantitative Reverse Transcription-Polymerase Chain Reaction (qRT-PCR)

hiPSC-CMs were prepared for qRT-PCR on day 1 and day 11 after plating the cells as previously described [35] to study the expression of several cardiac related genes. PET 5 and control samples (cells from glass coverslips) were collected from six independent experiments ($n = 6$). Two replicate samples from each independent experiment were collected. The cells were lysed with lysis solution of a CellsDirect One-Step qRT-PCR Kit (Invitrogen, Carlsbad, California, USA) following the manufacturer's protocol. The lysis was stored at -80 °C until genomic DNA degradation with DNase I and reverse transcription-specific target amplification (RT-STA) using the CellsDirect One-Step qRT-PCR Kit. Biomark HD (Fluidigm Corporation, San Francisco, California, USA) was used to perform the real-time qPCR according to the manufacturer's protocol. All samples were run as duplicates in Fluidigm Dynamic array-plates and the $2^{-\Delta\Delta CT}$ [36] method was used to calculate relative expression. TATA-box binding protein (*TBP*), eukaryotic translation elongation factor 1 alpha 1 (*EEF1A1*), and glyceraldehyde-3-phosphate dehydrogenase (*GAPDH*) were used as endogenous control genes for data normalization. In assessment of the relative expression, day one samples were used as a calibrator for the data. These samples were similar to the controls samples, the cells were plated to glass coverslips, but cells were lysed one day after plating. Cells were collected from four coverslips ($n = 4$). The TaqMan assays used are listed in Table 2.

Table 2. TaqMan assays used in the Quantitative Reverse Transcription-Polymerase Chain Reaction (qRT-PCR).

Gene	Description	Function	TaqMan Assay ID
<i>MYL2</i>	Myosin regulatory light chain 2	Sarcomeric gene	Hs00166405_m1
<i>MYL7</i>	Myosin regulatory light chain 7	Sarcomeric gene	Hs01085598_g1
<i>MYL9</i>	Myosin regulatory light chain 9	Sarcomeric gene	Hs00697086_m1
<i>MYH6</i>	Myosin heavy chain 6	Sarcomeric gene	Hs01101425_m1
<i>MYH7</i>	Myosin heavy chain 7	Sarcomeric gene	Hs01110632_m1
<i>TNNC1</i>	Slow skeletal and cardiac type troponin C1	Sarcomeric gene	Hs00896999_g1
<i>TNNI2</i>	Cardiac type troponin T2	Sarcomeric gene	Hs00165960_m1
<i>ACTN2</i>	α -actinin 2	Sarcomeric gene	Hs00153809_m1
<i>TTN</i>	Titin	Sarcomeric gene	Hs00399225_m1
<i>MYBPC3</i>	Myosin binding protein C, cardiac	Sarcomeric gene	Hs00165232_m1
<i>TPM1</i>	α -tropomyosin	Sarcomeric gene	Hs00165966_m1
<i>KCNH2</i>	Potassium voltage-gated channel subfamily H member 2	Potassium channel	Hs04234270_g1
<i>KCNH6</i>	Potassium voltage-gated channel subfamily H member 6	Potassium channel	Hs00229215_m1
<i>KCNA10</i>	Potassium voltage-gated channel subfamily A member 10	Potassium channel	Hs1563550_s1
<i>KCND3</i>	Potassium voltage-gated channel subfamily D member 3	Potassium channel	Hs00542597_m1
<i>KCNQ1</i>	Potassium voltage-gated channel subfamily Q member 1	Potassium channel	Hs00923522_m1
<i>HCN4</i>	Hyperpolarization activated cyclic nucleotide-gated potassium channel 4	Potassium channel	Hs00975492_m1
<i>SCN5A</i>	Voltage-gated sodium channel, V type, alpha subunit	Sodium channel	Hs00165693_m1
<i>CACNA1C</i>	Voltage-dependent calcium channel, L type, alpha 1C subunit/CaCNA1.2	Calcium channel	Hs00167681_m1
<i>SLC8A1</i>	Solute carrier family 8, member 1/NCX1	Sodium-calcium exchanger	Hs01062258_m1
<i>PLN</i>	Phospholamban	Protein kinase substrate	Hs01848144_s1
<i>ATP2A2</i>	ATPase, calcium transporting, cardiac muscle, slow twitch 2/ SERCA2a	Calcium ATPase	Hs00544877_m1
<i>EEF1A1; EE+</i>	Eukaryotic translation elongation factor 1 alpha 1	Housekeeping gene	Hs00265885_g1
<i>GAPDH</i>	Glyceraldehyde-3-phosphate dehydrogenase	Housekeeping gene	Hs02758991_g1
<i>TBP</i>	TATA-box binding protein	Housekeeping gene	Hs00427620_m1

2.9. Statistical Analysis

The statistical significance of the differences in circular variance, sarcomere length, and height to width ratio of the hiPSC-CMs was assessed by Mann–Whitney U test where $p < 0.05$ was considered statistically significant. Assessing the statistical significance of differences in gene expression levels was performed using the Kruskal–Wallis test with Bonferroni correction. When comparing the calcium baseline measurements to adrenaline measurements, related samples' Wilcoxon Signed Rank Test was used. $p < 0.05$ was considered statistically significant. The data are presented as mean \pm standard deviation.

3. Results

3.1. Attachment of the hiPSC-CMs to the PET Textiles

Five PET textiles (Figure 1) were tested as a scaffold for the hiPS-CMs. None of the fiber-related parameters (thickness range of the fibers and straight vs. textured quality of the fibers) or the weave pattern changed the behavior of the cells, but all the studied PETs (1–5) supported the growth of the hiPS-CMs in a similar manner (data not shown). PET 5, with a plain weave derivative pattern, was chosen for the following experiments. A combination of plain weave derivative pattern and the reed density used produced the most varying topography for the studied PET textile samples (Figure 1). PET 5 was also blue and had slight autofluorescence, which made the fibers visible with fluorescent imaging.

Gelatin has been used as a basic coating material for hiPS-CMs culturing in our laboratory; therefore, it was used also in the above-mentioned PET textile screening study. However, the number of the attached hiPS-CMs remained relatively low. To improve the cell attachment on the PET

textile, coating with commercial basement membrane matrix Geltrex™ was also tested. In addition, plasma treatment prior to gelatin coating and dopamine-bound gelatin were tested. There were no clear differences in the cell attachment (Figure S1) or structural maturation state of the hiPS-CMs (Table S1) with the coating material or plasma treatment. Thus, after testing multiple PET textile types and coatings, PET 5 with normal gelatin coating was chosen for further experiments.

3.2. hiPSC-CM Morphology, Sarcomere Orientation, and Sarcomere Length

hiPSC-CMs cultured on PET 5 and glass coverslips were immunolabeled with Troponin T and Myocin binding protein C3 (MyBPC3) antibodies. Qualitative analysis revealed that the cells aligned according to the PET 5 textile fibers and exhibited clearly elongated structures and increased sarcomere orientation, as shown in Figure 2. The orientation of the CM sarcomeres was significantly higher on PET 5 ($n = 98$) compared to controls ($n = 174$), which was indicated by the lower circular variance (0.611 ± 0.162 and 0.882 ± 0.069 , respectively; $p < 0.05$). Table 3 shows examples of the distribution of the sarcomeres in hiPSC-CM cultured on PET 5 and coverslip. Sarcomeres in CMs grown on PET 5 were more oriented than those in the controls. The difference in sarcomere length (Table 3) between PET 5 and control samples was not significant and was $1.736 \pm 0.187 \mu\text{m}$ and $1.749 \pm 0.122 \mu\text{m}$ on average, respectively. The shape of CMs was determined using the aspect ratio, and CMs grown on PET 5 had significantly higher aspect ratios than controls (4.915 ± 2.263 and 1.567 ± 0.455 , respectively; $p < 0.05$), indicating that the cells exhibited a more rod-like structure essential for efficient contraction (Figure 2). However, confocal imaging revealed that the hiPS-CMs are still flat and wrap around single PET fibers (Figure 3).

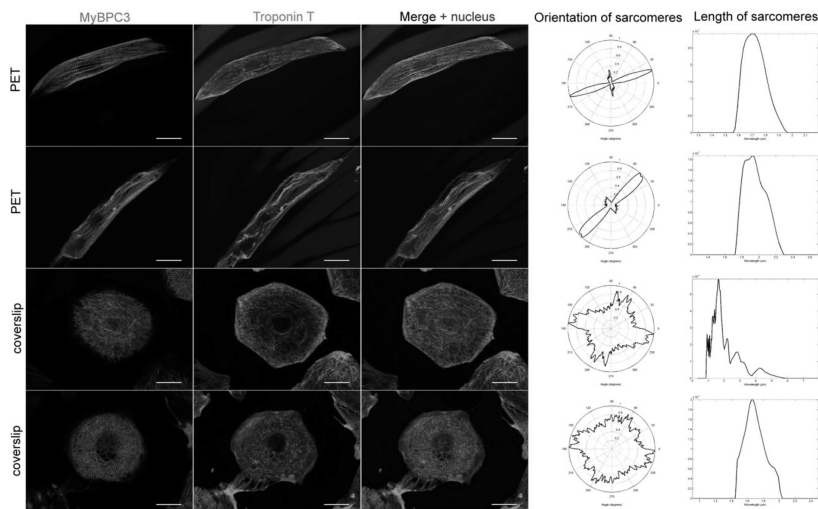


Figure 2. Two representative examples of the structure of human-induced pluripotent stem cell-derived cardiomyocytes (hiPSC-CMs) cultured on gelatin-coated polyethylene terephthalate (PET)-based textiles (PET) textiles and coverslips (controls). The hiPS-CMs were immunostained with myosin binding protein C (MyBPC3) (green) and Troponin T (red). The nuclei of the cells were stained with DAPI (blue). Scale bar is 25 μm . On PET 5, the cells and their sarcomeres clearly aligned according to the fibers of the textile, whereas the control cells exhibited no longitudinal axis or sarcomere orientation to one direction. Orientations of the sarcomeres were analyzed with CytoSpectre. The analysis results of sarcomere orientation and length of sarcomeres confirmed that the orientation of the sarcomeres improved when the cells were cultured on PET 5 textiles, but the sarcomere length distribution in the cells did not differ significantly.

Table 3. The data of the CytoSpectre analysis of cells grown on PET 5 and glass coverslips (control). The orientation of the CM sarcomeres was significantly higher on PET 5 compared to control ($p < 0.05$) as indicated by the average circular variance. The difference in sarcomere length between PET 5 and control samples was not significant. However, the shape of CMs was determined using the aspect ratio and CMs grown on PET 5 had a significantly higher ratio than the control ($p < 0.05$).

Sample	Average Circular Variance (0–1)	Average Modal Sarcomere Length (μm)	Average Aspect Ratio (Length to Width)	Number of Cells Analyzed
PET 5	0.611 ± 0.162	1.736 ± 0.187	4.915 ± 2.263	98
Control	0.882 ± 0.069	1.749 ± 0.122	1.567 ± 0.455	174

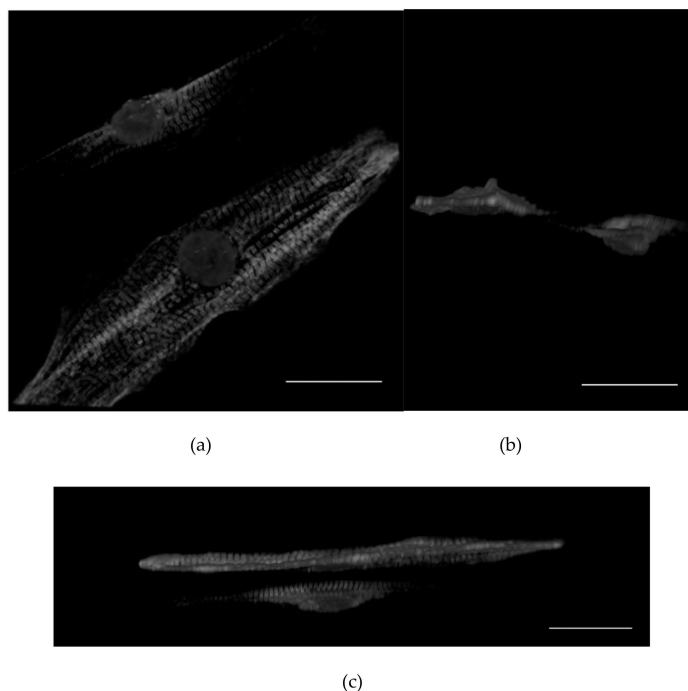


Figure 3. (a–c) Confocal images from single human induced pluripotent stem cell-derived cardiomyocytes (hiPSC-CMs) on the polyethylene terephthalate PET type 5 textiles, with Troponin T (red), myosin binding protein C, MYBPC (green), nuclear stain DAPI (blue) from different projections. Images reveal that the hiPS-CMs were aligned with the PET fibers. However, the cells wrapped around the single PET 5 fibers and exhibited a relatively flat structure. The sarcomeres of the cells were clearly oriented along the fibers. Scale bar is $25 \mu\text{m}$.

3.3. Calcium Handling

Differences in the calcium handling properties between hiPSC-CMs cultured on PET 5 textiles and coverslips were analyzed after 12 days of culture (the age of the cells was 33–39 days after initiation of differentiation). Cells exhibiting normal calcium transients were distinguished from those exhibiting arrhythmias and analyzed separately. The structure of the PET 5 did not hinder the Ca^{2+} imaging. There was no significant difference in the Ca^{2+} peak duration between CMs cultured on PET 5 ($n = 160$) or the control ($n = 40$) plates (582 ± 229 ms and 590 ± 202 ms, respectively; Table 4). However, there were statistically significant differences in rise and decay times, which were 112 ± 49 ms and 295 ± 131 for PET 5 samples and 90 ± 41 ms and 324 ± 96 ms for control samples ($p < 0.05$), respectively. This indicates that the release of calcium was slower while the uptake of calcium was faster for CMs grown on PET 5 compared to the control. Additionally, the amplitude of the peaks was significantly lower in CMs

grown on PET 5 compared to controls ($0.048 \pm 0.037 \Delta F/F_0$ and $0.067 \pm 0.030 \Delta F/F_0$ for PET and control samples, respectively; $p < 0.05$), indicating that control cells released more calcium during contraction cycles. The beating frequency was significantly higher in CMs grown on PET 5 compared to controls (0.93 ± 0.52 Hz and 0.75 ± 0.34 Hz, respectively; $p < 0.05$).

Table 4. Functionality of the hiPS-CMs cultured on PET 5 analyzed using Ca²⁺ imaging. The structure of the PET 5 textile did not hinder the Ca²⁺ imaging and the calcium handling properties were assessable from the hiPSC-CMs cultured on PET 5 textiles. Culturing on the PET 5 textiles slightly altered the calcium handling properties of the hiPSC-CMs; however, no significant changes were observed.

Sample	Peak Duration (ms)	Peak Amplitude ($\Delta F/F_0$)	Rise Time from 10% to 90% (ms)	Decay Time from 90% to 10% (ms)	Peak Frequency (Hz)	Cell Number
PET 5	582 ± 229	0.048 ± 0.037	112 ± 49	295 ± 131	0.93 ± 0.52	160
Control	590 ± 202	0.067 ± 0.030	90 ± 41	324 ± 96	0.75 ± 0.34	40

The response of hiPS-CMs cultured on PET 5 to adrenaline and its effect on calcium handling properties was studied ($n = 43$) (Table 5 and Figure 4). There were statistically significant differences in the peak parameters between baseline and adrenaline measurements ($p < 0.05$). The peak duration decreased by 4.8% (648 ± 101 ms at baseline vs. 614 ± 87 after adrenaline). The peak amplitude decreased by 61.4% ($0.0360 \pm 0.0183 \Delta F/F_0$ at baseline vs. $0.0310 \pm 0.0139 \Delta F/F_0$ after adrenaline). The rise time increased by 6.1% (115 ± 31 ms at baseline vs. 122 ± 34 ms after adrenaline). The decay time decreased by 7.6% (328 ± 73 ms at baseline vs. 303 ± 63 ms after adrenaline). The beating frequency increased by 21.2% (0.709 ± 0.254 Hz at baseline vs. 0.859 ± 0.242 Hz after adrenaline) as expected.

Table 5. Adrenaline significantly increased beating frequency and decreased peak duration in CMs grown on PET 5 textiles.

Sample	Peak Duration (ms)	Peak Amplitude ($\Delta F/F_0$)	Rise Time from 10% to 90% (ms)	Decay Time from 90% to 10% (ms)	Peak Frequency (Hz)
Baseline	648 ± 101	0.0360 ± 0.0183	115 ± 31	328 ± 73	0.709 ± 0.254
Adrenaline	614 ± 87	0.0310 ± 0.0139	122 ± 34	303 ± 63	0.859 ± 0.242

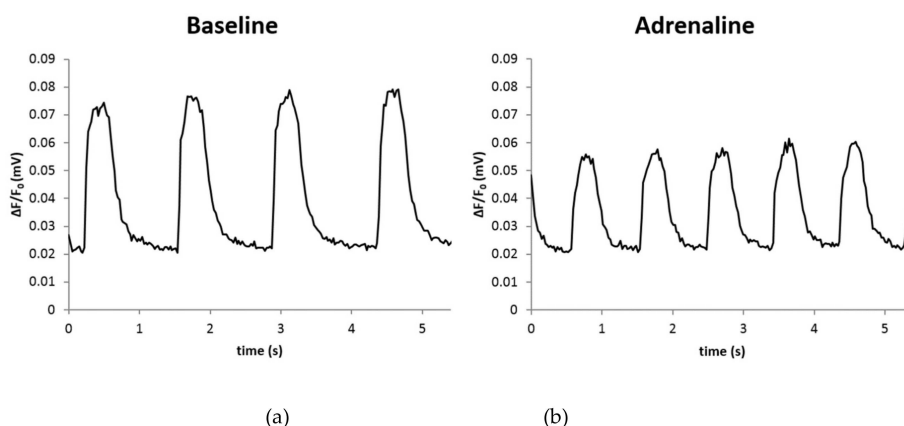


Figure 4. Adrenaline significantly increased beating frequency and decreased peak duration (a) when compared to the baseline (b) in hiPS-CMs grown on PET 5 textiles.

3.4. Expression of Cardiac-Specific Genes

The expression of cardiac specific genes was analyzed using qRT-PCR. Data from PET 5 ($n = 6$) and control coverslip ($n = 6$) samples collected at day 11 (the age of the cells was 32–38 days after differentiation initiation) were calibrated with the day 1 ($n = 4$) samples. Two biological replicates were analyzed from each sample, and all the samples were run as triplicates. TATA-box binding protein (*TBP*), eukaryotic translation elongation factor 1 alpha 1 (*EEF1A1*), and glyceraldehyde-3-phosphate dehydrogenase (*GAPDH*) were used as endogenous control genes for normalization. Overall, high variation was observed between the experiments. The expression levels of the genes coding for the contractile proteins, such as Troponin T (*TNNT2*), myosin binding protein C (*MYBPC*), and cardiac alpha actinin (*ACTN2*) had an increasing trend after the 11 days of culturing on both the PET 5 and control hiPS-CMs. However, only expression of *TNNT2* was significantly higher in the hiPSC-CMs cultured on PET 5 compared to controls on glass coverslips ($p < 0.05$, Figure 5). The expression levels of the genes coding for cardiac ion channels were similar for the CMs cultured on glass coverslips and PET 5 (Figure S2).

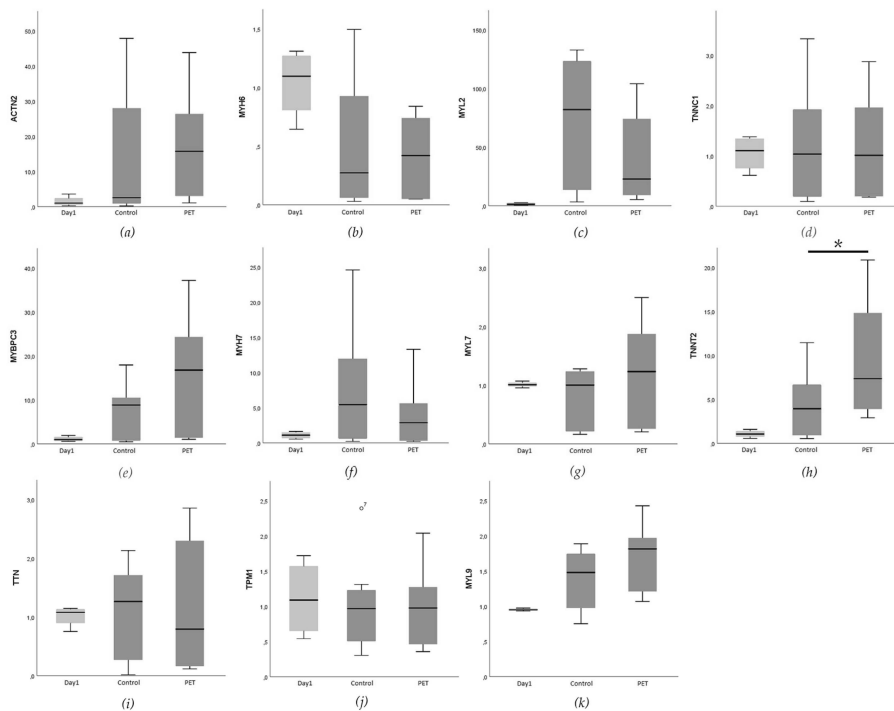


Figure 5. Expression levels of genes coding for the cardiac specific structural proteins: (a) α -actinin 2 (*ACTN2*), (b) myosin heavy chain 6 (*MYH6*), (c) myosin regulatory light chain 2 (*MYL2*), (d) slow skeletal and cardiac type troponin C1 (*TNNC1*), (e) myosin binding protein C, cardiac (*MYBPC3*), (f) myosin heavy chain 7 (*MYH7*), (g) myosin regulatory light chain 7 (*MYL7*), (h) cardiac type troponin T2 (*TNNT2*), (i) titin (*TTN*), (j) tropomyosin (*TPM1*), and (k) myosin regulatory light chain 9 (*MYL9*). Only the expression level of (h) *TNNT2* was significantly higher in hiPSC-CMs cultured on gelatin coated PET 5 textiles compared to the control sample ($p < 0.05$), marked with *.

4. Discussion

Several studies have reported the positive effects of a structured substrate on the maturation of hiPSC-CMs [16–18,37–39]. These findings have suggested that topographical cues can align the

hiPSC-CMs and improve their morphology. In this study, we assessed the possibilities of textile structures being used as a culturing scaffold for hiPSC-CMs. The differentiated hiPSC-CMs were cultured on textile constructs, and their structure, sarcomere orientation, cardiac function, as well as expression of cardiac specific genes were analyzed. Based on our results, culturing hiPSC-CMs on PET textiles improved their structural properties, such as elongation and sarcomere orientation, as well as improved the expression of sarcomeric genes such as *TNNT2*.

Textiles as scaffolds have beneficial properties for cell culture experiments. First, they provide topographical cues for the cells and enable the transportation of nutrients through the porous material. Secondly, textiles provide support to form tissue-like three-dimensional structures by superimposing multiple textile layers with one or multiple types of cells. In the present study, PET-based textiles were chosen as the scaffold for hiPSC-derived CMs, since PET is one of the most used polyesters in biomedical applications [40].

The hiPSC-CMs cultured on the PET textile were clearly elongated along the fibers of the textile and the sarcomeres were more aligned than in CMs cultured on the standard gelatin coated glass coverslips. A similar alignment of stem cell-derived CMs and their sarcomeric structures was reported when cultured on micro-grooved substrates [18]. Compared to the micro-grooved cultures, PET culturing had a similar effect on the hiPS-CMs even though the cells were wrapped around the fibers of PET textiles, and therefore exhibited rather flat and rounded shapes compared to the more 3D structure of the CMs cultured in the microgrooves [18]. Rao et al. suggested that the alignment of the sarcomeric structures and the orientation of the cell along the fibers are enhanced because the focal adhesion complexes of the cells are formed parallel to the microgrooves. Therefore, the contraction of the cell is directed along the grooves and this orients the sarcomeres as well as the whole cell along the grooves. Similar phenomena might cause the orientation of hiPSC-CMs on PET fibers. The hiPS-CMs focal adhesion complexes might be formed parallel to the fibers, and due to this, the sarcomeres are oriented toward the same direction as the fibers. In addition to the microgrooves, nanogrooves have been reported to facilitate the alignment of cardiomyocytes [41]. Both of these studies speculated that the edges of the grooves are especially crucial in the formation of the focal adhesion complexes. Our data also showed that single 22.0 ± 1.4 - μm -diameter fiber without any edges had a similar orienting effect on the hiPS-CMs.

Culturing of hiPS-CMs on PET textile did not have an effect on the sarcomere length, which was approximately $1.7 \mu\text{m}$ and still shorter compared to the average of $2.2 \mu\text{m}$ in primary adult human CMs [41]. The sarcomere lengths reported for stem cell-derived cardiomyocytes have ranged from 1.4 – $1.7 \mu\text{m}$ [42] and some studies have reported that structured culture substrates that provide topographical cues have increased the sarcomere length. However, the sarcomere length has not reached the length of primary CMs [16,39,43]. An elongated structure and sarcomere orientation are important in terms of the efficiency of the CM contraction as the magnitude the CMs can contract in one direction increases with increased elongation and sarcomere orientation [14].

As mentioned above, topographical cues have been shown to align and improve the morphology of hiPSC-CMs toward a more mature phenotype. However, their effects on functionality and gene expression of cardiac specific genes have been controversial. In the present study, PET culturing enhanced the expression of the sarcomeric gene *TNNT2* compared to the hiPSC-CMs cultured on a flat surface. No statistically significant changes were observed in the expression of other cardiac-specific structural genes or in the genes encoding cardiac ion channels. Similar results have been reported earlier; topographical cues have oriented the cells but there has been no significant improvement at the gene expression level [18,43]. However, culturing of iPS-CMs on electrospun fibers had positive effects on the gene expression levels of genes coding for cardiac structural proteins as well as ion channels when compared to culturing on cell culture plastic. Interestingly, positive effects were seen observed regardless of the alignment of the electrospun fibers [16]. The time scale in these studies had been similar, cells were cultured on the scaffolds for two weeks. The longer culturing time of the hiPS-CMs on the surfaces providing topographical cues might enhance the expression level of cardiac

cardiac-specific genes in addition to the structural maturation. Furthermore, the controversy in gene expression studies might be due to the other cell types present in the cultures. Even though hiPS-CMs were sorted in the present study, there are other cell types left remained in the cultures with in varying quantities. Due to the lack of cardiac cardiac-specific markers for normalization, this phenomenon can cause the variation in qPCR studies.

According to our previous study in which hiPSC-CMs were cultured with a vascular-like network formed by human foreskin fibroblasts and human umbilical vein endothelial cells, the construct improved the hiPS-CM structure toward a more rod-like shape [25]. hiPSC-CMs had more elongated morphology and aligned with the tubular structures of the vascular-like network. Thus, our hypothesis in this present study was whether textile fibers would have similar orientating effect on the hiPSC-CMs as the tubular vascular structures. Our results support this hypothesis: Culturing of hiPSC-CMs on the PET textile had a positive effect on the morphology of the cells.

Previous studies analyzing the effect of CM orientation and anisotropy on calcium handling of hiPSC CMs have reported inconsistent results [16,18,21,38,43,44]. According to our data, CMs cultured on PET textiles had slightly altered calcium handling properties, but no significant changes were observed. We also studied the adrenaline response of hiPSC-CMs. Adrenaline significantly increased beating frequency and decreased Ca^{2+} peak duration in CMs grown both on PET and on control coverslips. Adrenaline decreased the calcium transient decay time, indicating improved calcium reuptake. Therefore, the beta-adrenergic pathway is functional in the hiPS-CMs grown on PET 5 and the cells respond to adrenaline as expected.

Throughout the study, the attachment of the dissociated hiPS-CMs to the textile structure was poor. To improve the attachment, multiple coating materials were tested. Regardless of the coating material, the level of attachment remained the same. A portion of the cells slid through the textile fibers without attaching to the substrate. After PET textile removal from the cell culture well, a high number of vital hiPS-CMs was observed (data not shown). However, regardless of the low number of cells attached, the cells that were attached to the material remained viable for an extended period of time.

Culturing on PET textiles supports the formation of an oriented sarcomere structure as well as alignment of the hiPSC-CMs, thus inducing the structural maturation of these cells. However, the textile culturing had only minor effects on the expression levels of the cardiac-specific genes. Additionally, the functionality was comparable to the culturing on gelatin-coated glass surfaces. Notably, compared to the micro- and nano-grooved culture surfaces [18,41], one cross-sectionally round PET fiber had similar effects on the hiPS-CMs' structure. It was earlier speculated that the edges of the grooves are especially important in the orientation of the cells. Here, we showed that the cross-sectionally round fibers of the textile structure support the cells and have a similar orientation effect on hiPS-CMs.

According to the results of the present study, for disease modeling studies as well as for drug screening and toxicology experiments, culturing of hiPS-CMs on textile structures would be beneficial. Compared to 2D cultures, culturing of hiPS-CMs would produce more standardized cultures, so the hiPS-CM population is more homogeneous in terms of cell structure and orientation. Therefore, for example, the effects of potential drug molecules on the cell structure and sarcomeres could be more reliably studied. However, more optimization is needed for the textile material, and the time scale for cell culturing on the scaffolds should be extended in future studies. Softer and more elastic textile material may be more suitable for hiPS-CMS. Material optimization is left for future studies.

5. Conclusions

In the present study, cardiomyocytes differentiated from the hiPSCs were cultured on PET textiles, and their structural properties, expression of the cardiac specific genes, and calcium handling properties were assessed. Based on the results, culturing hiPSC-CMs on the PET textiles improved their structural properties, such as elongation and sarcomere orientation, as well as improved the expression of the sarcomeric genes such as *TNNT2*. However, no statistically significant changes in the expression of

the genes encoding cardiac ion channels or in the calcium handling properties of the hiPS-CMs were observed, and only minor changes were observed in their functionality as suggested by Ca^{2+} transients.

Supplementary Materials: The following are available online at <http://www.mdpi.com/1996-1944/12/11/1805/s1>, Figure S1: Immunostaining of hiPS-CMs on different coating materials, Figure S2: The expression levels of the genes coding cardiac ion channels, Table S1: Data describing the structural maturation state of the hiPS-CMs with the tested coating materials.

Author Contributions: Conceptualization, M.P.-M., J.K., M.K., and K.A.-S.; Data curation, M.P.-M.; Funding acquisition, M.K., and K.A.-S.; Investigation, M.P.-M., M.H., R.-P.P., T.M., A.J., E.T., and J.K.; Methodology, M.P.-M.; Project administration, M.P.-M., M.K., and K.A.-S.; Resources, E.T.; Supervision, M.P.-M., M.K., and K.A.-S.; Visualization, M.H.; Writing—original draft, M.P.-M., M.H., and R.-P.P.; Writing—review & editing, M.P.-M., J.K., M.K., and K.A.-S.

Funding: This research was funded by Business Finland, Päivikki and Sakari Sohlberg foundation, Pirkanmaa Regional Fund of the Finnish Cultural Foundation, the Finnish Foundation for Cardiovascular Research, Academy of Finland and Pirkanmaa Hospital District.

Acknowledgments: The authors acknowledge Henna Lappi and Markus Haponen for their technical expertise with the stem cell cultures and cardiac differentiation, as well as Kirsikka Stenlund for the design of the weave pattern. The authors acknowledge the Tampere facility of Electrophysiological Measurement, Tampere Imaging Facility (TIF), Tampere iPSC core facility and the Tampere CellTech Laboratories for their service.

Conflicts of Interest: The authors declare no conflict of interest.

References

1. GBD 2016 Causes of Death Collaborators. Global, regional, and national age-sex specific mortality for 264 causes of death, 1980–2016: A systematic analysis for the Global Burden of Disease Study 2016. *Lancet* **2017**, *390*, 1151–1210. [CrossRef]
2. Onakpoya, I.J.; Heneghan, C.J.; Aronson, J.K. Post-marketing withdrawal of 462 medicinal products because of adverse drug reactions: A systematic review of the world literature. *BMC Med.* **2016**, *14*, 10. [CrossRef] [PubMed]
3. Kannankeril, P.J.; Roden, D.M. Drug-induced long QT and torsade de pointes: Recent advances. *Curr. Opin. Cardiol.* **2007**, *22*, 39–43. [CrossRef]
4. Carlsson, L. In vitro and in vivo models for testing arrhythmogenesis in drugs. *J. Intern. Med.* **2006**, *259*, 70–80. [CrossRef] [PubMed]
5. Thomsen, M.B.; Matz, J.; Volders, P.G.A.; Vos, M.A. Assessing the proarrhythmic potential of drugs: Current status of models and surrogate parameters of torsades de pointes arrhythmias. *Pharmacol. Ther.* **2006**, *112*, 150–170. [CrossRef] [PubMed]
6. Sala, L.; Bellin, M.; Mummery, C.L. Integrating cardiomyocytes from human pluripotent stem cells in safety pharmacology: Has the time come? *Br. J. Pharmacol.* **2017**, *174*, 3749–3765. [CrossRef] [PubMed]
7. Takahashi, K.; Tanabe, K.; Ohnuki, M.; Narita, M.; Ichisaka, T.; Tomoda, K.; Yamanaka, S. Induction of Pluripotent Stem Cells from Adult Human Fibroblasts by Defined Factors. *Cell* **2007**, *131*, 861–872. [CrossRef]
8. Di Baldassarre, A.; Cimetta, E.; Bollini, S.; Gaggi, G.; Ghinassi, B.; Di Baldassarre, A.; Cimetta, E.; Bollini, S.; Gaggi, G.; Ghinassi, B. Human-Induced Pluripotent Stem Cell Technology and Cardiomyocyte Generation: Progress and Clinical Applications. *Cells* **2018**, *7*, 48. [CrossRef]
9. Smith, A.S.T.; Macadangang, J.; Leung, W.; Laflamme, M.A.; Kim, D.H. Human iPSC-derived cardiomyocytes and tissue engineering strategies for disease modeling and drug screening. *Biotechnol. Adv.* **2017**, *35*, 77–94. [CrossRef]
10. Denning, C.; Borgdorff, V.; Crutchley, J.; Firth, K.S.A.; George, V.; Kalra, S.; Kondrashov, A.; Hoang, M.D.; Mosqueira, D.; Patel, A.; et al. Cardiomyocytes from human pluripotent stem cells: From laboratory curiosity to industrial biomedical platform. *Biochim. Biophys. Acta* **2016**, *1863*, 1728–1748. [CrossRef]
11. Lundy, S.D.; Zhu, W.-Z.; Regnier, M.; Laflamme, M. a Structural and functional maturation of cardiomyocytes derived from human pluripotent stem cells. *Stem Cells Dev.* **2013**, *22*, 1991–2002. [CrossRef] [PubMed]
12. Robertson, C.; Tran, D.D.; George, S.C. Concise Review: Maturation Phases of Human Pluripotent Stem Cell-Derived Cardiomyocytes. *Stem Cells* **2013**, *31*, 829–837. [CrossRef] [PubMed]

13. Dias, T.P.; Pinto, S.N.; Santos, J.L.; Fernandes, T.G.; Fernandes, F.; Diogo, M.M.; Prieto, M.; Cabral, J.M.S. Biophysical study of human induced Pluripotent Stem Cell-Derived cardiomyocyte structural maturation during long-term culture. *Biochem. Biophys. Res. Commun.* **2018**, *499*, 611–617. [CrossRef]
14. Kuo, P.L.; Lee, H.; Bray, M.A.; Geisse, N.A.; Huang, Y.-T.; Adams, W.J.; Sheehy, S.P.; Parker, K.K. Myocyte shape regulates lateral registry of sarcomeres and contractility. *Am. J. Pathol.* **2012**, *181*, 2030–2037. [CrossRef] [PubMed]
15. Ronaldson-Bouchard, K.; Ma, S.P.; Yeager, K.; Chen, T.; Song, L.; Sirabella, D.; Morikawa, K.; Teles, D.; Yazawa, M.; Vunjak-Novakovic, G. Advanced maturation of human cardiac tissue grown from pluripotent stem cells. *Nature* **2018**, *556*, 239–243. [CrossRef] [PubMed]
16. Han, J.; Wu, Q.; Xia, Y.; Wagner, M.B.; Xu, C. Cell alignment induced by anisotropic electrospun fibrous scaffolds alone has limited effect on cardiomyocyte maturation. *Stem Cell Res.* **2016**, *16*, 740–750. [CrossRef] [PubMed]
17. Parrag, I.C.; Zandstra, P.W.; Woodhouse, K.A. Fiber alignment and coculture with fibroblasts improves the differentiated phenotype of murine embryonic stem cell-derived cardiomyocytes for cardiac tissue engineering. *Biotechnol. Bioeng.* **2012**, *109*, 813–822. [CrossRef] [PubMed]
18. Rao, C.; Prodromakis, T.; Kolker, L.; Chaudhry, U.A.R.; Trantidou, T.; Sridhar, A.; Weekes, C.; Camelliti, P.; Harding, S.E.; Darzi, A.; et al. The effect of microgrooved culture substrates on calcium cycling of cardiac myocytes derived from human induced pluripotent stem cells. *Biomaterials* **2013**, *34*, 2399–2411. [CrossRef] [PubMed]
19. Lee, J.; Cuddihy, M.J.; Kotov, N.A. Three-Dimensional Cell Culture Matrices: State of the Art. *Tissue Eng. Part B Rev.* **2008**, *14*, 61–86. [CrossRef]
20. Wickström, S.A.; Niessen, C.M. Cell adhesion and mechanics as drivers of tissue organization and differentiation: Local cues for large scale organization. *Curr. Opin. Cell Biol.* **2018**, *54*, 89–97. [CrossRef]
21. Rodriguez, M.L.; Beussman, K.M.; Chun, K.S.; Walzer, M.S.; Yang, X.; Murry, C.E.; Sniadecki, N.J. Substrate Stiffness, Cell Anisotropy, and Cell–Cell Contact Contribute to Enhanced Structural and Calcium Handling Properties of Human Embryonic Stem Cell-Derived Cardiomyocytes. *ACS Biomater. Sci. Eng.* **2019**. [CrossRef]
22. Tulloch, N.L.; Muskheli, V.; Razumova, M.V.; Korte, F.S.; Regnier, M.; Hauch, K.D.; Pabon, L.; Reinecke, H.; Murry, C.E. Growth of engineered human myocardium with mechanical loading and vascular coculture. *Circ. Res.* **2011**, *109*, 47–59. [CrossRef] [PubMed]
23. Thavandiran, N.; Dubois, N.; Mikryukov, A.; Massé, S.; Beca, B.; Simmons, C.A.; Deshpande, V.S.; McGarry, J.P.; Chen, C.S.; Nanthakumar, K.; et al. Design and formulation of functional pluripotent stem cell-derived cardiac microtissues. *Proc. Natl. Acad. Sci. USA* **2013**, *110*, E4698–E4707. [CrossRef]
24. Conant, G.; Lai, B.F.L.; Lu, R.X.Z.; Korolj, A.; Wang, E.Y.; Radisic, M. High-Content Assessment of Cardiac Function Using Heart-on-a-Chip Devices as Drug Screening Model. *Stem Cell Rev. Rep.* **2017**, *13*, 335–346. [CrossRef]
25. Vuorenää, H.; Penttinen, K.; Heinonen, T.; Pekkanen-Mattila, M.; Sarkanen, J.-R.; Ylikomi, T.; Aalto-Setälä, K. Maturation of human pluripotent stem cell derived cardiomyocytes is improved in cardiovascular construct. *Cytotechnology* **2017**, *69*, 785–800. [CrossRef] [PubMed]
26. Vuorenää, H.; Ikonen, L.; Kujala, K.; Huttala, O.; Sarkanen, J.-R.; Ylikomi, T.; Aalto-Setälä, K.; Heinonen, T. Novel in vitro cardiovascular constructs composed of vascular-like networks and cardiomyocytes. *Vitr. Cell. Dev. Biol. Anim.* **2014**, *50*, 275–286. [CrossRef] [PubMed]
27. Giol, E.D.; Schaubroeck, D.; Kersemans, K.; De Vos, F.; Van Vlierberghe, S.; Dubruel, P. Bio-inspired surface modification of PET for cardiovascular applications: Case study of gelatin. *Colloids Surf. B Biointerfaces* **2015**, *134*, 113–121. [CrossRef] [PubMed]
28. Ribeiro, V.P.; Silva-Correia, J.; Nascimento, A.I.; da Silva Morais, A.; Marques, A.P.; Ribeiro, A.S.; Silva, C.J.; Bonifácio, G.; Sousa, R.A.; Oliveira, J.M.; et al. Silk-based anisotropic 3D biotextiles for bone regeneration. *Biomaterials* **2017**, *123*, 92–106. [CrossRef]
29. Ribeiro, V.P.; Almeida, L.R.; Martins, A.R.; Pashkuleva, I.; Marques, A.P.; Ribeiro, A.S.; Silva, C.J.; Bonifácio, G.; Sousa, R.A.; Oliveira, A.L.; et al. Modulating cell adhesion to polybutylene succinate biotextile constructs for tissue engineering applications. *J. Tissue Eng. Regen. Med.* **2017**, *11*, 2853–2863. [CrossRef]

30. Lahti, A.L.; Kujala, V.J.; Chapman, H.; Koivisto, A.-P.; Pekkanen-Mattila, M.; Kerkelä, E.; Hyttinen, J.; Kontula, K.; Swan, H.; Conklin, B.R.; et al. Model for long QT syndrome type 2 using human iPSC cells demonstrates arrhythmogenic characteristics in cell culture. *Dis. Model. Mech.* **2012**, *5*, 220–230. [CrossRef]
31. Lian, X.; Hsiao, C.; Wilson, G.; Zhu, K.; Hazeltine, L.B.; Azarin, S.M.; Raval, K.K.; Zhang, J.; Kamp, T.J.; Palecek, S.P. Robust cardiomyocyte differentiation from human pluripotent stem cells via temporal modulation of canonical Wnt signaling. *Proc. Natl. Acad. Sci. USA* **2012**, *109*, E1848–E1857. [CrossRef] [PubMed]
32. Mummery, C.; Ward-van Oostwaard, D.; Doevendans, P.; Spijker, R.; van den Brink, S.; Hassink, R.; van der Heyden, M.; Opthof, T.; Pera, M.; de la Riviere, A.B.; et al. Differentiation of human embryonic stem cells to cardiomyocytes: Role of coculture with visceral endoderm-like cells. *Circulation* **2003**, *107*, 2733–2740. [CrossRef]
33. Pölonen, R.P.; Penttinen, K.; Swan, H.; Aalto-Setälä, K. Antiarrhythmic Effects of Carvedilol and Flecainide in Cardiomyocytes Derived from Catecholaminergic Polymorphic Ventricular Tachycardia Patients. *Stem Cells Int.* **2018**, *2018*, 1–11. [CrossRef] [PubMed]
34. Kartasalo, K.; Pölonen, R.-P.; Ojala, M.; Rasku, J.; Leikkala, J.; Aalto-Setälä, K.; Kallio, P. CytoSpectre: A tool for spectral analysis of oriented structures on cellular and subcellular levels. *BMC Bioinform.* **2015**, *16*, 344. [CrossRef] [PubMed]
35. Ojala, M.; Prajapati, C.; Pölonen, R.-P.; Rajala, K.; Pekkanen-Mattila, M.; Rasku, J.; Larsson, K.; Aalto-Setälä, K. Mutation-Specific Phenotypes in hiPSC-Derived Cardiomyocytes Carrying Either Myosin-Binding Protein C Or α -Tropomyosin Mutation for Hypertrophic Cardiomyopathy. *Stem Cells Int.* **2016**, *2016*, 1–16. [CrossRef] [PubMed]
36. Livak, K.J.; Schmittgen, T.D. Analysis of relative gene expression data using real-time quantitative PCR and the 2(-Delta Delta C(T)) Method. *Methods* **2001**, *25*, 402–408. [CrossRef]
37. Carson, D.; Hnilova, M.; Yang, X.; Nemeth, C.L.; Tsui, J.H.; Smith, A.S.T.; Jiao, A.; Regnier, M.; Murry, C.E.; Tamerler, C.; et al. Nanotopography-Induced Structural Anisotropy and Sarcomere Development in Human Cardiomyocytes Derived from Induced Pluripotent Stem Cells. *ACS Appl. Mater. Interfaces* **2016**, *8*, 21923–21932. [CrossRef]
38. Xu, C.; Wang, L.; Yu, Y.; Yin, F.; Zhang, X.; Jiang, L.; Qin, J. Bioinspired onion epithelium-like structure promotes the maturation of cardiomyocytes derived from human pluripotent stem cells. *Biomater. Sci.* **2017**, *5*, 1810–1819. [CrossRef]
39. Huehorst, E.; Hortigon, M.; Zamora-Rodriguez, V.; Reynolds, P.M.; Burton, F.; Smith, G.; Gadegaard, N. Enhanced Human-Induced Pluripotent Stem Cell Derived Cardiomyocyte Maturation Using a Dual Microgradient Substrate. *ACS Biomater. Sci. Eng.* **2016**, *2*, 2231–2239. [CrossRef]
40. Maitz, M.F. Applications of synthetic polymers in clinical medicine. *Biosurf. Biotribol.* **2015**, *1*, 161–176. [CrossRef]
41. Wang, P.Y.; Yu, J.; Lin, J.H.; Tsai, W.B. Modulation of alignment, elongation and contraction of cardiomyocytes through a combination of nanotopography and rigidity of substrates. *Acta Biomater.* **2011**, *7*, 3285–3293. [CrossRef]
42. Sarantitis, I.; Papanastopoulos, P.; Manousi, M.; Baikoussis, N.G.; Apostolakis, E. The cytoskeleton of the cardiac muscle cell. *Hell. J. Cardiol.* **2012**, *53*, 367–379.
43. Khan, M.; Xu, Y.; Hua, S.; Johnson, J.; Belevych, A.; Janssen, P.M.L.; Gyorke, S.; Guan, J.; Angelos, M.G. Evaluation of changes in morphology and function of human induced pluripotent stem cell derived cardiomyocytes (hiPSC-CMs) cultured on an aligned-nanofiber cardiac patch. *PLoS ONE* **2015**, *10*, e0126338. [CrossRef] [PubMed]
44. Feinberg, A.W.; Ripplinger, C.M.; Van Der Meer, P.; Sheehy, S.P.; Domian, I.; Chien, K.R.; Parker, K.K. Stem Cell Reports Report Functional Differences in Engineered Myocardium from Embryonic Stem Cell-Derived versus Neonatal Cardiomyocytes. *Stem Cell Rep.* **2013**, *1*, 387–396. [CrossRef] [PubMed]



PUBLICATION
II

**Human neurons form axon-mediated functional connections with
human cardiomyocytes in compartmentalized microfluidic chip**

Martta Häkli*, Satu Jäntti*, Tiina Joki, Lassi Sukki, Kaisa Tornberg, Katriina
Aalto-Setälä, Pasi Kallio, Mari Pekkanen-Mattila, Susanna Narkilahti

International Journal of Molecular Sciences (2022), 23(6)3148
<https://doi.org/10.3390/ijms23063148>

Publication reprinted with the permission of the copyright holders.



Article

Human Neurons Form Axon-Mediated Functional Connections with Human Cardiomyocytes in Compartmentalized Microfluidic Chip

Martta Häkli ^{1,†} , Satu Jääntti ^{2,†}, Tiina Joki ², Lassi Sukki ³, Kaisa Tornberg ³, Katriina Aalto-Setälä ^{1,4}, Pasi Kallio ³ , Mari Pekkanen-Mattila ¹ and Susanna Narkilahti ^{2,*}

- ¹ Heart Group, Faculty of Medicine and Health Technology, Tampere University, 33520 Tampere, Finland; martta.hakli@tuni.fi (M.H.); katriina.aalto-setala@tuni.fi (K.A.-S.); mari.pekkanen-mattila@tuni.fi (M.P.-M.)
 - ² Neuro Group, Faculty of Medicine and Health Technology, Tampere University, 33520 Tampere, Finland; satu.jaantti@tuni.fi (S.J.); tiina.joki@wikli.fi (T.J.)
 - ³ Micro- and Nanosystems Research Group, Faculty of Medicine and Health Technology, Tampere University, 33720 Tampere, Finland; lassi.sukki@tuni.fi (L.S.); kaisa.tornberg@tuni.fi (K.T.); pasi.kallio@tuni.fi (P.K.)
 - ⁴ Heart Hospital, Tampere University Hospital, 33520 Tampere, Finland
- * Correspondence: susanna.narkilahti@tuni.fi
† These authors contributed equally to this work.

Abstract: The cardiac autonomic nervous system (cANS) regulates cardiac function by innervating cardiac tissue with axons, and cardiomyocytes (CMs) and neurons undergo maturation during the heart innervation in embryogenesis. As cANS is essential for cardiac function, its dysfunctions might be fatal; therefore, cardiac innervation models for studying embryogenesis, cardiac diseases, and drug screening are needed. However, previously reported neuron-cardiomyocyte (CM) coculture chips lack studies of functional neuron-CM interactions with completely human-based cell models. Here, we present a novel completely human cell-based and electrophysiologically functional cardiac innervation on a chip in which a compartmentalized microfluidic device, a 3D3C chip, was used to coculture human induced pluripotent stem cell (hiPSC)-derived neurons and CMs. The 3D3C chip enabled the coculture of both cell types with their respective culture media in their own compartments while allowing the neuronal axons to traverse between the compartments via microtunnels connecting the compartments. Furthermore, the 3D3C chip allowed the use of diverse analysis methods, including immunocytochemistry, RT-qPCR and video microscopy. This system resembled the *in vivo* axon-mediated neuron-CM interaction. In this study, the evaluation of the CM beating response during chemical stimulation of neurons showed that hiPSC-neurons and hiPSC-CMs formed electrophysiologically functional axon-mediated interactions.

Keywords: neuron; cardiomyocyte; coculture; axon-mediated; functional interaction; human-induced pluripotent stem cell; organ-on-chip; microfluidic chip



Citation: Häkli, M.; Jääntti, S.; Joki, T.; Sukki, L.; Tornberg, K.; Aalto-Setälä, K.; Kallio, P.; Pekkanen-Mattila, M.; Narkilahti, S. Human Neurons Form Axon-Mediated Functional Connections with Human Cardiomyocytes in Compartmentalized Microfluidic Chip. *Int. J. Mol. Sci.* **2022**, *23*, 3148. <https://doi.org/10.3390/ijms23063148>

Academic Editor:
Alessandro Romano

Received: 7 February 2022

Accepted: 11 March 2022

Published: 15 March 2022

Publisher's Note: MDPI stays neutral with regard to jurisdictional claims in published maps and institutional affiliations.



Copyright: © 2022 by the authors. Licensee MDPI, Basel, Switzerland. This article is an open access article distributed under the terms and conditions of the Creative Commons Attribution (CC BY) license (<https://creativecommons.org/licenses/by/4.0/>).

1. Introduction

Cardiac function is modulated by the sympathetic and parasympathetic branches of the cardiac autonomic nervous system (cANS), which can stimulate or inhibit, e.g., the heart rate and contraction force. *In vivo*, neuronal axons innervate cardiac tissue [1–3], while neuronal somas reside in either central or peripheral nervous system (CNS and PNS, respectively) [1]. During embryonic cardiac innervation, neurons and cardiomyocytes (CMs) undergo maturation, where the growth and transmission properties of the innervating neurons are regulated by signals from cardiac tissue and CM maturation is influenced by neuronal signals [2]. As cANS plays a crucial role in cardiac function, the dysregulation of this system due to pathological conditions, such as arrhythmias or ischemic heart disease, can be fatal [4]. Furthermore, the modulation of cardiac function via drugs targeting the

cANS can be advantageous regarding drug development for cardiovascular diseases [5]. For example, therapeutic targeting of neurons to improve cardiac outcome after heart failure is important; however, studying this requires human cell-based models as drug responses and disease mechanisms between animal and human cells can be different [3,6,7]. Moreover, detection of adverse effects in cardiac tissue or the cANS is important to ensure drug safety [3]. Thus, relevant but reductionist models for human cardiac innervation are needed, where organ on a chip models could reduce the gap between animal models and human diseases [8,9].

Previously reported coculture devices used for neurons and CMs were compartmentalized polydimethylsiloxane (PDMS)-based chips that allowed the isolation of neuronal somas from the CMs and restricted cell-to-cell interactions to axons extending through microtunnels between the compartments [10–12]. Chips were integrated with microelectrode arrays (MEAs), allowing electrical stimulation and functional evaluation of the neurons and CMs. Studies have shown the formation of functional connections between rat superior cervical ganglion neurons and rat ventricular CMs [10], rat superior cervical ganglia neurons as sympathetic neurons, rat intracardiac ganglia neurons as parasympathetic neurons and rat atrial CMs [11], and rat primary sympathetic neurons and human-induced pluripotent stem cell (hiPSC)-derived CMs [12]. Moreover, a coculture of hiPSC-derived PNS neurons with hiPSC-CMs in a compartmentalized chip has been reported; however, only evidence of physical neuromuscular connections was shown, without further evaluation of electrophysiological functionality [13]. hiPSC-neurons and hiPSC-CMs have also been cocultured without restrictions of cell-to-cell contacts, showing the formation of functional interactions between the cell types [14,15]. Previously reported neuron–CM coculture models have not shown functional connections between human neurons and CMs via axon-mediated interactions alone. However, human cell-based models are desperately needed, e.g., in drug development, where animal and animal cell models are frequently used with poor predictive power for human response [6]. Possible differences in animal and human disease mechanisms complicate the translation of results to humans [16].

Primary human neurons and CMs are difficult to harvest, while hiPSCs can be easily differentiated into neurons and CMs in large quantities [6]. As many diseases have multicellular contributions, monocultures may not recapitulate the disease mechanism faithfully [17]. This study aimed to develop an advanced, functional, and completely human-based cardiac innervation on a chip for studying cardiac innervation and neuron–CM interactions. The coculture of spontaneously electrically active hiPSC-neurons [18] and hiPSC-CMs [19,20] was performed in a previously developed 3D3C chip [21,22] containing three separate culture compartments connected via microtunnels allowing only axonal connections between the compartments. In this study, we show that the 3D3C chip enables long-term coculture of the neurons and CMs in their respective media, with the neurons forming axon-mediated interactions with the cardiomyocytes, mimicking the *in vivo* situation. This study shows that during coculture in the 3D3C chip, neurons and CMs form both physical and functional connections via axons, as proven by immunocytochemical staining and gene expression analysis and by evaluating the CM beating response during chemical stimulation of the neurons. The presented cardiac innervation on a chip is a valuable tool for studying the neuromuscular junctions between neurons and CMs in disease modeling, drug screening, and toxicity assays.

2. Results

2.1. Cardiac Innervation in the 3D3C Chip

The 3D3C chip consists of three serial compartments connected via microtunnels, allowing the culture of up to three different cell or tissue types in a single chip. Here, it was used in the coculture of hiPSC-neurons and -CMs, as the chip isolated neuronal somas in their own compartment, allowing axonal growth to the cardiac compartment through the microtunnels (SEM image of the microtunnels presented in Supplementary Figure S1A). Neurons were seeded into one side compartment, and axons traversed into the middle

compartment for one week before seeding CMs. It has been shown that dendritic processes cannot traverse through microtunnels of 250- μm length [22], which was the length of microtunnels utilized in the chips here. Separate medium chambers for each compartment allowed culturing the cells in their respective media. The cocultures were evaluated at the 2- and 4-week timepoints, with a few being followed up to 8 weeks, showing good viability (data not shown). The 2- and 4-week timepoints in coculture were chosen based on previous data regarding neuronal activity. In microelectrode array (MEA) embedded cultures, neurons develop spontaneous network activity from two weeks onwards, activity peaking in ~4 weeks [18]. Here, at 2-week timepoint, the neurons have been cultured for 1 week alone and 2 weeks in coculture, and at 4-week timepoint for 1 week alone and 4 weeks in coculture.

Phase-contrast imaging of the 3D3C chips showed that neurons were viable and formed neuronal networks in their compartment (Figure 1A), and axons started to extend to the middle compartment through microtunnels immediately after seeding and elongated continuously throughout the experiments (Figure 1B, Supplementary Figure S1B). The CMs were viable among the axons (Figure 1B), and CM beating was observed during the whole coculture period (Supplementary Video S1). Immunocytochemical (ICC) staining showed that the monoclonal anti-neurofilament NF-H 200 and monoclonal anti- β -tubulin III (NF-H/ β III-Tub)-positive axons traversed through the microtunnels into the middle compartment and grew alongside the cardiac marker Troponin T (TropT)-positive CMs (Figures 1C and 2, Supplementary Figure S1C). The synaptic marker Synapsin I (SynI) was expressed in the axons showing that the formation of functional connections between neurons and CMs was possible (Figure 2B, Supplementary Figure S2). 3D projections of the fluorescent confocal images showed that the axonal synapses grew in close contact with the CMs (Figure 2C, Supplementary Videos S2 and S3).

2.2. Gene Expression of hiPSC-Neurons and -CMs Cocultured in the 3D3C Chip

The expressions of cardiac-specific genes *TNNT2* and *MYBPC3*, and neuron-specific gene *TUBB3* (Figure 3A) were evaluated to confirm that the samples from neuronal and cardiac compartments could be extracted without samples mixing. *TNNT2* and *MYBPC3* were expressed robustly in all cardiac samples, (2- and 4-week control samples, and 2- and 4-week coculture samples), whereas their expression in the neuronal samples was almost undetectable, with significant differences when compared to the cardiac samples. *TUBB3* was robustly expressed in neuronal samples, with significantly lower expression in cardiac samples. However, 4-week cardiac coculture samples had higher *TUBB3* expression than other cardiac samples suggesting an increase in the axonal expression of *TUBB3* in the coculture. It was shown earlier that *TUBB3* is detectable axon-specifically in neurons [23,24]. The detailed mean expressions and standard deviations, along with *p*-values for each gene and sample, are presented in Supplementary Table S1, and detailed information of the genes and TaqMan Assays used are presented in Supplementary Table S2.

The expression of the genes associated with the formation of the functional connection between neuronal axons and CMs was also evaluated. *CHRM2* and *CHAT* enable cholinergic signaling between neurons and CMs (Figure 3B), whereas *ADRB2*, *ADRB3*, *TH*, and *DBH* are related to adrenergic signaling (Figure 3C) [25]. *CHAT*, encoding choline O-acetyltransferase, was expressed mainly in the neuronal samples, with significant differences compared to the cardiac samples. However, *CHAT* expression in the cardiac coculture samples was higher compared to cardiac control samples, especially at the 4-week timepoint. The *CHRM2* gene, encoding muscarinic acetylcholine receptor M2, showed higher expression in the cardiac samples than the neuronal samples.

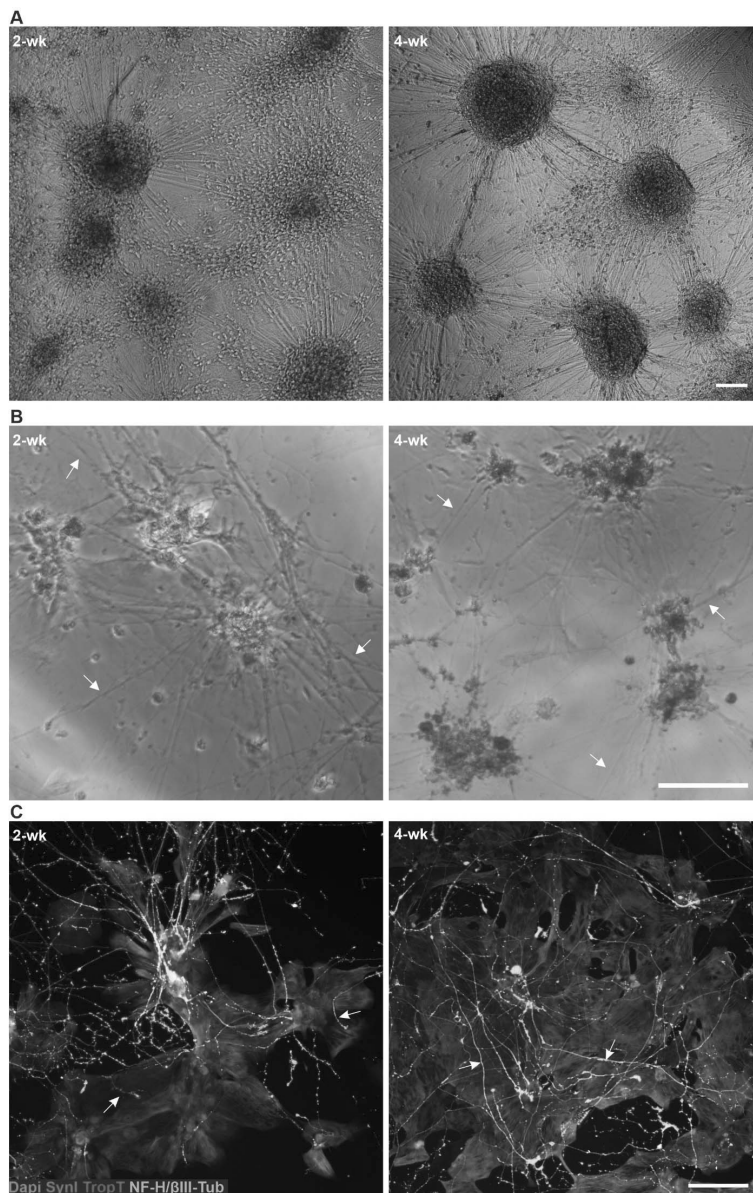


Figure 1. hiPSC-derived neurons and CMs in the 3D3C chip at 2- and 4-week timepoints of coculture. (A) A phase-contrast image showed viable neuronal somas isolated in their compartment and forming axonal networks. (B) Neuronal axons (white arrows) traversed to the middle compartment via microtunnels and CMs were viable among the axons. (C) ICC staining showed that neuronal axons stained against monoclonal anti-neurofilament NF-H 200 and monoclonal anti- β -tubulin III (NF-H/ β III-Tub, white) interacted with CMs stained against cardiac marker Troponin T (TropT, red) in the middle compartment. Evidence of synaptic interactions between CMs (TropT, red) and neurons (Synapsin I (SynI), green) can also be observed (white arrows). The scale bar is 100 μ m, and blue indicates a nuclear marker (DAPI).

TH and *DBH* encode tyrosine hydroxylase and dopamine beta-hydroxylase, respectively. *TH* is involved in the conversion of L-tyrosine to L-dopamine, whereas *DBH* is involved in the conversion of dopamine to norepinephrine, which can be further converted into epinephrine [25]. Generally, *TH* and *DBH* were expressed more in the neuronal than cardiac samples, with significant differences except for 4-week cardiac coculture samples, which could be due to increased axonal expression of these genes. Two types of beta-adrenergic receptors are present in cardiomyocytes: *ADRB2* encodes a beta-2 adrenergic receptor with affinity for epinephrine [25], and *ADRB3* encodes a beta-3 adrenergic receptor with affinity for norepinephrine [25]. Their expressions were lower in the neuronal samples than in the cardiac samples.

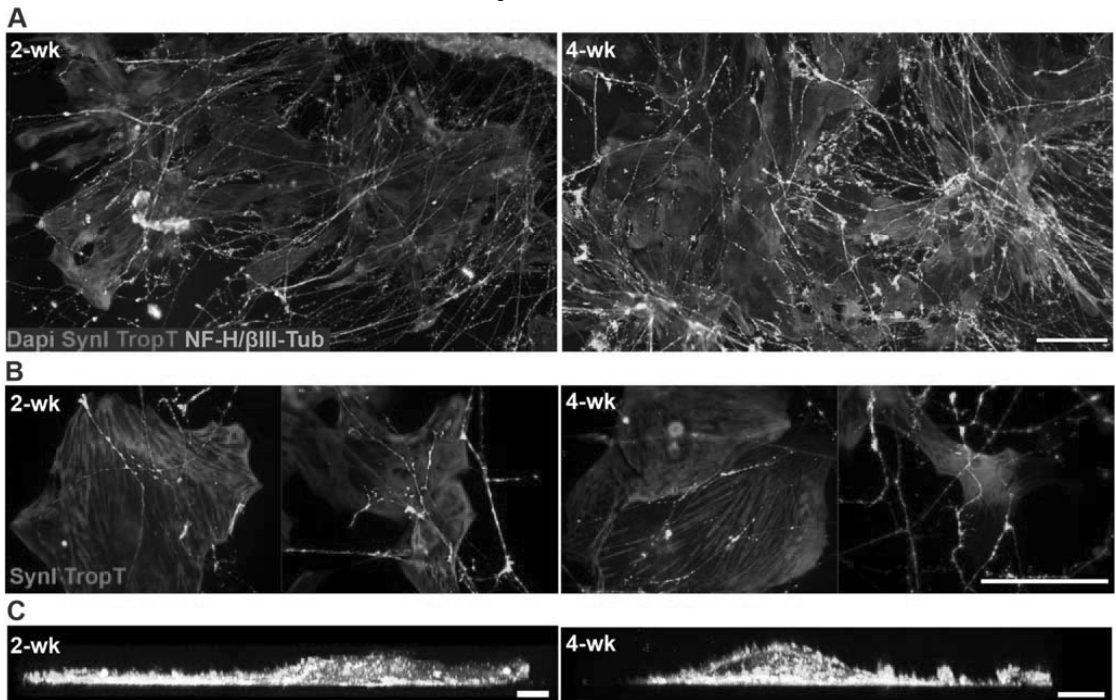
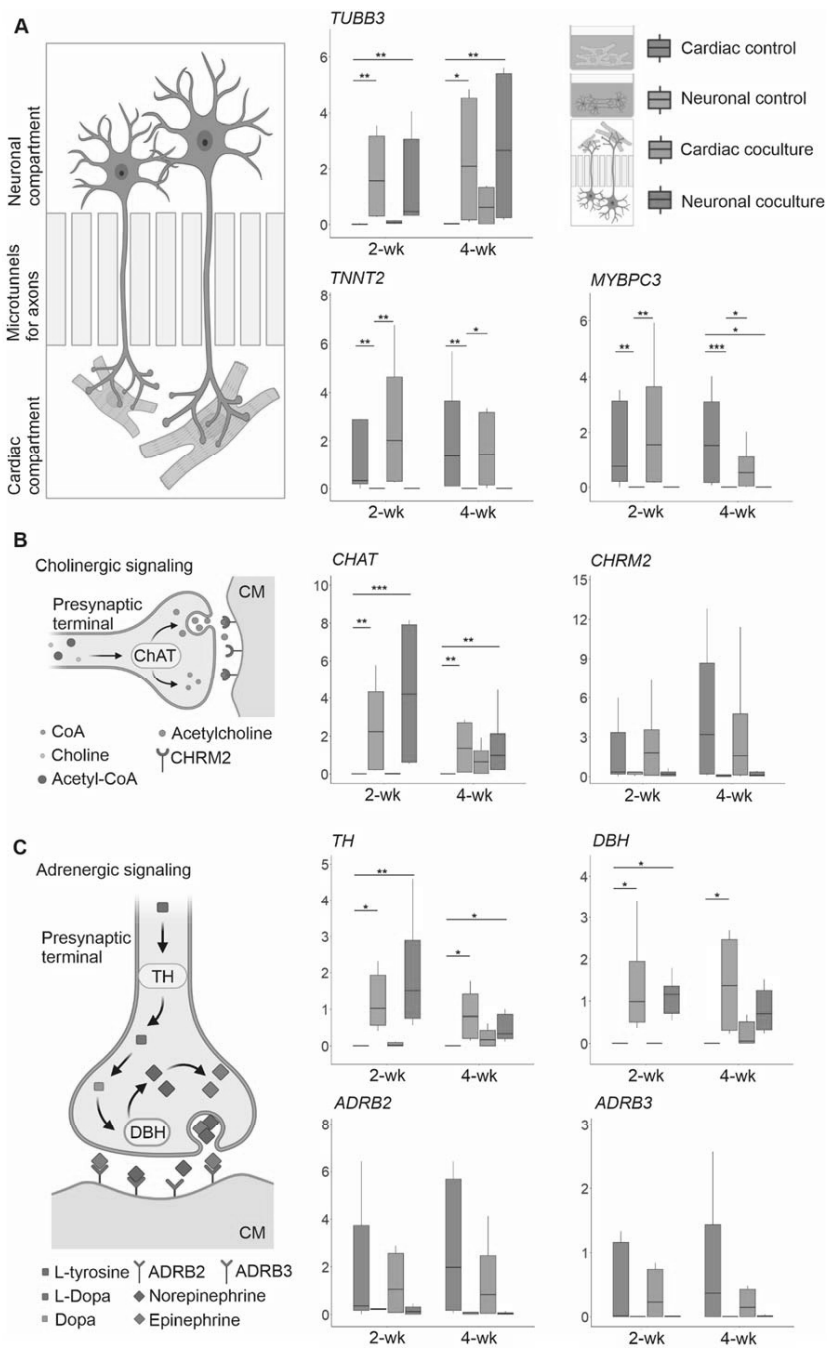


Figure 2. ICC staining of the hiPSC-derived neuron–CM coculture in the 3D3C chip at 2- and 4-week timepoints. (A) The staining showed the extension of the neuronal axons (NF-H/ β III-Tub, white) in the middle compartment among the CMs (TropT, red) and that both cell types were viable when in close contact with each other at both timepoints. (B) The staining of the synaptic marker (SynI, green) showed evidence of possible axon-mediated synaptic interactions with the CMs at both timepoints. The channels are shown separately in the Supplementary Figure S2. (C) 3D projection of the neuron–CM coculture showed that axonal synapses grew in close contact with CMs (NF-H/ β III-Tub, white; SynI, green; TropT, red). The scale bar is 100 μ m for (A) and (B) and 10 μ m for (C). Blue indicates a nuclear marker (DAPI).

2.3. Functional Connections Formed between hiPSC-Neurons and -CMs

Similar to 2D control samples, the hiPSC-CMs exhibited normal beating and contractile properties when cocultured with hiPSC-neurons in the 3D3C chip, and the elongated axons in the cardiac compartment did not disturb the video analysis (Supplementary Videos S1 and S4).



quartiles and minimum and maximum values. (A) A schematic illustration of the 3D3C chip compartments. The expression of neuron-specific *TUBB3* was higher in all neuronal samples than in cardiac samples, whereas cardiac-specific *TNNI2* and *MYBPC3* expression was higher in all cardiac samples. (B) A schematic illustration of the cholinergic signaling pathway between neurons and CMs. The expression of *CHAT* was higher in neuronal samples, whereas the expression of *CHRM2* was higher in cardiac samples. (C) A schematic illustration of the adrenergic signaling pathway. *TH* and *DBH* were more highly expressed in neuronal samples, whereas *ADRB2* and *ADRB3* were more highly expressed in cardiac samples. The illustrations were created using BioRender.com. * $p < 0.05$, ** $p < 0.01$, *** $p < 0.001$.

Fluorescent ICC images showed that CMs grew in close contact with axons, which expressed synaptic proteins when in contact with CMs (Figure 2). Furthermore, qPCR results showed that both cell types expressed necessary genes for the formation of functional connections (Figure 3). However, these results only implied that functional connections were possible; therefore, the functionality of neuron–CM connections in the cocultures was evaluated at 2- and 4-week timepoints using video microscopy recording of CM beating during neuronal stimulation by a high- K^+ solution. CM beating was recorded at baseline (1. rec), during medium change in the neuronal compartment (2. rec), during neuronal stimulation (3. rec) and at follow-up after approximately 2 min (4. rec) (Figure 4A). Videos were analyzed for contraction duration (10% above baseline), time to peak, relaxation time and peak-to-peak time using MUSCLEMOTION (Figure 4B). To observe the change in the CM beating and contractile properties during the neuronal stimulation, the baseline values for each evaluated parameter were subtracted from the medium change (MC), as well as the immediate (K^+) and follow-up (F/U) of neuronal stimulation. The CM response to MC was considered as the baseline response and K^+ and F/U responses were then compared to MC response.

The contraction duration indicates the time from the contraction start to the relaxation end and was observed to decrease during neuronal stimulation and follow-up at both timepoints with stronger at the 4-week timepoint (Figure 4C). The mean change in contraction duration when compared to baseline was -28.88 ± 122.77 for MC, -30.93 ± 102.98 for K^+ , and -52.63 ± 135.75 ms for F/U ($p = 0.021$ vs. MC) at the 2-week timepoint and -13.66 ± 195.20 for MC, -66.27 ± 214.63 for K^+ , and -90.61 ± 292.92 ms for F/U ($p = 0.005$ vs. MC) at the 4-week timepoint.

The time to peak and relaxation time were evaluated to determine whether neuronal stimulation affected CM contraction or relaxation. The time to peak indicates the time from the contraction start to the peak contraction. It decreased slightly during neuronal stimulation and follow-up at both timepoints (Figure 4C), the mean change being -12.49 ± 54.55 for MC, -14.76 ± 54.88 for K^+ ($p = 0.027$ vs. MC), and -22.77 ± 54.40 ms for F/U ($p = 0.004$ vs. MC) at the 2-week timepoint and -3.88 ± 35.82 ms for MC, -8.33 ± 47.86 ms for K^+ , and -14.74 ± 60.11 ms for F/U ($p = 0.031$ vs. MC) at the 4-week timepoint. On the other hand, the relaxation time indicates the time from the peak contraction back to the relaxed state. It did not change significantly at the 2-week timepoint (Figure 4C) but decreased during neuronal stimulation and follow-up at 4-week timepoint (Figure 4C). The mean change was -16.24 ± 108.36 for MC, -15.95 ± 99.53 for K^+ , and -29.29 ± 111.30 ms for F/U at the 2-week timepoint, whereas it was -11.02 ± 177.55 for MC, -59.00 ± 194.04 for K^+ , and -77.56 ± 269.28 ms for F/U ($p = 0.02$ vs. MC) at the 4-week timepoint.

The peak-to-peak time, describing the CM beating rate, decreased significantly during high K^+ exposure and follow-up at the 2-week and even more strongly at the 4-week timepoint, indicating an increased beating rate (Figure 4C). The mean change observed in the peak-to-peak time compared to baseline was -174.63 ± 242.31 for MC, -283.81 ± 411.11 for K^+ ($p = 0.00019$ vs. MC), and -299.27 ± 483.76 ms for F/U ($p = 0.00019$ vs. MC) at the 2-week timepoint while it was 118.14 ± 841.95 for MC, -51.55 ± 1280.77 for K^+ ($p = 0.00090$ vs. MC), and -181.07 ± 1426.18 ms for F/U ($p = 0.00035$ vs. MC and $p = 0.004$ vs. K^+) at the 4-week timepoint.

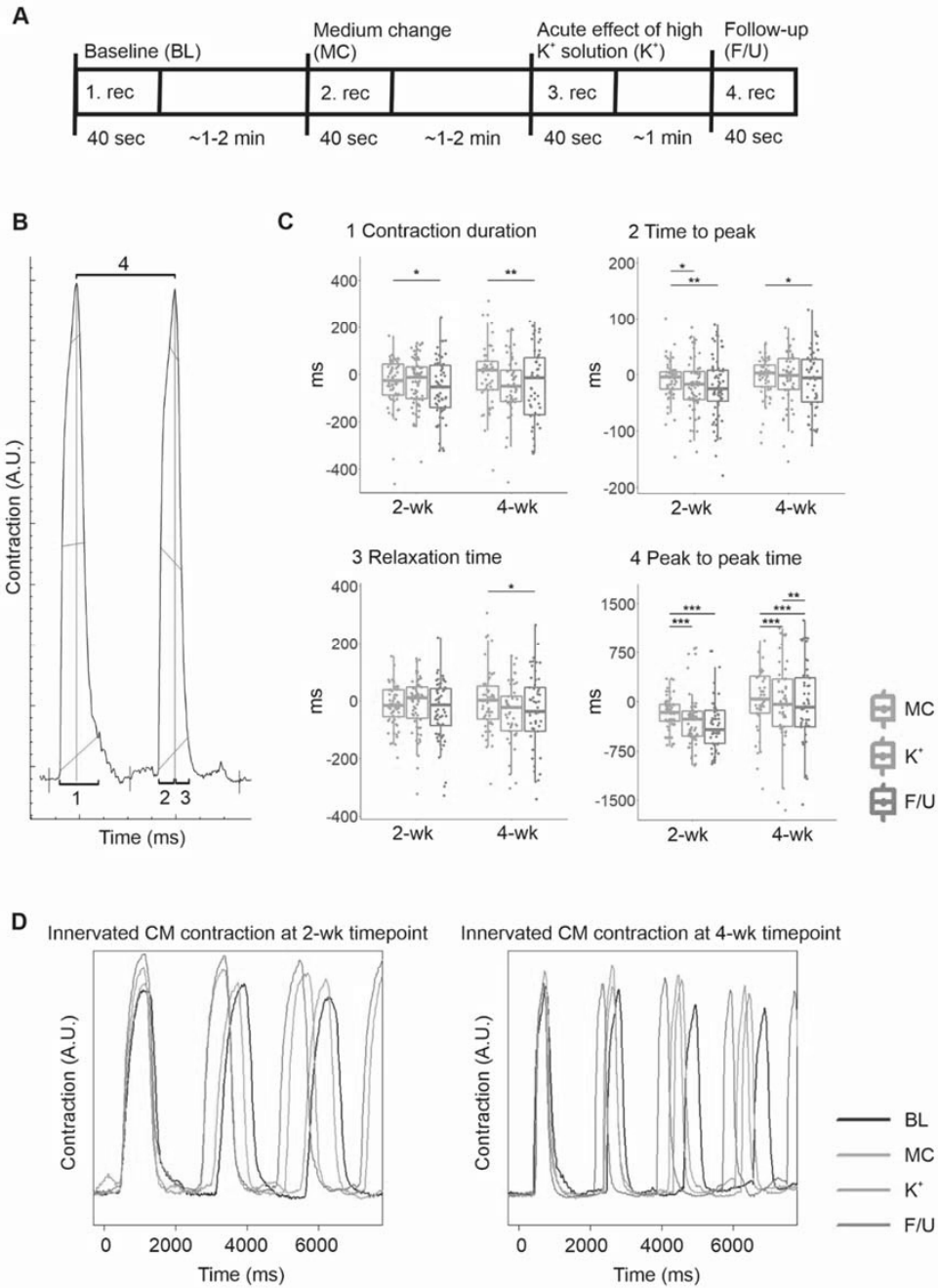


Figure 4. The evaluation of the functional connections between the cocultured hiPSC-neurons and hiPSC-CMs was performed by video microscopy recording of CMs beating during high K⁺ exposure

of the neurons. The data are presented as boxplots overlaid by individual datapoints. (A) Experimental timeline for the recording of CMs beating during neuronal exposure to a high- K^+ solution. (B) MUSCLEMOTION was used to analyze the videos for the contraction duration (1), time to peak (2), relaxation time (3), and peak-to-peak time (4). (C) The response to medium change (MC) was considered the baseline response, to which the immediate (K^+) and follow-up (F/U) responses to neuronal high K^+ exposure were compared. After K^+ exposure, the contraction duration was observed to decrease, mostly due to a decrease in the time to peak. Furthermore, the peak-to-peak time of cardiomyocyte beating was observed to decrease, indicating an increased beating rate. (D) Examples of contraction curves acquired from MUSCLEMOTION analysis of the recorded videos. * $p < 0.05$, ** $p < 0.01$, *** $p < 0.001$.

3. Discussion

Here, we present an advanced, completely human cell-based, functional cardiac innervation on a chip in which hiPSC-neurons and -CMs were cocultured long-term in a compartmentalized 3D3C chip. Both cell types were seeded in their respective compartments, allowing only axonal interaction between the cell types. The system allowed us to study interactions between the two cell types under more in vivo-like conditions, where the interaction between cANS and cardiac tissue is restricted to occur between axons and CMs. Furthermore, the separate medium chambers allowed the coculture of cells in their respective media, eliminating the need to compromise between the medium needs of each cell type. The 3D3C chip allowed the usage of diverse cell analysis methods, including RNA extraction for gene expression studies, ICC for evaluating protein expression and cellular morphology, and functionality studies with video microscopy. Furthermore, the analyses can be performed separately for each chip compartment, thus individually for each cell type. The elegant chip design enables long-term studies, which are crucial for functional maturation and innervation formation.

The phase-contrast and ICC images showed that both cell types remained viable in the chip for 4 weeks and even up to 8 weeks. Furthermore, axon-specific NF-H and β III-Tub and cardiac-specific TropT analyses showed that axons and CMs expressed the expected axonal and cardiac markers and their typical morphology, respectively. Axons expanded in the cardiac compartment throughout the experiments and created a visibly denser and longer network at the 4-week compared to the 2-week timepoint, providing more axonal connections for the CMs, and possibly enhancing the neuron–CM interaction. 3D projections of cocultures confirmed that axons and the clustered synaptic protein Syn1 were located very close to CMs, indicating that neurons and CMs can interact via axon-mediated synaptic connections. In previous neuron–CM coculture studies, the presence of synaptic proteins near CMs has not been evaluated except for by Takayama et al. [13], although later, they showed that hiPSC-neurons expressed synaptic proteins in free cocultures with CMs [15].

The RT-qPCR results showed that the hiPSC-neurons and -CMs expressed their cell-specific markers, *TUBB3* for neurons and *TNNT2* and *MYBPC3* for CMs, indicating the proper identity of the cells and that RNA can be extracted separately from the neuronal and cardiac compartments without samples mixing. This enabled the evaluation of gene expression separately for each cell type. Due to the low cell amount, RNA was pooled from three cell-specific compartments to form one sample. Although pooling RNA samples results in loss of information due to loss of sample variability, it is used in gene expression studies, e.g., for budgeting reasons or insufficient RNA input [26]. Gene expression has not been analyzed in previous publications regarding neuron–CM coculture in a chip [10–13] but is important in characterization of the cell types and their maturity, and a commonly used analysis method in organ and body on a chip studies [27,28].

We evaluated the expression of genes enabling cholinergic and adrenergic signaling between neurons and CMs. The expression of *CHAT* and *CHRM2* are required for cholinergic signaling; *CHAT* encodes protein involved in neurotransmitter acetylcholine conversion and *CHRM2* is acetylcholine receptor in CMs [25]. *CHAT* was expressed robustly in neuronal samples, whereas its expression in cardiac control samples was very low. The *CHAT* expression was higher in cardiac coculture samples, especially in the

4-week coculture, implying that the axonal *CHAT* expression increased temporally. Protein synthesis can occur locally in axons when mRNA translocates from the neuronal soma to the axonal regions [23,24,29]. The increase from the 2- to 4-week timepoint suggests a temporal increase in the growth and maturation of the axons. On the other hand, *CHRM2* expression was robust in cardiac samples, but low in neuronal samples. Regarding adrenergic signaling, *TH* and *DBH* were robustly expressed in the neuronal samples, whereas *ADRB2* and *ADRB3* showed higher expression in cardiac samples. Similar to *CHAT*, *TH* and *DBH* showed higher expression in 4-week cardiac coculture samples than in cardiac control samples, where their expression was almost absent, indicating increased axonal expression of these genes.

Together, the RT-qPCR results indicated that both cell types are capable of signaling via both cholinergic and adrenergic pathways, including neurons to synthesize their specific neurotransmitters, and CMs and their specific receptors to bind the neurotransmitters. The neurons expressed both cholinergic and adrenergic genes, suggesting that there are neurons with both sympathetic and parasympathetic characteristics. Although there has been an indication of the formation of functional connections between neurons and CMs when cocultured on chips in previous studies, they have not shown whether the two cell types express the genes or proteins necessary for the connections to form. Oiwa et al. showed that neurons cultured on their chip expressed *CHAT* and *DBH* at the protein level, but they did not evaluate the expression of cardiac receptors [11]. However, the earlier studies mostly used primary cells known to express these genes in vivo, even though harvesting the cells from their natural environment could affect the gene expression [30]. On the other hand, hiPSC-neurons and hiPSC-CMs differ from adult neurons and CMs in some respects, making it important to evaluate the capability of the cells to form functional connections [31,32].

Video microscopy analysis of CMs showed that the CMs exhibited normal beating characteristics when cocultured with the neurons in the chip. Importantly, the large video dataset collected and analyzed from CMs during high K^+ exposure to the neuronal compartment indicated that the axon-mediated connections between the neurons and CMs were electrophysiologically functional already at 2-week timepoint and became stronger at 4-week timepoint. When the neurons were exposed to high- K^+ solution, significant changes in the CM beating characteristics were observed in both the 2- and 4-week timepoints, including an increase in the beating frequency and a decrease in the contraction duration. The chip compartments have been previously shown to be fluidically isolated [33], indicating that the changes in cardiomyocyte beating is due to the neuronal stimulation and not due to potassium leakage through the microtunnels. This observation indicated that the activation of adrenergic signaling in neurons, as the CM response to neuronal stimuli was excitatory. The adrenergic signaling pathway is known to increase heart rate and strengthen the contractility of cardiomyocytes, whereas the cholinergic signaling pathway decreases heart rate [34].

Previously, the functionality of neuron–CM interactions has been reported in models utilizing rat primary neurons and CMs [10,11] and rat primary neurons and hiPSC-CMs [12] with integrated MEAs. Furthermore, MEAs have been utilized in cardiac innervation models where CMs have been seeded on top of neurons [15,35]. In these studies, neuronal stimulation evoked a response in the CMs. Depending on whether the neurons used were sympathetic or parasympathetic, an increase or decrease in cardiac beating frequency, respectively, was observed [10–12,15,35]. Furthermore, Oh et al. and Winbo et al. used video microscopy analysis for their unrestricted cocultures to evaluate the functionality of the neuron–CM interactions; however, they reported only cardiac beating frequency [14,35]. In the present study, we observed changes in several contractile parameters, including the contraction duration, and time to peak and relaxation time, when stimulating hiPSC-neurons during coculture in the 3D3C chip.

The present study has aspects to be developed further in the future. Here, we used neurons originally pruned towards cortical phenotypes [18]. However, according to the

gene expression and functional responses, neuronal population contained characteristics of both sympathetic and parasympathetic neurons, thus most likely they are able to adopt their phenotype according to the contact they made with cardiomyocytes. Furthermore, as the cardiomyocyte response to neuronal stimulation was observed, we have shown here that the cell types used form a functional connection. There are several protocols for differentiating specific types of neurons [15,36,37], which can be utilized in our future studies of the neuron–CM interaction and further evaluate the CM response to specific peripheral types of neurons. Moreover, we used neuronal high K^+ exposure and video microscopy to evaluate the functionality of the neuron–CM interactions, although previous studies [10–12] have used MEAs to electrically stimulate neurons and record the CM response, allowing better spatiotemporal induction of the stimulation and the measurement of the response in both neurons and CMs. However, high K^+ stimulation of hiPSC-neurons was previously characterized [38], and video analysis of the hiPSC–CM response to neuronal stimulation allows the evaluation of only the cardiac response, without axonal field potentials affecting the analysis. Furthermore, video analysis allows the extraction of multiple parameters of individual beating cardiomyocytes, which would require a single electrode per CM in chip models, not yet available. In the future, the 3D3C model should be further developed to include transparent MEAs [39] to facilitate both MEAs and video recording analyses of neuron–CM interactions.

We presented an advanced, electrophysiologically functional, and completely human-based cardiac innervation on a chip. The hiPSC-neurons and -CMs were cocultured with their respective media in separate compartments connected via microtunnels, enabling axonal growth from the neuronal to the cardiac compartment. The 3D3C chip enabled the use of several analysis methods to evaluate the functionality of the axon–CM connections. By combining immunocytochemical, gene expression and video recording analyses, we showed the formation of physical connections between the cell types that required signaling machinery for synaptic activation of CMs, which was further verified with a functional response to neuronal stimulation. The chip supported long-term cocultures, and functional innervation was detected at 2 weeks, with enhanced maturation at 4 weeks. The 3D3C cardiac innervation on a chip is a valuable tool for screening drug adverse effects on neurons or CMs via the functional connections between them, as well as for studying the development of neuromuscular junctions and comaturation of the two cell types.

4. Materials and Methods

4.1. Cell Lines

hiPSC line 10212.EURCCS [40] was used for neuronal differentiation towards cortical neurons, and the hiPSC line UTA.04602.WT [41] was used for cardiac differentiation. The hiPSCs used were acquired from voluntary subjects who had given written and informed consent. The institute has a supportive statement from Pirkanmaa Hospital District to generate iPSCs from donor cells (R08070 and R12123) and to use generated cell lines in neuronal research (R05116). The pluripotency of the lines was confirmed regularly, and all cultures maintained normal karyotypes and were free of mycoplasma.

4.2. Neuronal Differentiation

Before neuronal differentiation, hiPSCs were transferred to feeder-free culture on 15 $\mu\text{g}/\text{mL}$ of human recombinant laminin-521 (LN521, BioLamina, Sundbyberg, Sweden) using E8 medium (Thermo Fisher Scientific, Waltham, MA, USA) as previously described [42]. Neuronal differentiation included neuronal induction, precursor expansion and maturation phases and was performed as previously described [18]. On day 32 of differentiation, cells were seeded for experiments in neural maturation medium consisting of a 1:1 mixture of D-MEM/F12 (with GlutaMAX) and neurobasal medium, 0.5% N2, 1% B27 with retinoic acid, 0.5 mM of GlutaMAX, 0.5% NEEA, 50 μM of 2-mercaptoethanol, 0.1% penicillin/streptomycin (all from Thermo Fisher Scientific), 2.5 $\mu\text{g}/\text{mL}$ of insulin (Sigma-Aldrich, Saint Louis, MO, USA), 20 ng/mL of brain-derived neurotrophic factor

(BDNF, R&D Systems, Minneapolis, MN, USA), 10 ng/mL of glial-derived neurotrophic factor (GDNF, R&D Systems), 500 μ M of dibutyryl-cyclic AMP (db-cAMP, Sigma-Aldrich), and 200 μ M of ascorbic acid (AA, Sigma-Aldrich). During cell detachment on day 32, 10 μ M ROCK inhibitor (Sigma-Aldrich) was added to the medium to support cell survival.

4.3. Cardiac Differentiation

Before cardiac differentiation, hiPSCs were expanded on mouse embryonic fibroblasts (CellSystems GmbH, Troisdorf, Germany) in KSR medium (KnockOut DMEM, Gibco, Waltham, MA, USA) containing 10% KnockOut Serum Replacement (Gibco), 1% MEM NEAA (Gibco), 1% GlutaMAX, 0.2% β -mercaptoethanol (Gibco), and 0.5% penicillin/streptomycin (Lonza, Basel, Switzerland). Embryoid body (EB) differentiation was performed as recently described [20]. On day 21 of differentiation, CMs were isolated from other cell types using magnetic-activated cell sorting (MACS). The MultiTissue Dissociation Kit (Miltenyi Biotec, Bergisch Gladbach, Germany) was used to dissociate the EBs, and PSC-Derived Cardiomyocyte Isolation Kit, human (Miltenyi Biotec), was used to isolate CMs as described previously [31]. Isolated CMs were suspended in 20% EB medium (KnockOut DMEM containing 20% FBS (Gibco), 1% MEM NEAA, 1% GlutaMAX, and 0.5% penicillin/streptomycin).

4.4. Preparation of the 3D3C Chips and Coculture

4.4.1. Chip Manufacturing

The compartmentalized PDMS-based microfluidic device, called the 3D3C chip, originally designed for axonal isolation studies [21,22], was used to obtain neuronal soma isolation (Figure 5A). The 3D3C chip consists of two PDMS-based parts, the cell culturing part attached on glass coverslip and the medium chamber part attached on top of the cell culturing part. The cell culturing part of the chip consists of two neuronal compartments on both sides (length = 3, width = 4 mm) and a coculture compartment in the middle (length = 5, width = 4 mm). The three compartments are connected in series by 40 microtunnels (length = 250, width = 10, height = 3.5 μ m) (Figure 5A,B). The medium chamber part attached to the cell culture part consisted of three separate chambers to enable the use of cell-specific medium for each cell type.

Both parts were produced from PDMS of 10:1 base and curing agent ratio (SYLGARD 184, Dow Corning, Midland, MI, USA) using molds fabricated with the previously described combination of SU-8 photolithography and 3D printing [21,22]. The medium chambers were cut from a 4 mm thick PDMS sheet with Epilog Laser Fusion 120 W (Epilog Laser, Golden, CO, USA), 7% speed, 70% power, and 70% frequency. The larger debris was removed with pressurized air, and the medium chambers were washed using warm (+45 °C) distilled water containing dish soap and rinsed with distilled water. The medium chambers were placed in isopropanol-filled bubble bags (BuBclean, Enschede, The Netherlands) in a sonicator for 30 min, and isopropanol was replaced every 10 min, after which they were rinsed with distilled water, dried with pressurized air and cleaned with an acetone wipe. Thereafter, 5 min of sonication in isopropanol followed by distilled water rinsing and acetone wiping was repeated at least two times to remove any remaining residue from laser cutting. The parts were air-dried overnight. The 3D3C chips were imaged using scanning electron microscopy (SEM). The UltraPlus Scanning Electron Microscope (Zeiss, Oberkochen, Germany) was used for the imaging, and the 3D3C chip samples were prepared for the imaging by sputter-coating them with 4.5-nm-thick Pt/Pd.

4.4.2. Preparation of the Coculture in the 3D3C Chip

The study design is shown in Figure 5C and the detailed number of samples for each experiment and sample type are presented in Supplementary Table S3. The preparation of 3D3C chips was performed as described earlier [22]. HCl-washed glass coverslips (22 \times 22 mm) were coated with 0.25-mg/mL poly-L-ornithine (PLO, Sigma-Aldrich) for 1.5 h at +37 °C. Thereafter, coverslips were washed three times with sterile H₂O, air-dried

and stored at +4 °C. Polyvinylpyrrolidone (PVP)-treated 3D3C chips were immersed in 70% ethanol for sterilization and air-dried at RT. The 3D3C chips were assembled by manually attaching them on top of PLO-coated coverslips. The side cell culture compartments were coated with 30 µg/mL LN521, whereas the middle compartment was coated with 0.1% gelatin (Type A porcine gelatin, Sigma-Aldrich). After overnight incubation at +4 °C, the chips were ready to use.

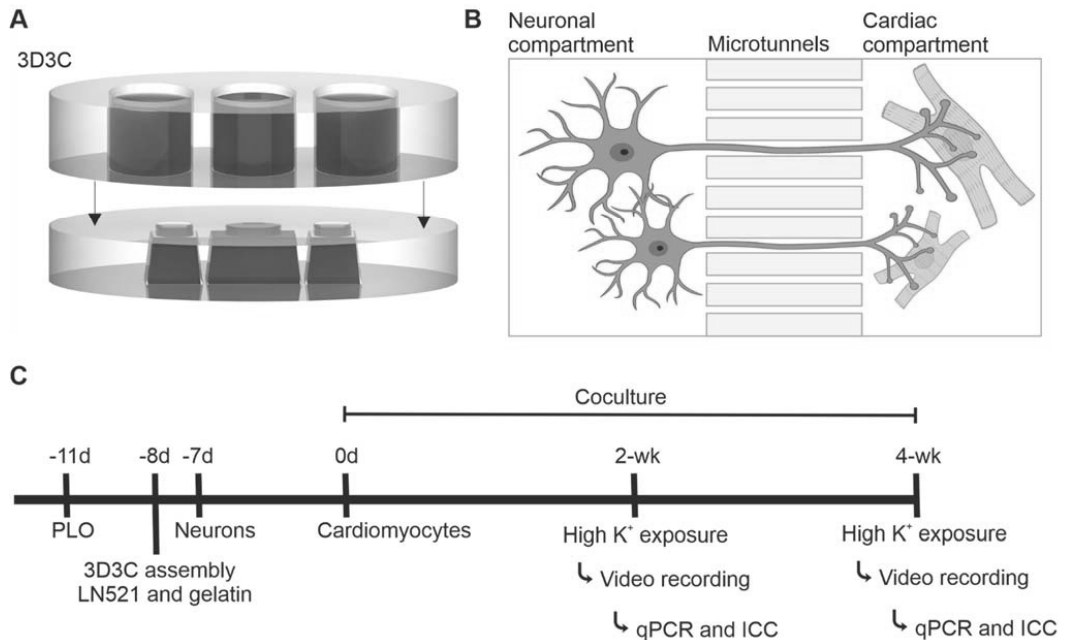


Figure 5. The compartmentalized microfluidic device (3D3C chip) and the timeline of the experiment. (A) A schematic illustration of the 3D3C chip containing two PDMS-based parts: the cell culturing part (lower) and the medium chamber part (upper). The cell culturing part had three separate compartments for the cells, and the medium chamber part had three separate chambers for each cell culture compartment. (B) A schematic illustration of the microtunnels between two cell culture compartments, allowing axonal growth into the adjacent compartment. Neurons and CMs can be cultured in their own cell compartments with their respective media. The illustration was created with BioRender.com. (C) The experimental design of the study. Neurons and CMs were cocultured for 2- or 4-week period, after which video microscopy analysis, immunocytochemical staining and RT-qPCR were performed.

Forty thousand neurons were seeded in one of the side compartments at day 32 of differentiation. Neurons were cultured alone for one week using neuronal medium in all chip compartments, after which MACS-sorted CMs were seeded in the middle compartment. A total of 3000–4000 cells produced the best CM sheets without extensive growth of unwanted cell types over the 2- or 4-week coculture. The neuronal medium was changed to both neuronal and empty side compartments whereas EB medium was changed to middle cardiac compartment three times a week. Very little medium diffusion occurred via the axonal microtunnels connecting the compartments (Figure 5A,B) [33].

Plastic and MatTek 48-well plate control samples were prepared following the same coating protocol except using 0.1 mg/mL PLO for 1 h and 15 µg/mL LN521. Wells for neurons and neuron–CM cocultures were coated with LN521, whereas wells for CMs were coated with gelatin. Neuron–CM cocultures were cultured in 1:1 neuronal and EB medium, while neuronal and cardiac monocultures were cultured in their respective media.

4.5. Analysis Methods of the Coculture in the 3D3C Chip

4.5.1. RT-qPCR

Samples were collected, and RNA was extracted with a NucleoSpin RNA kit (Macherey-Nagel, Düren, Germany) following the manufacturer's instructions immediately after video microscopy recording of CMs and chemical stimulation of neurons. Samples were lysed in buffer RA1, containing 3.5 μ L of β -mercaptoethanol separately from the neuronal and cardiac compartments, and the content of three cell-specific compartments of the 3D3C chips were pooled to make one sample. Control samples in plastic well plates were lysed similarly, with one well containing one sample. RNA was extracted from the cell lysate and eluted in 20 μ L of RNase-free H₂O provided in the kit, after which the RNA quality and concentration were measured using a NanoDrop (Thermo Scientific).

Reverse transcription was performed with a High-Capacity cDNA Reverse Transcription kit (Applied Biosystem, Waltham, MA, USA) following the manufacturer's instructions. Briefly, 10 μ L of prepared 2 \times RT Master Mix and 10 μ L of RNA sample were mixed. In some cases, RNA samples were diluted in nuclease-free water to even the RNA concentration in the reactions. Samples were then run in Mastercycler EP Gradient S (Eppendorf, Hamburg, Germany) using the following protocol: 10 min at +25 $^{\circ}$ C, 120 min at +37 $^{\circ}$ C, 5 min at +85 $^{\circ}$ C, and +4 $^{\circ}$ C until storage at -20° C.

cDNA preamplification was performed due to the low RNA concentration of the 3D3C chip samples by using 2 \times TaqMan PreAmp Master Mix (Applied Biosystem) following the manufacturer's instructions. The TaqMan 20 \times assays used are listed in Supplementary Table S2 and were tested with commercial Human Fetal Brain Total RNA (Takara Bio, Kusatsu, Japan) and Total RNA Normal Human Heart (Amsbio, Cambridge, MA, USA). Briefly, a 0.2 \times TaqMan Assay Pool was prepared using TaqMan 20 \times Assays for *ADRB2*, *ADRB3*, *CHRM2*, *MYBPC3*, *TNNT2*, *CHAT*, *TH*, *DBH*, *TUBB3*, *GAPDH*, *EEF1A1*; *EE+*, and *GUSB*. Reactions were prepared by mixing 25 μ L of TaqMan PreAmp Master Mix, 12.5 μ L of 0.2 \times TaqMan Assay Pool and 12.5 μ L of the cDNA sample. Samples were run in Mastercycler EP Gradient S using the following protocol: 10 min at +95 $^{\circ}$ C, 14 cycles of 15 s at +95 $^{\circ}$ C, and 4 min at +60 $^{\circ}$ C, 10 min at +99 $^{\circ}$ C, and at +4 $^{\circ}$ C until storage at -20° C.

qPCR for preamplified cDNA samples was performed by using TaqMan Fast Advanced Master Mix (Applied Biosystem) following the manufacturer's instructions. The same TaqMan 20 \times assays were used as in the preamplification step. Briefly, master mixes for each gene were prepared as instructed in the kit. Preamplified cDNA samples were diluted to nuclease-free water 1:5 (20 μ L of sample in 80 μ L of water). Two μ L of the diluted sample was added to 6 μ L of the master mix, and three technical replicates were used for each sample for each gene. The plates were run in a CFX384 Touch Real-Time PCR System (Bio-Rad, Hercules, CA, USA) with the following protocol: 2 min at +50 $^{\circ}$ C, 20 s at +95 $^{\circ}$ C, and 40 cycles of 3 s at +95 $^{\circ}$ C, and 30 s at +60 $^{\circ}$ C. The $2^{-\Delta\Delta C_t}$ method [43] was used to calculate the relative expression of the evaluated genes. *GAPDH*, *EEF1A1*; *EE+* and *GUSB* were used as endogenous controls. For *ADRB2*, *ADRB3*, *CHRM2*, *MYBPC3*, and *TNNT2*, a 2-week cardiac control was used for normalization, whereas for *CHAT*, *TH*, *DB*, and *TUBB3*, a 2-week neuron control was used for normalization.

4.5.2. ICC and Imaging

Immunocytochemistry (ICC) was performed at 2 and 4 weeks of coculture immediately after video microscopy recording of cardiomyocytes and chemical stimulation of neurons. The ICC protocol was used for 3D3C chip samples as described earlier [22], with the modification of washing samples with 4',6-diamidino-2-phenylindole (DAPI, 1:5000) diluted in PBS after secondary antibody incubation. The primary antibodies used included monoclonal anti-neurofilament NF-H 200 (NF-H, 1:500, mouse IgG1, N5389, Sigma-Aldrich), monoclonal anti- β -tubulin III (β III-Tub, 1:500, mouse IgG2b, T8660, Sigma-Aldrich), anti-synapsin I (SynI, 1:500, rabbit IgG, 574777, Merck, Darmstadt, Germany) and anti-troponin T (TropT, 1:750, goat IgG, ab64623, Abcam, Cambridge, UK). The secondary antibodies used included Alexa Fluor 488 (1:200, donkey anti-rabbit, A21206), Alexa Fluor 568 (1:200,

donkey anti-goat, A11057) and Alexa Fluor 647 (1:125, donkey anti-mouse, A31571, all from Thermo Fisher Scientific).

Forty-eight MatTek control samples were stained as previously described [18]. The dilutions of primary antibodies were 1:1000 for NF-H, β III-Tub and SynI and 1:1500 for TropT. The dilutions of the secondary antibodies were 1:400 for Alexa Fluor A488 and A568 and 1:200 for Alexa Fluor A647. All the samples were mounted with Vectashield including DAPI (Antifade Mounting medium with DAPI, H-1200, Vector Laboratories, Burlingame, CA, USA). The staining was visualized with an IX51 inverted fluorescence microscope (Olympus, Tokyo, Japan) and an LSM 780 laser scanning confocal microscope (Zeiss). Confocal images were deconvoluted with Hyugens and processed with Imaris (Oxford Instruments, Abingdon, UK).

4.5.3. Cardiac Video Recording and Analysis

Neurons were stimulated through the addition of a high- K^+ solution to the neuronal compartment. The extracellular solution contained 93 mM of NaCl, 10 mM of 4-(2-hydroxyethyl)-1-piperazineethanesulfonic acid (HEPES), 10 mM of D-glucose, 50 mM of KCl, 1.25 mM of NaH_2PO_4 , 2 mM of $CaCl_2$, and 1 mM of $MgCl_2$ (pH adjusted to 7.4 with NaOH). CM activity was recorded before neuronal stimulation for baseline measurement (1. Rec), during medium change in the neuronal compartment to evaluate the effect of the liquid change on CM beating (2. Rec), during neuronal high K^+ exposure to capture the immediate CM response (3. Rec) and approximately 2 min after neuronal stimulation as a follow-up (4. Rec). All videos of CM activity were recorded for 40 s at 44 fps using an Eclipse TS100 microscope (Nikon, Tokyo, Japan) and IGV-B1620M-KC000 camera (Imperx Incorporated, Boca Raton, FL, USA). MUSCLEMOTION (version 1.0) software [44] was used to extract CM beating characteristics from the videos. The data were further analyzed with R (version 4.0.2, R Foundation for Statistical Computing, Vienna, Austria) [45] using in-house-developed scripts. As a control, the high- K^+ solution was added directly to CMs, which caused the CMs to cease beating (Supplementary Videos S5–S8).

4.5.4. Statistical Analysis

Statistical analysis was performed using R and the *rstatix* (version 0.7.0) package [46]. A nonparametric Kruskal–Wallis rank sum test followed by Dunn’s post hoc test with Holm correction were used for independent samples from the qPCR analysis (6 samples for each condition) grouped by timepoint (2- or 4-week). A nonparametric Wilcoxon signed rank test was used for paired samples from video analysis (65 regions of interest from 27 chips at 2-week timepoint and 53 regions of interest from 19 chips at 4-week timepoint). A significance level of $p < 0.05$ was considered statistically significant. The data are presented as the mean \pm standard deviation in the text and as boxplots and boxplots with individual data points in the figures.

Supplementary Materials: The following supporting information can be downloaded at: <https://www.mdpi.com/article/10.3390/ijms23063148/s1>.

Author Contributions: Conceptualization, M.H., T.J., M.P.-M. and S.N.; Data curation, M.H.; Formal analysis, M.H. and S.J.; Funding acquisition, K.A.-S., P.K., M.P.-M. and S.N.; Investigation, M.H., S.J. and T.J.; Methodology, M.H., T.J., S.N. and M.P.-M.; Project administration, M.P.-M. and S.N.; Resources, K.A.-S., P.K., M.P.-M. and S.N.; Supervision, M.P.-M. and S.N.; Validation, M.H. and S.J.; Visualization, M.H. and S.J.; Writing—original draft, M.H. and S.J.; Writing—review & editing, M.H., S.J., T.J., L.S., K.T., K.A.-S., P.K., M.P.-M. and S.N. All authors have read and agreed to the published version of the manuscript.

Funding: This research was supported by grants from The Finnish Cultural Foundation (M.H.), Maud Kuistila Memorial Foundation (M.H.), Inkeri and Mauri Vänskä Foundation (M.H.), Paavo Nurmi Foundation (M.H.), Academy of Finland (grant number 336665 to S.N., 336783 to K.A.-S. and 312411 to P.K.), Finnish Foundation for Cardiovascular Research (K.A.-S.), Sigrid Juselius Foundation (K.A.-S.), and Pirkanmaa Hospital District (K.A.-S.).

Institutional Review Board Statement: Not applicable.

Informed Consent Statement: Not applicable.

Data Availability Statement: All data are available from the authors by request.

Acknowledgments: The authors thank Hanna Mäkelä, Eija Hannuksela, Markus Haponen, and Henna Lappi for technical assistance with cell maintenance and Matias Jokinen for help with laser cut protocols. SEM imaging was carried out by Anne Skogberg at the Tampere Microscopy Center (Tampere University). The work was supported by the Imaging Facility and iPS Cells Facility (Faculty of Medicine and Health Technology, Tampere University). The authors also thank Biocenter Finland for the support of the imaging and iPS cell facilities.

Conflicts of Interest: The authors declare no conflict of interest.

References

- Végh, A.M.D.; Duim, S.N.; Smits, A.M.; Poelmann, R.E.; Harkel, A.D.J.T.; DeRuiter, M.C.; Goumans, M.J.; Jongbloed, M.R.M. Part and Parcel of the Cardiac Autonomic Nerve System: Unravelling Its Cellular Building Blocks during Development. *J. Cardiovasc. Dev. Dis.* **2016**, *3*, 28. [CrossRef] [PubMed]
- Habecker, B.A.; Anderson, M.E.; Birren, S.J.; Fukuda, K.; Herring, N.; Hoover, D.B.; Kanazawa, H.; Paterson, D.J.; Ripplinger, C. Molecular and cellular neurocardiology: Development, and cellular and molecular adaptations to heart disease. *J. Physiol.* **2016**, *594*, 3853–3875. [CrossRef] [PubMed]
- Hasan, W. Autonomic cardiac innervation: Development and adult plasticity. *Organogenesis* **2013**, *9*, 176–193. [CrossRef] [PubMed]
- Merz, C.N.B.; Elboudwarej, O.; Mehta, P. The autonomic nervous system and cardiovascular health and disease. A complex balancing act. *JACC Heart Fail.* **2015**, *3*, 383–385. [CrossRef]
- Van Bilsen, M.; Patel, H.C.; Bauersachs, J.; Böhm, M.; Borggrefe, M.; Brutsaert, D.; Coats, A.J.; De Boer, R.A.; De Keulenaer, G.W.; Filippatos, G.S.; et al. The autonomic nervous system as a therapeutic target in heart failure: A scientific position statement from the Translational Research Committee of the Heart Failure Association of the European Society of Cardiology. *Eur. J. Heart Fail.* **2017**, *19*, 1361–1378. [CrossRef]
- Wang, Y.; Carmona, C.; Hickman, J.J.; Shuler, M.L. Multiorgan Microphysiological Systems for Drug Development: Strategies, Advances, and Challenges. *Adv. Healthc. Mater.* **2018**, *7*, 1701000. [CrossRef]
- Li, Q.; Wang, J.; Wu, Q.; Cao, N.; Yang, H.-T. Perspective on human pluripotent stem cell-derived cardiomyocytes in heart disease modeling and repair. *Stem Cells Transl. Med.* **2020**, *9*, 1121–1128. [CrossRef]
- Paloschi, V.; Sabater-Lleal, M.; Middeldkamp, H.; Vivas, A.; Johansson, S.; van der Meer, A.; Tenje, M.; Maegdefessel, L. Organ-on-a-chip technology: A novel approach to investigate cardiovascular diseases. *Cardiovasc. Res.* **2021**, *117*, 2742–2754. [CrossRef]
- Seidi, S.; Eftekhari, A.; Khusro, A.; Heris, R.S.; Sahibzada, M.U.K.; Gajdacs, M. Simulation and modeling of physiological processes of vital organs in organ-on-a-chip biosystem. *J. King Saud Univ.-Sci.* **2021**, *34*, 101710. [CrossRef]
- Takeuchi, A.; Nakafutami, S.; Tani, H.; Mori, M.; Takayama, Y.; Moriguchi, H.; Kotani, K.; Miwa, K.; Lee, J.-K.; Noshiro, M.; et al. Device for co-culture of sympathetic neurons and cardiomyocytes using microfabrication. *Lab Chip* **2011**, *11*, 2268–2275. [CrossRef]
- Oiwa, K.; Shimba, K.; Numata, T.; Takeuchi, A.; Kotani, K.; Jimbo, Y. A device for co-culturing autonomic neurons and cardiomyocytes using micro-fabrication techniques. *Integr. Biol.* **2016**, *8*, 341–348. [CrossRef] [PubMed]
- Sakai, K.; Shimba, K.; Ishizuka, K.; Yang, Z.; Oiwa, K.; Takeuchi, A.; Kotani, K.; Jimbo, Y. Functional innervation of human induced pluripotent stem cell-derived cardiomyocytes by co-culture with sympathetic neurons developed using a microtunnel technique. *Biochem. Biophys. Res. Commun.* **2017**, *494*, 138–143. [CrossRef] [PubMed]
- Takayama, Y.; Kida, Y.S. In Vitro Reconstruction of Neuronal Networks Derived from Human iPS Cells Using Microfabricated Devices. *PLoS ONE* **2016**, *11*, e0148559. [CrossRef] [PubMed]
- Winbo, A.; Ramanan, S.; Eugster, E.; Jovinge, S.; Skinner, J.R.; Montgomery, J.M. Functional coculture of sympathetic neurons and cardiomyocytes derived from human-induced pluripotent stem cells. *Am. J. Physiol. Circ. Physiol.* **2020**, *319*, H927–H937. [CrossRef]
- Takayama, Y.; Kushige, H.; Akagi, Y.; Suzuki, Y.; Kumagai, Y.; Kida, Y.S. Selective Induction of Human Autonomic Neurons Enables Precise Control of Cardiomyocyte Beating. *Sci. Rep.* **2020**, *10*, 9464. [CrossRef]
- McGonigle, P.; Ruggeri, B. Animal models of human disease: Challenges in enabling translation. *Biochem. Pharmacol.* **2014**, *87*, 162–171. [CrossRef]
- Passier, R.; Orlova, V.; Mummery, C. Complex Tissue and Disease Modeling using hiPSCs. *Cell Stem Cell* **2016**, *18*, 309–321. [CrossRef]
- Hyvärinen, T.; Hyysalo, A.; Kapucu, F.E.; Aarnos, L.; Vinogradov, A.; Eglen, S.J.; Ylä-Outinen, L.; Narkilahti, S. Functional characterization of human pluripotent stem cell-derived cortical networks differentiated on laminin-521 substrate: Comparison to rat cortical cultures. *Sci. Rep.* **2019**, *9*, 17125. [CrossRef]
- Prajapati, C.; Pölönen, R.-P.; Aalto-Setälä, K. Simultaneous recordings of action potentials and calcium transients from human induced pluripotent stem cell derived cardiomyocytes. *Biol. Open* **2018**, *7*, bio035030. [CrossRef]

20. Prajapati, C.; Ojala, M.; Lappi, H.; Aalto-Setälä, K.; Pekkanen-Mattila, M. Electrophysiological evaluation of human induced pluripotent stem cell-derived cardiomyocytes obtained by different methods. *Stem Cell Res.* **2021**, *51*, 102176. [CrossRef]
21. Ristola, M.; Sukki, L.; Azevedo, M.M.; Seixas, A.I.; Relvas, J.B.; Narkilahti, S.; Kallio, P. A compartmentalized neuron-oligodendrocyte co-culture device for myelin research: Design, fabrication and functionality testing. *J. Micromech. Microeng.* **2019**, *29*, 65009. [CrossRef]
22. Ristola, M.; Fedele, C.; Hagman, S.; Sukki, L.; Kapucu, F.E.; Mzezewa, R.; Hyvärinen, T.; Kallio, P.; Priimagi, A.; Narkilahti, S. Directional Growth of Human Neuronal Axons in a Microfluidic Device with Nanotopography on Azobenzene-Based Material. *Adv. Mater. Interfaces* **2021**, *8*, 2100048. [CrossRef]
23. Gummy, L.F.; Yeo, G.S.; Tung, Y.-C.L.; Zivraj, K.H.; Willis, D.; Coppola, G.; Lam, B.Y.; Twiss, J.L.; Holt, C.E.; Fawcett, J.W. Transcriptome analysis of embryonic and adult sensory axons reveals changes in mRNA repertoire localization. *RNA* **2010**, *17*, 85–98. [CrossRef] [PubMed]
24. Corradi, E.; Baudet, M.-L. In the Right Place at the Right Time: miRNAs as Key Regulators in Developing Axons. *Int. J. Mol. Sci.* **2020**, *21*, 8726. [CrossRef]
25. Lymperopoulos, A.; Cora, N.; Maning, J.; Brill, A.R.; Sizova, A. Signaling and function of cardiac autonomic nervous system receptors: Insights from the GPCR signalling universe. *FEBS J.* **2021**, *288*, 2645–2659. [CrossRef]
26. Assefa, A.T.; Vandesompele, J.; Thas, O. Correction: On the utility of RNA sample pooling to optimize cost and statistical power in RNA sequencing experiments. *BMC Genom.* **2020**, *21*, 312. [CrossRef] [PubMed]
27. Kitsara, M.; Kontziampasis, D.; Agbulut, O.; Chen, Y. Heart on a chip: Micro-nanofabrication and microfluidics steering the future of cardiac tissue engineering. *Microelectron. Eng.* **2019**, *203–204*, 44–62. [CrossRef]
28. Kim, S.H.; Im, S.-K.; Oh, S.-J.; Jeong, S.; Yoon, E.-S.; Lee, C.J.; Choi, N.; Hur, E.-M. Anisotropically organized three-dimensional culture platform for reconstruction of a hippocampal neural network. *Nat. Commun.* **2017**, *8*, 14346. [CrossRef]
29. Wells, D.G. mRNA translation: Regulating an out of soma experience. *Curr. Opin. Cell Biol.* **2012**, *24*, 554–557. [CrossRef]
30. Liu, X.; Zhang, Z.; Zhang, R.; Gregg, S.; Meng, H.; Chopp, M. Comparison of in vivo and in vitro gene expression profiles in subventricular zone neural progenitor cells from the adult mouse after middle cerebral artery occlusion. *Neuroscience* **2007**, *146*, 1053–1061. [CrossRef]
31. Pekkanen-Mattila, M.; Häkli, M.; Pölönen, R.-P.; Mansikkala, T.; Junnila, A.; Talvitie, E.; Koivisto, J.T.; Kellomäki, M.; Aalto-Setälä, K. Polyethylene Terephthalate Textiles Enhance the Structural Maturation of Human Induced Pluripotent Stem Cell-Derived Cardiomyocytes. *Materials* **2019**, *12*, 1805. [CrossRef] [PubMed]
32. De Leeuw, S.M.; Davaz, S.; Wanner, D.; Milleret, V.; Ehrbar, M.; Gietl, A.; Tackenberg, C. Increased maturation of iPSC-derived neurons in a hydrogel-based 3D culture. *J. Neurosci. Methods* **2021**, *360*, 109254. [CrossRef] [PubMed]
33. Pelkonen, A.; Mzezewa, R.; Sukki, L.; Rynnänen, T.; Kreutzer, J.; Hyvärinen, T.; Vinogradov, A.; Aarnos, L.; Lekkala, J.; Kallio, P.; et al. A modular brain-on-a-chip for modelling epileptic seizures with functionally connected human neuronal networks. *Biosens. Bioelectron.* **2020**, *168*, 112553. [CrossRef] [PubMed]
34. Shaffer, F.; McCraty, R.; Zerr, C.L. A healthy heart is not a metronome: An integrative review of the heart's anatomy and heart rate variability. *Front. Psychol.* **2014**, *5*, 1040. [CrossRef]
35. Oh, Y.; Cho, G.-S.; Li, Z.; Hong, I.; Zhu, R.; Kim, M.-J.; Kim, Y.J.; Tampakakis, E.; Tung, L.; Hugarir, R.; et al. Functional Coupling with Cardiac Muscle Promotes Maturation of hPSC-Derived Sympathetic Neurons. *Cell Stem Cell* **2016**, *19*, 95–106. [CrossRef] [PubMed]
36. Frith, T.J.; Gogolou, A.; Hackland, J.O.; Hewitt, Z.A.; Moore, H.D.; Barbaric, I.; Thapar, N.; Burns, A.J.; Andrews, P.W.; Tsakiridis, A.; et al. Retinoic Acid Accelerates the Specification of Enteric Neural Progenitors from In-Vitro-Derived Neural Crest. *Stem Cell Rep.* **2020**, *15*, 557–565. [CrossRef]
37. Wind, M.; Tsakiridis, A. In Vitro Generation of Posterior Motor Neurons from Human Pluripotent Stem Cells. *Curr. Protoc.* **2021**, *1*, e244. [CrossRef]
38. Paavilainen, T.; Pelkonen, A.; Mäkinen, M.E.-L.; Peltola, M.; Huhtala, H.; Fayuk, D.; Narkilahti, S. Effect of prolonged differentiation on functional maturation of human pluripotent stem cell-derived neuronal cultures. *Stem Cell Res.* **2018**, *27*, 151–161. [CrossRef]
39. Rynnänen, T.; Mzezewa, R.; Meriläinen, E.; Hyvärinen, T.; Lekkala, J.; Narkilahti, S.; Kallio, P. Transparent Microelectrode Arrays Fabricated by Ion Beam Assisted Deposition for Neuronal Cell In Vitro Recordings. *Micromachines* **2020**, *11*, 497. [CrossRef]
40. Kiamehr, M.; Klettner, A.; Richert, E.; Koskela, A.; Koistinen, A.; Skottman, H.; Kaarniranta, K.; Aalto-Setälä, K.; Juuti-Uusitalo, K. Compromised Barrier Function in Human Induced Pluripotent Stem-Cell-Derived Retinal Pigment Epithelial Cells from Type 2 Diabetic Patients. *Int. J. Mol. Sci.* **2019**, *20*, 3773. [CrossRef]
41. Ojala, M.; Rajala, K.; Pekkanen-Mattila, M.; Miittinen, M.; Huhtala, H.; Aalto-Setälä, K. Culture Conditions Affect Cardiac Differentiation Potential of Human Pluripotent Stem Cells. *PLoS ONE* **2012**, *7*, e48659. [CrossRef] [PubMed]
42. Hongisto, H.; Ilmarinen, T.; Vattulainen, M.; Mikhailova, A.; Skottman, H. Xeno- and feeder-free differentiation of human pluripotent stem cells to two distinct ocular epithelial cell types using simple modifications of one method. *Stem Cell Res. Ther.* **2017**, *8*, 291. [CrossRef] [PubMed]
43. Livak, K.J.; Schmittgen, T.D. Analysis of relative gene expression data using real-time quantitative PCR and the 2⁻ΔΔCT Method. *Methods* **2001**, *25*, 402–408. [CrossRef] [PubMed]

44. Sala, L.; van Meer, B.J.; Tertoolen, L.G.; Bakkers, J.; Bellin, M.; Davis, R.P.; Denning, C.N.; Dieben, M.A.; Eschenhagen, T.; Giacomelli, E.; et al. Musclemotion: A versatile open software tool to quantify cardiomyocyte and cardiac muscle contraction in vitro and in vivo. *Circ. Res.* **2018**, *122*, e5–e16. [CrossRef]
45. R Core Team. *R: A Language and Environment for Statistical Computing*; R Foundation for Statistical Computing: Vienna, Austria, 2020.
46. Kassambra, A. Rstatix: Pipe-Friendly Framework for Basic Statistical Tests. R Package Version 0.7.0. 2021. Available online: <https://CRAN.R-project.org/package=rstatix> (accessed on 6 February 2022).

PUBLICATION
III

**Human induced pluripotent stem cell-based platform for modeling
cardiac ischemia**

Martta Häkli, Joose Kreutzer, Antti-Juhana Mäki, Hannu Välimäki, Henna Lappi, Heini Huhtala, Pasi Kallio, Katriina Aalto-Setälä and Mari Pekkanen-Mattila

Scientific Reports (2021), 11(4153)
<https://doi.org/10.1038/s41598-021-83740-w>

Publication reprinted with the permission of the copyright holders.



OPEN Human induced pluripotent stem cell-based platform for modeling cardiac ischemia

Martta Häkli¹✉, Joose Kreutzer², Antti-Juhana Mäki², Hannu Välimäki², Henna Lappi¹, Heini Huhtala³, Pasi Kallio², Katriina Aalto-Setälä¹ & Mari Pekkanen-Mattila¹

Ischemic heart disease is a major cause of death worldwide, and the only available therapy to salvage the tissue is reperfusion, which can initially cause further damage. Many therapeutics that have been promising in animal models have failed in human trials. Thus, functional human based cardiac ischemia models are required. In this study, a human induced pluripotent stem cell derived-cardiomyocyte (hiPSC-CM)-based platform for modeling ischemia–reperfusion was developed utilizing a system enabling precise control over oxygen concentration and real-time monitoring of the oxygen dynamics as well as iPSC-CM functionality. In addition, morphology and expression of hypoxia-related genes and proteins were evaluated as hiPSC-CM response to 8 or 24 h hypoxia and 24 h reoxygenation. During hypoxia, initial decrease in hiPSC-CM beating frequency was observed, after which the CMs adapted to the conditions and the beating frequency gradually increased already before reoxygenation. During reoxygenation, the beating frequency typically first surpassed the baseline before settling down to the values close the baseline. Furthermore, slowing on the field potential propagation throughout the hiPSC-CM sheet as well as increase in depolarization time and decrease in overall field potential duration were observed during hypoxia. These changes were reversed during reoxygenation. Disorganization of sarcomere structures was observed after hypoxia and reoxygenation, supported by decrease in the expression of sarcomeric proteins. Furthermore, increase in the expression of gene encoding glucose transporter 1 was observed. These findings indicate, that despite their immature phenotype, hiPSC-CMs can be utilized in modeling ischemia–reperfusion injury.

Ischemic heart disease (IHD) is the most common cardiovascular disease and a major cause of death worldwide¹. In IHD, blood flow to myocardium is reduced or blocked leading to oxygen and nutrient deprivation, and accumulation of metabolic waste in the tissue. This causes damage and death to the cells in the myocardium, including cardiomyocytes (CMs) that are responsible for contraction of heart². While a lot of research resources has been invested to the study of the disease, reperfusion, i.e. restoring blood flow to the ischemic tissue, is currently the only available therapy to reduce damage to the ischemic area in addition to prevention of arrhythmias by anti-arrhythmic medication. However, reperfusion itself causes further damage to the tissue. Animal experiments have provided promising results for medical interventions at the time of reperfusion, but they have failed in human clinical trials³. As the difference between species is considered to be one reason behind the failure^{4,5}, it is important to establish functional human based models to evaluate and develop new therapies.

Human induced pluripotent stem cells (hiPSCs) can be endlessly produced and efficiently differentiated into cardiomyocytes (hiPSC-CMs) enabling development of human-based cell models for the research of cardiac diseases and therapies⁶. However, hiPSC-CMs are developmentally immature and structurally, functionally and metabolically resemble more fetal than adult CMs⁷. Especially, the metabolic immaturity affects the use of the hiPSC-CMs in ischemia modeling, as their metabolism relies on glucose making them more resistant to hypoxia and reperfusion. Adult CMs mainly utilize fatty acid oxidation in energy production and thus are more vulnerable to oxidative stress than fetal CMs^{8–10}.

Despite their drawbacks, hiPSC-CM based ischemia–reperfusion models have lately emerged^{8–23} and these models have been reported to recapitulate the typical cardiac ischemia responses in the cells, such as increased

¹Heart Group, Faculty of Medicine and Health Technology, Tampere University, Arvo Ylpön katu 34, 33520 Tampere, Finland. ²Micro- and Nanosystems Research Group, Faculty of Medicine and Health Technology, Tampere University, Tampere, Finland. ³Faculty of Social Sciences, Tampere University, Tampere, Finland. ✉email: martta.hakli@tuni.fi

cell death^{8–10} and disruption of the sarcomere structure^{9,10}. Furthermore, changes in the functionality and electrophysiology have been observed, including decrease in hiPSC-CM beating frequency^{11,12,15,16,24}, contractility, calcium overload and arrhythmias¹⁴. In these models, hypoxic conditions have been induced to the hiPSC-CMs by multiple methods, such as by using hypoxic gas^{8–10,13–15,24,25} or causing oxidative stress via peroxide treatment¹⁶. In addition, cell culture media composition has been modified to better recapitulate the ischemic conditions in several studies. The modifications include removal of glucose²³ or serum¹¹, or both^{8–10,13,14,22}, as well as acidosis to better mimic the physiological ischemic event^{8–10,13,22}.

In this study, we present a hiPSC-CM based platform for modeling cardiac ischemia–reperfusion. The base of the platform is an OxyGenie mini-incubator²⁶ combined with a microelectrode array (MEA) and a luminescence-based oxygen sensor^{12,24}. The system allows precise control over oxygen concentration, real-time monitoring of the cardiomyocyte functionality as well as the measurement of oxygen level in the cell culture area during hypoxia and reoxygenation without disturbing or interrupting the experiment. The main objective of the present study was develop a platform to assess the functional, structural and molecular responses of hiPSC-CMs to ischemia and reperfusion. The hiPSC-CMs were combined with an extensive set of analysis methods including a microelectrode array and oxygen measurement. In addition, the platform is compatible with collecting and analyzing samples for immunocytochemistry, qPCR and western blot. As the studies on the electrophysiology and functionality of hiPSC-CMs under hypoxia and reoxygenation are very limited in their number, this study strongly contributes to the hiPSC-CM based ischemia–reperfusion modeling.

Results

hiPSC-CM functionality during hypoxia and reoxygenation. Functionality of the hiPSC-CMs was studied with MEA to evaluate changes in the beating characteristics of the hiPSC-CMs during hypoxia and reoxygenation. For beating frequency, signals from 41 electrodes were analyzed (4–6 electrodes from 9 samples, 3 parallel samples from 3 differentiation batches). The luminescence-based oxygen measurement was incorporated to one sample to evaluate the oxygen dynamics of the platform. It was observed that after initiation of hypoxia or reoxygenation, the oxygen level in the culture stabilized within four hours. Clear and repeatable changes were observed in the beating frequency of the hiPSC-CMs during hypoxia and reoxygenation, which together with the observed oxygen dynamics were used to divide hypoxia and reoxygenation to periods for statistical analysis.

For beating frequency analysis, hypoxia was divided into two periods, 7–15 h hypoxia and 15–24 h hypoxia, as during 7–15 h hypoxia the oxygen level had already stabilized and the beating frequency of the hiPSC-CMs was lowest, while it gradually started to increase during 15–24 h of hypoxia. Reoxygenation was divided into two groups as well; 0–6 h reoxygenation to observe the immediate increase of the beating frequency during the increase of the pO₂, and 6–24 h reoxygenation, during which the beating of the hiPSC-CMs stabilized. Figure 1a presents a representative measurement of pO₂ and a normalized beating frequency from a single electrode of one MEA measurement, while Fig. S1 presents examples of a normalized beating rate from other experiments. Fig. S2 presents a representative MEA signal during different time points of hypoxia and reoxygenation and Fig. S3 presents the post-calibration of the oxygen measurement.

Beating frequency (beats per minute, BPM) was normalized for each electrode to a median baseline BPM value so that the results are comparable despite the differences in the baseline BPM. Median baseline BPM value was chosen for normalization instead of mean so that individual time points that deviate much from the baseline do not affect the normalization. The baseline was determined from measurements of 20 h before initiation of hypoxia and it was relatively stable throughout the time period. Mean of the normalized beating frequency of all the chosen electrodes at baseline was 1.081 ± 0.173 and started to decrease after hypoxia started. During 7–15 h hypoxia, the normalized beating frequency was 0.358 ± 0.336 ($p = 2.4 \times 10^{-8}$ compared to baseline) and during 15–24 h hypoxia, it increased to 0.656 ± 0.402 ($p = 8.8 \times 10^{-7}$ compared to baseline and $p = 2.6 \times 10^{-5}$ compared to 7–15 h hypoxia). During 0–6 h reoxygenation, the normalized beating frequency increased to 1.274 ± 0.396 ($p = 0.015$ compared to baseline and $p = 2.8 \times 10^{-8}$ compared to 15–24 h hypoxia) and then decreased close to the baseline level during 6–24 h reoxygenation, to 0.981 ± 0.333 ($p = 3.0 \times 10^{-6}$ compared to 0–6 h reoxygenation). Figure 1b presents the mean normalized beating frequency at the baseline, 7–15 h hypoxia, 15–24 h hypoxia, 0–6 h reoxygenation and 6–24 h reoxygenation.

Depolarization time and field potential duration (FPD) were evaluated from three samples at two timepoints of baseline measurement ($n_{\text{spikes}} = 19$ for both time points for all three samples), as well as from one sample after 6.5 h ($n_{\text{spikes}} = 4$) and from two samples after 8 h hypoxia ($n_{\text{spikes}} = 4$ for both samples), depending on whether beating had stopped already at 8 h. Depolarization time and FPD were also evaluated from the three samples after 24 h of hypoxia ($n_{\text{spikes}} = 13$ for all three samples), and 6 h ($n_{\text{spikes}} = 17$ for all three samples) and 24 h ($n_{\text{spikes}} = 14$ for all three samples) of reoxygenation. Depolarization time was determined as the time from the first peak to the second peak, whereas FPD was determined as the time from the first peak to the flat peak as shown in Fig. S4. Both parameters were normalized for each sample to the mean of their own baseline values. As a response to hypoxia, depolarization time increased while the total FPD decreased, whereas during reoxygenation, both values returned close to the baseline level again, as demonstrated in Fig. 1c,d. Compared to baseline, the mean depolarization time increased 1.26 ± 0.09 -fold at 6.5 h hypoxia ($p = 0.0044$), 1.65 ± 0.43 -fold at 8 h hypoxia ($p = 1.3 \times 10^{-5}$) and 1.49 ± 0.27 -fold at 24 h hypoxia ($p = 8.67 \times 10^{-17}$). At 6 h reoxygenation, the increase was 1.15 ± 0.24 -fold ($p = 0.00033$ compared to baseline, $p = 2.64 \times 10^{-7}$ compared to 24 h hypoxia) whereas at 24 h reoxygenation it was 1.52 ± 0.92 -fold (not significant) compared to baseline. On the other hand, compared to baseline, the total field potential duration decreased to 0.75 ± 0.01 at 6.5 h hypoxia ($p = 0.0007$), 0.87 ± 0.25 at 8 h hypoxia (not significant), and then increased to 0.96 ± 0.15 at 24 h hypoxia ($p = 0.0085$), 0.92 ± 0.14 at 6 h reoxygenation ($p = 1.0 \times 10^{-5}$), and 0.97 ± 0.19 at 24 h reoxygenation (not significant).

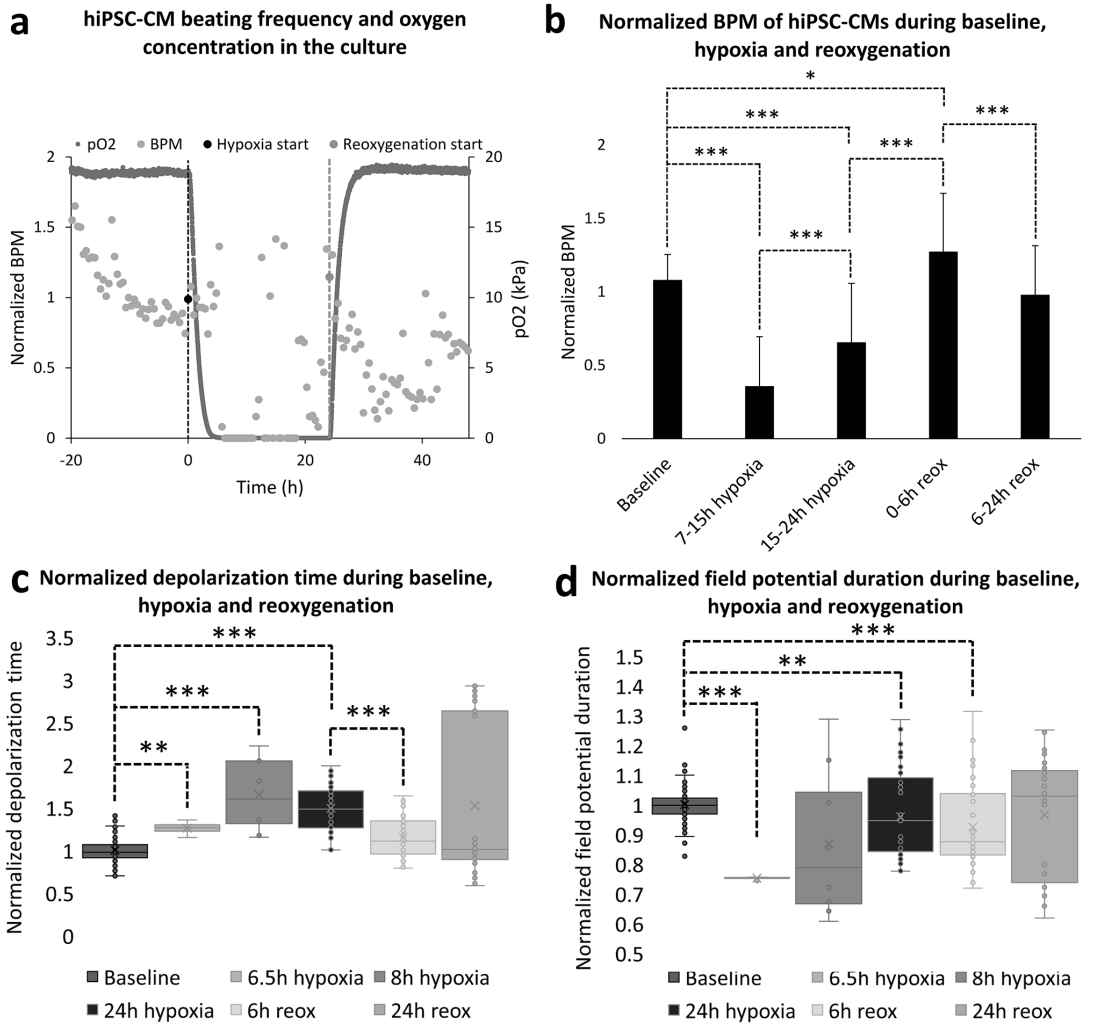


Figure 1. (a) Representative measurement of the partial pressure of oxygen and normalized beating frequency from a single experiment. Black line marks the initiation of hypoxia, after which the oxygen level of the culture starts to decrease and reaches 0 kPa approximately within 4 h. Green line marks the initiation of reoxygenation, after which the oxygen level starts to increase and reaches 19 kPa approximately within 4 h of reoxygenation. The beating frequency of the hiPSC-CMs clearly decreases during hypoxia and increases after reoxygenation. (b) The mean normalized beating frequency extracted from MEA recordings for hiPSC-CMs during baseline measurement, 7–15 h hypoxia, 15–24 h hypoxia, 0–6 h reoxygenation and 6–24 h reoxygenation presented as mean + standard deviation ($n_{\text{electrodes}} = 41$). Normalization is done to each electrode separately with regard to median baseline value, due to the variation observed in the beating frequency between different electrodes during baseline measurements. The beating frequency starts to decrease after hypoxia is initiated and was observed to be on its lowest during 7–15 h of hypoxia. The beating frequency started to recover already before reoxygenation was initiated and was statistically significantly greater during 15–24 h hypoxia compared to 7–15 h hypoxia. Furthermore, overcompensation in the beating frequency was observed during 0–6 h of reoxygenation, when the mean normalized beating frequency exceeded the baseline. After 6 h reoxygenation, the beating frequency returned close to the baseline level. (c) Normalized depolarization time of hiPSC-CMs at baseline, 6.5 h, 8 h and 24 h hypoxia as well as 6 h and 24 h reoxygenation. Depolarization time increased during hypoxia and returned close to the baseline level during reoxygenation. (d) Normalized field potential duration (FPD) of hiPSC-CMs at baseline, 6.5 h, 8 h and 24 h hypoxia as well as 6 h and 24 h reoxygenation. FPD decreased during hypoxia and returned close to the baseline level during reoxygenation * $p < 0.05$, ** $p < 0.01$, *** $p < 0.001$.

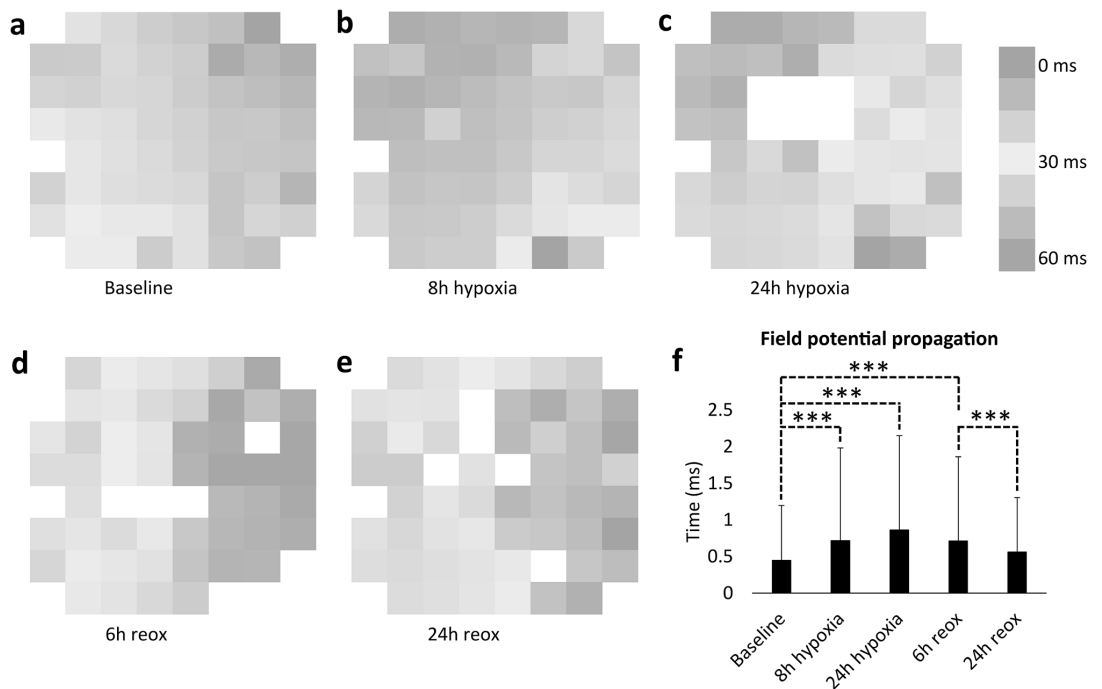


Figure 2. (a–e) Field potential propagation over hiPSC-CM sheet on microelectrode array at baseline before hypoxia, at 8 h and 24 h hypoxia and at 6 h and 24 h reoxygenation. The heatmaps clearly indicate slowing of the field potential conduction during hypoxia, but the conduction velocity is restored during reoxygenation. (f) Field potential conduction time from electrode to electrode at baseline, 8 h and 24 h hypoxia, and 6 h and 24 h reoxygenation (mean + standard deviation). Conduction time increased during hypoxia compared to baseline, whereas it was restored close to baseline level during reoxygenation. *** $p < 0.001$.

Signal propagation was evaluated at two baseline timepoints, as well as after 8 h and 24 h hypoxia and 6 h and 24 h reoxygenation from all signals of all electrodes of two samples that were showing field potential signals. The conduction velocity was observed to slow down during hypoxia and increase close to the baseline level during reoxygenation, as shown in Fig. 2a–f. At baseline, the mean duration of field potential propagation from one electrode to the adjacent (in x or y direction) was observed to be 0.45 ± 0.75 ms, whereas it was 0.72 ± 1.26 at 8 h hypoxia ($p = 6.4 \times 10^{-18}$), 0.86 ± 1.29 ms at 24 h hypoxia ($p = 5.2 \times 10^{-33}$). At 6 h reoxygenation, the time was observed to be 0.71 ± 1.15 ms ($p = 1.1 \times 10^{-40}$ compared to baseline) and at 24 h reoxygenation it was 0.56 ± 0.74 ms ($p = 3.8 \times 10^{-5}$ compared to 6 h reoxygenation).

hiPSC-CM morphology, sarcomere structure and nucleus size. The morphology, sarcomere structure, nucleus size and HIF1 α expression of the hiPSC-CMs was studied with immunocytochemistry. After exposure to hypoxia or hypoxia-reoxygenation, hiPSC-CMs were immunolabeled against MyBPC3 and HIF1 α and cell nuclei were visualized with DAPI (Fig. 3a). 6 hypoxia and control samples (2 parallel samples from 3 differentiation batches) from both 8 and 24 h experiments as well as 4 hypoxia-reoxygenation samples (2 parallel samples from 2 differentiation batches) from both 8 and 24 h experiments were stained and imaged. Qualitative analysis revealed changes in the cell morphology, expression of sarcomeres and the size of the nuclei, which were then quantitated and determined statistically significant. However, the expression of HIF1 α was not found to increase in any of the used time points.

Quantitative analysis on sarcomere expression and nuclei size of the cells revealed statistically significant differences in these parameters between hypoxia or hypoxia-reoxygenation and control samples (Fig. 3b,c). Sarcomere coverage was analyzed from 124 images of control samples, 47 images of 8 h hypoxia samples and 50 images of 24 h hypoxia samples. The mean coverage of clear and distinguishable sarcomeres of the total area of the MyBPC3 staining in control samples was $69.4 \pm 24.0\%$, whereas for 8 and 24 h hypoxia samples it was $30.1 \pm 36.0\%$ ($p = 4.3 \times 10^{-10}$) and $16.1 \pm 24.8\%$ ($p = 6.1 \times 10^{-18}$), respectively. Nucleus area was analyzed from the fluorescent microscopy images ($n_{8h \text{ hypoxia-reox}} = 18$, $n_{24h \text{ hypoxia-reox}} = 21$) using CellProfiler. The mean nucleus area was $35.7 \pm 16.4 \mu\text{m}^2$ for control samples ($n_{\text{nuclei}} = 3632$), whereas for 8 and 24 h hypoxia samples it was respectively $27.2 \pm 15.2 \mu\text{m}^2$ ($n_{\text{nuclei}} = 685$, $p = 8.9 \times 10^{-43}$) and $22.3 \pm 13.5 \mu\text{m}^2$ ($n_{\text{nuclei}} = 833$, $p = 1.5 \times 10^{-115}$), and 8 and 24 h

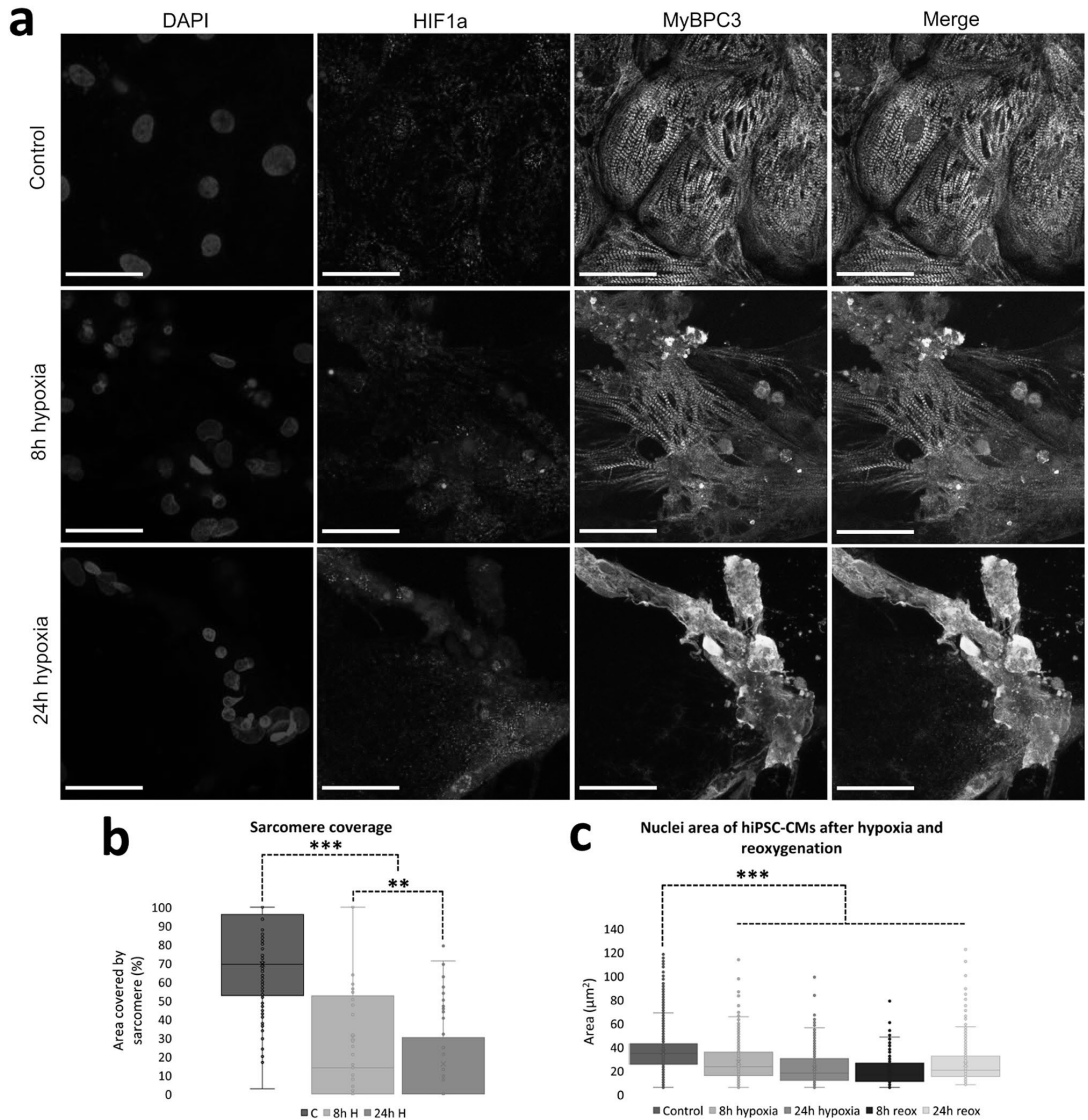


Figure 3. (a) The structure, sarcomere expression and nucleus size changes during hypoxia. Sarcomeres (MyBPC3, yellow) are clearly visible and the cells are spread and properly attached to the plate in control ($n_{\text{images}} = 124$) samples, whereas the cell structure seems to deteriorate after 8 h ($n_{\text{images}} = 47$) and 24 h ($n_{\text{images}} = 50$) hypoxia. Furthermore, the nucleus (DAPI, blue) size seems to decrease. On the other hand, no significant changes are seen in the expression of hypoxia marker HIF1 α (magenta). (b) Sarcomere coverage was quantified from the fluorescent images and calculated as the ratio between the area of visible sarcomeres to the total cell area and is expressed as percentage. The data are presented as mean + standard deviation. The expression of clear and visible sarcomeres decreases as the length of the hypoxia increases. (c) Area of the nuclei in control ($n_{\text{nuclei}} = 3632$), 8 h hypoxia ($n_{\text{nuclei}} = 685$), 24 h hypoxia ($n_{\text{nuclei}} = 833$), 8 h hypoxia-reoxygenation ($n_{\text{nuclei}} = 329$) and 24 h hypoxia-reoxygenation ($n_{\text{nuclei}} = 782$) samples presented as mean + standard deviation. The area of the nuclei decreases with hypoxia and reoxygenation compared to control. ** $p < 0.01$; *** $p < 0.001$.

hypoxia-reoxygenation samples it was respectively $19.8 \pm 11.1 \mu\text{m}^2$ ($n_{\text{nuclei}} = 329$, $p = 5.1 \times 10^{-74}$) and $25.4 \pm 14.6 \mu\text{m}^2$ ($n_{\text{nuclei}} = 782$, $p = 8.5 \times 10^{-74}$).

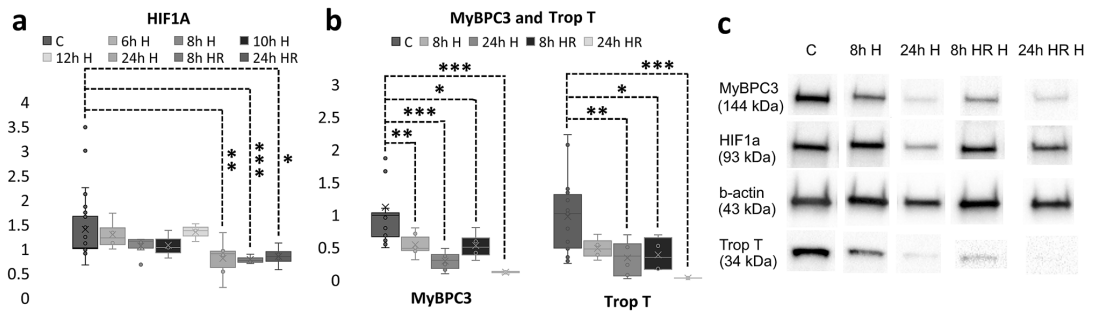


Figure 4. (a) HIF1 α expression in control ($n=26$) samples and in 6 h ($n=4$), 8 h ($n=6$), 10 h ($n=3$), 12 h ($n=3$) and 24 h ($n=6$) hypoxia or 8 h ($n=4$) and 24 h ($n=4$) hypoxia-reoxygenation time points from western blot analysis presented as mean + standard deviation. During the first 12 h of hypoxia, there seems to be no significant changes in the expression of the protein, although in 6 h and 12 h samples there is a slight increase. On the other hand, after 24 h of hypoxia, as well as after 8 h hypoxia-reoxygenation there is a statistically significant decrease in the HIF1 α expression. (b) Expression of MyBPC3 and Troponin T decreases during 8 h ($n=6$) and 24 h ($n=6$) hypoxia, and 8 h ($n=4$) and 24 h ($n=4$) hypoxia-reoxygenation compared to control ($n=20$) samples. The expression is especially low in 24 h hypoxia-reoxygenation samples but has decreased also in other hypoxia samples. (c) Examples of the western blot bands. * $p < 0.05$; ** $p < 0.01$; *** $p < 0.001$.

Western blot of HIF1 α , MyBPC3 and Troponin T. Western blot was used to quantitate the expression of HIF1 α , MyBPC3 and Troponin T after hypoxia or hypoxia-reoxygenation. After 6 h ($n=4$, 1 differentiation batch), 8 h ($n=6$, 2 parallel samples from 3 differentiation batches), 10 h ($n=3$, 1 differentiation batch) and 12 h ($n=3$, 1 differentiation batch) hypoxia, the HIF1 α expression remained close to control ($n=26$, 4–5 parallel samples from 6 differentiation batches), but after 24 h hypoxia as well as 8 and 24 h hypoxia-reoxygenation ($n=4$ for both time points, 2 parallel samples from 2 differentiation batches), there was a statistically significant decrease in the HIF1 α expression (Fig. 4a). The mean expression of HIF1 α in control samples was 1.39 ± 0.68 , whereas for 6, 8, 10, 12 and 24 h hypoxia samples it was respectively 1.29 ± 0.32 , 1.05 ± 0.20 , 1.06 ± 0.20 , 1.34 ± 0.18 and 0.80 ± 0.39 ($p=0.006$). For 8 and 24 h hypoxia-reoxygenation samples, the expression of HIF1 α was 0.77 ± 0.08 ($p=0.001$) and 0.84 ± 0.23 ($p=0.031$), respectively.

There were statistically significant decreases in the expressions of MyBPC3 and Troponin T after hypoxia and hypoxia-reoxygenation (Fig. 4b). The mean MyBPC3 expression in the control samples was 1.11 ± 0.76 , whereas for 8 and 24 h hypoxia samples it was 0.53 ± 0.18 ($p=0.006$) and 0.28 ± 0.32 ($p=0.000009$), respectively. For 8 and 24 h hypoxia-reoxygenation samples the expression of MyBPC3 was 0.52 ± 0.22 ($p=0.023$) and 0.11 ± 0.02 ($p=0.0002$), respectively. As for Troponin T, the mean expression in the control samples was 0.96 ± 0.55 . For 8 and 24 h hypoxia samples, the expression was respectively 0.47 ± 0.14 and 0.32 ± 0.27 ($p=0.007$), while for 8 and 24 h hypoxia-reoxygenation samples the expression was 0.37 ± 0.26 ($p=0.037$) and 0 ($p=0.0002$), respectively. In 24 h hypoxia-reoxygenation samples, the Troponin T band did not become visible with exposure times suitable for control samples. Examples of the western blot bands are presented in Fig. 4c, whereas full length blots of the examples are presented in Supplementary Figures S5–S6.

Gene expression of hiPSC-CMs. Expression of several genes related to glucose and fatty acid metabolism, calcium handling, sarcomeric proteins, hypoxia and apoptosis was analyzed from samples from 8 h ($n_{\text{hypoxia}}=6$, $n_{\text{control}}=5$, 1–2 parallel samples from 3 differentiation batches) and 24 h ($n_{\text{hypoxia}}=5$, $n_{\text{control}}=6$, 1–2 parallel samples from 3 differentiation batches) hypoxia and 8 and 24 h hypoxia-reoxygenation experiments ($n_{\text{hypoxia}}=4$, $n_{\text{control}}=4$ for both time points, 2 parallel samples from 2 differentiation batches) with qPCR. There were no statistically significant differences in the expression of most genes after 8 or 24 h hypoxia. However, after 24 h hypoxia-reoxygenation, there was a statistically significant decrease in several genes. A statistically significant increase was observed in the expression of SLC2A1 encoding glucose transporter 1 in all but 8 h hypoxia-reoxygenation samples (Fig. 5a). For 8 h control and hypoxia samples, the mean expressions of SLC2A1 were 1.70 ± 1.65 and 28.32 ± 24.13 ($p=0.03$), respectively. For 24 h control and hypoxia samples, the expressions were 1.88 ± 1.33 and 48.22 ± 42.47 ($p=0.004$), respectively. For 8 h control and hypoxia-reoxygenation samples, the expressions were 1.01 ± 0.16 and 0.85 ± 0.13 , respectively. For 24 h control and hypoxia-reoxygenation samples, the expressions were 1.77 ± 0.68 and 3.76 ± 0.77 ($p=0.029$), respectively.

In 8 and 24 h hypoxia-reoxygenation samples, there was also a statistically significant decrease in the expression of SLC8A1 encoding sodium/calcium exchanger 1 related to calcium handling of cardiomyocytes (Fig. 5b). Slight but not statistically significant decrease was also seen in 24 h hypoxia samples. For 8 h control and hypoxia samples, the expressions were 1.38 ± 0.99 and 1.34 ± 0.95 , while for 24 h control and hypoxia samples they were 1.64 ± 1.06 and 1.12 ± 0.57 . For 8 h control and hypoxia-reoxygenation samples, the expressions were 1.01 ± 0.16 and 0.53 ± 0.12 ($p=0.029$), respectively. For 24 h control and hypoxia-reoxygenation samples, the expressions were 1.06 ± 0.23 and 0.26 ± 0.12 ($p=0.029$), respectively.

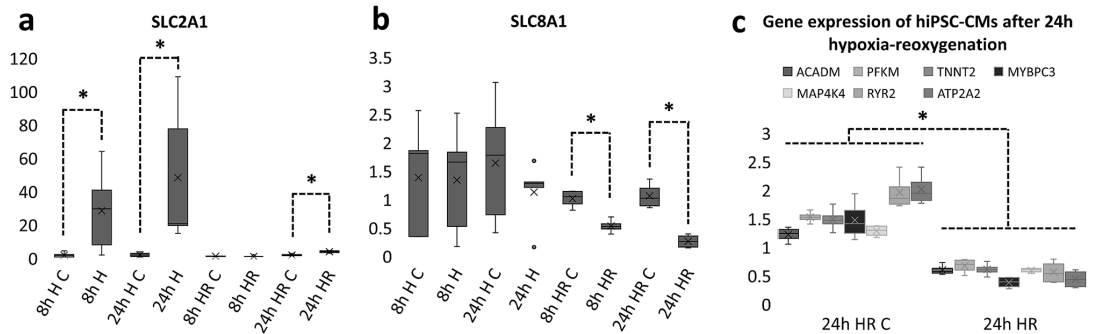


Figure 5. (a) SLC2A1 expression in hiPSC-CMs after 8 and 24 h hypoxia in control (C, $n_{8h}=6$, $n_{24h}=5$) and hypoxia (H, $n_{8h}=5$, $n_{24h}=6$) samples as well as 8 and 24 h hypoxia-reoxygenation (HR) in control (C, $n_{8h}=4$, $n_{24h}=4$) and hypoxia (H, $n_{8h}=4$, $n_{24h}=4$) samples from qPCR analysis presented as mean + standard deviation. SLC2A1 encodes glucose transporter 1 and is related to glucose uptake of the cells. As can be seen, SLC2A1 expression increases during hypoxia, and decreases during reoxygenation. However, after 24 h hypoxia-reoxygenation, the expression levels are still higher than in control. (b) SLC8A1 expression in hiPSC-CMs after 8 and 24 h hypoxia as well as 8 and 24 h hypoxia-reoxygenation. SLC8A1 encodes sodium/calcium exchanger and is related to calcium handling of hiPSC-CMs. As can be seen from the figure, the expression decreases after 8 and 24 h hypoxia-reoxygenation, but does not change significantly during hypoxia only. (c) Expression of several genes after 24 h hypoxia-reoxygenation. The expression of metabolic genes (ACADM and PFKM), sarcomeric genes (TNNT2 and MYBPC3), calcium handling genes (RYR2 and ATP2A2) and hypoxia marker MAP4K4 are all decreasing when compared to control. * $p < 0.05$.

In 24 h hypoxia-reoxygenation samples, there was also statistically significant decrease in the expression of ACADM ($c = 1.22 \pm 0.13$, 24 h HR = 0.60 ± 0.09 , $p = 0.029$), PFKM ($c = 1.52 \pm 0.10$, 24 h HR = 0.67 ± 0.13 , $p = 0.029$), TNNT2 ($c = 1.48 \pm 0.21$, 24 h HR = 0.60 ± 0.11 , $p = 0.029$), MYBPC3 ($c = 1.47 \pm 0.35$, 24 h HR = 0.38 ± 0.10 , $p = 0.029$), MAP4K4 ($c = 1.28 \pm 0.10$, 24 h HR = 0.59 ± 0.04 , $p = 0.029$), RYR2 ($c = 1.96 \pm 0.31$, 24 h HR = 0.56 ± 0.20 , $p = 0.029$) and ATP2A2 ($c = 2.01 \pm 0.28$, 24 h HR = 0.44 ± 0.16 , $p = 0.029$) (Fig. 5c).

Discussion

In the present study, a human based cardiac ischemia–reperfusion model which enables precise control and real time monitoring of oxygen combined with simultaneous measurement of the electrophysiological parameters of hiPSC-CMs is presented. Contrary to our previous studies, in which the similar system was used with hiPSC-CM aggregates^{11,12,24}, here the hiPSC-CMs were sorted and re-plated as a monolayer on top of the MEA-plates providing more homogenous iPS-CM population and enabling a detailed assessment of the structural characteristics of the cells. The more homogenous iPS-CM population also enables more precise qPCR analysis of cardiac markers while the samples contain approximately similar percentage of cardiomyocytes.

According to the results, hypoxia as well as reoxygenation alters the function of hiPSC-CMs significantly. The lowest beating frequency in the hiPSC-CMs was observed during 7–15 h hypoxia, whereas during 15–24 h hypoxia, the beating frequency gradually increased, suggesting that the hiPSC-CMs adapt to the low oxygen environment. During 0–6 h reoxygenation, the mean normalized beating frequency further increased and surpassed the baseline level but returned close to the baseline during 6–24 h reoxygenation. However, it is noteworthy that majority of the hiPSC-CMs retained their functionality after an initial drop in the beating frequency, during the late phase of hypoxia.

The decrease in cardiomyocyte beating frequency during ischemic stress has been earlier reported in primary CMs from rat^{27–29}, in perfused whole mouse heart³⁰. We and others have also reported the decrease with pluripotent stem cell derived-CMs^{11,12,24,31}, as well as the increase in the beating frequency upon reoxygenation^{11,12,24,27,29–31}.

The decrease in the beating rate might occur due to decrease in the ATP content in the CMs^{27,29} and due to the conduction block affecting the propagation of the action potential from pacemaker cells to other cells³¹. Reoxygenation is thought to reverse these changes, restoring the beating frequency close to the baseline^{27,29,31}. However, to our knowledge, this is the first time that an increase in the CM beating frequency already during a late phase of hypoxia has been reported. The reason behind the hiPSC-CM adaptation is likely balancing of the ATP supply and demand³², although the mechanisms for achieving the balance can only be speculated.

The immature metabolic phenotype of the hiPSC-CMs can be partially responsible for the observed adaptation of the cells and increase of the beating frequency with prolonged hypoxia. hiPSC-CMs are known to be more resistant to hypoxia and reoxygenation because of the enhanced ability of immature CMs to increase glycolytic flux^{33,34}. In the current study, increase in the expression of SLC2A1 encoding glucose transporter 1 was observed after 8 and 24 h hypoxia. During hypoxia, the CM metabolism relies on glycolysis, which is a relatively inefficient way to produce energy requiring increase in glucose uptake and expression of glucose transporters³⁵. However, the expression of PFKM gene encoding muscle type ATP-dependent 6-phosphofructokinase responsible for the

first committing step of glycolysis³⁵ did not increase after 8 or 24 h hypoxia. Furthermore, the medium used in the experiment did not contain either glucose or serum since presence of glucose attenuates the adverse effects of hypoxia³⁶. Thus, there must be also another mechanism for the hiPSC-CM functional adaptation.

In addition to changes in the beating frequency of the hiPSC-CMs as a response to hypoxia and reoxygenation, changes in depolarization time and field potential duration were investigated. Hypoxia increased the depolarization time, whereas it decreased the overall FPD. During reoxygenation, both the depolarization time and the FPD returned close to the baseline level. These findings are in line with other studies regarding prolongation of CM action potential depolarization time as well as shortening of the overall action potential duration during hypoxia and reoxygenation³⁷ and indicate that the hiPSC-CMs in the model function as expected.

Changes in the conduction velocity over the hiPSC-CM sheets were also investigated. During hypoxia, the signal propagation speed slowed down, and it took longer for the action potential to travel across the cell sheet. This could be due to the conduction blocks that are known to occur in ischemic conditions³⁸, which can prevent the action potential from traveling the shortest route through the cell sheet. The slowing was observed to be reversible, as the conduction velocity returned close to the baseline level during reoxygenation. These findings are in agreement with King et al. (2013), where delayed signal propagation has also been observed as response to ischemia³⁸.

There were no significant changes in the expression of genes related to calcium handling and contractility of the hiPSC-CMs after 8 or 24 h hypoxia. However, post-transcriptional changes in the proteins or changes in their activity due to hypoxia could in part explain the increase in the beating frequency. Electrophysiological alterations can include decrease in sodium and potassium currents, thus reducing the ATP demand of Na⁺/K⁺ ATPase. Decrease in calcium current could similarly reduce the ATP demand of Ca²⁺ ATPases as well as Na⁺/K⁺ ATPases. Reduced potassium current would also lead to increased resting membrane potential making the CMs more excitable, although the membrane potential must remain below the activation voltage of voltage-gated sodium channels³². The initial decrease in the hiPSC-CM beating frequency can thus later be accompanied by electrophysiological changes sufficiently reducing the ATP demand for the gradual increase in beating frequency during the late phase of hypoxia.

A peak in the HIF1 α expression was not found in this study. However, it is possible that the peak occurs already earlier than the chosen time points, or that the peak is subtle and thus difficult to observe. Since there was some variation in the expression between the samples from the same time points, it is possible that the subtle increase in the expression of HIF1 α was masked by the variation of the individual samples. It is also possible, that oxygen independent HIF1 α degradation pathways are activated³⁹. Furthermore, nuclear translocation of HIF1 α was not seen in the immunocytochemical staining, although it is known to play a crucial role in activation of hypoxia pathways⁴⁰.

Differences in hiPSC-CM morphology and sarcomere structure were observed after hypoxia and hypoxia-reoxygenation, which were supported by western blot analysis of the structural proteins. The morphological and structural changes in the hiPSC-CMs included partial detachment from the culture plate as well as disruption of the visible sarcomere structures. Furthermore, the area of the nuclei in the hiPSC-CMs decreased during hypoxia and hypoxia-reoxygenation. However, cell death was not observed (data not shown). The structural disintegration and the decrease in the nucleus size are associated with apoptotic cell death^{41,42}. However, the difference in the nucleus area could also partially be due to detachment of the cells, because in attached cells the nucleus is flat against the culture plate thus increasing the area in images, while in detached cells the nucleus has a more 3D spherical shape, which is not conveyed from 2D images. Furthermore, western blot analysis showed no band for cleaved caspase-3 associated with apoptosis.

The cellular damage in the hiPSC-CMs could also be indication of necrotic cell death, which is known to be the primary mechanism of cell death in ischemia-reperfusion^{41,42}. The decrease in MyBPC3 and Troponin T protein expression further supports the structural changes seen in the hiPSC-CMs. The decrease in Troponin T expression could be due to the release of Troponin T from the cells to the surroundings, although it was not measured in this study. However, Troponin T release from injured myocardium is a clinically used marker for myocardial infarction⁴³. Furthermore, necrotic cell death is associated with spillage of cellular contents into the extracellular space.

One limitation in this study was the immature phenotype of the hiPSC-CMs. As already mentioned, differences in hiPSC-CM metabolism make these cells more resistant to hypoxia-reoxygenation injury. Another limitation is the relatively constant pH throughout the hypoxia and reoxygenation treatments. Due to the large volume of medium compared to the cell mass, the pH of the culture did not change significantly during the hypoxia or reoxygenation. However, in heart, ischemia is accompanied by acidosis, a decrease in intracellular pH, which is known to affect the CM response to ischemia-reperfusion in primary animal CM models²⁸ and hiPSC-CMs^{8,10}. The third limitation is the slow speed in increase and decrease of the oxygen level in the culture, which gives the cells time to adjust to the conditions, whereas acute ischemic events are typically sudden in the clinical situation. Furthermore, electrical activity was recorded only in intervals, which could cause missing of potentially interesting events.

In summary, we conclude that hiPSC-CM model presented in this study can be used in modeling cardiac ischemia-reperfusion injury. With the iPS-CM based platform, we are able to monitor the temporal changes in cardiomyocyte function as well as electrophysiological parameters during different stages of ischemia-reperfusion event. There were significant differences in the beating frequency, depolarization time and field potential duration as well as conduction velocity. In addition, hypoxia altered the cell morphology and caused changes in the expression of structural proteins. With the presented hiPS-CM based platform, cardiac ischemia-reperfusion can be modeled and these parameters can be utilized when evaluating the effects of putative ischemia drugs and treatments in the future.

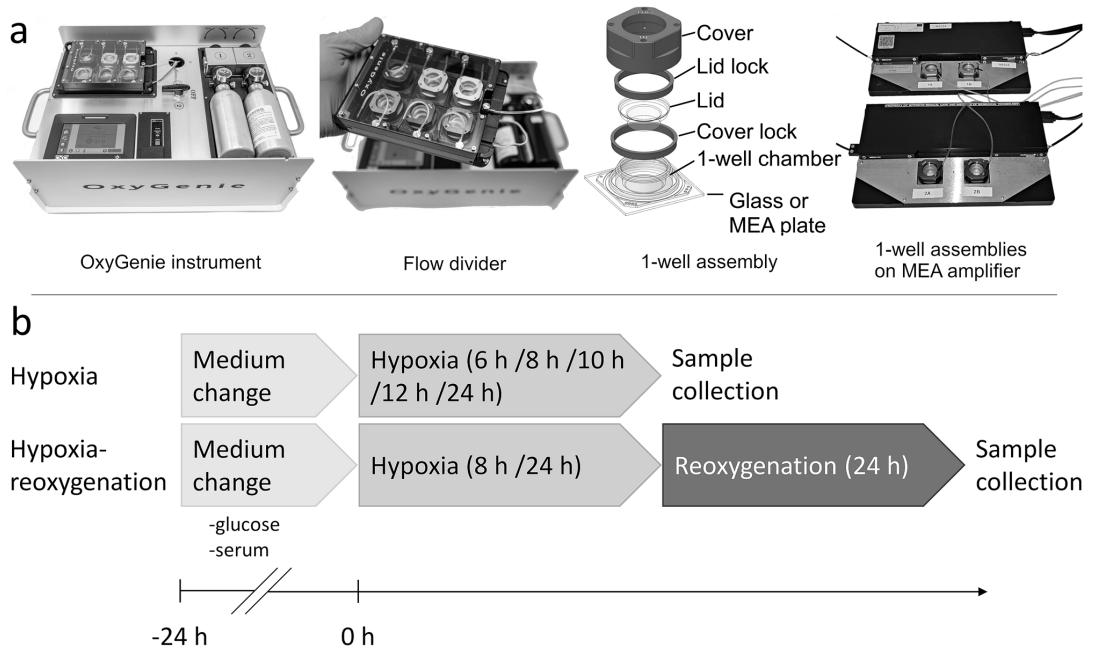


Figure 6. (a) Portable cell culture instrument include battery operated temperature controller and heat plate, two gas cylinders and flow divider allowing six individual 1-well assemblies. 1-well assembly includes 1-well chamber on plate (glass or MEA), the lid and the lid lock to seal the cell culture and to avoid evaporation, the cover and the cover lock to create and maintain the gas environment around gas permeable 1-well chamber. 1-well assembly on MEA plate can be fitted also to MCS signal amplifier and thus use it for long-term recordings outside the incubator. (b) Hypoxia and hypoxia-reoxygenation protocol.

Materials and methods

Cardiomyocyte differentiation and cell culture. UTA.04602.WT hiPSC line⁴⁴ was used in the experiments. hiPSCs were cultured on mouse embryonic fibroblast feeder cells (Applied StemCells, Inc) in KSR medium (KnockOut DMEM (Gibco) containing 10% KnockOut Serum Replacement (Gibco), 1% MEM NEAA (Gibco), 1% GlutaMAX (Gibco), 0.2% β -mercaptoethanol (Gibco) and 0.5% Penicillin/streptomycin (Lonza)). Embryoid body differentiation modified from Karakikes and coworkers⁴⁵ and Lian and coworkers⁴⁶ was used to differentiate the hiPSCs into cardiomyocytes (full protocol in Supplementary Information).

Magnetic activated cell sorting. Magnetic activated cell sorting (MACS) was performed on day 20 to enrich the cardiomyocyte concentration in the culture. MultiTissue Dissociation Kit (Miltenyi Biotec) was used according to manufacturer's instructions as described earlier⁴⁷. PSC-Derived Cardiomyocyte Isolation Kit, human (Miltenyi Biotec) was used to separate the cardiomyocytes from other cell types according to manufacturer's instructions⁴⁷. The CMs were suspended to 20% EB medium (KnockOut DMEM containing 20% FBS (Gibco), 1% MEM NEAA, 1% GlutaMAX and 0.5% Penicillin/streptomycin) and seeded to 1-well chambers on glass or MEA coated with 0.1% gelatin as cell sheets (density \sim 93,000 cells/cm²). The cells were cultured for 7–9 days before starting the hypoxia experiments. Half of the culture medium was exchanged three times a week.

Hypoxia and hypoxia-reoxygenation. Hypoxia and reoxygenation were performed using OxyGenie mini-incubator (Baker, USA), which is based on our previous studies^{26,48,49}. The portable cell culture incubator includes a battery-operated temperature controller with a heat plate, two prefilled and replaceable gas cylinders and a flow divider to hold six individual 1-well chamber assemblies on a glass plate (Fig. 6a). The 1-well assembly on an MEA plate fits to a MultiChannel Systems signal amplifier allowing long-term recordings outside an incubator. Portability of the OxyGenie and the individual 1-well chambers enable sample preparation and collection one at a time, minimizing the cell culture exposure to ambient air.

Day before exposing cells to hypoxia, serum- and glucose-free EB medium (glucose-free DMEM (Gibco) containing 1% MEM NEAA, 1% GlutaMAX and 0.5% Penicillin/streptomycin) was changed. On the following day, the samples were loaded into pre-warmed (37 °C) OxyGenie mini-incubator and hypoxia was initiated using 0% O₂ and 5% CO₂ (hypoxic) gas. The used time periods included 6, 8, 10, 12 and 24 h. Control samples were cultured in serum- and glucose-free EB medium in a standard 5% CO₂ incubator without the lids and covers for the same time periods.

Hypoxia-reoxygenation experiments were performed similarly to the hypoxia experiments, but after 8 or 24 h hypoxia, the gas was exchanged to 19% O₂ and 5% CO₂ (normoxic) gas for 24 h. The control cells were kept in the 1-well chambers on the glass inside the incubator for the whole experiment. Samples were collected after the hypoxia or hypoxia-reoxygenation one by one to minimize the exposure to ambient air. pH was measured from cell culture medium during sample collection using Sentron SI600 pH meter with Sentron MicroFET pH probe.

With MEA plates, hypoxia-reoxygenation was performed so that first the samples were connected to normoxic gas to measure a baseline overnight, after which, hypoxia was initiated using the hypoxic gas for 24 h. After the hypoxia, reoxygenation was performed by connecting the samples again to the normoxic gas for another 24 h. Hypoxia and hypoxia-reoxygenation protocols are presented in Fig. 6b.

Microelectrode array. Microelectrode array (MEA) plates (60MEA200/30iR-Ti, 8 × 8) were ordered from MultiChannel Systems MCS GmbH (Reutlingen, Germany) and PDMS 1-well chambers attached to the MEA were manufactured inhouse⁵⁰. MEA measurements were performed using MultiChannel Experimenter (version 2.14.0.19346, Multi Channel Systems, GmbH, Reutlingen, Germany). Sampling frequency was set to 25 kHz and the baseline was recorded for 1 min every hour for 20 h. During hypoxia and reoxygenation, MEA signals were recorded for 1 min every 30 min. The data were converted from MSRD into HDF5 format using MultiChannel DataManager (version 1.12.0.20014, Multi Channel Systems, GmbH, Reutlingen, Germany). The HDF5 files were analyzed with MATLAB (version R2018B, MathWorks, Inc., Natick, MA, USA) using scripts developed inhouse for beating frequency, depolarization time and field potential duration. Multi Channel Analyzer (version 2.14.0.19346, Multi Channel Systems, GmbH, Reutlingen, Germany) was used to detect peaks from the recorded data. The analyzed data was converted into ASCII files using Multi Channel DataManager and these files were analyzed for field potential propagation.

Oxygen measurement. The partial pressure of oxygen (pO₂) was measured from one sample to verify that the oxygen dynamics in the cell culture were as expected. In the verification experiment, a luminescence-based sensor together with a highly biocompatible sensing material, developed by Välimäki and coworkers⁵⁴ was used to monitor the oxygen level in the culture. The pO₂ was measured once a minute during the entire experiment, while MEA signals were recorded for 1 min every 30 min throughout the experiment at 20 kHz sampling frequency. After the experiment was finished, the cells were removed from the MEA plate and the oxygen measurement was calibrated using the same MEA.

Immunocytochemistry. Immunocytochemistry (full protocol in Supplementary Information) was performed right after hypoxia or hypoxia-reoxygenation for 8 and 24 h hypoxia, and 8 and 24 h hypoxia-reoxygenation samples. Mouse anti-MyBPC3 (1:500; Santa Cruz; sc-166081) and rabbit anti-HIF1 α (1:1000; Invitrogen; 700505) were used as primary antibodies and donkey anti-mouse Alexa Fluor 568 and donkey anti-rabbit Alexa Fluor 488 (1:800; Thermo Fisher Scientific) as secondary antibodies. Fluorescence was visualized with Zeiss LSM 800 Laser Scanning Confocal Microscope using Zeiss EC Plan-Neofluar 40x/0.75, WD 0.71 mm (Air) objective and 2 channel spectral detection with high-sensitivity PMT detector.

Analysis of hiPSC-CM sarcomere coverage. The area of visible sarcomeres and the total cell area was analyzed from the MyBPC3 channel of the fluorescent microscopy images using Paint.net (version 4.1.5, Dot-PDN, LLC, USA) and ImageJ⁵¹. The wand tool in Paint.net was used to determine the total area of the cells covering the image and the area covered by sarcomeres. ImageJ was then used to calculate the areas. Sarcomere coverage was calculated as the ratio between the area of visible sarcomeres and the total cell area and is expressed as percentage.

Analysis of hiPSC-CM nuclei area. The nucleus area was determined using Cell Profiler⁵². IdentifyPrimaryObjects was used to identify the nuclei in the DAPI channel of the fluorescent images. The minimum and maximum object size values were set as 50 and 250, respectively. Objects outside the set minimum and maximum as well as objects touching borders were discarded. Threshold strategy was set as global and the thresholding method used was two class Otsu. Shape was set for the method to distinguish clumped objects and MeasureObjectSizeShape was used to determine the nuclei area from the objects identified in the IdentifyPrimaryObjects.

Western blot. Protein samples were collected in 2 × Laemmli buffer (Bio-Rad) containing 5% β -mercaptoethanol (Sigma) and run in 4–20% Mini PROTEAN TGX Precast Protein Gel with 10 50 μ l wells (Bio-Rad). The proteins were blotted from the gel to PVDF membrane using Trans-Blot Turbo Transfer System (Bio-Rad) and Trans-Blot Turbo RTA Mini PVDF Transfer Kit (Bio-Rad). Mouse anti- β -actin (1:1000; Santa Cruz; sc-47778), rabbit anti-HIF1 α (1:1000), rabbit anti-cleaved caspase-3 (1:500; Abcam; ab32042), mouse anti-MyBPC3 (1:500) and mouse anti-Troponin T (1:1000; Abcam; ab33589) were used as primary antibodies and horseradish peroxidase-conjugated anti-mouse IgG (1:3000; Santa Cruz; sc-516102) and anti-rabbit IgG (1:2000; Dako; P0217) as secondary antibodies (full protocol in Supplementary Information). The protein-antibody complexes were detected using Amersham ECL Prime Western Blotting Detection Reagent (GE Healthcare Life Sciences) and ChemiDoc MP Imaging System (Bio-Rad) was used for imaging. The images were analyzed using Image Lab Software (Bio-Rad).

RNA extraction, reverse transcription and qPCR. Samples for qPCR from hypoxia and hypoxia-reoxygenation experiments were collected in QIAzol Lysis Reagent (Qiagen) and RNA was extracted using

Gene	Description	Function	Assay ID
ACADM	Acyl-CoA Dehydrogenase Medium Chain	Fatty acid metabolism	Hs00936584_m1
ACAA1	Acetyl-CoA acyltransferase 1	Fatty acid metabolism	Hs01576070_m1
PFKM	Phosphofructokinase, muscle	Glycolysis metabolism	Hs01075411_m1
SLC2A1	Solute carrier family 2, member 1/GLUT-1	Glycolysis metabolism	Hs00892681_m1
TNNT2	Cardiac type troponin T2	Sarcomeric	Hs00165960_m1
MYBPC3	Myosin binding protein C3, cardiac	Sarcomeric	Hs00165232_m1
RYR2	Ryanodine receptor 2, cardiac	Calcium handling	Hs00892883_m1
ATP2A2	ATPase, calcium transporting, cardiac muscle, slow twitch 2/ SERCA2a	Calcium handling	Hs00544877_m1
SLC8A1	Solute carrier family 8, member 1/NCX1	Calcium handling	Hs01062258_m1
HIF1A	Hypoxia inducible factor 1 alpha	Hypoxia marker	Hs00153153_m1
MAP4K4	Mitogen-activated protein kinase kinase kinase kinase 4	Hypoxia marker	Hs00377415_m1
CASP3	Caspase-3	Apoptosis	Hs00234387_m1
GAPDH	Glyceraldehyde-3-phosphate dehydrogenase	Housekeeping	Hs02758991_g1
TBP	TATA-box binding protein	Housekeeping	Hs00427620_m1
EEF1A1; EE+	Eukaryotic translation elongation factor 1 alpha 1	Housekeeping	Hs00265885_g1

Table 1. TaqMan 20 × Assays used in qPCR.

miRNeasy Mini Kit (Qiagen) following manufacturer's instructions. RNA quality was ensured using. Reverse transcription (RT) was performed using High-Capacity cDNA Reverse Transcription Kit (Applied Biosystems), following manufacturer's instructions. Shortly, 2X RT Master Mix was prepared based on instructions of the kit and 10 µl of 2X RT Master Mix was mixed with 10 µl of sample. Samples were run in thermal cycler with following protocol: 10 min at 25 °C, 120 min at 37 °C, 5 min at 85 °C and at 4 °C until samples were stored at -20 °C.

qPCR for mRNA samples was performed using TaqMan Gene Expression Master Mix (Applied Biosystems) following manufacturer's instructions. TaqMan 20 × Assays for TNNT2, MYBPC3, ACADM, ACAA1, SLC2A1, PFKM, RYR2, ATP2A2, SLC8A1, MAP4K4, HIF1A, CASP3, GAPDH, EEF1A1 and TBP were used, details of the assays are presented in Table 1. Master mixes were prepared as instructed in the kit. Three technical replicates were used for each sample with each gene. 1 µl of diluted cDNA (diluted 2:1 to Milli-Q water) was pipetted into 9 µl of master mix (total reaction volume 10 µl). Plates were run in ABI7300 thermal cycler (Applied Biosystems) with following protocol: 2 min at 50 °C, 10 min at 95 °C and 40 cycles of 15 s at 95 °C and 1 min at 60 °C.

Statistical analysis. Statistical analyses were performed with IMB SPSS Statistics for Windows (version 25.0, IMB Corp., Armonk, NY, USA). Independent samples Mann–Whitney U test was used to test the statistical significance between control and hypoxia or hypoxia-reoxygenation groups for data extracted from qPCR, western blot, immunostaining, depolarization time and field potential duration and field potential propagation, while related-samples Wilcoxon Signed Rank Test was used for beating frequency. $p < 0.05$ was considered as statistically significant. The data are presented as mean ± standard deviation.

Data availability

All data are available from the authors by request.

Received: 10 September 2020; Accepted: 5 February 2021

Published online: 18 February 2021

References

- Nowbar, A. N., Gitto, M., Howard, J. P., Francis, D. P. & Al-Lamee, R. Mortality from ischemic heart disease: Analysis of data from the world health organization and coronary artery disease risk factors from NCD risk factor collaboration. *Circ. Cardiovasc. Qual. Outcomes* **12**, 1–11 (2019).
- Hausenloy, D. J. & Yellon, D. M. Myocardial ischemia-reperfusion injury: A neglected therapeutic target. *J. Clin. Invest.* **123**, 92–100 (2013).
- Chen, T. & Vunjak-Novakovic, G. In vitro models of ischemia-reperfusion injury. *Regen. Eng. Transl. Med.* **4**, 142–153 (2018).
- Milani-Nejad, N. & Janssen, P. M. L. Small and large animal models in cardiac contraction research: Advantages and disadvantages. *Pharmacol. Ther.* **141**, 235–249 (2014).
- Harding, J. D. Nonhuman primates and translational research: Progress, opportunities, and challenges. *ILAR J.* **58**, 141–150 (2017).
- Karakikes, I., Mohamed, A., Termglinchan, V. & Wu, J. C. Human induced pluripotent stem cell-derived cardiomyocytes: Insights into molecular, cellular, and functional phenotypes. *Circ. Res.* **117**, 80–88 (2015).
- Robertson, C., Tran, D. D. & George, S. C. Concise review: maturation phases of human pluripotent stem cell-derived cardiomyocytes. *Stem Cells* **31**, 829–837 (2013).
- Hidalgo, A. *et al.* Modelling ischemia-reperfusion injury (IRI) in vitro using metabolically matured induced pluripotent stem cell-derived cardiomyocytes. *APL Bioeng.* **2**, 026102 (2018).
- Sebastião, M. J. *et al.* Bioreactor-based 3D human myocardial ischemia/reperfusion in vitro model: A novel tool to unveil key paracrine factors upon acute myocardial infarction. *Transl. Res.* **215**, 57–74 (2020).
- Chen, T. & Vunjak-Novakovic, G. Human tissue-engineered model of myocardial ischemia-reperfusion injury. *Tissue Eng. Part A* **25**, 711–724 (2019).
- Shah, D. *et al.* Modeling of LMNA-related dilated cardiomyopathy using human induced pluripotent stem cells. *Cells* **8**, 594 (2019).

12. Välimäki, H. *et al.* Fluorimetric oxygen sensor with an efficient optical read-out for in vitro cell models. *Sens. Actuators B Chem.* **249**, 738–746 (2017).
13. Fernández-Morales, J.-C., Hua, W., Yao, Y. & Morad, M. Regulation of Ca²⁺ signaling by acute hypoxia and acidosis in cardiomyocytes derived from human induced pluripotent stem cells. *Cell Calcium* **78**, 1–14 (2019).
14. Wei, W. *et al.* Danshen-enhanced cardioprotective effect of cardioplegia on ischemia reperfusion injury in a human-induced pluripotent stem cell-derived cardiomyocytes model. *Artif. Organs* **41**, 452–460 (2017).
15. Wei, H., Wang, C., Guo, R., Takahashi, K. & Naruse, K. Development of a model of ischemic heart disease using cardiomyocytes differentiated from human induced pluripotent stem cells. *Biochem. Biophys. Res. Commun.* **520**, 600–605 (2019).
16. Kirby, R. J. *et al.* Discovery of novel small-molecule inducers of heme oxygenase-1 that protect human ipsc-derived cardiomyocytes from oxidative stress. *J. Pharmacol. Exp. Ther.* **364**, 87–96 (2018).
17. Canfield, S. G. *et al.* High glucose attenuates anesthetic cardioprotection in stem-cell-derived cardiomyocytes: The role of reactive oxygen species and mitochondrial fission. *Anesth. Analg.* **122**, 1269–1279 (2016).
18. Lu, Y., Bu, M. & Yun, H. Sevoflurane prevents hypoxia/reoxygenation-induced cardiomyocyte apoptosis by inhibiting PI3KC3-mediated autophagy. *Hum. Cell* **32**, 150–159 (2018).
19. Zhao, X. *et al.* Comparison of non-human primate versus human induced pluripotent stem cell-derived cardiomyocytes for treatment of myocardial infarction. *Stem Cell Rep.* **10**, 422–435 (2018).
20. Fiedler, L. R. *et al.* MAP4K4 inhibition promotes survival of human stem cell-derived cardiomyocytes and reduces infarct size in vivo. *Cell Stem Cell* **24**, 579–591.e12 (2019).
21. Robertson-Gray, O. J. *et al.* 1- α -Lysophosphatidylinositol (LPI) aggravates myocardial ischemia/reperfusion injury via a GPR55/ROCK-dependent pathway. *Pharmacol. Res. Perspect.* **7**, 1–12 (2019).
22. Sebastião, M. J. *et al.* Human cardiac progenitor cell activation and regeneration mechanisms: Exploring a novel myocardial ischemia/reperfusion in vitro model. *Stem Cell Res. Ther.* **10**, 1–16 (2019).
23. Ward, M. C. & Gilad, Y. A generally conserved response to hypoxia in iPSC-derived cardiomyocytes from humans and chimpanzees. *Elife* **8**, 1–32 (2019).
24. Välimäki, H. *et al.* Covalent immobilization of luminescent oxygen indicators reduces cytotoxicity. *Biomed. Microdevices* **22**, 41 (2020).
25. Hsieh, A., Feric, N. T. & Radisic, M. Combined hypoxia and sodium nitrite pretreatment for cardiomyocyte protection in vitro. *Biotechnol. Prog.* **31**, 482–492 (2015).
26. Kreutzer, J. *et al.* Mini-incubator for prolonged cell culture and hypoxia studies outside an incubator. *Front. Neurosci.* **10**, (2016).
27. Laubriet, A. *et al.* Changes in HSP70 and P53 expression are related to the pattern of electromechanical alterations in rat cardiomyocytes during simulated ischemia. *Mol. Cell. Biochem.* **220**, 77–86 (2001).
28. Tissier, C. *et al.* Specific electromechanical responses of cardiomyocytes to individual and combined components of ischemia. *Can. J. Physiol. Pharmacol.* **80**, 1145–1157 (2002).
29. Durot, L., Athias, P., Oudot, F. & Grynberg, A. Influence of phospholipid long chain polyunsaturated fatty acid composition on neonatal rat cardiomyocyte function in physiological conditions and during glucose-free hypoxia-reoxygenation. *Mol. Cell. Biochem.* **175**, 253–262 (1997).
30. Conklin, D. J. *et al.* TRPA1 channel contributes to myocardial ischemia-reperfusion injury. *Am. J. Physiol. Hear. Circ. Physiol.* **316**, H889–H899 (2019).
31. Wenzel, F., Dittrich, M., Hescheler, J. & Grote, J. Hypoxia influences generation and propagation of electrical activity in embryonic cardiomyocyte clusters. *Comp. Biochem. Physiol. A Mol. Integr. Physiol.* **132**, 111–115 (2002).
32. Stecky, J. A. W., Galli, G. L., Shiels, H. A. & Farrell, A. P. Cardiac survival in anoxia-tolerant vertebrates: An electrophysiological perspective. *Comp. Biochem. Physiol. C Toxicol. Pharmacol.* **148**, 339–354 (2008).
33. Patterson, J. A. & Zhang, L. Hypoxia and fetal heart development. *Curr. Mol. Med.* **10**, 653–666 (2010).
34. Neary, M. T. *et al.* Hypoxia signaling controls postnatal changes in cardiac mitochondrial morphology and function. *J. Mol. Cell. Cardiol.* **74**, 340–352 (2014).
35. Rosano, G., Fini, M., Caminiti, G. & Barbaro, G. Cardiac metabolism in myocardial ischemia. *Curr. Pharm. Des.* **14**, 2551–2562 (2008).
36. Jovanović, S., Jovanović, N. & Jovanović, A. High glucose protects single beating adult cardiomyocytes against hypoxia. *Biochem. Biophys. Res. Commun.* **341**, 57–66 (2006).
37. Klabunde, R. E. Cardiac electrophysiology: Normal and ischemic ionic currents and the ECG. *Adv. Physiol. Educ.* **41**, 29–37 (2017).
38. King, J. H., Huang, C. L. H. & Fraser, J. A. Determinants of myocardial conduction velocity: Implications for arrhythmogenesis. *Front. Physiol.* **4**, 154 (2013).
39. Mylonis, I., Simos, G. & Paraskeva, E. Hypoxia-inducible factors and the regulation of lipid metabolism. *Cells* **8**, 214 (2019).
40. Lee, J. W., Ko, J., Ju, C. & Eltzschig, H. K. Hypoxia signaling in human diseases and therapeutic targets. *Exp. Mol. Med.* **51**, 1–13 (2019).
41. Kwon, H. K., Lee, J. H., Shin, H. J., Kim, J. H. & Choi, S. Structural and functional analysis of cell adhesion and nuclear envelope nano-topography in cell death. *Sci. Rep.* **5**, 1–15 (2015).
42. Fink, S. L. & Cookson, B. T. Apoptosis, pyroptosis, and necrosis: Mechanistic description of dead and dying eucaryotic cells. *Infect. Immun.* **73**, 1907–1916 (2005).
43. Mair, J. *et al.* How is cardiac troponin released from injured myocardium?. *Eur. Hear. J. Acute Cardiovasc. Care* **7**, 553–560 (2018).
44. Ojala, M. *et al.* Culture conditions affect cardiac differentiation potential of human pluripotent stem cells. *PLoS ONE* **7**, e48659 (2012).
45. Karakikes, I. *et al.* Small molecule-mediated directed differentiation of human embryonic stem cells toward ventricular cardiomyocytes. *Stem Cells Transl. Med.* **3**, 18–31 (2014).
46. Lian, X. *et al.* Directed cardiomyocyte differentiation from human pluripotent stem cells by modulating Wnt/ β -catenin signaling under fully defined conditions. *Nat. Protoc.* **8**, 162–175 (2013).
47. Pekkanen-Mattila, M. *et al.* Polyethylene terephthalate textiles enhance the structural maturation of human induced pluripotent stem cell-derived cardiomyocytes. *Materials (Basel)* **12**, 1805 (2019).
48. Kreutzer, J. *et al.* Cell culture chamber with gas supply for prolonged recording of human neuronal cells on microelectrode array. *J. Neurosci. Methods* **280**, 27–35 (2017).
49. Metsälä, O. *et al.* Transportable system enabling multiple irradiation studies under simultaneous hypoxia in vitro. *Radiat. Oncol.* **13**, 1–11 (2018).
50. Kreutzer, J. *et al.* Structured PDMS chambers for enhanced human neuronal cell activity on MEA platforms. *J. Bionic Eng.* **9**, 1–10 (2012).
51. Schindelin, J. *et al.* Fiji: An open-source platform for biological-image analysis. *Nat. Methods* **9**, 676–682 (2012).
52. McQuin, C. *et al.* Cell Profiler 3.0: Next-generation image processing for biology. *PLoS Biol.* **16**, 1–17 (2018).

Acknowledgements

We thank Tampere University Electrophysiology Core, Imaging Core and iPS Core.

Author contributions

Conception and design: M.H. and M.P-M. Main manuscript text: M.H. and M.P-M. Conducting experiments: M.H., J.K, H.V. and H.L. Data analysis and interpretation: M.H. and A-J.M. Formal analysis: M.H., A-J.M. and H.H. Figure preparation: Figs. 1–5 and S1 M.H., Fig. 6 M.H and J.K., Supplementary Fig. S2 M.H and A-J.M., Supplementary Fig. S3 M.H. and H.V., supplementary Fig. S4 A-J.M. Resources: K.A-S. and P.K. Funding acquisition: K.A-S., P.K. and M.H. Supervision: M.P-M. and K.A-S. All authors reviewed and accepted the manuscript.

Funding

This work was supported by grants from Academy of Finland, Finnish Foundation of Cardiovascular Research, Biocenter Finland Stem Cell Platform, Juselius Foundation, Pirkanmaa Regional Foundation, Maud Kuistila Memorial Foundation, and Inkeri and Mauri Vänskä Foundation.

Competing interests

The authors declare no competing interests.

Additional information

Supplementary Information The online version contains supplementary material available at <https://doi.org/10.1038/s41598-021-83740-w>.

Correspondence and requests for materials should be addressed to M.H.

Reprints and permissions information is available at www.nature.com/reprints.

Publisher's note Springer Nature remains neutral with regard to jurisdictional claims in published maps and institutional affiliations.



Open Access This article is licensed under a Creative Commons Attribution 4.0 International License, which permits use, sharing, adaptation, distribution and reproduction in any medium or format, as long as you give appropriate credit to the original author(s) and the source, provide a link to the Creative Commons licence, and indicate if changes were made. The images or other third party material in this article are included in the article's Creative Commons licence, unless indicated otherwise in a credit line to the material. If material is not included in the article's Creative Commons licence and your intended use is not permitted by statutory regulation or exceeds the permitted use, you will need to obtain permission directly from the copyright holder. To view a copy of this licence, visit <http://creativecommons.org/licenses/by/4.0/>.

© The Author(s) 2021

MANUSCRIPT
IV

Electrophysiological changes of human induced pluripotent stem cell-derived cardiomyocytes during acute hypoxia and reoxygenation

Martta Häkli, Joose Kreutzer, Antti-Juhana Mäki, Hannu Välimäki, Reeya Maria Cherian, Pasi Kallio, Katriina Aalto-Setälä, Mari Pekkanen-Mattila

Publication reprinted with the permission of the copyright holders.

